Structure, Magnetism, and Binding of Novel Two-Dimensional Materials:

Europium-Intercalated Graphene, Cluster Lattices, and Polar Oxide Bilayers

I n a u g u r a l - D i s s e r t a t i o n

zur

Erlangung des Doktorgrades

der Mathematisch-Naturwissenschaftlichen Fakultät

der Universität zu Köln

vorgelegt von

Dipl.-Phys. Stefan Schumacher

aus Köln

Köln 2014

Berichterstatter:	Prof. Dr. Thomas Michely
(Gutachter)	Prof. Dr. Tim O. Wehling
	Prof. Dr. Heiko Wende
Vorsitzender der Prüfungskommission:	Prof. Dr. Sanjay Mathur
Beisitzer:	Priv.-Doz. Dr. Carsten Busse
Tag der mündlichen Prüfung:	22. Mai 2014

Abstract

In this thesis, novel two-dimensional materials are grown by molecular beam epitaxy and studied in detail. The surface structure is investigated by scanning tunneling microscopy (STM) and low energy electron diffraction (LEED), whereas the magnetic properties are determined by X-ray magnetic circular dichroism (XMCD). The experimental results are supported by density functional theory (DFT) calculations.

The rare earth metal europium (Eu) intercalates at elevated temperatures underneath graphene (Gr) on iridium (Ir), driven by a large energy gain. Low energy electron microscopy (LEEM) and photoemission electron microscopy (PEEM) show that penetration at wrinkles is the dominating pathway for intercalation. Depending on the coverage, the Eu atoms arrange in a (2×2) or a $(\sqrt{3} \times \sqrt{3})$R30° superstructure with respect to Gr. The intercalated material forms complex patterns of stripes and islands. The underlying mechanism is explained to be an interplay of local binding inhomogeneities and relaxation of pre-exisiting strain in Gr. As a side benefit, the initial strain distribution is directly visualized by local variations in the intercalation step density.

Angle-resolved photoemission spectroscopy (ARPES) reveals that Eu and cesium (Cs) intercalation induce a strong local n-doping. By deposition of cationic adsorbates onto partially intercalated Gr a preferential binding to the non-intercalated regions is found. This preference is attributed to changes in the local work function caused by the n-doping. DFT calculations show that charge redistributions and substrate-dependent screening yield corrections to this elementary model.

Moreover, fully closed Eu monolayers are grown on intercalated Gr and structurally compared with the growth of Eu on pristine Gr. Furthermore, the structure of Eu on Ir(111) is investigated. For deposition of gadolinium (Gd) on Ir(111), alloying with the substrate is observed and a comparison to other surface alloys is drawn.

The two intercalated Eu layers have fundamentally different magnetic properties: Whereas the (2×2) structure is paramagnetic, the $(\sqrt{3} \times \sqrt{3})$R30° layer shows a substantial magnetic coupling. For the latter, a strong in-plane anisotropy arising from the low aspect ratio is found. DFT calculations indicate the relevance of the Ir substrate for the magnetic coupling, which explains deviations from the corresponding graphite intercalation compound. For samples with Eu adsorbed on top of Gr a partial oxidation to europium oxide (EuO) is identified, which dominates the magnetic properties.

Moreover, the magnetic properties of cobalt (Co) clusters on the Gr/Ir(111) moiré are investigated. An improved recipe for the cluster growth reduces undesired effects of cluster coalescence. Small platinum-seeded $Pt_{15}Co_{28}$ clusters are superparamagnetic at 10 K, whereas larger $Ir_{50}Co_{500}$ and Co_{2700} clusters exhibit a hysteresis due to the higher blocking temperature. The orbital moment is enhanced for the smallest clusters and gradually decreases towards the bulk value with increasing cluster size. The clusters do not show magnetic anisotropy, indicating a weak interaction with the substrate. Furthermore, rhodium (Rh) clusters are analyzed, but they do not reveal magnetic moments.
Finally, an O terminated polar EuO(111) bilayer of high quality and exceptional stability is grown on Ir(111). DFT calculations show that the interlayer spacing is strongly reduced compared to the bulk material, which results in an expanded in-plane lattice parameter and rotational epitaxy. The layer contraction reduces together with a surface metalization the electrostatic potential of the film. For higher coverages and Eu rich growth conditions the polarity is additionally reduced by a partial Eu adlayer. The apparent height of the EuO(111) islands in STM strikingly depends on the type of co-adsorbed species on the adjacent Ir terraces, which can be attributed to different work functions. The EuO(111) bilayer does not exhibit ferromagnetism down to 45 K as revealed by magneto-optical Kerr effect (MOKE) measurements.

Kurzdarstellung

Im Rahmen dieser Arbeit werden verschiedene neuartige zweidimensionale Materialien mittels Molekularstrahlepitaxie gewachsen und detailliert untersucht. Zur Bestimmung der Oberflächenstruktur dienen dabei Rastertunnelmikroskopie (STM) und niederenergetische Elektronenbeugung (LEED), während die magntischen Eigenschaften mit zirkularem Röntgendichroismus (XMCD) gemessen werden. Die experimentellen Ergebnisse werden durch Dichtefunktionaltheorie-Rechnungen (DFT) gestützt.

Das Seltenerdmetall Europium interkaliert bei erhöhten Temperaturen getrieben durch einen großen Energiegewinn unter Graphen auf Iridium. Niederenergetische Elektronenmikroskopie (LEEM) und Photoemissionselektronenmikroskopie (PEEM) zeigen, dass die Europiumatome dabei hauptsächlich an Falten der Graphenlage eindringen. Abhängig von der Bedeckung, formen die Europiumatome entweder eine (2×2)- oder eine $(\sqrt{3} \times \sqrt{3})$R30°-Überstruktur in Bezug auf Graphen. Das interkalierte Material bildet komplexe Muster aus Streifen und Inseln. Der zugrundeliegende Mechanismus wird durch das Zusammenspiel von lokalen Bindungsinhomogenitäten und der Relaxation von präexistenter Dehnung im Graphen erklärt. Als Nebeneffekt, wird die ursprüngliche Dehnungsverteilung direkt durch die Interkalationsstufendichte abgebildet.

Winkelaufgelöste Photoemissionsspektroskopie (ARPES) zeigt, dass sowohl Europium- als auch Cäsiuminterkalation eine starke n-Dotierung des Graphens verursacht. Bei der Deposition von kationischen Adsorbaten auf teilinterkaliertem Graphen wird eine bevorzugte Bindung an die nichtinterkalierten Bereiche beobachtet. Diese Bevorzugung liegt in einer Veränderung der lokalen Austrittsarbeit durch die Dotierung begründet. DFT-Rechnungen zeigen, dass Ladungsumverteilungen und ein substratabhängiges Abschirmverhalten Korrekturen zu diesem eingängigen Modell liefern.

Des Weiteren werden volle Europiummonolagen auf interkaliertem Graphen gewachsen und strukturell mit dem Wachstum von Europium auf nichtinterkaliertem Graphen verglichen. Zudem wird die Struktur von Europium auf Ir(111) untersucht. Bei der Deposition von Gadolinium auf Ir(111) bildet sich eine Legierung mit Substrat, sodass ein ein Vergleich zu anderen Oberflächenlegierungen gezogen werden kann.

Die beiden interkalierten Europiumlagen besitzen grundsätzlich verschiedene magnetische Eigenschaften: Während die (2×2)-Struktur paramagnetisch ist, weist die $(\sqrt{3}\times\sqrt{3})$R30°-Lage eine substantielle magnetische Kopplung auf. Für die letztere Struktur liegt die

Magnetisierung bevorzugt in der Ebene, was aus der Zweidimensionalität der Lage resultiert. DFT-Rechnungen weisen auf eine besondere Bedeutung des Iridiumsubstrats hin, was Unterschiede zur entsprechenden Graphitinterkalationsverbindung erklärt. Für alle Proben, bei denen Europium in adsorbierter Form vorliegt, findet eine teilweise Oxidation zu Europiumoxid statt, welches die magnetischen Eigenschaften dominiert.
Darüber hinaus werden die magnetischen Eigenschaften von Cobalt-Clustergittern auf dem Moiré von Graphen mit Ir(111) untersucht. Ein verbessertes Wachstumsrezept minimiert dabei unerwünschte Effekte durch die Koaleszenz von Clustern. Während kleine $Pt_{15}Co_{28}$-Cluster mit Platin-Keimen superparamagnetisch sind, weisen größere $Ir_{50}Co_{500}$- und Co_{2700}-Cluster auf Grund der höheren Blockingtemperautur hysteretisches Verhalten auf. Das magnetische Bahnmoment ist für die kleinsten Cluster erhöht und nähert sich mit zunehmender Clustergröße stetig dem Wert im Festkörper an. Die Cluster besitzen keine magnetische Anisotropie, was auf eine schwache Wechselwirkung mit dem Substrat hindeutet. Des Weiteren werden Rhodium-Cluster untersucht, die jedoch keine messbaren magnetischen Momente aufweisen.
Zuletzt wird eine sauerstoffterminierte polare EuO(111)-Doppellage von hoher Qualität und außergewöhnlicher Stabilität auf Ir(111) untersucht. DFT-Rechnungen zeigen, dass die Doppellage einen stark reduzierten Lagenabstand aufweist, der einen erhöhten Gitterparameter in der Ebene sowie Rotationsepitaxie nach sich zieht. Der reduzierte Lagenabstand verringert gemeinsam mit einer Metallisierung der Doppellage das elektrostatische Potential. Für höhere Bedeckungen und europiumreiche Wachstumsbedingungen wird die Polarität zusätzlich durch eine adsorbierte Europium-Teillage minimiert. Die scheinbare Höhe der EuO(111)-Inseln im STM hängt stark von der Art der Adsorbate auf den umgebenden Ir(111)-Terrassen ab, was in unterschiedlichen Austrittsarbeiten begründet liegt. Die Doppellage zeigt keinen Ferromagnetismus bis hinab zu 45 K, wie Messungen des magneto-optischen Kerr Effekts (MOKE) belegen.

Contents

Frequently Used Abbreviations

Chemical elements frequently used in this thesis are carbon (C), oxygen (O), iron (Fe), cobalt (Co), rhodium (Rh), cesium (Cs), iridium (Ir), platinum (Pt), europium (Eu), and gadolinium (Gd). Furthermore, graphene is abbreviated by Gr.

ARPES	-	Angle-Resolved Photoemission Spectroscopy
CVD	-	Chemical Vapor Deposition
DFT	-	Density Functional Theory
fcc	-	face-entered cubic
FWHM	-	Full Width at Half Maximum
GIC	-	Graphite Intercalation Compound
hcp	-	hexagonal close-packed
(L)DOS	-	(Local) Density of States
LEED/LEEM	-	Low Energy Electron Diffraction/Microscopy
MBE	-	Molecular Beam Epitaxy
ML/BL	-	Monolayer/Bilayer (see each chapter for definition)
MOKE	-	Magneto-Optical Kerr Effect
(N)NN	-	(Next) Nearest Neighbor
PEEM	-	Photoemission Electron Miscoscopy
RKKY	-	Ruderman-Kittel-Kasuya-Yoshida (interaction)
STM/STS	-	Scanning Tunneling Microscopy/Spectroscopy
TBA	-	Tight-Binding Approximation
TEY	-	Total Electron Yield
TPG	-	Temperature Programmed Growth
UHV	-	Ultra High Vacuum
vdW	-	van der Waals
XAS	-	X-Ray Adsorption Spectroscopy
XMCD	-	X-Ray Magnetic Circular Dichroism

CHAPTER 1

Introduction

Magnetism has fascinated mankind at least since the invention of the compass by the early Chinese civilization. The applications of magnetism are manifold and range in size from several meters down to the nanometer regime. When reducing the dimensions, often novel magnetic phenomena occur which cannot be deduced from the bulk counterpart [1]. Thus, the field of *nanomagnetism*, which deals with nanoparticles and -wires, thin films, and multilayer systems, is a fertile field for scientific research.

Small magnetic particles often occur in nature: They are found in living beings from bacteria [2] to higher organisms, such as insects or birds [3], and allow them to orient in the Earth´s magnetic field. Fossils of magnetotactic bacteria [4] and naturally occurring magnetic nanoparticles in rocks and soils contain comprehensive information about geology, environmental conditions, and past anthropic activities [5].

Also in the view of technological applications, nanomagnetism is an integral part of today's world: In medicine, it may be used for drug delivery to specific organs and tissues [6], cancer therapy by magnetic hyperthermia [7], or magnetic resonance imaging [8]. Moreover, small magnetic structures are indispensable for magnetic recording and data storage: The discovery of the giant magnetoresistance (GMR) effect [9–11] made it possible to reduce the bit size in hard disk drives down to the nanometer regime [12]. Closely related to nanomagnetism is the field of spintronics, which wants to use the electron's spin instead of its charge as information carrier [13, 14]. Since a pure spin current does not produce ohmic losses, spintronics potentially offers highly energy-efficient logic devices.

In order to either improve existing or to develop novel nanomagnetic materials, it is of fundamental importance to understand not only the magnetic behavior, but also the structural and binding properties. Therefore, this thesis combines classical techniques of surface science such as scanning tunneling spectroscopy and low energy electron diffraction

with magnetic measurements by means of X-ray magnetic circular dichroism. Supported by density functional theory calculations, a profound understanding on structure, magnetism, and binding of novel two-dimensional materials is obtained.

A promising material in the view of spintronics is graphene (Gr). The two-dimensional carbon allotrope has a high electron mobility [15] and a long spin diffusion length [16], which turns it into an excellent spin conductor. Since the electrons in Gr are inherently not spin-polarized, one needs to bring Gr in contact with magnetic materials to make full use of this potential. However, the extended d orbitals of the ferromagnetic transition metals Fe, Co, and Ni destroy the unique band structure of Gr by forming covalent bonds [17, 18]. Therefore, it is a promising approach to contact Gr with rare earth elements, since most of them do not possess occupied d orbitals, and the magnetic moment carried by the localized 4f shell is highly robust to the chemical environment.

With this in view, the intercalation of Eu underneath Gr on Ir(111) is investigated. Intercalation has previously been shown to be a flexible means to manipulate the properties of Gr [19–23]. Furthermore, it allows to efficiently protect a reactive layer against oxidation [24]. Several points motivate the choice of Eu as intercalant: First, Eu has a large magnetic moment of $7\,\mu_B$ and displays magnetic order in the bulk [25–27]. Second, the binding of Eu to Gr is predominantly of ionic character and thus leaves the band structure of Gr intact [28, 29]. Finally, the corresponding graphite intercalation compound EuC_6 shows an unusual metamagnetic behavior [30, 31]. Thus, one may conjecture also exceptional magnetic properties for Eu intercalated Gr. Moreover, changes in magnetism when going from the bulk compound to a single monolayer can be analyzed.

While investigating the intercalation of Eu, two side benefits were discovered: First, it became apparent that the intercalated material forms complex and appealing patterns. Pattern formation has always fascinated surface scientists, ranging from early investigations of the Si(111) (7×7) reconstruction [32], via self-assembly of Pb on Cu(111) [33], right up to ion beam induced pattern formation on Si [34]. Hence, it is interesting to reveal whether novel pattern formation mechanisms are involved in the present system. Second, it turned out that the binding of ionic adsorbates to Gr is influenced by the intercalation. Although similar effects have been reported before [35–38], the Eu intercalation pattern with patches of intercalated and non-intercalated Gr side by side is a unique tool to directly visualize a preferred binding to certain regions.

In addition to the interest for Gr itself in the context of nanomagnetism, the moiré pattern of Gr with Ir(111) can serve as a template for the growth of well-ordered, monodisperse clusters with tunable size [39, 40]. Lattices of ferromagnetic transition metal clusters

are highly interesting in respect of their potential use in magnetic data storage devices, since they provide a high density of well-separated magnetic domains [41]. Furthermore, their systematic investigation allows to address several fundamental questions: How do the magnetic properties change with the cluster size? Do the clusters show an anisotropy as strong as the one predicted for Co dimers on Gr [42] or measured for adsorbed and intercalated Co layers on Gr on Ir(111) [43, 44]? And finally, is there a magnetic coupling between the clusters, since they are separated by only 2.5 nm? Moreover, it is interesting to investigate clusters made of 4d transition metals such as Rh, Ru, or Pd which are non-magnetic in the bulk, but have been either predicted or proven to exhibit magnetic moments when present in the form of small clusters [45, 46].

Besides ferromagnetic metals, also ferromagnetic semiconductors such as EuO are promising materials for spintronics [47]. Previously, EuO(100) films on Ni(100) [48, 49] and Gr [50, 51] have been successfully investigated by our group. In this thesis, EuO is grown on Ir(111), resulting in the formation of a EuO(111) bilayer, where the oppositely charged Eu and O layers are stacked on top of each other. Such a polar surface orientation is usually avoided by nature since it involves a high electrostatic energy [52, 53]. Hence, it is inviting to discover which polarity-compensating mechanisms are at work to stabilize the surface. Moreover, polar surfaces are of special interest since their magnetic, electronic, and catalytic properties often strongly differ from the corresponding bulk material [54–56]. Whereas in the past polar oxide bilayers based on a variety of transition and earth alkali metals have been investigated [57–61], the properties of rare earth polar oxide bilayers have never been studied up to now.

The thesis at hand is organized as follows: In Chap. 2, I introduce the fundamental properties of the investigated materials and the basic concepts of nanomagnetism. Chap. 3 reviews the experimental techniques used in this thesis. The corresponding setups and procedures are described in Chap. 4. In the following chapters, I present the structural and electronic properties of intercalated Eu (Chap. 5), the impact of intercalation on the binding of ionic adsorbates (Chap. 6), and the growth of rare earth layers on Ir(111) (Chap. 7). Afterwards, I discuss in Chaps. 8 and 9 the magnetic properties of intercalated and adsorbed Eu monolayers, and of different metal cluster lattices. Results on the polar EuO bilayer on Ir(111) are presented in Chap. 10. To conclude, a summary with perspectives for future research is given in Chap. 11.

CHAPTER 2

Background

Secs. 2.1.1, 2.1.3, 2.2.3 and 2.4 are partially published in Refs. [62], [63] and [64].

In this chapter, I review the properties of the two main ingredients of this thesis, which are (i) epitaxial Gr on Ir(111), and (ii) Eu in intercalated, adsorbed, or oxidized form. Furthermore, I introduce the basic concepts of nanomagnetism, and give a short overview of polar oxide surfaces.

2.1 Graphene

As shown in Fig. 2.1(a), Gr is a two-dimensional layer of C atoms arranged in a hexagonal lattice with a two-atom basis (honeycomb lattice). The lattice constant is $a_{\mathrm{Gr}} = 2.46\,\text{Å}$. Gr naturally occurs in graphite, where Gr layers are stacked on top of each other. By mechanical exfoliation using a scotch tape single Gr layers can be isolated [65]. However, this method yields only sparsely distributed and micrometer-sized Gr flakes. A more controlled and large-scale fabrication of Gr can be achieved by thermal decomposition of SiC [66, 67], or epitaxial growth on a variety of metal surfaces [68–74].
The C atoms in Gr are sp^2 hybridized. Whereas neighboring sp^2 orbitals overlap in-plane to form σ bonds, the remaining p_z orbitals form a delocalized π system; its dispersion within the first Brillouin zone (see Fig. 2.1(b)) is shown in Fig. 2.1(c). Most prominent is the linear dependence of the energy E on the modulus of the wave vector $\vec{k}$

$$E = \hbar v_{\mathrm{F}} \sqrt{k_x^2 + k_y^2} \tag{2.1}$$

in the vicinity of the K and K' points with a Fermi velocity v_{F} of about $10^6\,\mathrm{m/s}$. The peculiar band structure arises from its monoatomic thickness and the lattice symmetry of

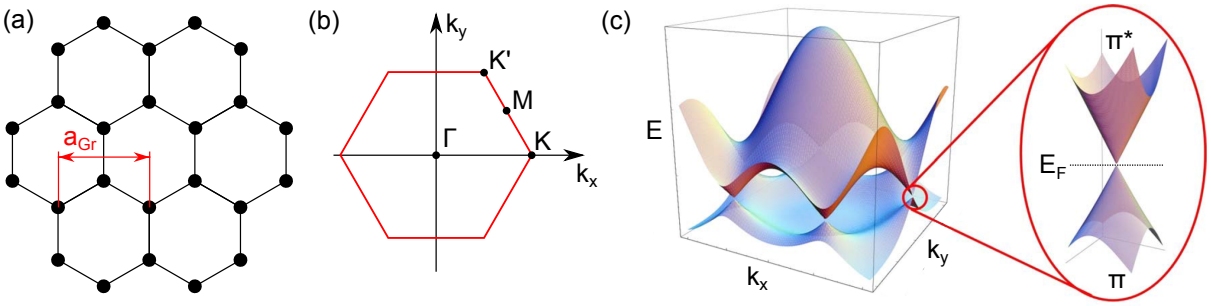

Figure 2.1: (a) Hexagonal crystal structure of Gr. The lattice constant a_{Gr} is indicated. (b) First Brillouin zone of Gr with the high symmetry points Γ, M, K, and K'. (c) Electron dispersion of the π and π^* bands within the first Brillouin zone. The zoom shows one of the Dirac points. Panel (c) is adapted from Ref. [15].

Gr [75]. As it resembles the dispersion of massless fermions described by the relativistic Dirac equation, the regions around the K points are denoted as Dirac cones [15]. For pristine Gr the occupied π and unoccupied π^* bands touch each other at the Fermi energy (Dirac point). Since there are no other bands around E_F, the density of states (DOS) vanishes here, making Gr a zero-gap semiconductor.

Transport measurements [76] and theoretical considerations [77] show that Gr has a remarkably high electron mobility at room temperature. Furthermore, the Dirac fermions show in comparison to ordinary electrons new physical phenomena such as the anomalous integer quantum Hall effect [78] or Klein tunneling [79]. These extraordinary properties caused a rapid increase in Gr research. In 2010, A. Geim and K. Novoselov were awarded by the Nobel Prize in Physics for their groundbreaking experiments [80].

Gr has been proposed for use in versatile applications; some of them have already been demonstrated on a laboratory scale. For example, since Gr is optically almost transparent [81] and has a high conductivity, it is a promising candidate for transparent electrodes needed in touchscreens and solar cells [82, 83]. In comparison to the standard material indium tin oxide, Gr would be cheaper and more flexible.

Gr can furthermore be integrated in a field-effect transistor geometry [84]. However, such transistors cannot be effectively turned off due to the absence of a band gap. To overcome this problem for logic devices several ways of inducing a band gap have been proposed, such as constraining Gr in one dimension by forming nanoribbons [85], biasing bilayer Gr [86], or applying strain [87]. On the other hand, for radiofrequency applications like small signal amplifiers a complete switch-off is not required. Hence, high-frequency transistors making use of the high charge carrier mobility have been successfully fabricated [88].

The high sensitivity of the charge carrier density of Gr to chemical doping by adsorbates can be exploited to build gas sensors that are able to detect single molecules [89]. Moreover, the high heat conductivity of Gr might solve heat dissipation problems in nanoelectronics [90]. Another potential application are ultracapacitors that combine the advantages of conventional capacitors (high speed charging) with the ones of batteries (high energy density). Therefore, electrodes made of a material with large surface to volume ratio and high conductivity are needed, both provided by Gr. Finally, Gr is a promising material for spintronics which will be discussed in more detail in Sec. 2.1.4. For a comprehensive overview of the properties and potential applications of Gr the reader is referred to Refs. [76], [15] or [91].

2.1.1 Graphene on Ir(111)

Epitaxial Gr on Ir(111) can be grown by thermal decomposition of hydrocarbons in exceptionally high quality, and self-limited to a single monolayer [39, 71, 92, 93]. Two growth methods will be presented in Sec. 4.5. In the following, I briefly summarize the most important structural and electronic properties of Gr on Ir(111).

The Moiré Unit Cell and Binding to the Substrate

Fig. 2.2(a) shows an atomically resolved STM topograph of Gr on Ir(111). The small black dots correspond to the centers of the C rings. Additionally, due to the lattice mismatch between Gr and Ir a superstructure arises which is called *moiré* and visible as bright spots in Fig. 2.2(a). The moiré mesh consists of (10.32×10.32) Gr unit cells resting on (9.32×9.32) Ir atoms [93], resulting in a periodicity of 2.53 nm.
Due to the varying lateral position of the C atoms with respect to the Ir lattice, one can identify three high symmetry configurations: in an atop (fcc, hcp) area, the centers of the C rings are located above atop (regular hollow or fcc, faulted hollow or hcp) Ir sites. In Fig. 2.2(a) the moiré unit cell is schematically tiled by white, green, and red hexagons, representing atop, fcc, and hcp areas. This model will be frequently used later.
The binding of Gr to Ir(111) was investigated by Busse *et al.* using nonlocal van der Waals (vdW) DFT [95]. The unit cell was commensurably approximated by (10×10) Gr honeycombs resting on (9×9) Ir atoms as shown in Fig. 2.2(b). The authors find a small average binding energy of -50 meV per C atom indicating that the binding of Gr to Ir is largely vdW mediated physisorption. The weak binding causes a large average height of Gr above Ir, which was calculated to be 3.41 Å, in excellent agreement with the experimental value of (3.38 ± 0.04) Å determined by X-ray standing waves, and similar

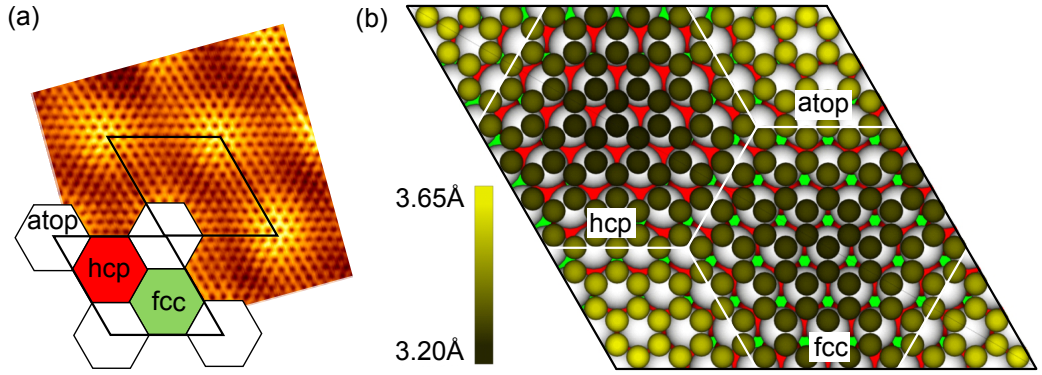

Figure 2.2: (a) STM topograph of Gr on Ir(111) (6 nm × 6 nm). The moiré cell is schematically tiled by white, green, and red hexagons, representing atop, fcc, and hcp areas. Partially adapted from Ref. [94]. (b) Top view of the relaxed moiré unit cell obtained by vdW-DFT. The brightness of the C atoms represents their height above the Ir substrate according to the adjacent color scale. Adapted from Ref. [95].

to the interlayer distance in graphite of 3.36 Å [96]. The weak average bonding of Gr to Ir(111) was also confirmed by X-ray photoemission spectroscopy [97].
The nonlocal vdW binding is modulated by weak chemical bonds resulting in a height corrugation of Gr. As visible in Fig. 2.2(b), the largest distance of 3.62 Å between Gr and Ir is found in the atop regions, indicating a chemical repulsion in these areas. The hcp and fcc regions have a lower height of 3.27 Å and 3.29 Å, respectively, resulting from weak attractive chemical bonds. They arise from a slight hybridization between C $2p_z$ orbitals and Ir $5d_{3z^2-r^2}$ orbitals for C atoms that sit exactly atop of Ir atoms [95]. The weak hybridization is also visible in angle-resolved photoemission spectra [98].

Orientation of the Moiré Unit Cell

As shown in Ref. [93], the atop areas of the moiré lattice always appear as dark depressions in a bright surrounding, or as bright protrusions in a dark surrounding depending on the contrast. Hence, it is easy to identify them in STM. However, to distinguish between fcc and hcp areas additional information about the sample orientation is needed.
This information can be gained by looking at equilibrated vacancy islands or stacks of them, which occasionally remain on the Ir surface if the annealing temperature after sputtering was not sufficiently high. The sputtering crater with a flat bottom shown in Fig. 2.3(a) is a stack of equilibrated vacancy islands. From Ref. [99] it is known that the longer edges of the threefold symmetric equilibrium shape correspond to {111}-microfacetted steps, while the shorter ones correspond to {100}-microfacetted steps. This

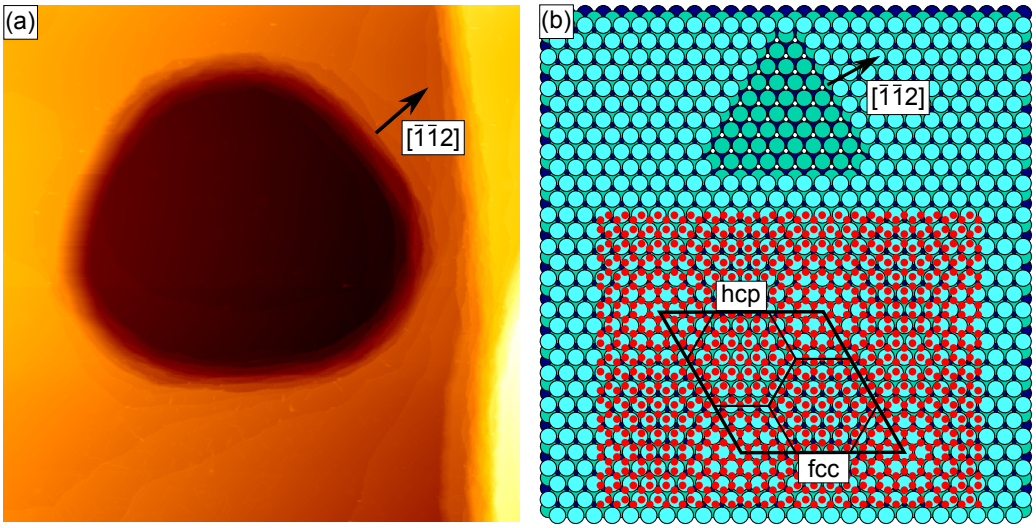

Figure 2.3: (a) STM topograph displaying a stack of vacancy islands resulting from sputtering and annealing to 1200 K (630 nm×630 nm). The arrow is pointing in [1̄1̄2] direction perpendicular to {111}-microfacetted ascending steps. (b) Ball model for the orientation of the Ir single crystal (surface layer: light blue; second layer: green; third layer: dark blue). In the upper part a vacancy island is drawn to illustrate the long {111}- and short {100}-microfacetted steps. In the lower part, the Gr lattice (red) is put on top and the moiré unit cell is indicated.

implies a sample orientation as shown in Fig. 2.3(b) and indicated by the arrow in Fig. 2.3(a). Putting the Gr lattice on top reveals that the moiré unit cell is oriented with the hcp area in the upper left and the fcc area in the lower right part. As the rotational alignment of our sample with respect to the STM is fixed, this orientation will be used for the analysis of all experiments presented in this thesis.

Pre-existing Strain

The growth of Gr on Ir(111) is conducted at high temperatures. Because of a mismatch between the thermal expansion coefficients of Gr and Ir, the Gr layer becomes compressively strained during cool down to room temperature. A significant part of this strain relaxes by formation of one-dimensional wrinkles. However, even at room temperature a small residual compressive strain is left [100].

A detailed picture of the strain release process is shown in Fig. 2.4 which is adapted from Ref. [101]: During cool down from the growth temperature (A) the Gr layer builds up compressive strain until the strain energy is large enough to overcome the activation energy for wrinkle formation at point B. This happens approximately 400 K below the growth temperature. The wrinkles nucleate between B and C, and grow from C to D,

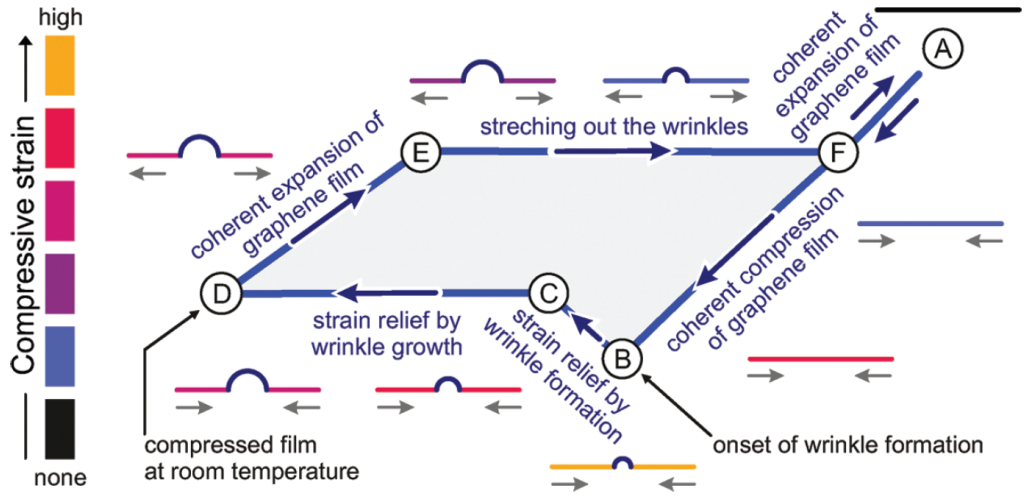

Figure 2.4: Interplay of compression/expansion of the Gr lattice and wrinkle formation during a cycle of cooling (A to D) and heating (D to F). The gray arrows indicate the thermal compression/expansion of the Ir substrate. The remaining strain in the Gr layer is indicated by the colors shown on the left side. Taken from Ref. [101].

while the Gr lattice remains slightly compressed compared to the graphite lattice constant at the same temperature. Heating the sample again leads first to an expansion of the Gr lattice (D to E), while the wrinkles are stretched out only between E and F. After complete disappearance of the wrinkles at point F the Gr layer is again stretched by the expanding Ir lattice, resulting in tensile strain when going above the original growth temperature.

2.1.2 Graphene as Cluster Template

The moiré pattern of Gr on Ir(111) can be used as a template for the growth of cluster lattices [39, 40]. Fig. 2.5 shows STM topographs after deposition of the indicated metals onto Gr flakes on Ir(111). As visible in Figs. 2.5(a) and (b), Ir and Pt clusters grow close to perfection. The clusters are oriented with their (111) planes parallel to the substrate surface, and their $\langle 1\bar{1}0 \rangle$ parallel to the $\langle 1\bar{1}20 \rangle$ directions of Gr [40]. The atomic structure has been studied in detail in Ref. [102] by surface X-ray diffraction.

The mechanism of cluster formation is provided by rehybridization of Gr from its sp^2 configuration to diamond-like sp^3 beneath and in the vicinity of the clusters [103, 104]. The rehybridized C atoms bind with their fourth bond alternately to Ir atoms below and cluster atoms above, thereby locally reducing the average Gr height above Ir from 3.4 Å to 2.1 Å. As this is only possible where Ir atoms are directly located below C atoms, the en-

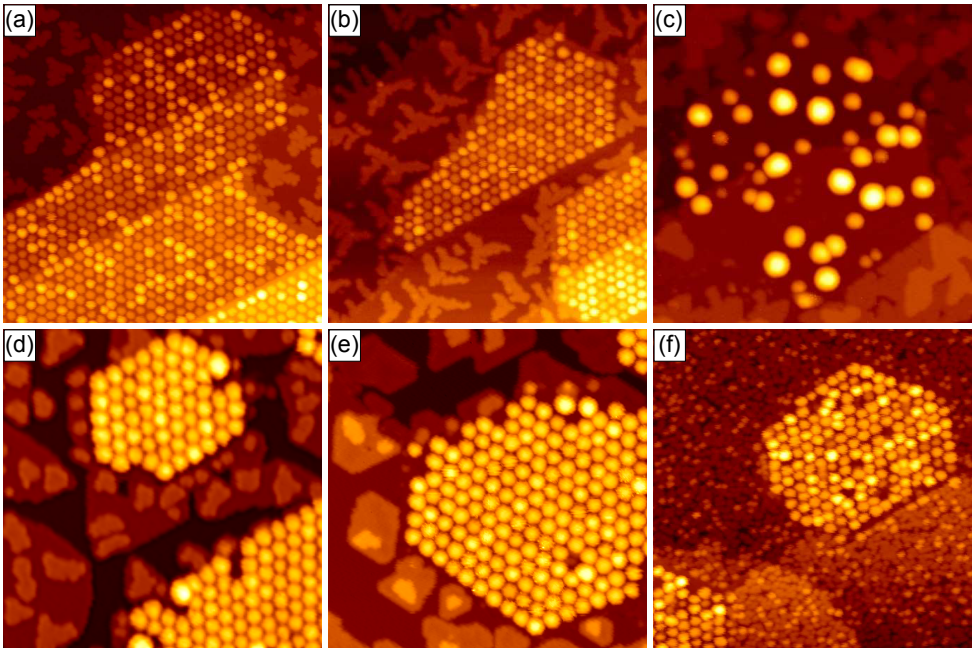

Figure 2.5: STM topographs of Gr flakes covered with different metal clusters grown at room temperature except for (f). The deposited amounts are given in monolayers with respect to Ir(111). (a) 0.20 ML Ir. (b) 0.25 ML Pt. (c) 0.77 ML Fe. (d) 0.10 ML Ir plus 0.70 ML Fe. (e) 0.10 ML Ir plus 0.45 ML Co. (f) 0.45 ML Re deposited at 200 K. Image sizes are (800 nm × 800 nm) for (a) - (c) and (f), and (500 nm × 500 nm) for (d) - (e). Panels adapted from Ref. [40].

ergetically preferred adsorption sites are the hcp regions. The rehybridization mechanism is experimentally supported by X-ray photoemission spectroscopy [94].

The ability to form clusters strongly depends on the deposited material. For example Fe does not form a well-ordered cluster lattice as shown in Fig. 2.5(c). Zhou *et al.* suggested that a high metal-C bond strength, which can be estimated from the metal-C bond dissociation energy, is an indicator for cluster formation [105].

Nevertheless, well-ordered clusters can also be grown for materials with weak metal-C bonds, either by seeding with small Ir or Pt clusters (see Figs. 2.5(d) and (e) for Fe and Co), or deposition at low temperatures as shown for Re in Fig. 2.5(f) [40].

2.1.3 Intercalation Underneath Graphene

In chemistry, intercalation describes the incorporation of atoms or molecules into a chemical compound without essentially changing its structure. The most common examples are graphite intercalation compounds (GIC) [106]. In these compounds the intercalants (often alkali metals) are located between the Gr layers. GIC are classified by a stage

n denoting the number of Gr layers between adjacent intercalation layers. Staging is a general phenomenon in GIC, even for very dilute concentrations of the intercalants.
Intercalation into graphite can effectively change the physical properties of the host material: As the free charge carrier concentration in graphite is very low, doping by the intercalants permits a wide variation of the charge carrier concentration, and thus of the electrical, thermal, and magnetic properties [106]. For example, AsF_5C_x has a room temperature conductivity exceeding that of Cu [107]. Furthermore, several GIC are superconducting as for example CaC_6 with a critical temperature of 11.5 K [108].
Intercalation is not restricted to graphite, but also intercalation of gases, semiconductors, or metals underneath epitaxial Gr on a substrate has become an intensively studied topic [19]. This strong interest is driven by several effects, some of which I want to illustrate:

- **Decoupling from the Substrate**
  The interaction between Gr and its supporting substrate can be modified by intercalation [20, 21, 109–112]. For example, *electronic* decoupling has achieved by intercalation of H under Gr on SiC(0001) [21]. The decoupling can be utilized for an enhanced device performance in Gr transistors [112]. *Chemical* decoupling and thereby exfoliation of epitaxial Gr was realized by Br_2 intercalation [113, 114].

- **Container for Chemical Reactions**
  Reactions occurring in a nano-sized space are often influenced by confinement effects [115]. To investigate such reactions the confined space underneath Gr on Ru(0001) or Pt(111) has been considered as a suitable container [22, 116, 117].

- **Protection against Oxidation**
  To be able to use thin epitaxial layers under ambient conditions it is important to protect them against contamination from the environment. In this context, it has been shown that an intercalated Fe layer can be efficiently protected against oxidation by the covering Gr sheet [24].

- **Doping of Graphene**
  Intercalation provides a flexible means to drastically modify the chemical potential of the Dirac electrons. For the shift of the Dirac point energy E_D with respect to the Fermi level E_F a range from $E_D = 0.8\,eV$ by p-doping through F intercalation [23] to $E_D = -1.5\,eV$ by n-doping through Eu intercalation [63] is obtained. The span of 2.3 eV is about an order of magnitude larger than the span of 0.2 eV typically achieved by gating of Gr [36].

2.1.4 Magnetism and Graphene

Since C atoms do not carry magnetic moments, pristine Gr is intrinsically diamagnetic just like graphite [118]. However, motivated by the observation of room temperature ferromagnetism in proton irradiated graphite [119], it has been calculated that single-atom defects in Gr give rise to localized states at the Fermi level [120] which carry a magnetic moment on the order of $1\,\mu_B$ [121]. The moments are even larger in the presence of H or N close to the vacancies [122, 123]. The coupling between the defects depends on their distribution on the two Gr sublattices [121].

In addition to vacancies also doping of Gr with B or N can induce magnetic moments which favor ferromagnetic coupling. This makes such a material an interesting candidate for metal-free ferromagnets [124]. Furthermore, the adsorption of H [125], C [126], or N [127] is expected to lead to the occurrence of magnetic moments in Gr.

Beside such *static* effects Gr is also a promising material concerning spin *transport* due to its long spin relaxation length arising from two reasons: First, the spin-orbit coupling - originating from the interaction of the electron spin with the magnetic field generated by the nucleus moving in the electron's rest frame - scales with the fourth power of the proton number. Therefore, it is expected to be small in the light element C [128, 129]. In addition to this relativistic effect, the electron spin interacts with the magnetic moment of the nucleus, which is known as hyperfine interaction. As the dominating isotope ^{12}C has spin zero, the hyperfine interaction plays only a marginal role in Gr [130, 131]. Together with the high charge carrier mobility, the low spin-orbit and hyperfine interactions cause that a spin-polarized current can travel a long distance in Gr without loosing its polarization. Experimentally, ballistic spin transport over several micrometers at room temperature [16, 132, 133] and more than 100 µm at 2 K [134] has been reported.

In the context of Gr based spintronic devices often nanoribbons are discussed: While armchair nanoribbons are non-magnetic, the edge states in zigzag ribbons show a magnetic order, which is ferromagnetic along the edges, and antiferromagnetic between opposite edges as shown in Fig. 2.6(a) [136]. Concerning the LDOS, this means that on both sides of the ribbon the majority and minority spins are separated by a band gap as shown in Fig. 2.6(b). As sketched in Fig. 2.6(c), when applying a transversal electrical field the LDOS shifts on both sides of the ribbon in opposite directions [137]. In this half-metallic state, the system is metallic for one spin direction and insulating for the other one. If realized in practice, this device would offer an easy way to control spin transport.

Alternatively, Gr nanoribbons have been proposed as magnetoresistive junctions, which are of importance as magnetic field sensors, needed for example in read heads of hard

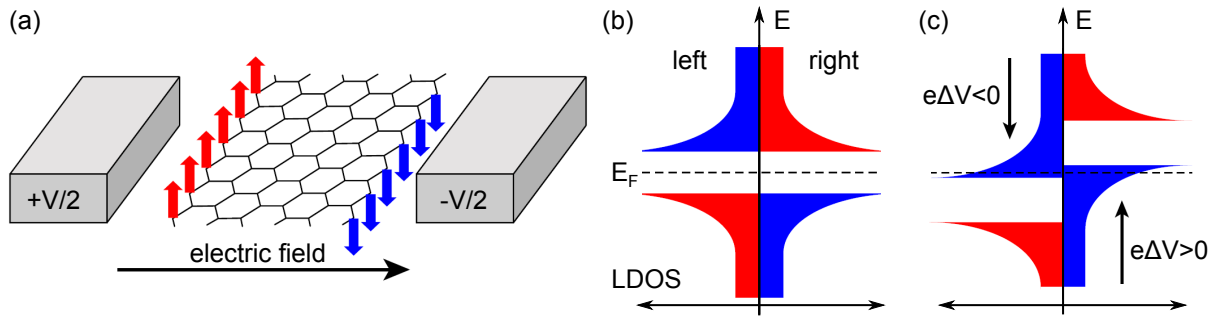

Figure 2.6: (a) Model for inducing half-metallicity in a zigzag nanoribbon by an electric field. (b) Schematic spin-resolved LDOS for the opposite edges without applied field. (c) A field across the ribbon selectively closes the band gap for spin down electrons. Adapted from Ref. [135].

disk drives. Such devices - conventionally built of two ferromagnets separated by a non-magnetic spacer - show a large change in electric resistance depending on the relative orientation of the magnetization of the two ferromagnetic layers [138]. For a zigzag nanoribbon between two ferromagnetic contacts a high magnetoresistance ratio has been predicted [139]. Here, the low resistance state corresponds to the parallel configuration where the moments at the edges are coupled ferromagnetically (Fig. 2.7(a)), while in the antiparallel configuration a domain wall with high resistance develops (Fig. 2.7(b)).

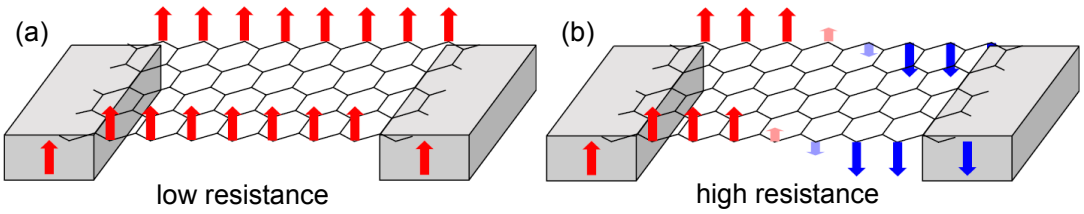

Figure 2.7: Model for a magnetoresistive device: A zigzag nanoribbon connects two ferromagnetic contacts. The low and high resistance configurations are shown. Adapted from Ref. [135].

A way to achieve spin dependent transport in an extended Gr sheet is to put it in close proximity to a ferromagnetic insulator. Via the magnetic proximity effect, an exchange splitting will be induced in Gr (see Fig. 2.8(a)). In this context, EuO has been predicted as a suitable material inducing an exchange splitting of about 5 meV [140]. By appropriate doping or gating (see Fig. 2.8(b)) the Fermi level can be adjusted such that only one spin orientation contributes to the conduction.

Another way for efficient spin filtering has been proposed for multilayer Gr embedded between two Ni(111) or Co(0001) layers. As the electronic structures of Gr and metal

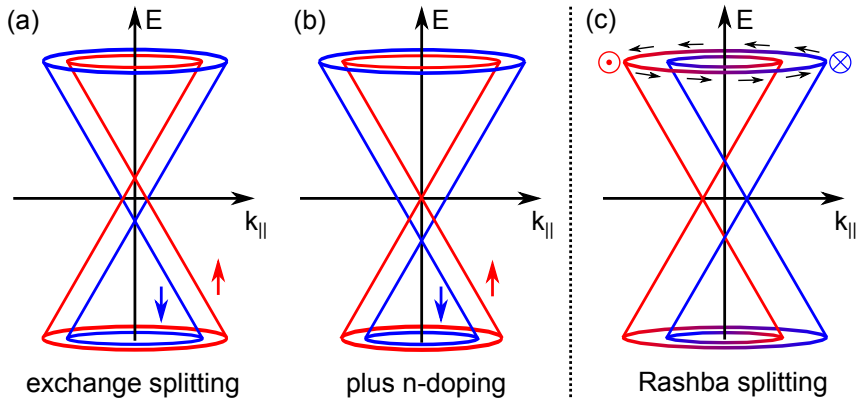

Figure 2.8: Band structure of Gr around the K point. (a) Exchange splitting induced by the magnetic proximity effect. (b) After appropriate n-doping only the spin down channel contributes to the transport. (c) Rashba splitting induced by an electric field.

overlap in reciprocal space only for one spin direction, perfect spin filtering can be achieved [141]. The formation of chemical bonds between Gr and metal could be prevented by intercalation of a separating Au or Cu layer.

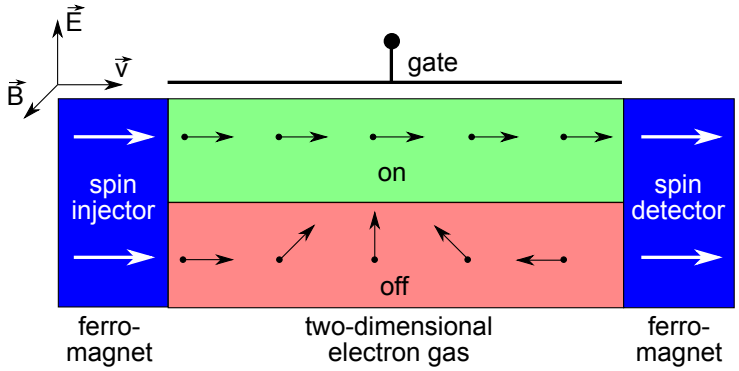

Figure 2.9: Scheme of a spin field effect transistor. Source and drain (spin injector/detector) are ferromagnets with parallel magnetization. The injected spin-polarized electrons travel through the two-dimensional electron gas while their spins precess around the effective magnetic field $\vec{B}$, which is tunable by the gate voltage. The current is large if the spins point at the drain in the initial direction (on), and small if the direction is reversed (off). Adapted from Ref. [14].

A splitting of the Dirac cone may not only be achieved by a *magnetic*, but also by an *electric* field (Rashba effect [142]). As the inversion symmetry is broken perpendicular to the surface, a term in the form of an electric field $\vec{E}$ has to be added to the Hamiltonian. As relativistic consequence, an electron moving with velocity $\vec{v}$ experiences an effective magnetic field $\vec{B}$ perpendicular to $\vec{v}$ and $\vec{E}$. By spin-orbit coupling $\vec{B}$ causes a momentum-

dependent splitting of the Dirac cone (see Fig. 2.8(c)). Experimentally, a large Rashba splitting has been observed for Au intercalated Gr on Ni(111) [20, 143].
The Rashba splitting can be controlled by an external electric field [144] which opens the way to a spin field effect transistor [14, 145]. As shown in Fig. 2.9, spins injected from a ferromagnetic layer precess around the effective magnetic field and are detected by a second ferromagnetic layer. The spin rotation angle during the time of flight is controlled by a gate voltage. For parallel spin alignment at the detector a low resistance is achieved (on), while the resistance is high for antiparallel alignment (off). Semenov *et al.* proposed a similar mechanism with a ferromagnetic dielectric between Gr and gate. Here, not the Rashba interaction, but the exchange interaction with the dielectric is tuned by the gate voltage [146]. To conclude, I refer the reader to Ref. [135] for a comprehensive overview of the magnetic properties of Gr and their potential applications.

2.2 Europium

Eu is the chemical element with the atomic number 63. It is a member of the lanthanide series and therefore belongs to the rare earths. Pure Eu is a silverly, white metal and crystallizes in the bcc crystal structure with a lattice constant of 4.582 Å [147]. Eu has the ground state electron configuration $[Xe]4f^7 6s^2$. According to the Hund's rules all spins in the half-filled 4f shell are parallelly aligned resulting in a high magnetic moment of $7\,\mu_B$. As shown by Mössbauer spectroscopy, metallic Eu is divalent such that the magnetic moment of the atom is preserved in the bulk [148].

2.2.1 Magnetism of Bulk Europium

First evidence for magnetic ordering in metallic Eu below around 90 K was found in 1960 by anomalies in the magnetic susceptibility [149], electrical resistivity [150], and later also in the heat capacity [151]. Using neutron diffraction, Olsen, Nereson, and Arnold determined the order to be an antiferromagnetic helical structure [25–27] as depicted in Fig. 2.10. The spins order ferromagnetically within the {100} planes of the bcc crystal structure, but form spirals along the ⟨100⟩ directions. Such a structure has a vanishing net magnetic moment and is therefore antiferromagnetic. There are six different domains (three spatial directions each with two helicities), which occur in equal proportions.
At the Néel temperature T_N the spiral is commensurate with a pitch of 3.5 Eu lattice constants a_{Eu} corresponding to a turning angle of 51.4° between neighboring (100) planes. At lower temperatures the periodicity of the spiral slightly increases to $3.6a_{Eu}$ (corresponding

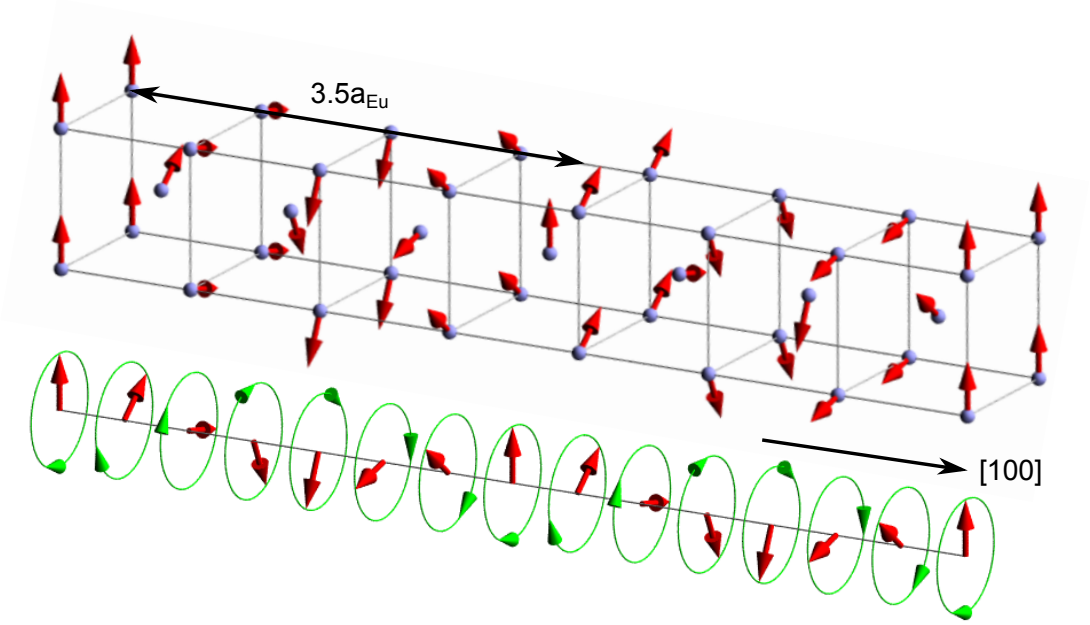

Figure 2.10: Helical spin structure of bulk Eu (commensurate phase at T_N). The upper part shows the spin arrangement on the bcc lattice. Two unit cells along the [100] direction are shown. For better visibility, in the lower part only one atom per (100) plane is depicted.

to a smaller turning angle of 50°), thus making the spin structure incommensurate with respect to the crystallographic lattice.

As for most rare earth materials, the magnetic behavior of Eu is governed by the localized 4f magnetic moments interacting indirectly with each other through the sea of delocalized 5d and 6s valence electrons. This type of magnetic coupling is known under the name Ruderman-Kittel-Kasuya-Yosida (RKKY) interaction [152–154]. As proposed by Andersen *et al.*, the wave vector of the spin spiral is given by a nesting vector $\vec{k}_n$, i.e., a vector connecting approximately parallel sheets of the Fermi surface [155]. It can be shown that a helical array with a wave vector equal to $\vec{k}_n$ is the minimum energy state [156]. Using DFT calculations of the Fermi surface, the nesting vector corresponding to the experimentally observed helix pitch has been identified [157].

2.2.2 Europium Graphite Intercalation Compounds

The first stage Eu GIC EuC_6 was first investigated in 1980 by El Makrini *et al.* [158]. The samples were prepared by heating an HOPG single crystal and Eu metal under vacuum at 723 K for 20 days. Despite the long reaction time the intercalation stayed superficial so that only 25% of the sample were intercalated. Later experiments have shown that

the intercalation yield can be enhanced by using very small samples [159] or intercalation from a molten Li-Eu alloy [160, 161].
The crystal structure of EuC_6 is depicted in Fig. 2.11(a). Using X-ray diffraction, the in-plane arrangement of the Eu atoms was found to be a $(\sqrt{3} \times \sqrt{3})R30°$ structure with respect to the honeycomb lattice of graphite, whereby the Eu atoms are located above the centers of the C rings. The interlayer stacking of the Eu atoms follows the hcp crystal structure. Upon intercalation the distance between two adjacent graphite layers is increased from 3.36 Å for pristine graphite to 4.87 Å [158].

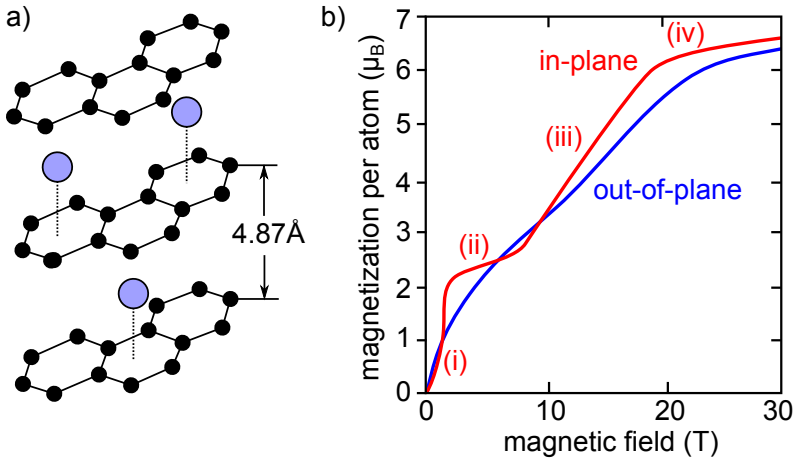

Figure 2.11: (a) Crystal structure of the first stage Eu GIC EuC_6 (adapted from Ref. [159]). (b) Magnetization loops at 4.2 K for a magnetic field applied within (red) and perpendicular (blue) to the basal planes of graphite (adapted from Ref. [31]). For the in-plane field four different regions of the magnetization loop are labeled with (i) - (iv).

Suematsu *et al.* investigated the magnetic properties of EuC_6 using pulsed fields up to 40 T [162]. Two characteristic magnetization curves taken at 4.2 K are shown in Fig. 2.11(b) for an external field applied in-plane (red) and out-of-plane (blue) with respect to the graphite layers. For an out-of-plane field, the magnetization increases rather linear and saturates at around 30 T. In contrast, for a magnetic field applied in-plane, the magnetization loop consists of four different regions which are denoted as (i) -(iv) in Fig. 2.11(b):

(i) In the initial magnetization region up to 2.2 T the magnetization steeply increases with the applied magnetic field. A substructure of this region was reported in Ref. [159], but has not been analyzed in the subsequent literature.

(ii) The magnetization only slightly increases between 2.2 T and 8.2 T thereby forming a broad plateau at about 2.5 μ_B.

(iii) Between 8.2 T and 20.5 T the magnetization increases linearly following a line that crosses the origin.

(iv) Above 20.5 T the magnetization saturates at a value of about 6.5 μ_B.

Such a complex magnetization behavior is indicative for the phenomenon of *metamagnetism* which denotes that the magnetic ordering of a material changes with the magnitude of the applied field. From temperature dependent magnetization loops as in Fig. 2.11(b), the magnetic phase diagram shown in Fig. 2.12 has been derived [30, 31].

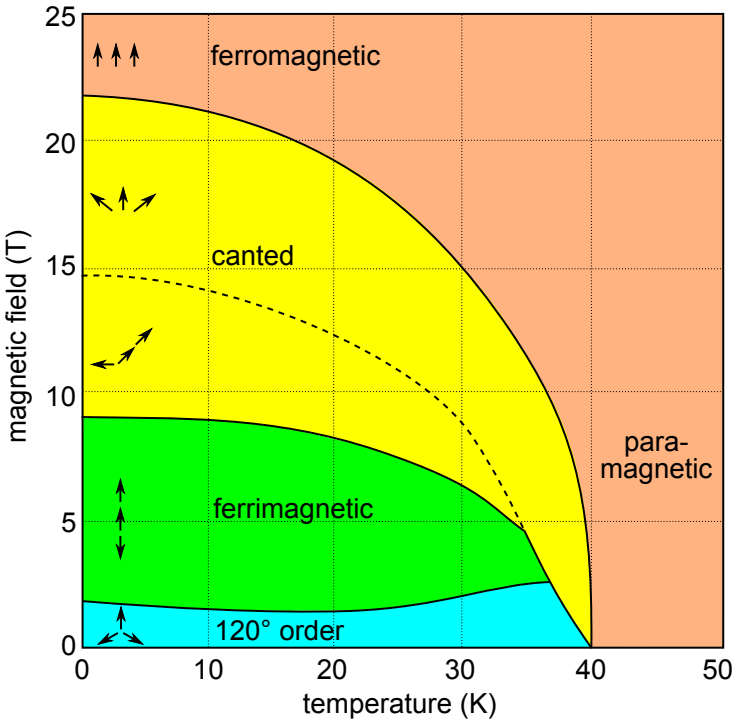

Figure 2.12: Magnetic phase diagram of EuC_6 for fields applied within the basal planes of graphite. The different spin arrangements are schematically depicted. Adapted from Ref. [31].

In the low field range neighboring spins always enclose angles of 120°. This is a typical ground state for a frustrated antiferromagnet on a triangular lattice [163]. When applying higher fields the 120° order changes to ferrimagnetic order, i.e., two of three spins align parallel and one antiparallel to the magnetic field. This yields a magnetization of one third of the value for fully aligned moments, and thus explains the plateau in the magnetization curves. A further increase of the field changes the spin structure to a canted spin state, which shows a linear magnetization behavior. It was shown by magnetoresistive measurements that this canted state actually consists of two slightly different ordering types as shown by the dashed line in Fig. 2.12 [31]. Finally, for very high magnetic fields the order

turns to be ferromagnetic. Above a temperature of 40 K the system stays paramagnetic for all applied magnetic fields.
The magnetic interaction between the localized Eu 4f moments is dominated by RKKY interactions within the highly conductive graphite planes [30, 164]. Sakakibara *et al.* showed that antiferromagnetic nearest neighbor (NN) coupling (J_0) and ferromagnetic next nearest neighbor (NNN) coupling (J_1) within the Eu planes, as well as a small ferromagnetic interlayer (IL) coupling (J'), and four-spin interactions are necessary to explain the metamagnetic behavior [165–167]. Based on the resulting Hamiltonian

$$\begin{aligned}\mathcal{H} &= -J_0 \sum_{\mathrm{NN}} \vec{S}_i \vec{S}_j - J_1 \sum_{\mathrm{NNN}} \vec{S}_i \vec{S}_j - J' \sum_{\mathrm{IL\ NN}} \vec{S}_i \vec{S}_j - g\mu_B \sum_i \vec{S}_i \vec{H} - B \sum_{\mathrm{NN}} (\vec{S}_i \vec{S}_j)^2 \\ &\quad + K \sum_{4\ \mathrm{spins}} ((\vec{S}_i \vec{S}_j)(\vec{S}_k \vec{S}_l) + (\vec{S}_i \vec{S}_l)(\vec{S}_j \vec{S}_k) - (\vec{S}_i \vec{S}_k)(\vec{S}_j \vec{S}_l)) \end{aligned} \tag{2.2}$$

Chen *et al.* established the different spin configurations of the magnetic phase diagram by Monte Carlo simulations [31]. Furthermore, the zero-field 120° spin order was experimentally confirmed by muon spectroscopy [161].

2.2.3 Europium Oxide

Eu is the most reactive element of the rare earths and has several oxides [168]. Preferentially, the sesquioxide Eu_2O_3 is formed, which is non-magnetic as it contains only Eu^{3+} ions with $J = 0$. However, under limited O feed also the monoxide EuO with 2+ valency can be prepared. EuO crystallizes in the rocksalt structure with a lattice constant of 5.144 Å [47] and has an ionic character with Eu^{2+} and O^{2-} ions. EuO belongs to the rare class of ferromagnetic semiconductors and has a Curie temperature of $T_C = 69$ K. While the band gap is 1.1 eV above T_C [169], EuO shows upon appropriate doping a semiconductor to metal transition when cooling below T_C [170]. Due to its high spin polarization in the ferromagnetic state [47], EuO is an attractive material for semiconductor-based spintronic devices [171, 172]. Beside this, EuO shows further interesting effects such as a colossal magnetoresistance (CMR) effect [173], photoconductivity [174], and large magneto-optical effects [175, 176].
As the $4f^7$ ground state - corresponding to a pure spin moment of $7\,\mu_B$ - is spherically symmetric, the magnetic exchange interactions are isotropic. Therefore, EuO is a typical material for which the Heisenberg model with the effective Hamiltonian

$$\mathcal{H} = -\sum_{i,j} J_{ij} \vec{S}_i \vec{S}_j \tag{2.3}$$

can be applied [177]. The most important exchange mechanism in EuO is an indirect exchange between NN Eu atoms, consisting of virtual transitions of 4f electrons to 5d or 6s orbitals [177, 178]. It can be represented by an exchange constant J_1, whereby the sum in Eq. 2.3 has to be taken over NN atoms. Additional contributions come from superexchange between NNN Eu atoms mediated by O p electrons [177]. The corresponding sum in Eq. 2.3 has to be taken over NNN atoms using an exchange constant J_2. Inelastic neutron-scattering studies on EuO single crystals determined J_1 and J_2 to be both ferromagnetic [179], whereby J_2 is much smaller than J_1 [178]. For a comprehensive overview of the properties of EuO the reader is referred to Refs. [29] and [180].

2.3 Nanomagnetism

In this section, I explain why the magnetic properties at the nanoscale often differ from the bulk properties. This has mainly three reasons: First, the magnetic moments change when going from a single atom to the bulk. Second, the magnetic anisotropy depends on size and geometry of the sample. Third, small particles consist of single magnetic domains, which leads to the phenomenon of superparamagnetism.

2.3.1 Magnetic Moments

An atom with total electron spin $\vec{S}$ has a magnetic spin moment of

$$\vec{m}_S = -g_S \frac{\vec{S}}{\hbar} \mu_\mathrm{B} \tag{2.4}$$

Herein, μ_B is the Bohr magneton, which is defined as

$$\mu_\mathrm{B} = \frac{e\hbar}{2m} \tag{2.5}$$

with the elementary charge e, the reduced Planck constant $\hbar$ and the electron mass m. The spin Landé factor g_S equals 2, or more accurately about 2.002319 according to quantum electrodynamics [181]. Analogously, the total electron orbital angular momentum $\vec{L}$ of an atom is related to a magnetic orbital moment of

$$\vec{m}_L = -g_L \frac{\vec{L}}{\hbar} \mu_\mathrm{B} \tag{2.6}$$

with the orbital Landé factor $g_L = 1$. In this thesis, only projections of $\vec{m}_S$ and $\vec{m}_L$ onto the quantization axis are considered and denoted as m_S and m_L omitting the usual index z. In the following, I exemplarily discuss the magnetic moment of Co: An isolated Co

atom has seven electrons in the 3d level. According to Hund's rules five spins point up and two spins down (see Fig. 2.13(a)), which results in a spin moment of $m_S = 3\,\mu_B$. The two spin down electrons ($L_z = 2$ and $L_z = 1$) yield an orbital moment of $m_L = 3\,\mu_B$. However, for bulk Co only a spin moment of about $1.6\,\mu_B$, and a very small orbital moment of about $0.15\,\mu_B$ are measured [182].

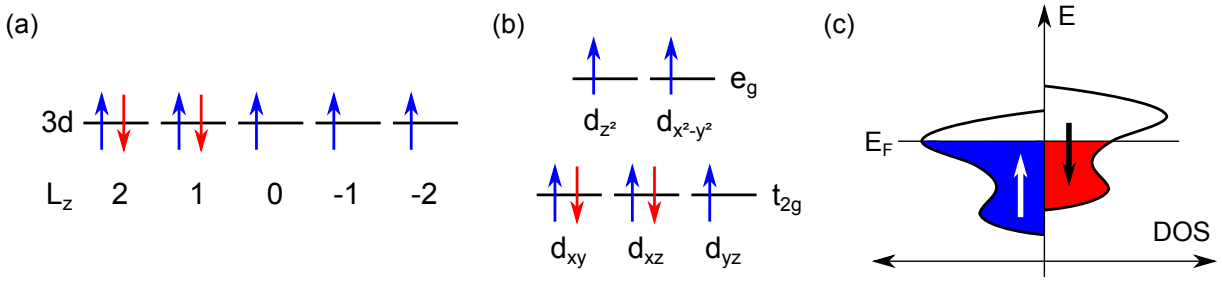

Figure 2.13: (a) Occupation of the 3d orbitals for Co according to Hund's rules. (b) Crystal field splitting for octahedral symmetry. Note that for large crystal field splittings one spin up electron from the e_g orbitals might alternatively occupy a t_{2g} orbital with spin down, resulting in a total spin moment of only $1\,\mu_B$ (low spin state). (c) Schematic spin-dependent DOS according to the Stoner model of ferromagnetism.

First, I address the quenching of m_L: The orbital angular momentum L_z is a good quantum number for an isolated atom as the Coulomb potential between electron and nucleus is rotationally invariant. However, this is not the case when the electrons feel the potential from a surrounding crystal. In consequence, states with different L_z couple to new eigenstates which are linear combinations of the atomic orbitals as shown in Fig. 2.13(b) (crystal field splitting) [183]. For the common octahedral crystal field symmetry, the new orbitals do not carry orbital angular momentum so that m_L is fully quenched. Deviations from the perfect symmetry lead to a partial quenching of m_L.

To understand the reduced *spin* moment one has to proceed from the localized atomic levels to a band description as sketched in Fig. 2.13(c). In the itinerant model, the 3d bands consist of two sub-bands for spin up and down electrons. If electrons are transferred from the spin down to the spin up band, the system gains exchange energy. However, emptying one sub-band in favor of the other increases the kinetic energy. The corresponding energy cost is the smaller the higher the DOS $D(E_F)$ at the Fermi edge, while the gain in exchange energy is larger the higher the exchange interaction I. This can be quantified in the Stoner criterion [184]: If the product $2ID(E_F)$ is greater than 1, the sub-bands shift with respect to each other resulting in ferromagnetism. Otherwise, there will be no

spin-dependent shift and the metal stays non-magnetic. Note that a charge transfer from the 4s to the 3d band can additionally influence the magnetic moments.
Based on this knowledge, one can understand why the magnetic moments of nanostructures differ from the bulk ones. First, the quenching of the orbital moment is partially lifted as the coordination is lowered [185, 186]. Second, the electronic structure of small particles differs from the bulk counterpart due to confinement effects [1, 187]. Furthermore, a charge transfer to the substrate may influence the filling of the magnetic bands.

2.3.2 Magnetic Anisotropy

The exchange interaction that couples the magnetic moments in a ferromagnet is isotropic, i.e., independent of the spin orientation relative to the bond direction. Consequently, it does not cost energy to rotate two spin moments in space as long as they stay parallel or antiparallel with respect to each other. Nevertheless, the magnetization behavior usually depends on the orientation of the sample. Often materials show an uniaxial magnetic anisotropy, i.e., the magnetization aligns preferentially along particular directions (easy axes). The magnetic energy can be expressed in the form

$$E = KV \sin^2 \phi, \tag{2.7}$$

where V is the sample volume, $K > 0$ the anisotropy constant, and ϕ the angle between easy axis and magnetization. If K is negative, the lowest energy term does not determine the direction of the easy axes within the basal plane, and higher-order terms depending on the crystal system are needed. Magnetic anisotropy has different reasons, some of which are listed below; a comprehensive overview can be found in Refs. [188] and [189].

- **Magnetocrystalline Anisotropy**
  For isotropically shaped bulk samples the magnetic anisotropy essentially arises from the crystal lattice. The orbital angular moment is usually tightly fixed to the crystal lattice [190], while the spin moment is coupled to the orbital moment via spin-orbit coupling. In consequence, the magnetization preferentially aligns along certain high symmetry directions of the crystal.

- **Surface and Interface Anisotropy**
  The local breaking of symmetry at a surface or interface induces corrections to the magnetocrystalline anisotropy [191, 192]. Their direction is in general complicated to predict, and depends strongly on the electronic details of the system.

- **Magnetoelastic Anisotropy**
  As previously discussed, the spin is coupled to the lattice. Therefore, also lattice deformations due to strain have influence on the magnetic anisotropy [193].

- **Shape Anisotropy**
  In contrast to the exchange interaction, the dipolar interaction depends on the orientation of the magnetic moments with respect to their connection vector. This causes for example magnetic moments to lie within a planar sample, or to point along the long axis of a thin rod. An alternative, but equivalent formalism introduces the shape anisotropy as a way to reduce the stray field of the sample.

Based on these effects, one can explain why the anisotropy strongly differs between bulk samples and nanostructures. (i) The crystal structure of small particles often differs from the bulk one. For example, epitaxial Co can grow either in hcp or fcc structure, resulting in different magnetocrystalline anisotropies [194]. (ii) Small particles or thin layers have a high surface contribution so that the surface anisotropy can easily dominate the bulk term [195]. (iii) A lattice mismatch with respect to the substrate may induce substantial strain in a thin film, giving rise to a strong magnetoelastic anisotropy [38, 196]. (iv) Small particles and especially thin layers are often more anisotropically shaped than bulk samples and have thus a higher shape anisotropy.

2.3.3 Superparamagnetism

Although the exchange interaction of a ferromagnet favors all spins to be parallelly aligned, such a single-domain state has a high magnetostatic energy stored in the stray field [197]. As a consequence, the sample will split into magnetic domains to minimize the stray field. However, thereby domain walls have to be introduced, which also cost energy. One can estimate a critical radius R_c below which the energy gain by reducing the stray field is smaller than the energy cost for introducing a domain wall [197]. Consequently, a particle with radius $r < R_c$ adapts a single-domain state. Typical values of R_c lie in the order of 10 - 100 nm depending on the material.
When trying to reverse the magnetization of a single-domain particle usually all atomic moments rotate in a coherent fashion. Thus, one can associate a *superspin* to the particle, in analogy to the spin of a single atom. The magnetization behavior can be described using the Stoner-Wohlfarth model [198–200]. The model assumes a particle with uniaxial magnetic anisotropy and effective anisotropy constant K. The superspin is represented by the saturation magnetization $\vec{M}_s$, and restricted to the plane containing the magnetic

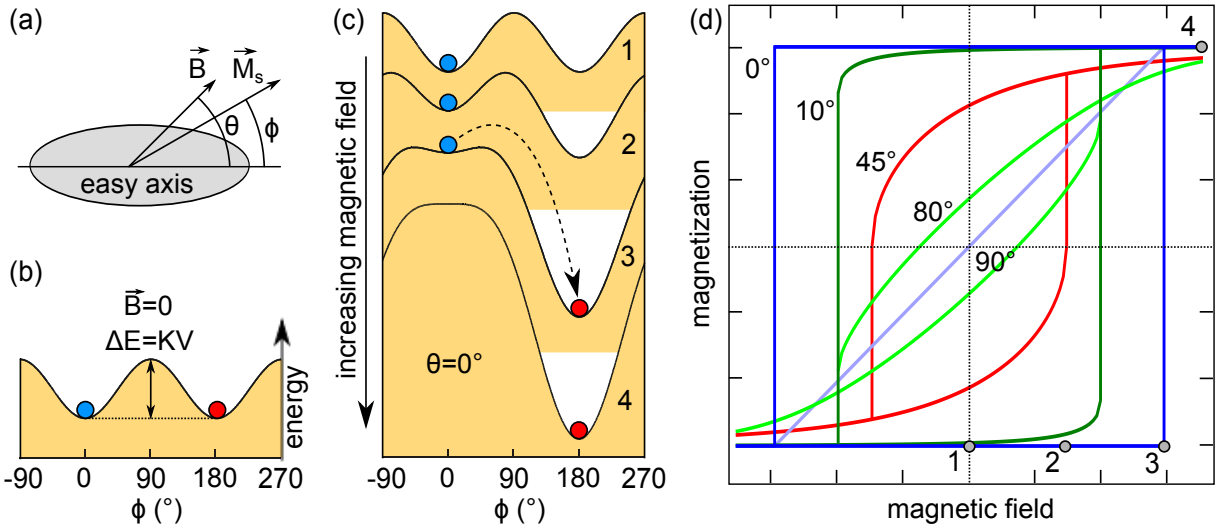

Figure 2.14: (a) Ellipsoidal single domain particle with uniaxial anisotropy. The magnetization $\vec{M}_\mathrm{s}$ and the external magnetic field $\vec{B}$ form angles ϕ and θ with the easy axis, respectively. (b) Without applied field the magnetization has two energetic minima along the easy axis which are separated by a barrier of height $\Delta E = KV$. (c) Schematic energy landscape for an increasing field along the easy axis ($\theta = 0°$). The magnetization suddenly reverses at the switching field (3). (d) Hysteresis for different angles θ. The points of the four diagrams in (c) are indicated.

field $\vec{B}$ and the easy axis of the particle. Therefore, the whole system is represented by the angles ϕ between magnetization and easy axis, and θ between applied field and easy axis (see Fig. 2.14(a)). The energy of the system is given by

$$E = KV \sin^2 \phi - M_\mathrm{s} V B \cos(\theta - \phi), \tag{2.8}$$

where the first term is the magnetic anisotropy energy, and the second one the Zeeman energy. Without applied field there are two degenerate energy minima at $\phi = 0°$ and $\phi = 180°$ (see Fig. 2.14(b)). The minima are separated by an energy barrier $\Delta E = KV$. If the barrier is on the order of the thermal energy $k_\mathrm{B}T$ or smaller, spontaneous switching of the superspin can occur. The mean time between two flips is called Néel relaxation time τ_N, and given by the Néel-Arrhenius equation [201]

$$\tau_\mathrm{N} = \tau_0 \exp\left(\frac{KV}{k_\mathrm{B}T}\right). \tag{2.9}$$

The prefactor τ_0 is the inverse attempt frequency to surmount the energy barrier. The observed magnetic behavior depends on the measurement time τ_m: If τ_m is longer than τ_N, the superspin will flip several times during the measurement so that the net magnetization

averages to zero (superparamagnetic regime). If τ_m is shorter than τ_N, the superspin stays in its initial configuration during the measurement (blocked regime).
Keeping the measurement time and the particle volume constant, the transition between superparamagnetic and blocked state occurs as a function of temperature. The temperature at which τ_m equals τ_N is called the blocking temperature

$$T_\mathrm{B} = \frac{KV}{k_\mathrm{B} \ln\left(\frac{\tau_\mathrm{m}}{\tau_0}\right)}. \tag{2.10}$$

For a typical measurement time of 100 s and an attempt time of 10^{-9} s, the value of the logarithm is about 25. Eq. 2.10 has an important consequence for magnetic data storage, where information shall be stored in particles with small V for long times τ_M at room temperature. Consequently, one needs materials with high anisotropy constant K.
The two magnetic regimes of a single-domain particle correspond to two types of magnetization curves: In the superparamagnetic state the loops appear closed and S-shaped as for an ordinary paramagnet. In the case of vanishing anisotropy, the projection M of the magnetization onto the field direction is given by the classical Langevin function

$$M(B) = M_\mathrm{s}\left(\coth\left(\frac{M_\mathrm{s}B}{k_\mathrm{B}T}\right) - \frac{k_\mathrm{B}T}{M_\mathrm{s}B}\right). \tag{2.11}$$

The initial slope of $M(B)$ is the zero-field susceptibility χ, which is given by

$$\chi = \frac{M_\mathrm{s}^2}{3k_\mathrm{B}T}. \tag{2.12}$$

The equation shows that the zero-field susceptibility of a superparamagnet is much higher than of an atomic paramagnet as the superspin M_s is much larger than a single spin.
In the blocked regime, for non-vanishing anisotropy hysteresis occurs as for a conventional ferromagnet. The corresponding curves can be derived by calculating the component of $\vec{M}_\mathrm{s}$ from the set of angles ϕ that minimize Eq. 2.8 for different field magnitudes B at a given angle θ. Some example curves are show in Fig. 2.14(d). The loop is broadest for $\theta = 0$, and gets thinner as θ increases, till it collapses into a single line for $\theta = 90°$.

2.4 Polar Oxide Surfaces

In ionic crystals, surface orientations terminated by alternating layers of positively and negatively charged ions are called *polar surfaces* [52] and have been subject of intense work for the last decades [53, 202, 203]. As the elementary building blocks are double layers, each bearing a net dipole moment, their consecutive stacking would result in an

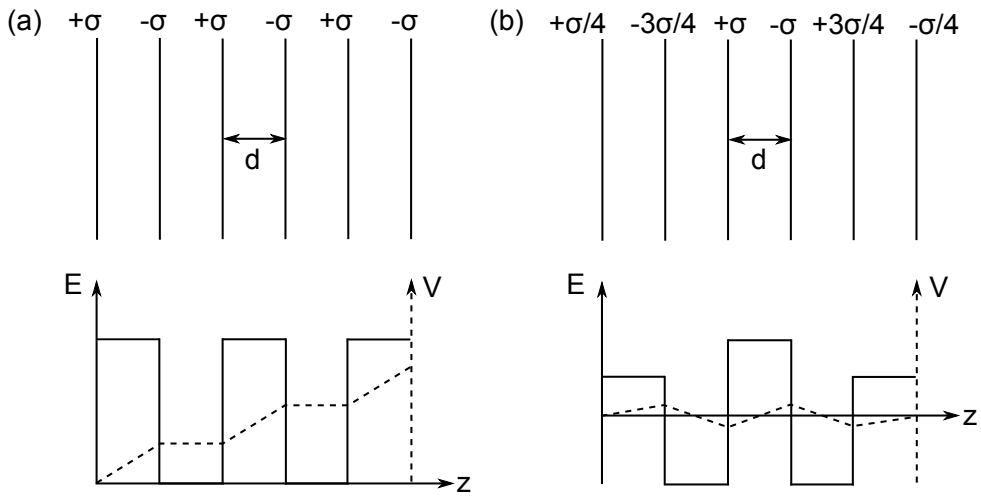

Figure 2.15: Plate capacitor model of a polar surface with layers separated by d and carrying each a surface charge density σ. The electric field E (solid line) and the electrostatic potential V (dashed line) are sketched. (a) In the ideal case V diverges with increasing number of layers. (b) V averages to zero by reducing σ in the two outermost layers. Adapted from Ref. [204].

infinite increase of the electrostatic potential and the corresponding surface energy as shown in Fig. 2.15(a). Evidently, such ideal polar surfaces cannot exist.
Nevertheless, polar surfaces can be prepared experimentally as nature avoids the truncated bulk situation through a variety of structural and electronic surface modifications that supply compensating surface charges [202]. For example, an octopolar (2×2) reconstruction - removal of 75% of the topmost and 25% of the second layer atoms by forming {100} nanofacets (see Fig. 2.15(b)) - is suitable to fully release the polarity [205]. This type of reconstruction occurs for a number of different oxides [206–209], but also a variety of other reconstructions has been observed [210]. Moreover, adsorption of light elements [211] or hydroxyl groups [212, 213] can supply charge and thus stabilize the surface.
In ultrathin polar films, the electrostatic contribution to the surface energy does not diverge as the number of double layers is limited, with the low thickness limit being just a single bilayer. Correspondingly, the existence of uncompensated polarity has been theoretically predicted for such films [214]. However, up to now it was invariably found that also for ultrathin polar films a lowering of the energy associated with the dipole layer takes place. To mention a few examples, for an FeO(111) bilayer on Pt(111) a strong reduction of the interlayer spacing was measured [215, 216], for a MgO(111) bilayer on Ag(111) an in-plane expansion reducing the surface charge density as well as a metalization of the bilayer was reported [54], and for a NaCl(111) trilayer on Al(111) a change of the ionic valence state of the Na ions was calculated [217].

CHAPTER 3

Experimental Methods

In this chapter, I briefly summarize the basic concepts of the experimental techniques used in this thesis. For more detailed reviews of the methods, references to corresponding articles are given in each section.

3.1 Scanning Tunneling Microscopy

In scanning tunneling microscopy (STM) a sharp tip is located a few Ångström above a sample surface [218]. A bias voltage U_s applied to the sample causes a tunneling current I to flow between tip and sample. By piezo actuators the tip is laterally scanned over the surface while a feedback loop regulates the vertical distance such that the tunneling current stays constant. The control voltage is plotted for imaging.

A comprehensive overview about the theory of STM can be found for example in Ref. [219]. Here, I restrict myself to a simple one-dimensional model as depicted in Fig. 3.1, which is sufficient to derive two work function measurements techniques used in this thesis. Within this model, a negative sample bias voltage U_s enables tunneling of electrons from occupied sample states between $E_{\mathrm{F,s}}-eU_\mathrm{s}$ and $E_{\mathrm{F,s}}$ into unoccupied tip states through a trapezoidal barrier. The main contribution comes from electrons close to the sample Fermi edge $E_{\mathrm{F,s}}$ as the tunneling probability is exponentially suppressed for electrons with lower energies. Within the Wentzel-Kramers-Brillouin (WKB) approximation the distance dependence of the tunneling current can be approximated [220] as

$$I(z) \propto \exp\left(-k\sqrt{\bar{\Phi}}z\right) \tag{3.1}$$

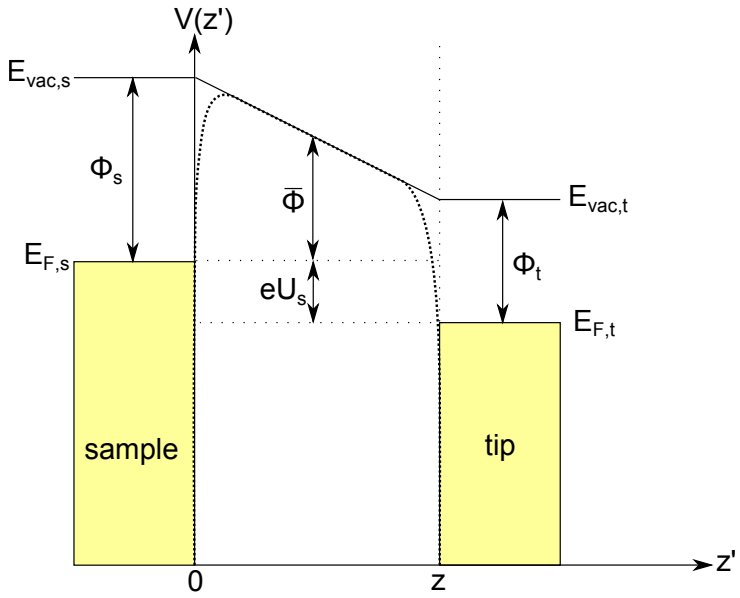

Figure 3.1: One-dimensional model of the tunneling barrier in STM. A bias voltage U_s is applied to the sample that has a work function Φ_s (correspondingly Φ_t is the work function of the tip). Electrons from the sample Fermi edge tunnel through the trapezoidal barrier with apparent height $\bar{\Phi}$ into unoccupied tip states. A potential regarding image potential effects is indicated by a dotted line. Adapted from Ref. [204]

with the constant $k = 2\frac{\sqrt{2m}}{\hbar} \approx 1.025\,\mathrm{eV}^{-\frac{1}{2}}\mathrm{\AA}^{-1}$. Herein, m is the free electron mass. The apparent barrier height depends on the work functions of sample and tip and is given by

$$\bar{\Phi} = \frac{\Phi_\mathrm{s} + \Phi_\mathrm{t} - eU_\mathrm{s}}{2}. \tag{3.2}$$

Herein, the influence of a Coulomb-like image potential from surface charges induced by the tunneling electrons (indicated by a dotted line in Fig. 3.1) is neglected. Although an exact treatment of this potential is difficult [221], it reduces in general the area under tunneling barrier, which leads to an overestimation of the apparent barrier height.

$I(z)$ Spectrosopy

A possible technique to determine work function differences by STM is $I(z)$ spectroscopy. From Eq. 3.1 one can directly derive the apparent barrier height

$$\bar{\Phi} = \left(\frac{1}{k}\frac{\mathrm{d}\ln I}{\mathrm{d}z}\right)^2. \tag{3.3}$$

By measuring the decay of the tunneling current with the same tip above two positions A and B one can determine the apparent barrier height difference

$$\Delta\bar{\Phi} = \bar{\Phi}_\mathrm{A} - \bar{\Phi}_\mathrm{B} = \frac{\Phi_\mathrm{A} + \Phi_\mathrm{t} - eU_\mathrm{s}}{2} - \frac{\Phi_\mathrm{B} + \Phi_\mathrm{t} - eU_\mathrm{s}}{2} = \frac{\Phi_\mathrm{A} - \Phi_\mathrm{B}}{2} = \frac{\Delta\Phi}{2}. \tag{3.4}$$

This means that under the assumption of a trapezoidal barrier the work function difference $\Delta\Phi$ is just twice the apparent barrier height difference $\Delta\bar{\Phi}$. Note that the overestimation of the apparent height by neglecting the image potential is mainly eliminated by taking the difference $\Delta\bar{\Phi}$.

Gundlach Oscillations

As further method to determine work function differences by STM makes use of *Gundlach oscillations* (also called *field emission resonances* or *Stark-shifted image potential states*) [222]. The origin of these oscillations can be understood using the model shown in Fig. 3.2. Upon applying a positive sample bias voltage U_s that exceeds the sample work function Φ_s (field emission regime) electrons tunnel from the tip, and are trapped in the triangular potential in front of the sample surface. In consequence, standing electron waves emerge at characteristic energies.

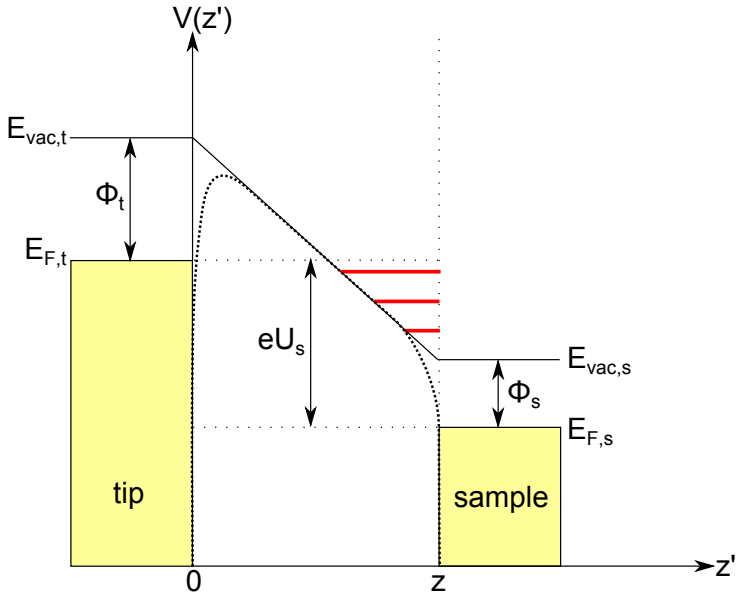

Figure 3.2: Schematic energy diagram showing the origin of Gundlach oscillations: In the field emission regime ($eU_\mathrm{s} \geqslant \Phi_\mathrm{s}$) electrons can form at discrete energies standing waves in the triangular potential well in front of the surface. Adapted from Ref. [204]

These discrete states occur as peaks in scanning tunneling spectroscopy (STS). Here, I will only give the basic idea of this technique and refer again to Ref. [219] for more details. According to Ref. [219], the tunneling current can be approximated by

$$I \propto \int_{E_\mathrm{F}}^{E_\mathrm{F}+eU_\mathrm{s}} \rho_\mathrm{t}(E - eU_\mathrm{s})\rho_\mathrm{s}(E)T(E,U_\mathrm{s})\mathrm{d}E. \tag{3.5}$$

This means that the tunneling current is a convolution of the local density of states (LDOS) of tip ρ_t and sample ρ_s weighted with an energy dependent transmission probability T. Under the assumptions that the tip LDOS is featureless around E_F and T is constant in the energy interval of interest, one gets as central result

$$\frac{\mathrm{d}I}{\mathrm{d}U_\mathrm{s}} \propto \rho_\mathrm{s}(E_\mathrm{F} + eU_\mathrm{s}), \tag{3.6}$$

i.e., the differential tunneling resistance is proportional to the sample LDOS. As the Gundach oscillation states have a high LDOS they appear as pronounced peaks in STS. The absolute position of the peaks strongly depends on the work function and the geometrical shape of the tip [223] as well as the tunneling current chosen for tip stabilization. Nevertheless, Lin *et al.* have shown in Ref. [224] that the peaks shift by a constant energy value when measuring on sample areas with different work functions, whereby the shift is equal to the work function difference.

3.2 X-Ray Magnetic Circular Dichroism

X-ray magnetic circular dichroism (XMCD) denotes the difference in absorption of left and right circularly polarized X-rays by a magnetized sample. It was theoretically predicted in 1975 by Erskine and Stern [225] and first experimentally observed in 1987 by Schütz *et al.* [226]. Since then XMCD has been developed as a powerful tool for element specific and highly (surface) sensitive determination of magnetic moments. Detailed reviews can be found for example in Refs. [227] and [228].

3.2.1 X-ray Absorption Spectroscopy

XMCD is based on X-ray absorption spectroscopy (XAS), which is a widely used technique to determine the electronic and local geometric structure of matter. In XAS, a sample is illuminated by monochromatic X-rays which get absorbed by exciting bound electrons into unoccupied states. Upon choosing suitable photon energies mainly core electrons are excited, which possess element specific binding energies. This leads to characteristic absorption edges in the spectra, which are designated by progressive letters and numbers depending on the level from where the core electrons are excited (K for 1s, L_1 for 2s, L_2 for $2p_{\frac{1}{2}}$, L_3 for $2p_{\frac{3}{2}}$, M_1 for 3s, etc.) [229].

There are different ways to measure the absorption coefficient: The most direct method is to compare the X-ray beam intensity before and after the sample (transmission yield mode). However, this is only suitable for very thin samples (on the order of 1 µm) due to the low penetration depth of soft X-rays. Since the contribution from the surface is much smaller than from bulk, this method is not surface sensitive.
In the fluorescence yield mode, one detects photons which are emitted when filling core holes by outer electrons. For soft X-rays this radiative decay is improbable compared to Auger electron emission, which results in a low signal-to-noise ratio. The method is also not surface sensitive, and corrections for self-absorption effects are needed [230].
In the total electron yield (TEY) mode, all electrons leaving the sample (photoelectrons, Auger electrons, secondary electrons) are detected by measuring the current that flows to the sample to balance the lost charge. The TEY has been shown to be nearly proportional to the absorption coefficient [231]. In contrast to the transmission and fluorescence yield modes, which are based on the measurement of X-rays, the short escape depth of the electrons [232] makes this mode highly surface sensitive. I note that alternatively only the high energy Auger electrons could be detected (Auger electron yield mode), which results in even more surface sensitivity, but at the cost of lower counting rates.

3.2.2 Two Step Model

Although a full description of the XMCD effect is complex, its concept can be illustrated in a simple two step model [233]. In the first step, a circularly polarized photon excites a core electron. If the core state is split by spin-orbit interaction, the probability to excite spin up and down electrons is not equal (*Fano effect*) [234, 235]. This leads to an effective spin polarization of the exited electrons. For example, at the $2p_{\frac{3}{2}}$ level a right circularly polarized photon excites more spin up electrons (62.5%), while at the $2p_{\frac{1}{2}}$ level more spin down electrons are excited (75%) as sketched in Fig. 3.3(a). For left circularly polarized light the spin polarization is reversed (see Fig. 3.3(b)).
In the second step, the spin polarized electrons are used to probe the magnetism of the sample. For a non-magnetic sample there is no effect as spin up and down contribute to the absorption in equal shares. In contrast, for a ferromagnetic sample the exchange interaction induces a valence band splitting, whereby the energy for one spin orientation is lowered (majority spin, here spin down) and enhanced for the opposite one (minority spin, here spin up) as shown in Fig. 3.3. Consequently, the total transition probability is higher for spin up electrons as there are more final states at the Fermi edge. Thus, the spin polarization causes that absorption of right circularly polarized photons is dominating

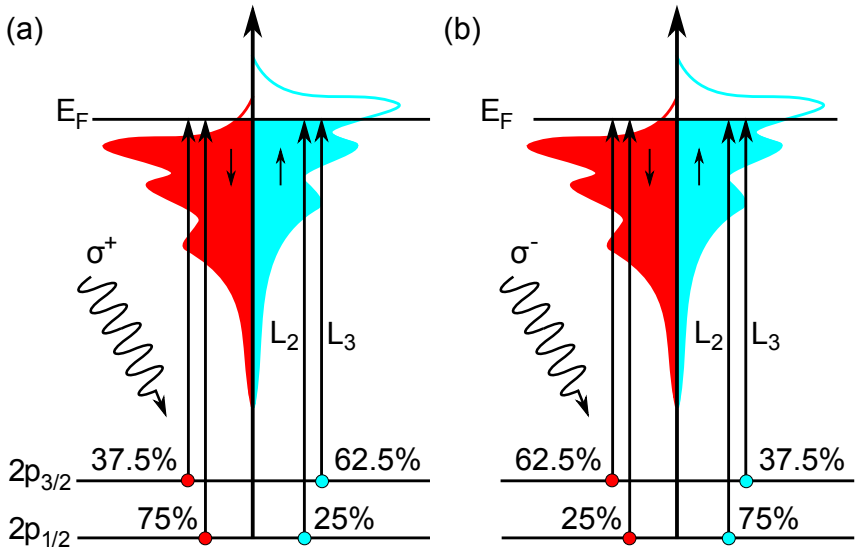

Figure 3.3: (a) A right circularly polarized photon excites (σ^+) more spin up electrons at the $2p_{\frac{3}{2}}$ level, but more spin down electrons at the $2p_{\frac{1}{2}}$ level. Relevant for absorption are mainly spin up states which have a higher density of final states. (b) For absorption of a left circularly polarized photon (σ^-) the situation is reversed. Partially adapted from Ref. [236].

at the L_3 edge, while at the L_2 edge preferentially left circularly polarized photons are absorbed as shown in Figs. 3.4(a) and (b). Note that an inversion of the magnetization has the same effect as an inversion of the photon helicity.

To summarize, one needs electronic transitions from a spin-orbit split core level into the band that carries the magnetism in order to observe an XMCD effect. Regarding that dipole transitions ($\Delta l = \pm 1$) have the highest transition probability [237], all transitions relevant for this thesis are listed in Tab. 3.1.

In principle, for Rh also the $L_{2,3}$ edges, i.e., transitions from 2p to 4d, show an XMCD effect [238]. However, they lie at higher energies than accessible at the beamline used for our experiments. To conclude, I refer the reader who is interested in a theory of XMCD going beyond the simple one electron picture to Ref. [239].

element	spin-orbit split levels	magnetic level	absorption edges
Fe, Co	$2p_{\frac{1}{2}}$, $2p_{\frac{3}{2}}$	3d	L_2, L_3
Rh	$3p_{\frac{1}{2}}$, $3p_{\frac{3}{2}}$	4d	M_2, M_3
Eu	$3d_{\frac{3}{2}}$, $3d_{\frac{5}{2}}$	4f	M_4, M_5

Table 3.1: Overview of the relevant electronic transitions with the names of the corresponding absorption edges for all elements investigated by XMCD in this thesis.

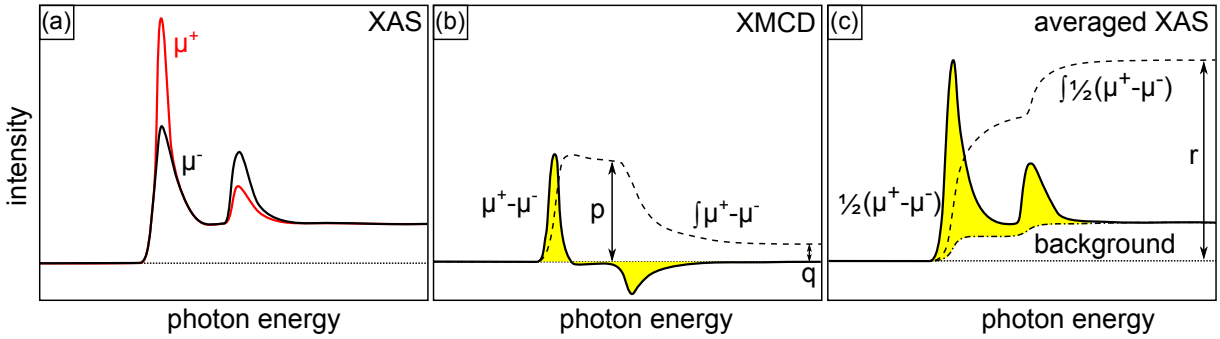

Figure 3.4: (a) Absorption spectra for left (μ^-) and right (μ^+) circularly polarized X-rays by a magnetized sample. (b) Difference spectrum $\mu^+ - \mu^-$ (XMCD signal) and the corresponding integral function. The integrals over the first edge (p) and both edges (q) are indicated. (c) Averaged absorption spectrum $\frac{1}{2}(\mu^+ + \mu^-)$ and the corresponding integral function after subtraction of a steplike background. r denotes the integral over both edges. Sketch after Ref. [182].

3.2.3 Sum Rules

The power of XMCD increased with the derivation of sum rules by Thole and Carra *et al.* [240, 241], which allow to quantitatively determine orbital (m_L) and spin (m_S) magnetic moments. Using their general formula, one derives for the $L_{2,3}$ edges (investigated in the case of Co and Fe) the sum rules

$$\frac{m_L}{n_\mathrm{h}\mu_\mathrm{B}} = \frac{2}{3}\frac{q}{r} \tag{3.7}$$

$$\frac{m_S}{n_\mathrm{h}\mu_\mathrm{B}} = \frac{3p-2q}{r} - 7\frac{\langle T_z\rangle}{n_\mathrm{h}}\,. \tag{3.8}$$

Herein, n_h is the number of holes in the magnetic 3d band, and μ_B the Bohr magneton. p and q denote the integrals of the XMCD spectrum $(\mu^+ - \mu^-)$ over the L_3 edge only and both edges, respectively (compare Fig. 3.4(b)):

$$p = \int_{L_3} (\mu^+ - \mu^-)\mathrm{d}E \quad \text{and} \quad q = \int_{L_3+L_2} (\mu^+ - \mu^-)\mathrm{d}E \tag{3.9}$$

Furthermore, r denotes the integral of the polarization averaged spectrum over both edges after subtraction a steplike background (see Fig. 3.4(c)), which originates from transitions into other unoccupied valence states such as 4s bands:

$$r = \int_{L_3+L_2} \frac{1}{2}(\mu^+ + \mu^-)\mathrm{d}E \tag{3.10}$$

The observable quantity $m_S + 7\langle T_z \rangle$ is called *effective spin moment* and includes the expectation value $\langle T_z \rangle$ of the projection of the magnetic dipole operator onto the beam direction. It is a measure for the quadrupole moment of the spin density, or in other words for the asymmetry of the spin distribution. As such an asymmetry mainly arises from crystal field splitting or spin-orbit coupling [241], it is usually negligible for cubic symmetry and vanishing orbital moment [241–243].
As the principal quantum number does not enter the sum rules, one gets the same result for the $M_{2,3}$ edges investigated for Rh by replacing $L_{2,3}$ by $M_{2,3}$ in the formulas. For the $M_{4,5}$ edges (investigated in the case of Eu) one derives the sum rules

$$\frac{m_L}{n_\mathrm{h}\mu_\mathrm{B}} = \frac{q}{r} \tag{3.11}$$

$$\frac{m_S}{n_\mathrm{h}\mu_\mathrm{B}} = \frac{5p-3q}{2r} - 6\frac{\langle T_z \rangle}{n_\mathrm{h}}\,. \tag{3.12}$$

with the number n_h of holes in the 4f band. p and q are defined analogously to above:

$$p = \int_{M_5} (\mu^+ - \mu^-)\mathrm{d}E \quad \text{and} \quad q = \int_{M_5+M_4} (\mu^+ - \mu^-)\mathrm{d}E \tag{3.13}$$

Schillé *et al.* pointed out that here also the isotropic spectrum μ^0 has to be taken into account to determine r as it may differ form the polarization averaged one [244]:

$$r = \int_{M_5+M_4} \frac{1}{3}(\mu^+ + \mu^- + \mu^0)\mathrm{d}E \tag{3.14}$$

Although the sum rules are based on several assumptions (see Ref. [237] for details), they yield for Fe, Ni and Co magnetic moments that fit to the values obtained from other techniques within a few percent [182, 245]. Also for rare earths a reasonable accuracy was found [246, 247]. Note that the ratio m_L/m_S has in general a higher precision as it does not depend on the hole number n_h and the polarization averaged integral r.

3.3 Low Energy Electron Diffraction

Low energy electron diffraction (LEED) is a technique to determine the crystal structure of surfaces [248, 249]. Therefore, the sample is bombarded by electrons with energies of about 20 - 300 eV. Due to the strong interaction of low energy electrons with matter, their penetration depth is only on the order of a few atomic layers, thus making LEED highly surface sensitive. The electrons are diffracted at the surface and accelerated onto a fluorescence screen where the diffraction pattern becomes visible.

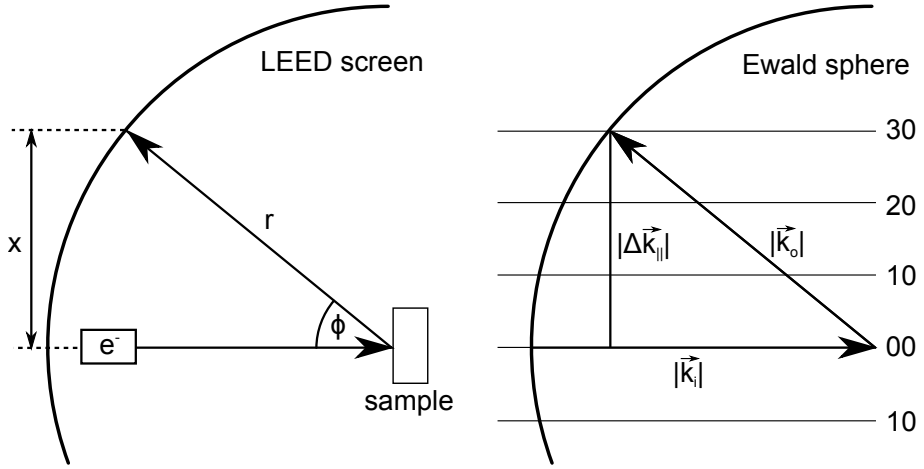

Figure 3.5: Connection between LEED geometry and Ewald construction. (a) Electrons emitted from an electron gun are diffracted at the sample surface under an angle ϕ. They reach the hemispherical screen with radius r at the projected position x. (b) The diffraction condition for electrons with wave vector $\vec{k}_i$ is fulfilled where the Ewald sphere intersects the reciprocal surface lattice rods as demonstrated here for the (30) spot. Partially adapted from Ref. [204].

As shown in Fig. 3.5 the geometry of the LEED is directly connected to the Ewald construction of diffraction. The wave vector of the incoming electrons $\vec{k}_\mathrm{i}$ is perpendicular to the sample surface. The elastically scattered electrons leave the sample with wave vector $\vec{k}_\mathrm{f}$ of the same length as $\vec{k}_\mathrm{i}$. As the reciprocal lattice of a surface is a two-dimensional lattice with rods extending perpendicular from each lattice point, the diffraction condition is fulfilled if the difference $\Delta\vec{k}_{||}$ of the parallel wave vectors components equals a reciprocal space vector. Hence, analyzing the positions x of the spots on the screen reveals information about size, symmetry and rotational alignment of the reciprocal lattice.

For completeness, I note that also the atomic positions within the unit cell and relaxations of the topmost layers can be determined by recording the spot intensities as a function of the primary electron energy (LEED I-V) [250].

Beside spots belonging to the atomic lattices, additional superstructure spots are frequently observed. They are located at positions corresponding to linear combinations of reciprocal lattice vectors pointing to the main spots. Hence, they are often interpreted to arise from multiple scattering processes. These events substantially contribute to LEED since electrons strongly interact with matter. Alternatively, the superstructure spots may be assumed to result from diffraction at the unit cell of a corrugated overlayer [249, 251]. As both descriptions lead to the same spot positions, only a profound analysis of the spot intensities may give insight which effect is dominating.

3.4 Low Energy Electron Microscopy

Low energy electron microscopy (LEEM) is a technique that allows to study the surface of a conductive crystalline sample with nanometer spatial resolution in real time [252, 253]. Its principle is shown in Fig. 3.6. High energy electrons (typically 20 keV) are emitted from an electron gun and focused by a sequence of condenser lenses. The beam is deflected by 60° while passing through a magnetic sector field so that it enters the surface under perpendicular incidence. Before reaching the sample, the electrons are decelerated down to low energies by applying a bias voltage of typically -5 V to 100 V between sample and electron gun, which leads to the high surface sensitivity of LEEM.

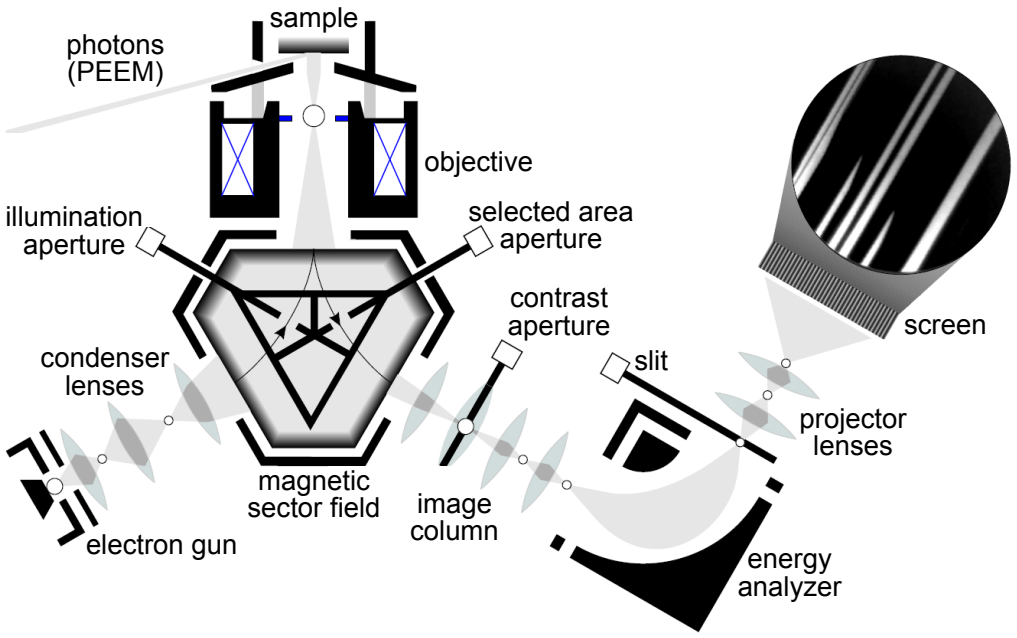

Figure 3.6: Experimental setup of the LEEM system used for this thesis. The beam emitted by the electron gun is focused by condenser lenses and deflected to the sample by a magnetic sector field. The back-scattered electrons are deflected in the image column, pass through the energy analyzer and are projected on a fluorescence screen. For imaging also photoelectrons excited by an external light source can be used. Adapted from Ref. [254].

For crystalline samples, the elastically backscattered electrons are confined to several specific angles due to diffraction just as previously described for LEED. The electrons are reaccelerated by the objective lens and focused to points in the back focal plane as shown in Fig. 3.7, i.e., here the diffraction pattern is formed. At the same time a real image of the sample is formed in a different plane as also visible in Fig. 3.7.

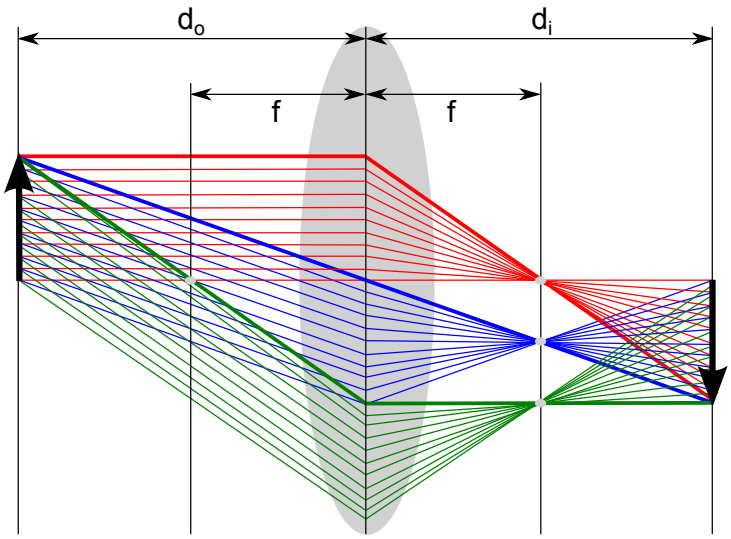

Figure 3.7: Rays leaving the object at different points, but under the same angle, intersect in the back focal plane. Here, the diffraction pattern is formed. The real image can be constructed using three principal rays (indicated in bold). Adapted from Ref. [254].

On their further way, the electrons are deflected by the sector field into the imaging column where they pass through several lenses. Depending on the adjustment of these lenses either the reciprocal or the real space image is transferred (see Ref. [255] for details). Finally, the image is magnified by projector lenses onto a fluorescence screen. The opportunity to choose between reciprocal and real space image opens together with a set of apertures a variety of imaging modes, some of which I want to mention:

- **LEED**
  By projecting the diffraction pattern onto the screen the LEEM setup can be used like a conventional LEED. Inserting the selected area aperture at the site of the first real image improves the imaging quality by removing abaxial rays.

- **Microdiffraction (µ-LEED)**
  Microdiffraction is conceptually identical to LEED, but by inserting an illumination aperture the electron spots on the sample can be reduced down to about $1\,\mu m^2$. So, a diffraction pattern of a particular island or domain can be obtained.

- **Bright Field Imaging**
  If one selects the electrons contributing to the central spot in LEED by inserting a contrast aperture, the real space image originates only from electrons that leave the surface almost perpendicular. This results in a high vertical contrast which typically

arises from interference of electrons on opposite sides of step edges (step contrast). Interference between electrons reflected at the surface and interface of a thin film can yield a different contrast mechanism (quantum size contrast) [252, 253].

- **Dark Field Imaging**
  Alternatively, a different LEED spot of particular interest can be selected by the contrast aperture. Consequently, in the real space image all areas that contribute to the selected spot appear bright, while the other areas stay dark. This method yields contrast between different structural phases.

- **Mirror Electron Microscopy (MEM)**
  In this mode, electrons are decelerated to such low energies that they only interact with the near-surface region (typically for -5 V to 0 V sample bias voltage). The exact contrast mechanism is complicated to understand, but mainly arises from differences in the electric field caused for example by height and work function differences. MEM can also be applied for non-crystalline samples.

- **Spectroscopic LEEM (SPE-LEEM)**
  Up to now I did not mention the electron analyzer in Fig. 3.7, which is not part of a conventional LEEM setup. Its presence allows to spatially separate the electrons according to their kinetic energy so that a particular energy can simply be chosen by a slit. This is for example useful to probe the local chemical and electronic structure of a sample, or to filter the background of secondary electrons in LEED [255].

3.5 Photoemission Electron Microscopy

For photoemission electron microscopy (PEEM) one uses - instead of the electron gun in LEEM - an external light source to excite electrons via the photoelectric effect [256, 257]. The photoelectrons are then used for imaging in the same way as the diffracted electrons in LEEM. Therefore, switching between both techniques is easy and fast.
As light source usually a Hg discharge lamp is used, which emits in the ultraviolet spectral range ($E \approx 5\,\mathrm{eV}$). As the photoemission yield depends on sample work function, the imaging contrast is mainly determined by local work function differences. Alternatively, tunable and particularly polarized soft X-rays from a synchrotron allow to retrieve topographical, element specific, or magnetic contrast. Finally, pulsed femtosecond lasers can be used for pump-probe experiments [258].

3.6 Angle-Resolved Photoemission Spectroscopy

Angle-resolved photoemission spectroscopy (ARPES) is an experimental technique to investigate the valence band structure of solids with high surface sensitivity. A comprehensive introduction can be found in Ref. [259].

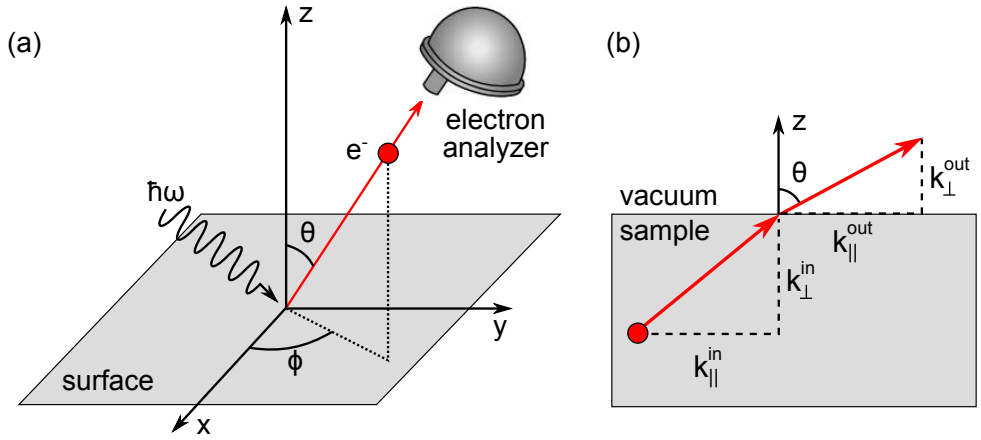

Figure 3.8: Perspective (a) and side view (b) sketch the ARPES geometry. An incident photon leads to emission of an electron under polar angle θ and azimuthal angle ϕ. The parallel component of the electron momentum is conserved upon emission. Partially adapted from Ref. [259].

Just as PEEM, ARPES is based on the photoelectric effect: If an electron with binding energy E_b absorbs a photon of energy $\hbar\omega$, it can leave the solid with a kinetic energy of

$$E_\mathrm{kin} = \hbar\omega - E_\mathrm{b} - \Phi, \tag{3.15}$$

where Φ is the work function of the sample. If the electron is emitted under a polar angle θ with respect to the surface, its momentum parallel to the surface is given by

$$k_\parallel^\mathrm{out} = \sqrt{\frac{2mE_\mathrm{kin}}{\hbar^2}}\sin(\theta) \tag{3.16}$$

using the dispersion relation for free electrons. The corresponding geometry is depicted in Fig. 3.8. Due to the translational symmetry within the surface the parallel component is conserved upon photoemission (modulo a reciprocal lattice vector and neglecting the small photon momentum):

$$k_\parallel^\mathrm{in} = k_\parallel^\mathrm{out} \tag{3.17}$$

The perpendicular component of the electron momentum is not conserved, which is not a problem for two-dimensional structures with few dispersion in this direction. Based on

the equations above, the surface band structure $E_{\mathrm{b}}(k_{\parallel}^{\mathrm{in}})$ can be determined by measuring $E_{\mathrm{kin}}(\theta)$. Experimentally, therefore the sample is illuminated by a beam of monochromatic radiation supplied either by a gas discharge lamp or a synchrotron beamline. To excite mainly valence electrons ultraviolet light with energies of 10 - 50 eV is used. The emitted electrons are collected by an energy analyzer with angular resolution.

CHAPTER 4

Setup and Procedures

Parts of Secs. 4.5 and 4.6 are literally taken from my publications [62], [63] and [64].

In this chapter, I introduce the setups used for the STM, ARPES, and LEEM/PEEM experiments. Furthermore, I present the methods for sample preparation and molecular beam epitaxy (MBE), and details of the DFT calculations performed in this thesis.

4.1 Ultrahigh Vacuum System ATHENE

Most experiments were performed in the ultra high vacuum (UHV) system ATHENE in Cologne, which is schematically shown in Fig. 4.1 in front and side view. A detailed description can be found in Ref. [29]. A base pressure of 3×10^{-11} mbar is achieved by a turbomolecular pump (1), an ion getter pump (2) and a Ti sublimation pump (3) directly attached to the chamber. An additional small turbomolecular pump (4) is used for pumping the load lock system (8), and for differential pumping of the ion source (9). During measurements a cooling trap (5) is filled with liquid N_2.

The sample holder (6) is hosted on a base plate which is mounted on a manipulator (7). The manipulator can be horizontally moved by 300 mm and is rotatable by $\pm 180°$. Using a load lock system (8) one can extract the sample holder from the chamber or store it in a sample garage without breaking the vacuum.

By electron bombardment from a W/Re filament the samples can be heated to temperatures of more than 1600 K. Cooling down to 35 K is provided by a liquid He flow cryostat, which is connected to the base plate via Cu braids. The temperature is measured with a type K thermocouple directly attached to the sample. Cleaning of the sample is achieved

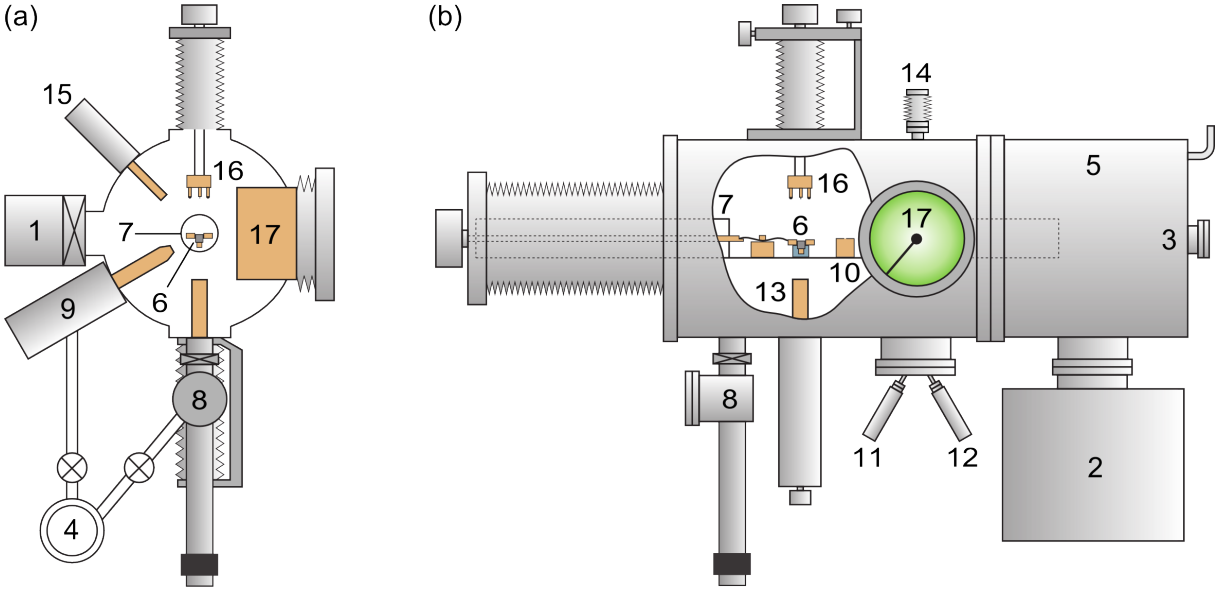

Figure 4.1: Sketch of the UHV chamber ATHENE in (a) front and (b) side view. For the numeration of the equipment see the description in the text.

by a differentially pumped ion source (9). The ion flux can be accurately measured in a Faraday cup (10) mounted on the manipulator.

Samples can be grown by (reactive) molecular beam epitaxy (MBE) using two water-cooled Knudsen cells for Eu (11) and Gd (12) as well as a four pocket e-beam evaporator for deposition of transition metals (13). The fluxes of the effusion cells can be precisely measured with a quartz microbalance (14) which is movable to the exact sample position. Gases can be supplied via three different leak valves (not shown in the sketch) and are guided through tubes directly to the substrate, which increases the local pressure at the sample position by a factor of 50 compared to the chamber pressure. The latter can be measured with a quadrupole mass spectrometer (15).

The sample can be characterized with a home-built, magnetically stabilized variable temperature STM (16) [260]. Imaging was conducted at room temperature if not specified otherwise. Typical parameters are $U_s \leqslant -1\,\mathrm{V}$ for the sample bias voltage and $I_t \leqslant 1\,\mathrm{nA}$ for the tunneling current. All images are digitally post-processed with the WSxM software [261]. LEED measurements were performed with a three grid rear view analyzer (17). To measure lattice constants, the spot positions were determined from images taken by a video camera directly mounted onto the LEED flange. By averaging over the positions of equivalent spots and calibrating with respect to the substrate spots, lattice constants can be determined with an error of less than 1%. LEED patterns are displayed with inverted contrast to enhance the visibility of the diffraction spots.

4.2 XMCD Beamline

All XMCD experiments were conducted at the ID08 Dragon beamline of the European Synchrotron Radiation Facility (ESRF) in Grenoble, France. Two undulators provide an intense beam of $(99 \pm 1)\%$ circularly polarized monochromotic X-rays. With photon energies tunable in the range from 300 eV to 1.6 keV the beamline is well suited to study the magnetic properties of transition metals and rare earths.

The end station of the beamline consists of two interconnected UHV chambers. One is used for *in situ* sample preparation and has a base pressure in the low 10^{-10} mbar range. It is equipped with an electron bombardment sample heating and an ion source for sample cleaning. Via leak valves O_2 and ethylene can be dosed. Several e-beam evaporators for transition metal deposition and a Knudsen cell with Eu were additionally mounted. The sample quality can be checked *in situ* by LEED and room temperature STM.

After preparation the samples are transferred through a transfer tube (middle 10^{-9} mbar pressure) into the high-field magnet (low 10^{-10} mbar pressure). The sample temperature can be adjusted between 300 K and 10 K using a helium bath cryostat. The magnetic field can be varied from -5 T to $+5$ T with a maximum rate of 3 T per minute.

The magnetic field direction is fixed parallel (or antiparallel) to the beam, which comes horizontally from the side. Therefore, the angle θ between surface normal and beam can be adjusted by rotating the sample around its vertical axis. Since the projected area of the beam is proportional to $\cos(\theta)$ and goes to zero as θ approaches 90°, the incidence angle is practically limited to around 70°. The in-plane orientation of the incoming beam with respect to the surface lattice is undefined as the sample was not mounted in a particular direction and cannot be rotated around the surface normal.

XMCD spectra have been recorded in the total electron yield mode and were normalized to the photon flux probed by the photocurrent on a gold grid. In principle, also fluorescence yield and transmission measurements are possible at the beamline ID08.

4.3 ARPES Setup

The ARPES measurements presented in this thesis were performed at the Institut za fiziku (Zagreb, Croatia) in the group of M. Kralj. A detailed description of the chamber can be found in Ref. [262]. The UHV chamber is built of mu-metal for magnetic shielding. A base pressure in the low 10^{-9} mbar range is reached by a turbomolecular and a Ti sublimation pump. The Ir crystal is mounted on a sample holder (see Fig. 4.2), which is

movable in x-, y- and z-direction, and fully rotatable around the z-axis. The polar angle θ can be accurately adjusted by rotating the whole manipulator and is read from a vernier scale with a precision of 0.1°. In contrast, the azimuthal angle has to be changed with a wobble stick and can be adjusted only within ±1°.

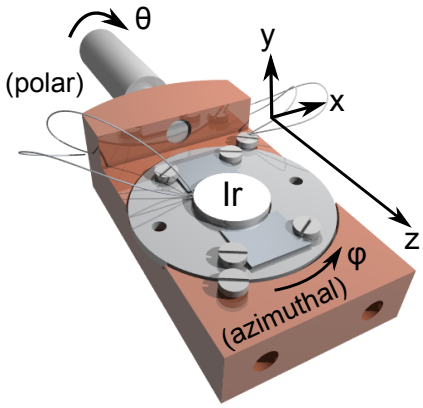

Figure 4.2: Sample holder of the ARPES chamber at the Institut za fiziku. The polar angle ϕ and the azimuthal angle θ are indicated. Adapted from Ref. [262].

Heating is provided by electron bombardment from a filament on the backside of the sample. For cooling down to 45 K the coldhead of a closed-cycle helium refrigerator is attached to an adapter which is connected to the sample holder via a copper braid. The sample can be cleaned using a ion gun, and several gases can be provided via leak valves. For Eu evaporation a Knudsen cell from Cologne was mounted to the chamber. The sample orientation and quality can be checked by LEED.
As light source a noble gas discharge lamp is used. For the data presented in this thesis He with a dominating photon energy of 21.2 eV was used; the light of the discharge lamp is not polarized. A hemispherical electron energy analyzer resolves emission angles in the range of ±5 °. The photoelectron intensity is collected on a microchannel plate in the form of two-dimensional maps in dependence of kinetic energy and emission angle. All spectra were post-processed using the Lucy-Richardson deconvolution procedure [263].

4.4 LEEM/PEEM Setup

All LEEM and PEEM measurements were performed at the university Duisburg-Essen in the group of M. Horn von Hoegen using a commercial SPELEEM (Spectroscopic Photo-Emission and Low Energy Electron Microscope) system. The basics setup of a SPELEEM

system and its principle of function have already been discussed in Sec. 3.4, and are described in detail in Ref. [255].
For LEEM experiments 20 keV electrons emitted from a LaB_6 cathode were used. To perform PEEM experiments the sample was illuminated with light from a Hg short arc lamp ($h\nu = 5\,\mathrm{eV}$) under 15° grazing incidence. Samples can be prepared *in situ* in a low 10^{-10} mbar base pressure. Therefore, an electron bombardment heating and an ion gun are provided. Several gases can be supplied via leak valves. For Eu evaporation a Knudsen cell from Cologne was mounted to the chamber.

4.5 Sample Preparation

Preparation of Ir(111)

As substrate, the (111) surface of a hat shaped Ir single crystal was used. The surface was initially annealed at 1120 K in a 10^{-6} mbar O_2 atmosphere in order to reduce C impurities. Before each experiment the sample was cleaned by repeated cycles of sputtering with 2 keV Kr^+ ions between room temperature and 920 K, and annealing to 1530 K. This method results in clean, flat terraces with sizes in the order of 100 nm.

Growth of Graphene

Gr can be grown on a clean Ir(111) surface by a well-established two step method [264]:

(i) Room temperature adsorption of ethylene (C_2H_4) to full saturation and consecutive thermal decomposition at about 1490 K (*temperature programmed growth*, TPG) [39]. The method yields compact Gr flakes, whose average size can be tuned by the annealing temperature [71].

(ii) Continuous dosing of 5×10^{-7} mbar ethylene at sample temperatures between 1170 K and 1490 K for 600 s (*chemical vapor deposition*, CVD) [92, 93]. Both steps together yield a well-oriented, coherent, and closed Gr monolayer.

The exact growth time and temperature as well as the ethylene pressure were varied for different preparations in this thesis; details are given in the corresponding sections.

(Reactive) Molecular Beam Epitaxy

High purity Eu was evaporated from a water-cooled Knudsen cell. Prolonged degassing of the Eu (which usually has a high H_2 content) ensured a background pressure below

1×10^{-10} mbar during evaporation. Prior to each experiment a quartz crystal microbalance was moved to the precise sample position in order to accurately measure the Eu deposition rate Q, which is typically on the order of 1 Å/min. The corresponding Eu flux can be calculated by multiplying Q with the atomic density of Eu ($\rho_{\mathrm{at,Eu}} = 2.08\times10^{28}$ atoms m^{-3}) according to the equation

$$f_{\mathrm{Eu}}\ [\text{atoms m}^{-2}\text{s}^{-1}] = \rho_{\mathrm{at,Eu}} \cdot Q = 3.47 \times 10^{16} \cdot Q\ [\text{Å/min}]. \tag{4.1}$$

Also Gd was evaporated from a water-cooled Knudsen cell after prolonged degassing. Using the atomic density of Gd ($\rho_{\mathrm{at,Gd}} = 3.02 \times 10^{28}$ atoms m^{-3}) one gets for the Gd flux

$$f_{\mathrm{Gd}}\ [\text{atoms m}^{-2}\text{s}^{-1}] = \rho_{\mathrm{at,Gd}} \cdot Q = 5.03 \times 10^{16} \cdot Q\ [\text{Å/min}]. \tag{4.2}$$

Molecular O_2 was supplied via a leak valve and guided through a tube directly to the substrate. By that, the local O_2 pressure p_{O_2} at the sample position is increased by a factor of 50 compared to the chamber pressure, resulting in a fast pressure decrease at the end of the growth. The O_2 partial pressure in the chamber was measured by a quadrupole mass spectrometer. The local O_2 pressure was calibrated using adsorption experiments on Ni(100) as described in Ref. [48]. Within the kinetic gas theory p_{O_2} can be expressed as an atomic O flux

$$f_{\mathrm{O}}\ [\text{atoms m}^{-2}\text{s}^{-1}] = 2\frac{p_{O_2}}{\sqrt{2\pi m_{O_2} k_{\mathrm{B}} T}} = 5.37 \times 10^{24} \cdot p_{O_2}\ [\text{mbar}] \tag{4.3}$$

assuming $f_{\mathrm{O}} = 2f_{O_2}$ and using the mass m_{O_2} of an O_2 molecule. Here, $T = 300$ K is the deposition temperature. For EuO growth reactive MBE was used, i.e., O_2 and Eu were supplied simultaneously. More details can be found in Ref. [29].
High purity transition metals (Ir, Pt, Fe, Co, Rh) were sublimated from a commercial e-beam evaporator. The chamber pressure remained in the 10^{-11} mbar range during evaporation. The deposition rate was calibrated by determining the coverage of a submonolayer metal film with STM. Cs was evaporated in the low 10^{-9} mbar range from a well degassed Cs dispenser. The Cs flux was also calibrated with STM.

4.6 Density Functional Theory

All density functional theory (DFT) calculations [265, 266] concerning Eu and EuO were performed by T. Wehling and members of his working group in Bremen. Additional data concerning Cs were calculated by P. Lazić in Zagreb.

The DFT calculations were performed spin-polarized using the generalized gradient approximation (GGA) [267] and the projector augmented wave (PAW) basis sets [268, 269] as implemented in the Vienna Ab Initio Simulation Package (VASP) [270]. The strong local Coulomb interaction of the Eu 4f electrons was taken into account within the GGA+U approach using the Coulomb parameters $U = 7\,\mathrm{eV}$ and $J = 1\,\mathrm{eV}$ which have previously been shown to be well suited to describe rare earth systems [271, 272].
As Gr on Ir(111) is incommensurate and even an approximation of (10×10) Gr honeycombs on (9×9) Ir atoms is demanding in computational time, the calculations presented here are restricted to a smaller unit cell: A four layer Ir(111) slab is compressed to an fcc lattice with a lattice constant of 3.5 Å so that the Ir(111) surface and Gr have the same surface lattice constant of 2.46 Å. Previous calculations for Eu adsorption on Gr/Ir(111) have shown that this approximation is adequate to describe the system on the relevant energy scale [28]. If not stated otherwise, the centers of the C rings rest above regular Ir hollow sites corresponding to the fcc area of the moiré unit cell.
To model adsorption or intercalation of Eu or Cs, the adsorbed (intercalated) atoms were placed above (beneath) the centers of the C rings, which have been shown to be the preferred adsorption sites (compare Ref. [28]). The C as well as the Eu/Cs atoms have been relaxed until forces were below $0.02\,\mathrm{eV\,Å^{-1}}$. The geometrical details for EuO calculations are given in the corresponding section as they require a larger context.

CHAPTER 5

Intercalation of Europium

The content of Sec. 5.1 is published in Phys. Rev. Lett. ***110*** *086111 (2013) [62] and its supplement, and also partially contained in Ref. [29]. I conducted all STM and work function measurements, partially together with D. F. Förster. DFT calculations were performed by T. O. Wehling and M. Rösner. The data presented in Sec. 5.2 were measured and analyzed by F. Huttmann in Ref. [273], and are similarly contained in Ref. [29]. I measured and discussed the ARPES data presented in Sec. 5.3 together with M. Petrović and M. Kralj. The LEEM data in Sec. 5.4 were measured in collaboration with C. Witt, A. J. Martínez-Galera, and F.-J. Meyer zu Heringdorf.*

In this chapter, I present a detailed analysis of Eu intercalation underneath Gr on Ir(111), which reveals the atomic structure, the intercalation energetics, and the mechanism of pattern formation. I show that the intercalated layer can be compacted by progressive Eu deposition. I investigate the electronic structure of Eu intercalated Gr by ARPES, and conclude with an analysis of the intercalation mechanism.

5.1 Submonolayer Regime

All experiments were performed at the UHV system ATHENE described in Sec. 4.1. On the clean Ir(111) surface, a fully closed Gr layer was grown by a TPG step at 1500 K followed by CVD at 1170 K (see Sec. 4.5 for details). Eu was deposited while the sample was kept at 720 K during cool down from the Gr growth temperature. Intercalated Eu amounts θ are specified in monolayers (ML), where $\theta = 1$ ML (or 100% ML) corresponds to a full (2×2) intercalation layer with respect to Gr. Hence, the numbers are directly comparable to the apparent coverage in the STM images.

5.1.1 Atomic Structure

After Eu deposition onto Gr at 720 K elevations on the surface become visible in STM, as shown in the lower part of Fig. 5.1(a). They have an apparent height of 1.5 - 2.5 Å, depending on the tunneling resistance. In low temperature STM images such as Fig. 5.1(a),the Gr lattice is resolved in the low areas (indicated as Gr/Ir) as well as in the elevated areas (indicated as Gr/Eu/Ir). Within the Gr/Eu/Ir area a weak (2×2) modulation of the Gr lattice is visible as indicated by a diamond in Fig. 5.1(a). Furthermore, the image shows that the Gr lattice bends continuously over the edge of the elevation. These findings prove that upon exposure at 720 K Eu intercalates underneath Gr, where it forms a (2×2) structure with respect to the Gr lattice.

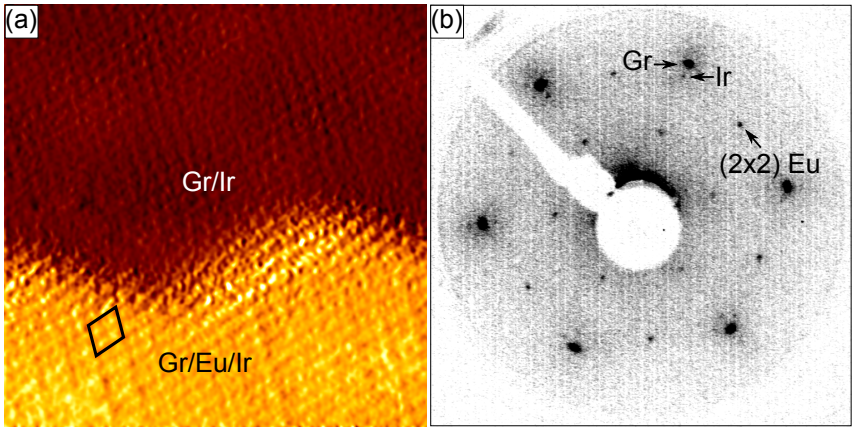

Figure 5.1: (a) Atomically resolved STM topograph (imaged at 35 K, 5.8 nm × 5.8 nm) of Gr continuously bending from bare Gr (Gr/Ir) to an intercalated Eu island (Gr/Eu/Ir). The (2×2) unit cell of the intercalated Eu is indicated by a diamond. (b) LEED pattern of Gr/Ir with intercalated Eu close to layer completion. First-order Ir, Gr and (2×2) Eu intercalation superstructure reflections are indicated. The primary electron energy is 108 eV.

The atomic structure of the intercalated regions becomes also evident by LEED: The LEED pattern in Fig. 5.1(b) taken after Eu intercalation close to layer completion displays the first-order Gr spots which are aligned to the Ir substrate, and additional weak half-order spots with respect to the Gr reflections, indicative of a (2×2) superstructure pinned to Gr. For smaller intercalation coverages the (2×2) reflections become rather diffuse. This can be explained by the smaller extension of the Eu intercalation pattern elements (see later) and therefore smaller (2×2) Eu domains.

5.1.2 Energy Gain upon Intercalation

The energetics driving the Eu intercalation and the pattern formation have been investigated by means of spin-polarized DFT as described in Sec. 4.6. As a quick reminder, the fcc region of the moiré unit cell is modeled by putting Gr pseudomorphically on a compressed Ir slab. The adsorbed/intercalated Eu atoms are located above/below the centers of the C rings. We calculate the total energies of Eu adsorbed on Gr on Ir(111) (E_{ads}) as well as of Eu intercalated between Gr and the Ir(111) substrate (E_{int}) considering a $(\sqrt{3} \times \sqrt{3})$R30° as well as a (2×2) superstructure in both cases. The calculations yield the binding energies $E_{\mathrm{b}} = E_{\mathrm{ads/int}} - (E_{\mathrm{Ir}} + E_{\mathrm{Gr}} + E_{\mathrm{at}})$ per Eu atom listed in Tab. 5.1, where E_{Ir}, E_{Gr} and E_{at} are the total energies of the bare Ir(111) surface, the Gr supercell and a Eu atom. For both structures, there is an energy gain on the order of 2 eV driving the intercalation process. The intercalated (2×2) structure is energetically most favorable, in agreement with the experimental finding presented above.

structure	Eu adsorbed	Eu intercalated
(2×2)	-1.43 eV	-3.80 eV
$(\sqrt{3} \times \sqrt{3})$ R30°	-1.63 eV	-3.59 eV

Table 5.1: Binding energies E_{b} per Eu atom for Eu adsorbed on Gr on Ir(111) and intercalated between Gr and Ir(111) in (2×2) and $(\sqrt{3} \times \sqrt{3})$R30° structure, respectively.

We further simulated for the (2×2) structure different areas of the moiré unit cell by displacing Gr together with the intercalated Eu laterally with respect to the Ir substrate. In this way, additional structures with Eu above faulted Ir hollow sites (hcp area) as well as Eu directly above Ir atoms (atop area) have been considered. For these cases, very similar binding energies per Eu atom of 3.8 eV and 3.7 eV are found.
Furthermore, one could imagine that the compression of the Ir substrate in the calculations affects the binding energies of Eu. Therefore, additional calculations for an Ir(111) substrate with the experimental Ir lattice constant and correspondingly stretched Gr have been performed. For the (2×2) structure, we find $E_{\mathrm{b}} = -1.38$ eV and -4.38 eV in the case of adsorbed and intercalated Eu, respectively. For the $(\sqrt{3} \times \sqrt{3})$R30° structure, we find $E_{\mathrm{b}} = -1.23$ eV and -3.91 eV for adsorbed and intercalated Eu, respectively. Thus, the uncompressed Ir substrate even enhances the energy gain upon intercalation and also yields the (2×2) structure as energetically most favorable.
In Fig. 5.2, the local density of states (LDOS) of the C p_z and the Eu $6s$ orbitals (obtained with a compressed Ir substrate) is compared for the adsorbed and intercalated (2×2)

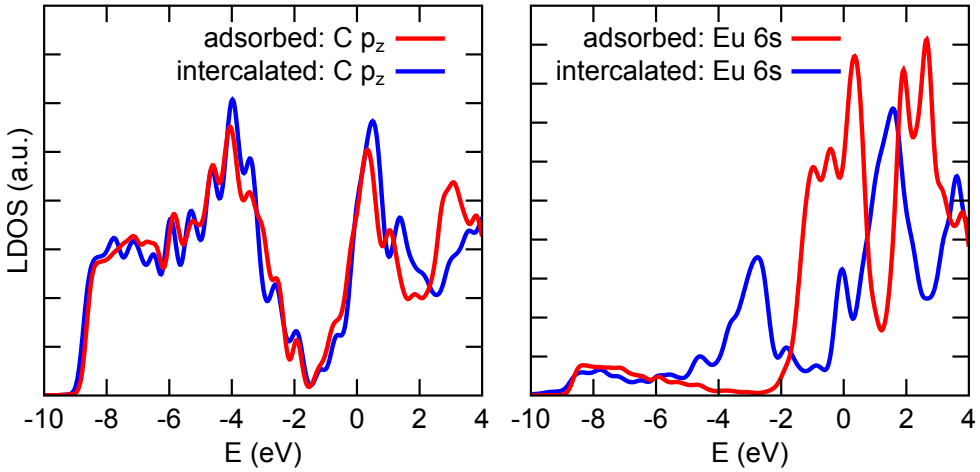

Figure 5.2: LDOS of the C p_z (left) and Eu 6s orbitals (right) for the (2×2) superstructure of Eu adsorbed on Gr (red) and intercalated between Gr and Ir(111) (blue), respectively.

structure. The Gr LDOS and thus the doping level of Gr remains mostly unchanged upon intercalation, whereas the Eu 6s LDOS broadens and clearly shows additional spectral weight between -4 eV and -2 eV below the Fermi level. This additional spectral weight and the broadening of the Eu 6s LDOS are in line with a metallic bond between Eu and the Ir(111) surface, which might explain the large adsorption energy gain upon intercalation.

5.1.3 Pattern Formation

Figs. 5.3(a) - (d) display the evolution of the surface pattern with increasing amount of Eu deposited onto Gr/Ir at 720 K. For all Eu exposures, elevations with rather sharp and straight edges form; the edges are oriented along three directions forming angles of 120° with respect to each other.

For the smallest Eu exposure (18% ML coverage) in Fig. 5.3(a), the deposited Eu causes the formation of thin stripes (t-stripes). The t-stripes have a width of (2.35 ± 0.15) nm measured at half height. The standard deviation specifies the spread, not the much smaller error. At a coverage of 39% ML as shown in Fig. 5.3(b) the t-stripes are complemented by compact islands, which preferentially have a triangular shape with one tip pointing upwards. The symmetry of the morphology is thus only threefold and not sixfold. At a coverage of 72% ML as shown in Fig. 5.3(c) the t-stripes tend to form bundles with a periodicity of (3.75 ± 0.15) nm. Beside bundles also large compact islands of irregular hexagonal shape and wider stripes are visible. All pattern elements are separated by strait channels (s-channels) with a width of (1.4 ± 0.1) nm at half height. Finally, close

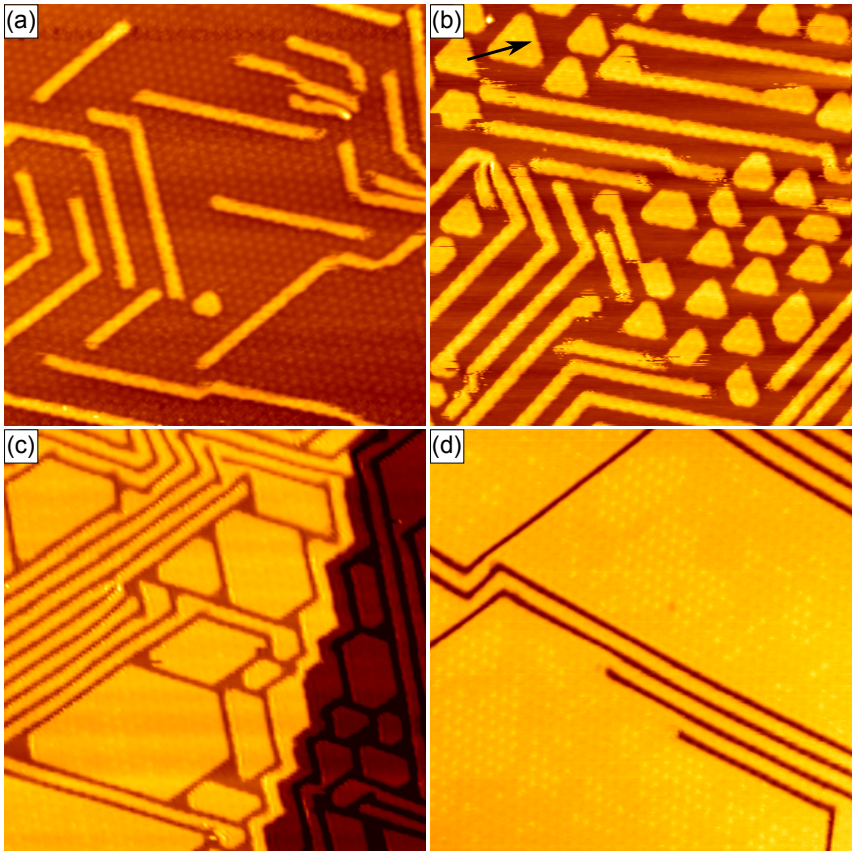

Figure 5.3: (a) - (d) STM topographs (80 nm × 80 nm) after intercalation of Eu resulting in successively larger intercalation coverages of (a) 18 % ML, (b) 39 % ML, (c) 72 % ML, and (d) 89 % ML. The arrow in (b) indicates the Ir $[\bar{1}\bar{1}2]$ direction.

to layer completion as shown in Fig. 5.3(d) (89 % ML coverage) the islands have become large and the number of *s*-channels has decreased, but still *t*-stripe bundles are present.

The Eu intercalation patterns under Gr/Ir represent close to equilibrium structures at 300 K and are not limited by mobility. Evidence for this comes from repeated scanning of the same surface area. Specifically for $\theta \approx 50\,\%$ ML frequent changes in the pattern are observed as shown by the consecutive topographs of Fig. 5.4. Island shape changes (denoted as I in Fig. 5.4), lateral displacements of islands and stripes (II), coalescence and splitting of islands (III), and interconversion of stripes and islands (IV) are observed. Despite these variations with time, the global appearance remains unchanged. This implies that one observes fluctuations around an equilibrium state.

In Fig. 5.3(a), a hexagonal lattice of bright protrusions with a separation of $a_\mathrm{m} = 2.53$ nm is visible in between intercalation islands and *t*-stripes marking the periodicity of the moiré of Gr on Ir(111) (see Sec. 2.1.1). Islands and stripes display straight edges with respect to

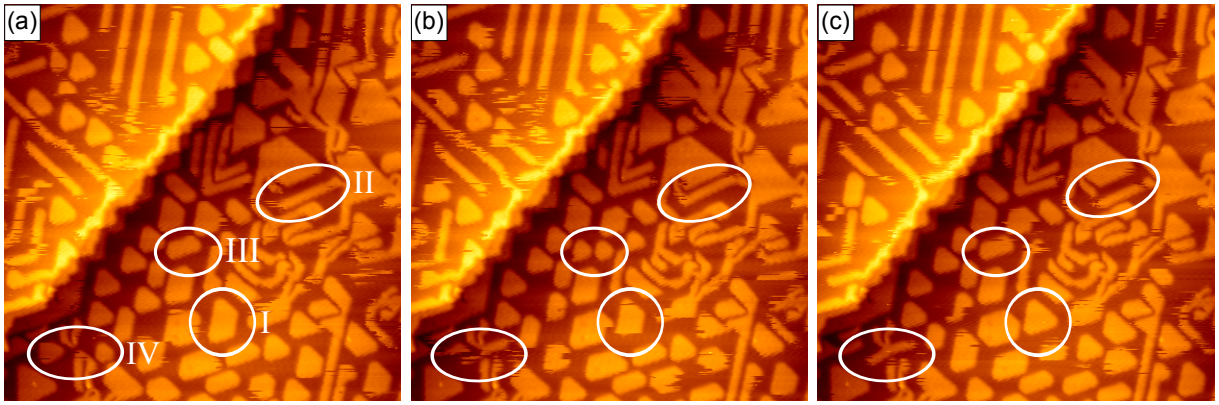

Figure 5.4: Time lapse sequence after Eu intercalation (120 nm × 120 nm). (b) and (c) were imaged 54 s and 108 s after (a). The ellipses highlight specific changes described in the text.

this lattice and grow in multiples of the protrusion distances , i.e., the intercalated areas are always quantized in units of a_{m}.

To demonstrate that the intercalated patterns are aligned with respect to the moiré lattice and not along the atomic Gr lattice, one can make use of the following effect: For Gr grown

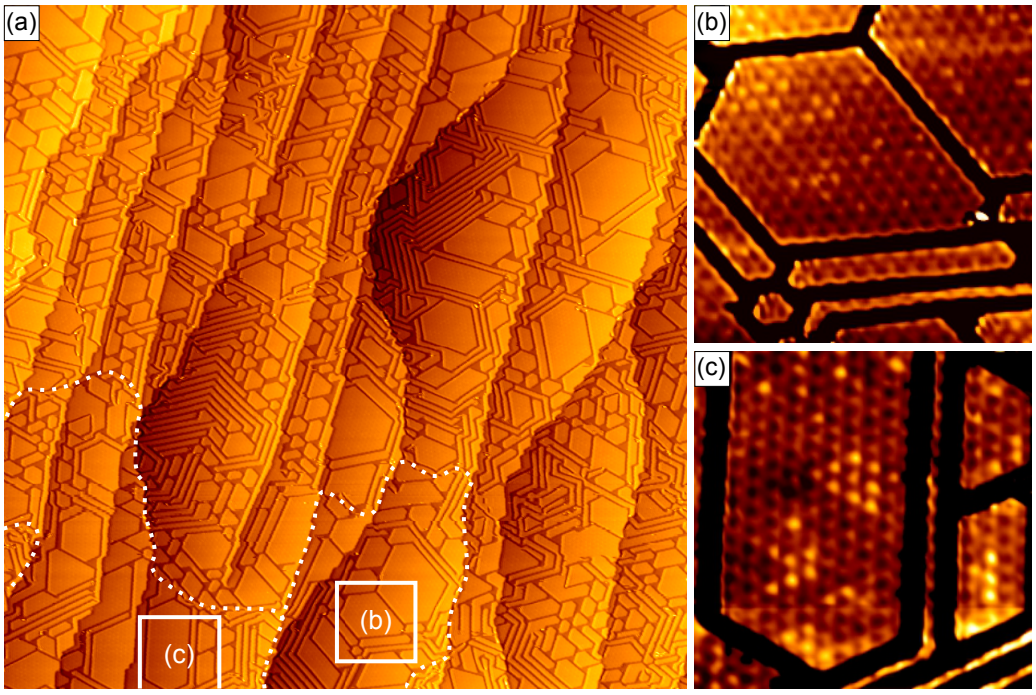

Figure 5.5: STM topograph (370 nm × 370 nm) after intercalation of Eu resulting in a coverage of 72% ML. A few tilt boundaries are highlighted by white dotted lines. The white squares indicate the regions of the contrast-enhanced zooms in (b) and (c) (40 nm × 40 nm each). The pattern elements follow in both regions the moiré.

using the TPG+CVD method Gr and Ir are aligned parallel with an angular scatter of $\pm 1°$. This slight misalignment results in small angle tilt boundaries. While the rotational misalignment of the atomic Gr rows is quite small, the misalignment of the moiré pattern is strongly amplified by a factor of $a_{\mathrm{m}}/a_{\mathrm{Gr}} = 10.32$ [93]. In Fig. 5.5(a) the white dotted lines indicate tilt boundaries, which separate intercalated areas with different pattern orientation. The contrast-enhanced zooms in Figs. 5.5(b) and (c) show that the patterns are in both cases perfectly aligned with respect to the moiré lattice. This implies that the edges of the intercalated pattern elements are not aligned along the Gr lattice whose misorientation is an order of magnitude smaller.

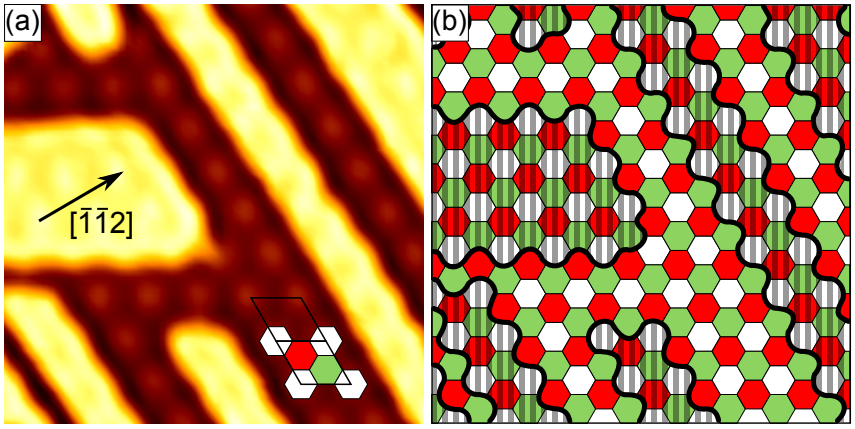

Figure 5.6: (a) STM topograph (21 nm × 21 nm) after intercalation of 50% ML Eu. The moiré unit cell (black rhomboid) is tiled in white (atop), green (fcc) and red (hcp) hexagons. The arrow indicates the Ir [$\bar{1}\bar{1}$2] direction. (b) Schematic sketch of (a) redrawn into the tiled moiré pattern.

To analyze the pattern in more detail, the model developed in Sec. 2.1.1 is used, which represents the atop, fcc, and hcp areas of the moiré unit cell schematically by white, green, and red tiles (see Fig. 5.6(a)). The identification of the areas was achieved following the procedure described in Sec. 2.1.1. In Fig. 5.6(b), the morphology of Fig. 5.6(a) is redrawn into the tiled moiré pattern, with the boundaries of the intercalation islands and *t*-stripes following the boundaries between tiles. The thinnest intercalation object, the *t*-stripe incorporates two rows of white tiles and one row of red and green tiles each. Stripes wider by N moiré unit cells incorporate N additional rows of each color. All intercalation objects as well as *s*-channels are bounded by red and green tiles without any white tile. I note that the two edges of a *t*-stripe are not equivalent: One edge is predominantly bounded by red tiles (*r*-edge), the other one by green tiles (*g*-edge). Comparison with Fig. 5.3(b) shows that the triangular intercalation islands are predominantly bounded by *r*-edges, thus explaining the only threefold pattern symmetry. Further evidence for the

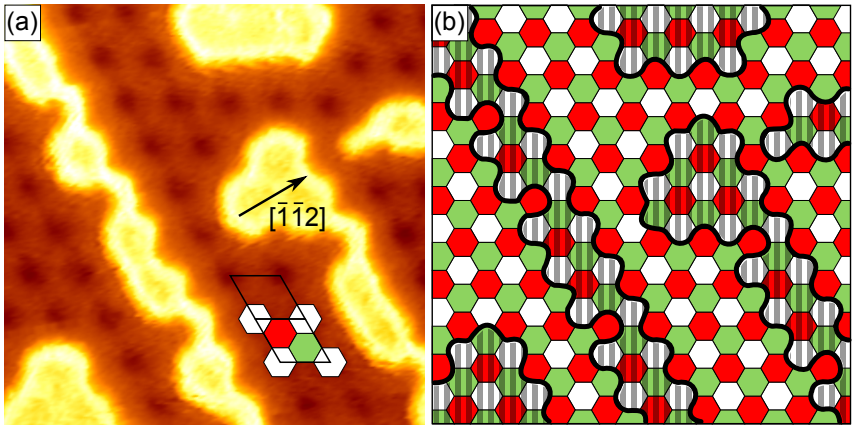

Figure 5.7: (a) STM topograph imaged at 35 K after Eu intercalation (21 nm × 21 nm). The contrast is inverted with the atop areas now imaged as dark spots. The arrow indicates the Ir [1̄1̄2] direction. (b) Schematic sketch of (a) redrawn into the tiled moiré pattern.

inequivalence of r- and g-edges can be found by low temperature STM imaging: As shown in Fig. 5.7(a), the appearance of intercalation patterns has substantially changed compared to 300 K. Based on the analysis of Fig. 5.7(b), where the morphology of Fig. 5.7(a) is redrawn into the tiled moiré pattern, it becomes apparent that the g-edge rearranges to avoid delamination of hcp areas at the expense of fcc areas. I note that it cannot be decided on the basis of the present data, whether the differences in the morphology of the intercalation objects at 300 K and 35 K are due to freezing of fluctuations, or real morphological changes upon cooling.

Influence of the Binding Inhomogeneity of the Moiré

Although intercalation islands with sizes of multiples of the Gr moiré mesh [111, 274, 275] and sharp intercalation fronts [22, 116, 276] have been reported in the past, pattern formation by intercalation underneath epitaxial Gr is a new phenomenon. Moreover, for pattern formation in a two phase system with competing short range attractive and long range repulsive interactions a reversed sequence of stripe and island formation is observed [33, 277]. Thus, a new mechanism of pattern formation has to be concerned here.
Therefore, I recall that the binding of Gr to Ir is mainly mediated by physisorption with weak chemical bonds in the fcc and hcp areas and chemical repulsion in the atop areas as described in Sec. 2.1.1. Hence, one can assume that the delamination energy per C atom in the atop area (E_{atop}) is substantially smaller than the corresponding energies E_{fcc} and E_{hcp} in the fcc and hcp areas. It appears thus reasonable that t-stripes are the preferred morphological entities just for their high fraction of delaminated atop areas,

which decreases from 1/2 for a t-stripe via 3/7 for a $(t+1)$-stripe to 1/3 in the limit of very wide stripes. For the same reason the red and green tiles - which are energetically most costly to delaminate - accumulate in the remaining non-intercalated areas, for instance as s-channels. As intercalated islands are preferentially bounded by r-edges, it is plausible that the hcp areas are even more strongly bound than the fcc ones.

In order to investigate the influence of the moiré binding inhomogeneity quantitatively, we use a one-dimensional model to obtain the intercalation energy cost per Eu atom as a function of the stripe width. This energy cost $E_{\mathrm{in,Eu}}$ includes the energy cost for delaminating the Gr layer from the substrate, and the energy associated with the formation of intercalation steps. The much larger value of 2.4 eV per Eu atom gained upon Eu intercalation (compare Sec. 5.1.2) is not relevant for the pattern formation energetics and thus omitted as an offset on the energy scale.

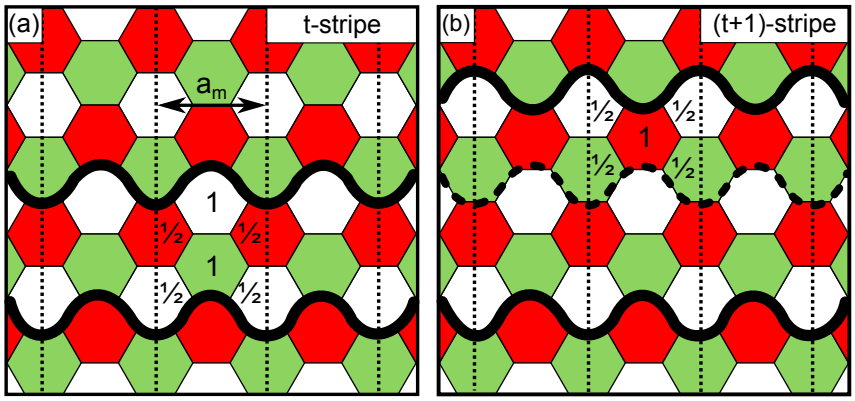

Figure 5.8: Sketch of a t-stripe (a) and a $(t+1)$-stripe (b) drawn into the tiled moiré pattern. Dotted lines partition the stripes in sections of length a_{m}. Numbers indicate the tiles that have to be delaminated per section.

In Fig. 5.8(a), a t-stripe is drawn into the tiled moiré pattern, and partitioned in sections of length a_{m}. Per section, a complete moiré unit cell (white, green, and red tile), and an additional atop area (white tile) have to be delaminated as indicated by the numbered tiles. For lifting one moiré cell an energy $E_{\mathrm{del,m}}$ is needed, which has a value of $n_{\mathrm{C,m}} \cdot 50\,\mathrm{meV} = 10.6\,\mathrm{eV}$ since the number of C atoms per moiré cell is $n_{\mathrm{C,m}} = \sqrt{3}/2 \cdot a_{\mathrm{m}}^2 \cdot \rho_{\mathrm{at,Gr}} = 212$ and the average binding energy per C atom is 50 meV [95]. Herein, $\rho_{\mathrm{at,Gr}}$ is the atomic density of the C atoms. The delamination of the additional atop area costs $n_{\mathrm{C,m}}/3 \cdot E_{\mathrm{atop}}$, where E_{atop} is the average binding energy per C atom in the atop area. The section contains $x \cdot a_{\mathrm{m}}/2a_{\mathrm{Gr}}$ Eu atoms with x being the number of atomic Eu rows along the

stripe and $a_\mathrm{m}/2a_\mathrm{Gr} = 5.16$ the number of atomic Eu rows perpendicular to the stripe. With this, one gets for a t-stripe an intercalation energy per Eu atom of

$$E_\mathrm{in,Eu}(t) = \frac{E_\mathrm{del,m} + \frac{1}{3}n_\mathrm{C,m} \cdot E_\mathrm{atop} + 2E_\mathrm{edge,m}}{x \cdot \frac{a_\mathrm{m}}{2a_\mathrm{Gr}}} \tag{5.1}$$

including the edge energy $2E_\mathrm{edge,m}$ for two edges of length a_m. When going from a t-stripe to a $(t+1)$-stripe as sketched in Fig. 5.8(b), only one additional moiré cell per section has to be delaminated while the number of Eu atoms increases by $(a_\mathrm{m}/2a_\mathrm{Gr})^2$. More general, one gets for a $(t+N)$-stripe an intercalation energy per Eu atom of

$$E_\mathrm{in,Eu}(t+N) = \frac{(N+1) \cdot E_\mathrm{del,m} + \frac{1}{3}n_\mathrm{C,m} \cdot E_\mathrm{atop} + 2E_\mathrm{edge,m}}{x \cdot \frac{a_\mathrm{m}}{2a_\mathrm{Gr}} + N \cdot \left(\frac{a_\mathrm{m}}{2a_\mathrm{Gr}}\right)^2}. \tag{5.2}$$

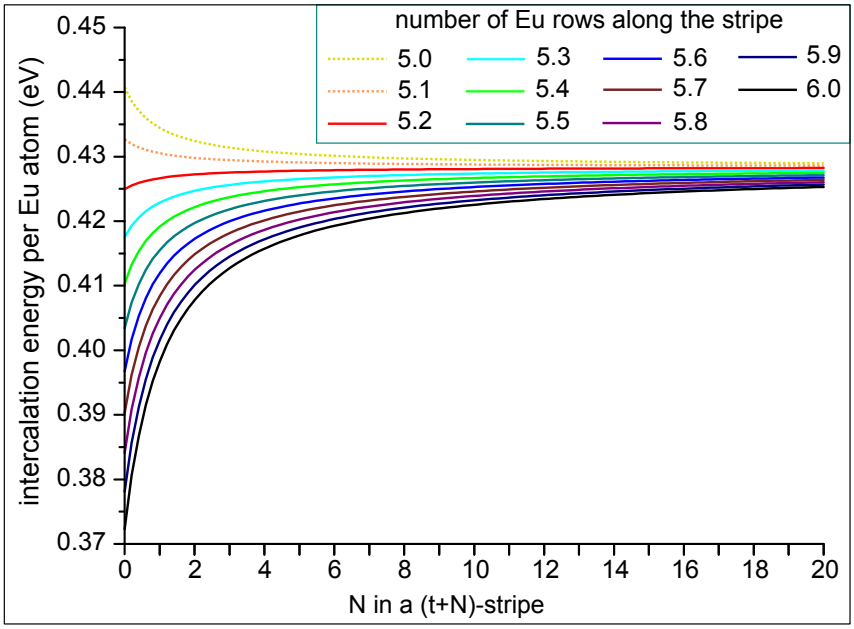

Figure 5.9: Intercalation energy $E_\mathrm{in,Eu}$ per Eu atom as a function of stripe width (N is proportional to the width of a $(t+N)$-stripe) for different numbers x of atomic Eu rows along the stripe. Thereby, $E_\mathrm{atop} = 0$ and $E_\mathrm{edge,m} = 0\,\mathrm{eV}$ is assumed. For $x \leqslant 5.1$ the functions are monotonically decreasing and convex (dotted), for $x \geqslant 5.2$ monotonically increasing and concave (solid).

In Fig. 5.9, Eq. 5.2 is plotted as a function of N for $5 \leqslant x \leqslant 6$, $E_\mathrm{atop} = 0\,\mathrm{eV}$ and $E_\mathrm{edge} = 0\,\mathrm{eV}$. As I will show in the next section, these values are reasonable estimates for the parameters. For $x \leqslant 5.1$ (dotted lines) all functions are monotonically decreasing and convex, meaning that the formation of a single wide stripe with large N is energetically preferred. On the other hand, for $x \geqslant 5.2$ (solid lines) the functions are monotonically

increasing and concave so that the formation of t-stripes is preferred. Larger values of E_{atop} or $E_{\mathrm{edge,m}}$ will require a larger number of Eu rows x in a t-stripe to keep it as a the preferred morphological entity. With the reasonable assumptions $E_{\mathrm{atop}} = 0\,\mathrm{eV}$, $E_{\mathrm{edge}} = 0\,\mathrm{eV}$ and $x = 5.5$ Eu rows in a t-stripe one obtains a preference by about 0.7 eV per moiré unit cell to accommodate Eu in t-stripes compared to a single island.

Estimates of the Relevant Parameters

Probably most important for the energetic preference or avoidance of t-stripes is the amount of Eu that fits in in a t-stripe, which can be expressed by the number x of atomic Eu rows along the stripe. In average, 5.16 Eu rows fit in a moiré unit cell of 2.19 nm width in the (2×2) structure. Based on the experimental FWHM of 2.35 nm, we calculate for a t-stripe 5.53 Eu rows. Thus, $5 \leqslant x \leqslant 6$ is assumed to be a reasonable range for x.
Based on the fact that the hcp and fcc areas display weak chemical bonds, whereas the local binding yields an average repulsion of 20 meV over the moiré unit cell, $E_{\mathrm{atop}} = 0\,\mathrm{eV}$ is a reasonable assumption for the binding energy per C atom in the atop area.
A reliable calculation of the edge energy E_{edge} is only possible in spin-polarized *ab initio* calculation taking into account the full moiré unit cell and vdW interactions, which are important for the binding of Gr to Ir(111) [95]. Such calculations are demanding and beyond the scope of this work. Thus, I restrict myself to simple estimates and less demanding *ab initio* calculations to obtain some insight to the physics related to E_{edge}.

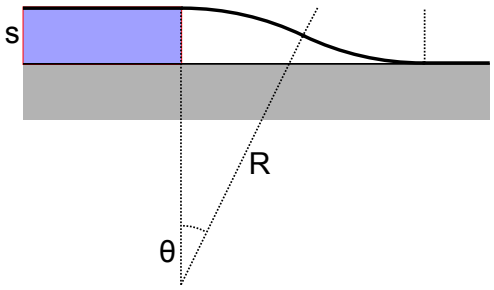

Figure 5.10: Gr bending over an intercalate step of height s modeled by two identical arcs of radius R and opening angle θ.

First, the contribution of Gr bending is determined by using the elementary model shown in Fig. 5.10 (compare also Ref. [92]). The Gr layer bent over an intercalation step of height s is modeled by two identical arcs of radius R and opening angle θ. The bending causes an arc length increase $\Delta s_{\mathrm{t}}/2 = 2R(\theta - \sin\theta)$ in the Gr layer. Using furthermore the boundary condition $s/2 = R(1 - \cos\theta)$, one gets a system of nonlinear equations. As we will see later,

the arc length increase can experimentally determined to be $\Delta s_\mathrm{t}/2$ =0.185 Å. Furthermore, under a broad range of tunneling resistances (except very small ones) an intercalation step height of s =1.6 Å is found in STM. Using these parameters, the equations can be solved and one gets a radius of R = 13.5 Å, and an opening angle of θ = 19.8 °. According to Ref. [100] this radius of curvature corresponds to a bending energy per C atom of

$$E_\mathrm{bend} = \frac{a}{R^2} + \frac{b}{R^4} \tag{5.3}$$

with the empirical constants a =0.99 eVÅ^{-2} and b =12.3 eVÅ^{-4}. Within the bent Gr area there are $\theta R \cdot a_{mathrmm} \cdot \rho_\mathrm{at,Gr}$ C atoms per moiré unit cell length a_m, where $\rho_\mathrm{at,Gr}$ = 38.2 nm^{-2} is the atomic density of the C atoms. Thus, we obtain for R = 13.5 Å a bending energy of $E_\mathrm{bend,m}$ = 520 meV per edge and length a_m.

As second step, E_edge is estimated by DFT calculations for a small commensurate unit cell disregarding vdW interactions and Gr bending. Therefore, we calculate the total energy of Eu stripes (2 Eu atoms in width) intercalated between Gr and the Ir(111) substrate (E_stripe). The stripe structures were obtained by cutting out half of the Eu atoms from (4 × 1) supercells of the (2 × 2) Eu structures between Gr and the Ir(111) substrate. No further relaxations have been performed. Comparison to the corresponding fully intercalated Gr/Eu/Ir structure (E_full) and the non intercalated Gr/Ir structures ($E_\mathrm{Gr+Ir}$) yields as estimate the edge energies per Eu atom according to $E_\mathrm{edge} = \frac{1}{2}(E_\mathrm{stripe} - \frac{1}{2}(E_\mathrm{full} + E_\mathrm{Gr+Ir})) = -0.2\,\mathrm{eV}$, resulting in $E_\mathrm{edge,m} = -1.0\,\mathrm{eV}$ per edge and length a_m. Without the Ir substrate, the corresponding energy is of similar magnitude, but positive. A negative E_edge implies an energy gain due to edge formation. Although this result seems at first glance implausible in view of the reduced coordination of the edge Eu atoms and should be considered with care in view of the approximations made, it is in line with experiments related to Eu adsorption *on* Gr on Ir(111) [28]. Binding of Eu to Gr is due to lowering of the kinetic energy of Eu s electrons, which delocalize in Gr. Because of the low density of states in Gr, the Fermi level moves quickly upwards with electron transfer and doping therefore ceases. Thus, a smaller local Eu concentration may allow per Eu atom a larger electron transfer to Gr and thus a stronger binding to Gr and thereby overcompensate the loss of coordination due to stripe formation.

By construction, the energy cost for Gr bending upon stripe formation is not included in the *ab initio* calculation. The two contributions to the edge energy are of opposite sign and thus tend to cancel each other. Hence, I just state that the magnitude of $E_\mathrm{edge,m}$ is on the order of 1 eV per length a_m, and may be of positive or negative sign so that $E_\mathrm{edge,m} = 0\,\mathrm{eV}$ is a reasonable estimate.

Relaxation of Pre-existing Strain

The quantitative analysis for a one-dimensional stripe situation has shown that a delicate balance of E_{atop}, E_{edge} and the width x available in a t-stripe for intercalation can lead to an energetic preference of t-stripes. This predicts a linear growth of the intercalation step density ρ with increasing θ until the entire surface is covered with t-stripes at $\rho = 0.27\,\mathrm{nm}^{-1}$ (compare blue line in Fig. 5.11). A further increase of the coverage causes a linear decrease of ρ until it vanishes for full coverage.

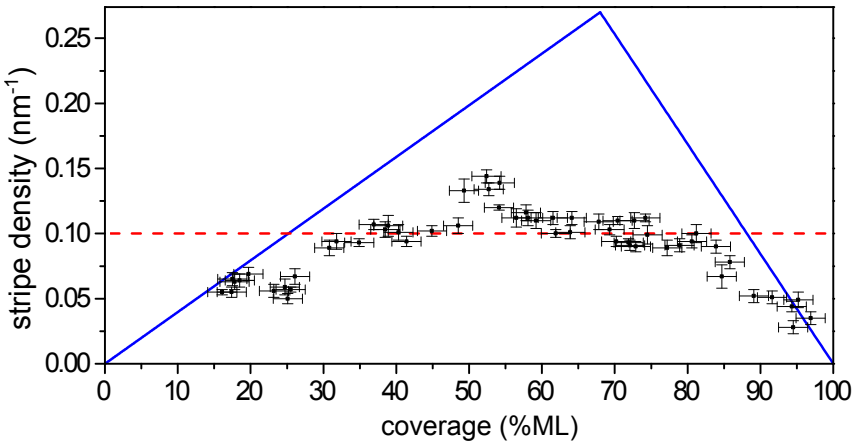

Figure 5.11: Intercalation step density ρ as a function of intercalated Eu amount θ. Blue line: expected $\rho(\theta)$ if t-stripes are energetically preferred (no strain). Red dashed line: expected $\rho(\theta)$ taking only strain relaxation of Gr into account (no binding inhomogeneity and edge energy).

A quantitative analysis of the experimentally observed intercalation step density ρ as a function of θ is presented also in Fig. 5.11. ρ is obtained by counting steps along a grid of orthogonal lines in areas free of pre-existing substrate steps. Although the scatter of ρ is substantial, it is obvious that for small θ first a rapid increase of ρ takes place, then for $30\%\,\mathrm{ML} < \theta < 80\%\,\mathrm{ML}$ a broad plateau with $\rho = 0.09 - 0.12\,\mathrm{nm}^{-1}$ is reached, before ρ finally decreases again rapidly to zero. While ρ agrees for small and large θ reasonably well with the expectations, the broad plateau is inconsistent with the assumption that the intercalation pattern is only driven by the chemical binding inhomogeneity.

To explain this, we need to take a close look to other changes in the surface energetics associated with intercalation. Fig. 5.12 displays a single t-stripe with the surrounding moiré well resolved. The height profile along the blue line shows a rather regular spacing of the depressions of $\sqrt{3}a_{\mathrm{m}} = 4.38\,\mathrm{nm}$. As discussed before, the bending over the t-stripe causes an arc length increase, which gives rise to a lateral shift of the moiré by $\Delta s_{\mathrm{m}} = 0.33\,\mathrm{nm}$. The corresponding lateral shift of the C atoms is $\Delta s_{\mathrm{t}} = 0.032\,\mathrm{nm}$, as

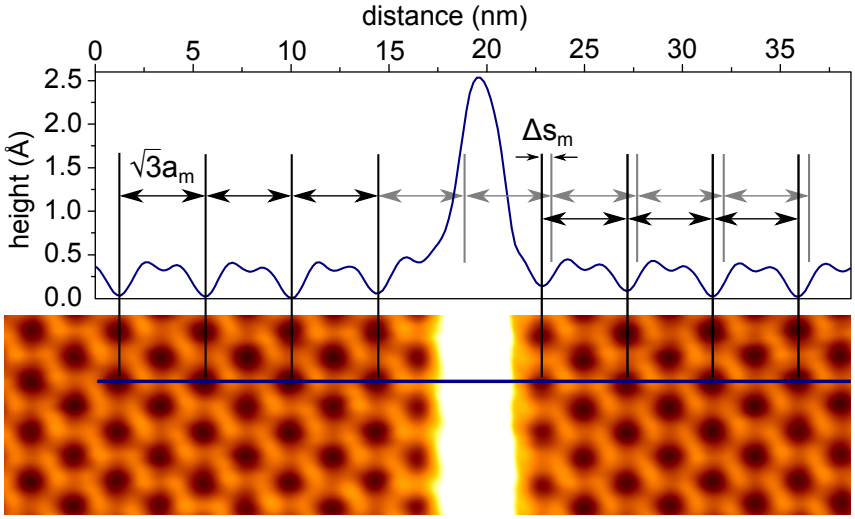

Figure 5.12: Height profile over a t-stripe taken along the blue line in the STM image (43 nm × 10 nm). The moiré periodicity of $\sqrt{3}a_\mathrm{m}$ in path direction is displaced by Δs_m due to the t-stripe.

obtained from Δs_m using standard moiré methods [92]. Averaging over similar situations results in $\Delta s_\mathrm{t} = (0.037 \pm 0.005)\,\mathrm{nm}$ for single stripes. For stripe bundles, the arc length increase of $\Delta s_\mathrm{t,b} = (0.060 \pm 0.012)\,\mathrm{nm}$ per stripe is significantly larger .

The arc length increase upon intercalation is associated with a change in the strain state of Gr. As discussed in Sec. 2.1.1, the mismatch in the thermal expansion coefficients of Gr and Ir causes compressive strain in Gr upon cool down. For a growth temperature of 1170 K it amounts to 0.6% [100]. Without intercalation a significant part of the strain relaxes by formation of wrinkles, but a residual strain of about 0.3% is left in the Gr lattice [100, 101]. Here, it is plausible that all of the 0.6% strain is released by formation of intercalation steps since there are hardly any wrinkles after intercalation.

In the following, I want to quantify this. According to Ref. [100], the elastic energy in a rectangular area of strained Gr with length L and width a_m is given by

$$E_\mathrm{el} = \frac{1}{2}\epsilon^2 \cdot L \cdot Y \cdot \rho_\mathrm{at,Gr} \cdot a_\mathrm{m}. \tag{5.4}$$

Herein, $Y = 56\,\mathrm{eV}$ per C atom is the elastic modulus of Gr, and ϵ the strain, which is defined as $\epsilon = \Delta L/L$ with ΔL being the difference between the length of free Gr and strained Gr/Ir. Intercalation of a single Eu stripe perpendicular to L reduces the strain by $\Delta s_\mathrm{t}/L$ due to the arc-length increase Δs_t. By calculating the difference in the elastic energy of the Gr area before and after inserting a Eu stripe, one gets an energy gain of

$$\begin{aligned}\Delta E_{\mathrm{el}} &= \frac{1}{2}\epsilon^2 \cdot L \cdot Y \cdot \rho_{\mathrm{at,Gr}} \cdot a_{\mathrm{m}} - \frac{1}{2}\left(\epsilon - \frac{\Delta s_{\mathrm{t}}}{L}\right)^2 \cdot L \cdot Y \cdot \rho_{\mathrm{at,Gr}} \cdot a_{\mathrm{m}} \\ &= \frac{1}{2}\left(2\epsilon\frac{\Delta s_{\mathrm{t}}}{L} - \left(\frac{\Delta s_{\mathrm{t}}}{L}\right)^2\right) \cdot L \cdot Y \cdot \rho_{\mathrm{at,Gr}} \cdot a_{\mathrm{m}}. \end{aligned} \tag{5.5}$$

Assuming that the elastic energy is reduced over a large distance L, i.e., for $\Delta s_{\mathrm{t}}/L \ll \epsilon$, Eq. 5.5 can be approximated by

$$\Delta E_{\mathrm{el}} = \epsilon \cdot \Delta s_{\mathrm{t}} \cdot Y \cdot \rho_{\mathrm{at,Gr}} \cdot a_{\mathrm{m}}. \tag{5.6}$$

Using $\Delta s_{\mathrm{t}} = 0.037\,\mathrm{nm}$ from the experimental analysis and 0.6% pre-existing strain, we arrive at a sizable energy gain of 1.2 eV. In order to derive an expression for the change in elastic energy with increasing number of Eu stripes, I proceed to a continuum description. Therefore, I consider the elastic energy density w_{el}, i.e., the elastic energy E_{el} normalized to the area $L \cdot a_{\mathrm{m}}$. Furthermore, the linear stripe density $\rho = N/L$ is introduced, where N denotes the number of stripes per length L. With this we get

$$w_{\mathrm{el}} = \frac{1}{2}\left(\epsilon - \Delta s_{\mathrm{t}} \cdot \rho\right)^2 \cdot Y \cdot \rho_{\mathrm{at,Gr}}. \tag{5.7}$$

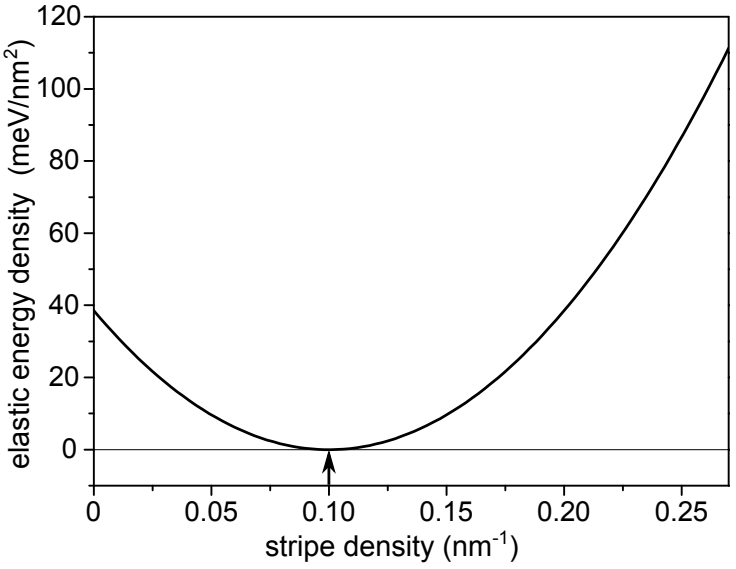

Figure 5.13: Elastic energy density w_{el} as a function of the linear stripe density ρ assuming $\epsilon = 0.6\%$ and $\Delta s_{\mathrm{t}} = 0.06\,\mathrm{nm}$. The arrow indicates the corresponding energetic minimum.

This function is plotted in Fig. 5.13 assuming a pre-existing strain of $\epsilon = 0.6\%$. Herein, $\Delta s_{\mathrm{t}} = 0.06\,\mathrm{nm}$ is used, which is a good approximation for intermediate and high coverages. As indicated by the black arrow and the dashed line in Fig. 5.11, a total strain

relaxation occurs at a stripe density of $0.10\,\mathrm{nm}^{-1}$. If some wrinkles were still present after intercalation, the dashed line in Fig. 5.11 would be shifted to somewhat smaller values. The relaxation of pre-existing strain through intercalation steps yields a simple explanation for the broad plateau in ρ at intermediate coverages: After complete strain relaxation additional intercalation would drive Gr into tensile strain. Therefore, the formation of additional t-stripes ceases when the associated tensile strain energy becomes larger than the energetic advantage of t-stripe formation due to the binding inhomogeneity.

I note that relaxation of pre-existing compressive strain in Gr *alone* would be unable to explain the observed patterns as one would expect in this case the formation of stripes (channels) even thinner than the t-stripes (s-channels) for very small (very large) θ to achieve a maximum in strain relaxation, contrary to observations. Finally, the question remains why the strain relief pattern is dominated by one-dimensional stripes for low and high coverages, although the Gr layer should be isotropically strained and there are more isotropic pattern elements than t-stripes with a comparable delamination energy per Eu atom (same fraction of white tiles). In the present case, such structures are probably unfavored due to higher costs for Gr bending contributing to the edge energy.

5.1.4 Visualization of Strain by Intercalation

The catchy view of intercalation pattern formation presented above provides a natural explanation for the inhomogeneous distribution of intercalation steps over the sample.

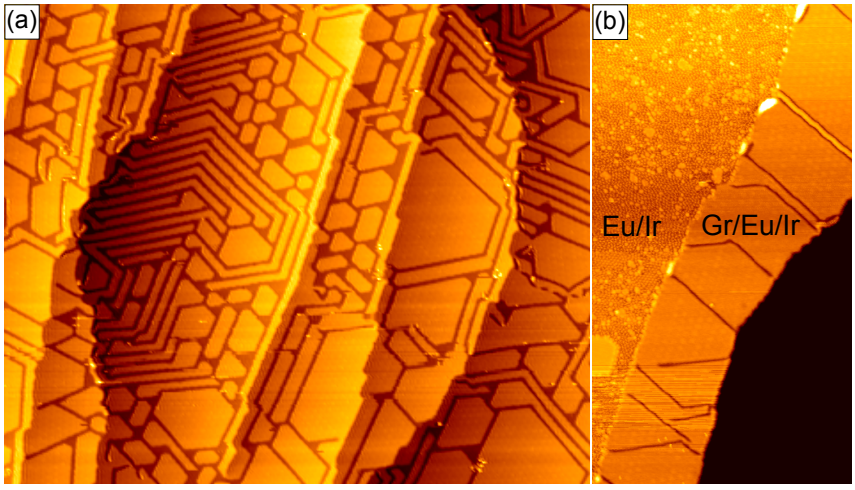

Figure 5.14: (a) STM topograph after intercalation of 72% ML Eu (195 nm × 160 nm). (b) Topograph after Eu deposition on Ir(111) covered by 40% with Gr (70 nm × 130 nm).

Since the optimal ρ is defined by the situation where the preference for t-stripe formation is balanced by the built-up of tensile strain, the local variation of ρ reflects initial variations in the distribution of pre-existing compressive strain. The examples visualized in Fig. 5.14 support this view: In Fig. 5.14(a) an unusually high intercalation step density realized by t-stripe bundles is visible on the terrace near a concave substrate step, which shortly merges with a second one to a double step (large initial Gr compression). In contrast, ρ is low on the terrace next to the descending convex substrate step (strain was released by the Gr moving out). Similarly, for a Gr band next to a substrate step as shown in Fig. 5.14(b) (only partial Gr coverage) the s-channels are oriented perpendicularly to the long axis of the band, where strain relaxation could not be achieved during cool down.

5.2 Compaction of the Monolayer

As shown by the analysis in Sec. 5.1.1, Eu adsorbs in the submonolayer regime always in a (2×2) superstructure with respect to Gr. Upon further Eu deposition onto a saturated (2×2) intercalation layer a $(\sqrt{3} \times \sqrt{3})$R30° phase arises as shown in Fig. 5.15 (compare Ref. [29]). Also here, the structure is attached to the Gr lattice. It has a saturation coverage of 1.33 ML with respect to the (2×2) structure, i.e., it is 33% denser. A further compaction has never been observed and the intercalation process is self-limited to one monolayer. The occurrence of the $(\sqrt{3} \times \sqrt{3})$R30° structure is consistent with the DFT calculations in Sec. 5.1.2: although the binding energy per atom is slightly lower in the $(\sqrt{3} \times \sqrt{3})$R30° structure than in the (2×2) (-3.59 eV compared to -3.80 eV), intercalation is still much more favorable than adsorption on top of Gr.

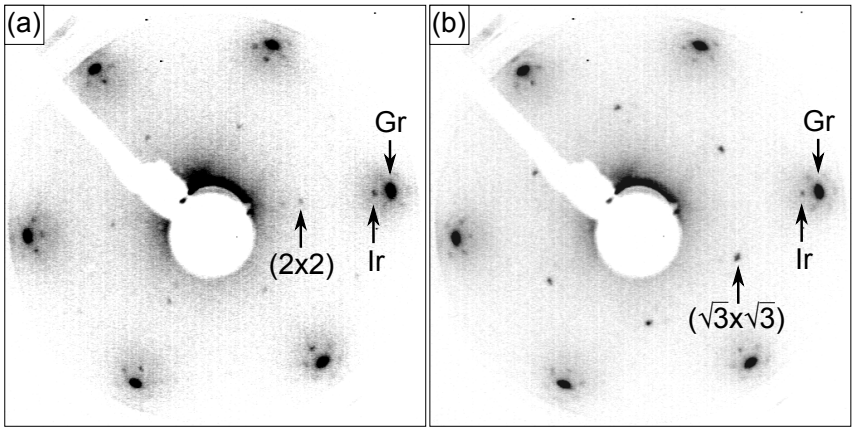

Figure 5.15: LEED images of the (2×2) (a) and $(\sqrt{3} \times \sqrt{3})$R30° (b) intercalation structures at 82 eV primary electron energy. The corresponding first-order spots are indicated.

Occasionally, both phases are simultaneously observed in LEED (not shown here, but in Ref. [29]). Here, I demonstrate such a coexistence also in STM: Fig. 5.16(a) shows two different moiré contrasts on both sides of a wrinkle: dark dots on a bright background in the lower left, and bright dots on a dark background in the upper right. Atomic resolution and the corresponding Fourier transforms in Figs. 5.16(b) - (d) prove that the two areas correspond to the (2×2) and the $(\sqrt{3} \times \sqrt{3})$R30° intercalation phases. However, I note that the moiré contrast strongly depends on tip and tunneling parameters so that it is only coincidence that the two phases here appear with opposite contrast.

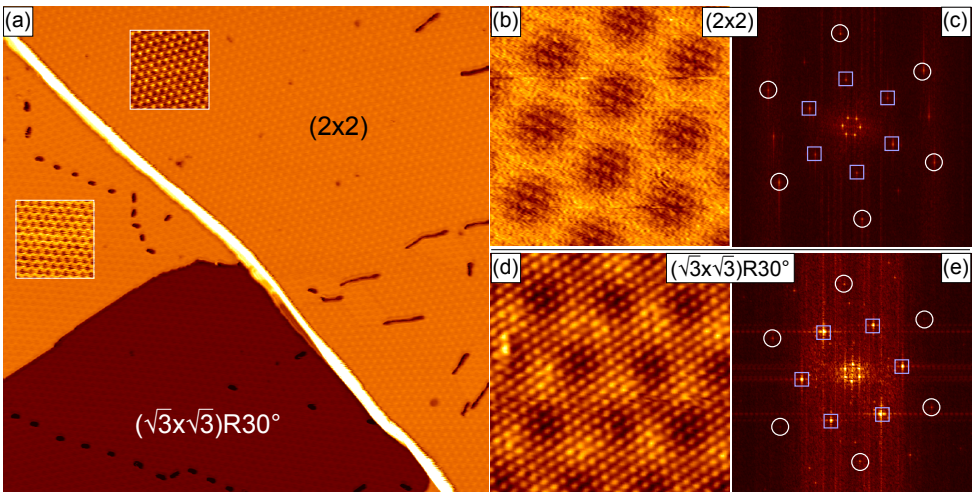

Figure 5.16: (a) Coexistence of the (2×2) (upper right) and the $(\sqrt{3} \times \sqrt{3})$R30° (lower left) intercalation phase separated by a wrinkle (180 nm × 180 nm). The insets (same scale) enhance the moiré contrast. (b), (d) Atomically resolved topographs of both structures (8.5 nm × 8.5 nm) with the corresponding Fourier transforms (c), (e). Circles and squares surround the spots belonging to Gr and Eu, respectively. Additional second-order Eu spots are weakly visible in (c).

5.3 Band Structure and Doping

The band structure of Eu intercalated Gr has been previously calculated by DFT in Ref. [29]. As shown in Fig. 5.17(a), for the (2×2) structure the Dirac cone is preserved, and shows a substantial exchange splitting of about 50 meV. Such a spin splitting is highly interesting in the view of spintronic applications: By shifting the Dirac cone back to the Fermi edge via p-doping, and fine adjustment by backgating only a single spin orientation would contribute to the transport (compare Sec. 2.1.4). For the $(\sqrt{3} \times \sqrt{3})$R30° structure shown in Fig. 5.17(b) also a small spin splitting occurs at the Dirac point (here backfolded to the Γ point), but accompanied by a band gap opening of about 300 mV.

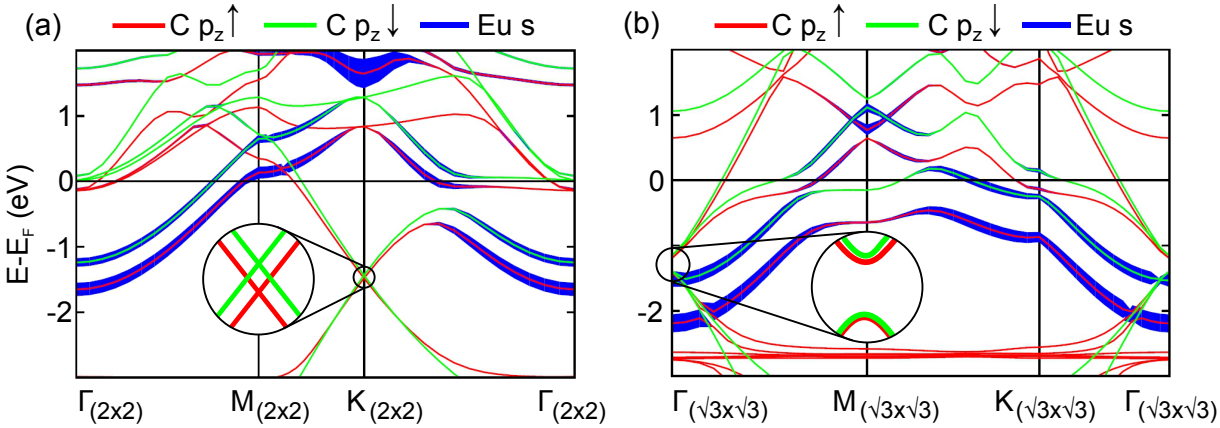

Figure 5.17: Spin-resolved band structures of freestanding Gr intercalated by Eu in (2×2) (a) and $(\sqrt{3} \times \sqrt{3})$R30° (b) structure . Majority and minority spin C p_z bands are colored in red and green, whereas Eu s bands are marked in blue. Schematic blowups of the Dirac points are shown. Note that the band structures are reduced to the superstructure Brillouin zones whose high symmetry points are indicated. Partially adapted from Ref. [29].

Experimentally, the band structure has been investigated by D. F. Förster in Ref. [29] by means of ARPES (see Sec. 4.3 for experimental details). Fig. 5.18 shows two spectra in the vicinity of the K point taken along the ΓKM direction for the (2×2) and the $(\sqrt{3}\times\sqrt{3})$R30° intercalation layer, respectively. Both show that the Dirac cone is shifted down in energy by about -1.5 eV due to strong n-doping. The noticeable anisotropy between the two branches is due to the electronic chirality of Gr [278].

It appears as if a substantial band gap of about 500 meV has opened. However, by determining the position of the Gr minigaps [279] prior to Eu intercalation a small azimuthal misalignment $\Delta\phi$ with respect to the ΓKM direction was identified (see Fig. 5.19(a)). As shown in Fig. 5.19(b), the Dirac cone is consequently not exactly cut across the Dirac point resulting in an apparent band gap, which is of the same size as the measured one. I note that the presence of a real gap smaller than 500 meV cannot be excluded.

In order to circumvent the mechanical difficulties to properly align the azimuthal angle, new ARPES measurement were performed after rotating the electron analyzer by 90° so that maps perpendicular to the ΓKM direction can be taken. By changing the finely adjustable polar angle θ in small steps the K point can be reached even in the presence of a small $\Delta\phi$. The corresponding geometry is shown in Fig. 5.19(b).

The data obtained for the (2×2) intercalation structure after conversion from angle- to k-space are shown in Fig. 5.20. We compare the band structure to the well-known result

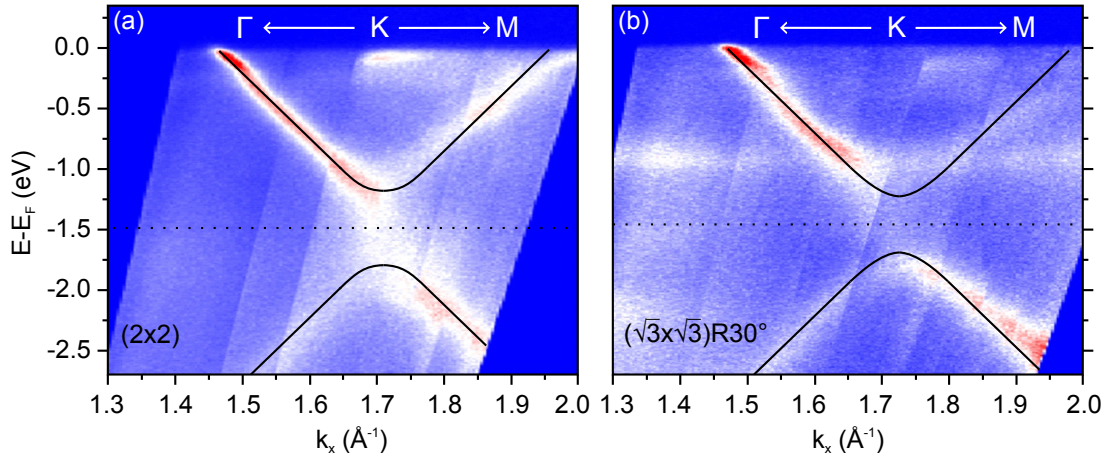

Figure 5.18: ARPES spectra of Eu intercalated Gr on Ir(111) in ΓKM direction. An azimuthal offset $\Delta\phi$ leads to an apparent band gap at the Dirac cone. (a) (2×2) structure with an azimuthal offset $\Delta\phi \approx 1.5°$. (b) $(\sqrt{3}\times\sqrt{3})$R30° structure with $\Delta\phi \approx 1°$. The dotted black lines indicate the doping level. Adapted from Ref. [29].

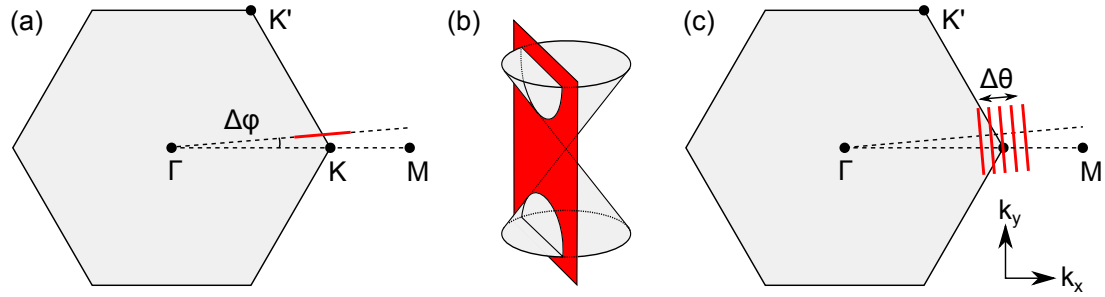

Figure 5.19: (a) ARPES measurement in ΓKM direction with an azimuthal offset $\Delta\phi$. (b) $\Delta\phi \neq 0$ leads to an apparent band gap at the K point. (c) Measurement perpendicular to the ΓKM direction for $\Delta\phi \neq 0$. By finely adjusting the polar angle θ the K point can be reached.

from the NN tight-binding approximation (TBA) [15], which turned out to show only marginal deviations from an exact DFT calculation of the whole system:

$$E(k) = \pm t\sqrt{3 + 2\cos\left(a_{\mathrm{Gr}}k_x\right) + 4\cos\left(\frac{a_{\mathrm{Gr}}}{2}k_x\right)\cos\left(\frac{\sqrt{3}a_{\mathrm{Gr}}}{2}k_y\right)} + E_{\mathrm{D}} \qquad (5.8)$$

As NN hopping energy, $t = -2.848\,\mathrm{eV}$ is used from Ref. [280]. For the present geometry, k_x is varied in $0.02\,\mathrm{Å}^{-1}$ steps around $1.70\,\mathrm{Å}^{-1}$ (K point), and k_y covers a range of $\pm 0.15\,\mathrm{Å}^{-1}$. The doping level E_{D} was fitted to the data. At the K point in Fig. 5.20(d), best coincidence is found for a doping level of $E_{\mathrm{D}} \approx -1.4\,\mathrm{eV}$, in good agreement with the previous result of $E_{\mathrm{D}} \approx -1.5\,\mathrm{eV}$ obtained in Ref. [29].

Upon scanning towards the M point (Figs. 5.20(e) - (f)) the opening of the apparent gap is well reproduced by the TBA. In contrast, towards the Γ point (Figs. 5.20(a) - (c)) the bands diverge much faster from the Dirac point than predicted by TBA. However, such deviations are expected as TBA does not include many body interactions such as phonon-mediated electron-electron interactions or plasmons [281, 282]. The fact that the deviation from TBA is large here might indicate that many body interactions or other contributing effects such as hybridization are strong in the Gr/Eu/Ir system.

In addition to the Dirac cone, a non-dispersing band at about -0.25 eV is visible, as highlighted by two arrows in Fig. 5.20(c). This band can be interpreted as the Ir surface state S_1 (compare Ref. [279] for nomenclature), which is close to the Fermi edge for bare Gr on Ir(111), and here shifted down by doping from the intercalated Eu layer.

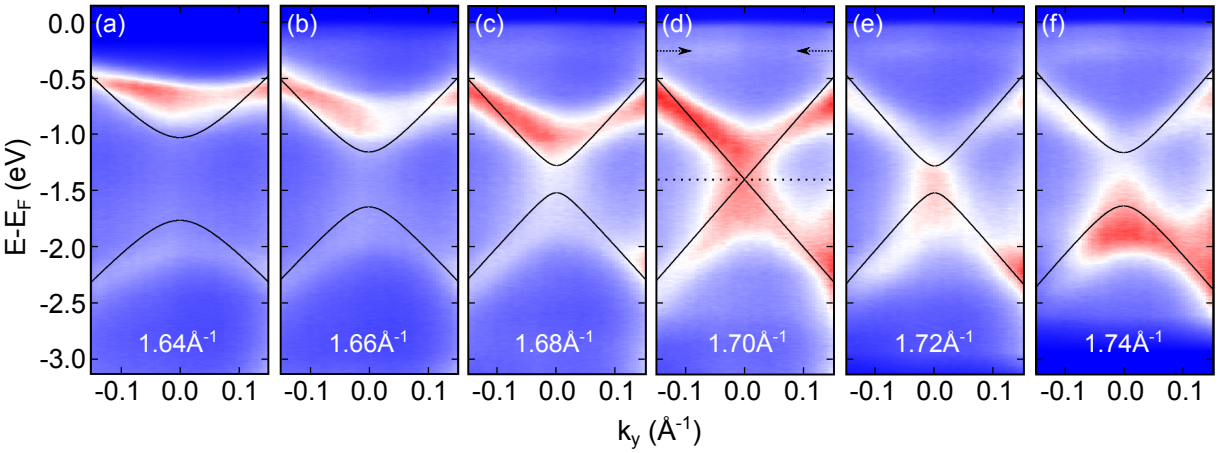

Figure 5.20: ARPES spectra of an intercalated (2×2) Eu layer measured perpendicular to the ΓKM direction at the indicated values of k_x. The black lines correspond to the π/π^* bands in TBA rigidly shifted by $E_D = -1.4$ eV. The arrows in (d) highlight a flat band at -0.25 eV.

The ARPES data for the $(\sqrt{3} \times \sqrt{3})$R30° structure are shown in Fig. 5.21. At the K point visible in Fig. 5.21(c), the TBA again fits to the measured cone using a slightly higher doping level of about -1.5 eV compared to the (2×2) intercalation structure. Again, the opening of the apparent band gap is better reproduced by TBA in KM direction than towards the Γ point. The flat band related to the Ir surface state S_1 is also present here, but shifted to a lower energy of -0.4 eV. This indicates also a higher doping of Ir by the $(\sqrt{3} \times \sqrt{3})$R30° layer compared to the (2×2) structure.

The π^* band is more diffuse for the $(\sqrt{3} \times \sqrt{3})$R30° intercalation structure than for the (2×2) layer. This may be related to hybridization with a flat band at -1.0 eV, which is highlighted by arrows in Fig. 5.21(a), and more clearly visible in Fig. 5.18(b). In principle,

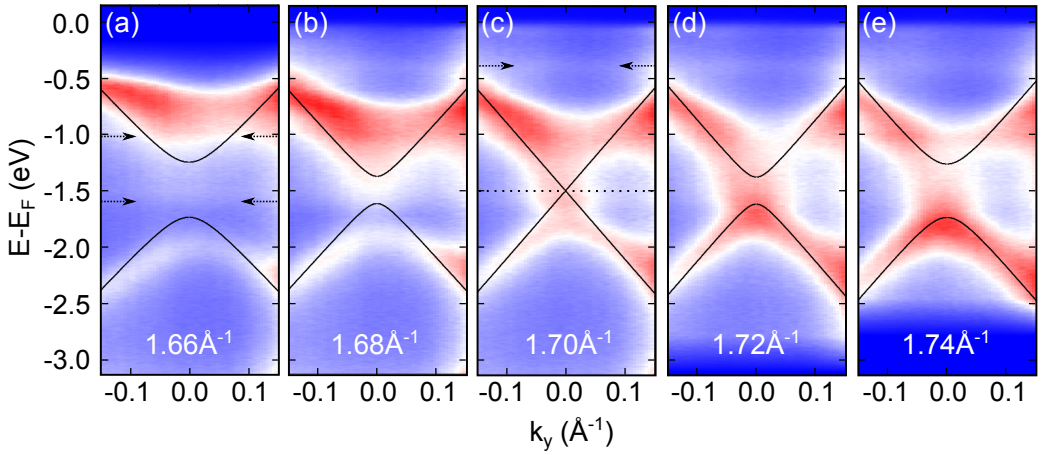

Figure 5.21: ARPES of the $(\sqrt{3} \times \sqrt{3})$R30° Eu structure perpendicular to the ΓKM direction at the indicated values of k_x. The black lines correspond to the π/π^* bands in TBA rigidly shifted by $E_\mathrm{D} = -1.5\,\mathrm{eV}$. The arrows in (a) highlight two flat bands at -1.0 eV and -1.6 eV.

the Ir surface state S_2 is located at this energy (compare Ref. [279]), but this state should be present also for the (2×2) intercalation structure. Since it is not observed there, the band is probably related to Eu. Finally, I note that there might also be a weak non-dispersing band around -1.6 eV, which was not visible in Fig. 5.18(b).

5.4 Mechanism of the Intercalation Process

In Sec. 5.1.2, it was calculated that Eu atoms gain a considerable amount of energy upon intercalation. Nevertheless, the experiments show that Eu intercalation requires elevated temperatures way above 300 K [28]. This means that intercalation is an activated process, whose mechanism I want to address in this section. As foundation for the following discussion, I first give a brief overview of known intercalation mechanisms:

- **Intercalation from Edges**
  Grånäs *et al.* found that a fully closed layer of Gr on Ir(111) cannot be intercalated by molecular O_2 [283]. In contrast, for Gr flakes or a holey Gr layer sharp intercalation fronts proceed from the edges towards the interior above a temperature of 355 K. The authors reasoned that O_2 intercalation takes place by delaminating the Gr edges from the substrate. A similar behavior was found for O_2 intercalation underneath Gr on Ru(0001) [22].

- **Intercalation at Wrinkles**
  Petrović *et al.* showed that Cs intercalation also takes place for a fully closed Gr

layer on Ir(111) [284]. The intercalation always nucleates next to wrinkles, and especially at their crossing points. The authors argue that the entrance points for Cs are nano-scale cracks in the wrinkles which are present due to extensive local forces. A significant role of wrinkles in the intercalation process has also been observed for Br_2 and O_2 intercalation under atmospheric conditions [114, 285].

- **Intercalation through Defects**
  Riedl *et al.* demonstrated that H_2 can be intercalated underneath Gr on SiC(0001) at 870 K [21]. In this context, Markevich *et al.* calculated by DFT that H_2 is not able to penetrate a perfect Gr layer at this temperature, but defects such as Stone-Wales defects, divacancies, or tetravacancies allow the penetration [286]. A similar mechanism has also been proposed for intercalation of Si [287, 288], Li [289] and atomic O [290]. Experimentally, Sicot *et al.* observed for Ni and Fe under Gr on Rh(111) that the intercalated islands are mainly located underneath defects in the Gr lattice, supporting that defects are starting points for intercalation [275].

- **Reactive Passage by Defect Formation**
  However, Sicot *et al.* also observed intercalated islands covered by perfect Gr [275]. Thus, they speculate on a further intercalation mechanism: DFT calculations show that transition metals reduce the vacancy formation energies in Gr [291]. Therefore, atomic-scale defects might be induced at elevated temperatures through which the metal atoms can diffuse. After completion of the intercalation process they vanish again by restoring the C bonds. The mechanism is in line with the observation that Li ions can induce defects in Gr upon intercalation [292].

To investigate which of these mechanisms are of importance for Eu intercalation, the intercalation process was imaged in real time by electron microscopy. We used PEEM which turned out to yield a better contrast than LEEM, probably because of its high sensitivity to the work function difference between intercalated and pristine Gr (compare Sec. 6.1). Since there was no possibility on site to calibrate the Eu evaporator, I do not give absolute values for the deposited amounts in this section.
At an intercalation temperature of 720 K, only a homogeneous brightness change on the whole sample is observed during Eu deposition. This indicates that Eu at this temperature is too mobile to identify where it has penetrated. Therefore, the intercalation temperature was lowered to 620 K. Furthermore, the CVD growth temperature was increased from 1170 K to 1470 K. This results in more wrinkles, but less defects, making it easier to distinguish between the relevance of both.

Fig. 5.22(a) shows a µ-LEED image of the Gr layer prior to Eu deposition, confirming its high quality. As apparent in the PEEM image in Fig. 5.22(b) taken in the initial stage of Eu deposition, the intercalation starts at a few distinct points separated by several 100 nm. With increasing coverage, the intercalated material spreads in large islands with a preferred orientation from the top left to the bottom right (Figs. 5.22(c) to (f)). At the end, the Gr layer is fully intercalated (Fig. 5.22(g)), and shows a $(\sqrt{3} \times \sqrt{3})$R30° diffraction pattern in µ-LEED (Fig. 5.22(h)).

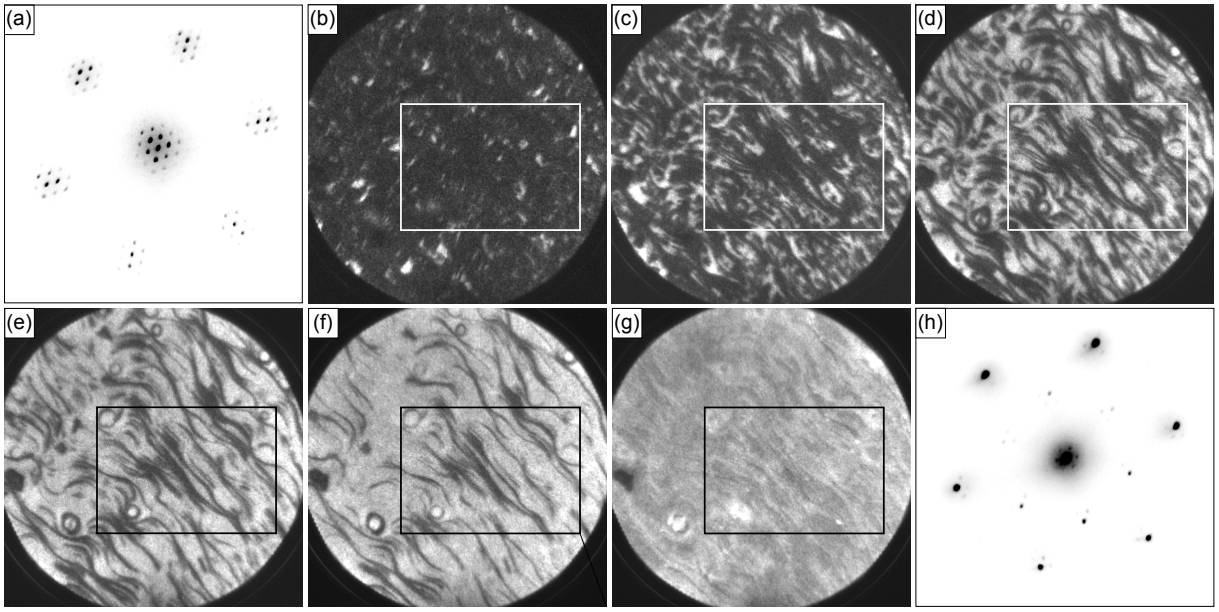

Figure 5.22: (a) µ-LEED of pristine Gr (1 µm aperture, 45 eV electron energy). (b) - (g) PEEM series during Eu deposition at 620 K starting with the nucleation of intercalation, and ending with a fully saturated layer (25 µm field of view). The boxes indicate the region which will be overlayed to LEEM images in the following figures. (h) µ-LEED after complete intercalation showing the $(\sqrt{3} \times \sqrt{3})$R30° superstructure (1 µm aperture, 45 eV electron energy).

Since intercalation under a fully closed Gr layer takes place, one can conclude that Gr edges are not of importance for Eu intercalation. One might argue that the points visible in Fig. 5.22(b) are small holes in the Gr layer that permit Eu penetration, since the CVD growth process is exponentially self-limited, i.e., the Gr coverage θ reaches 1 upon increasing ethylene flux ϕ only according to $\theta(\phi) = \left(1 - e^{-\phi/\phi_0}\right)$ with a constant ϕ_0. However, F. Huttmann estimated in Ref. [273] that for the ethylene dosages used in the experiments there should be no holes larger than atomic vacancies.

First, it is plausible that Eu intercalation does not need Gr edges: Whereas O_2 does not stick to Gr and consequently has to adsorb to Ir prior to intercalation, the ionic binding

of Eu to Gr permits a longer residence time during which the atoms can find a pathway for intercalation. Furthermore, in contrast to the case of large O_2 molecules, Eu ions are so small that intercalation via defects is conceivable.
Second, a dominating role of reactive passage via defect formation can be excluded. If this was the case, one would expect a spatially more homogeneous start of intercalation, whereas here only a few nucleation points are found. Therefore, I focus in the following on pre-existing defects and wrinkles. Unfortunately, PEEM is not able to image steps or wrinkles on the surface. Therefore, it is helpful to overlay the PEEM images to LEEM images of the same surface area to match the intercalated areas to the surface topography.

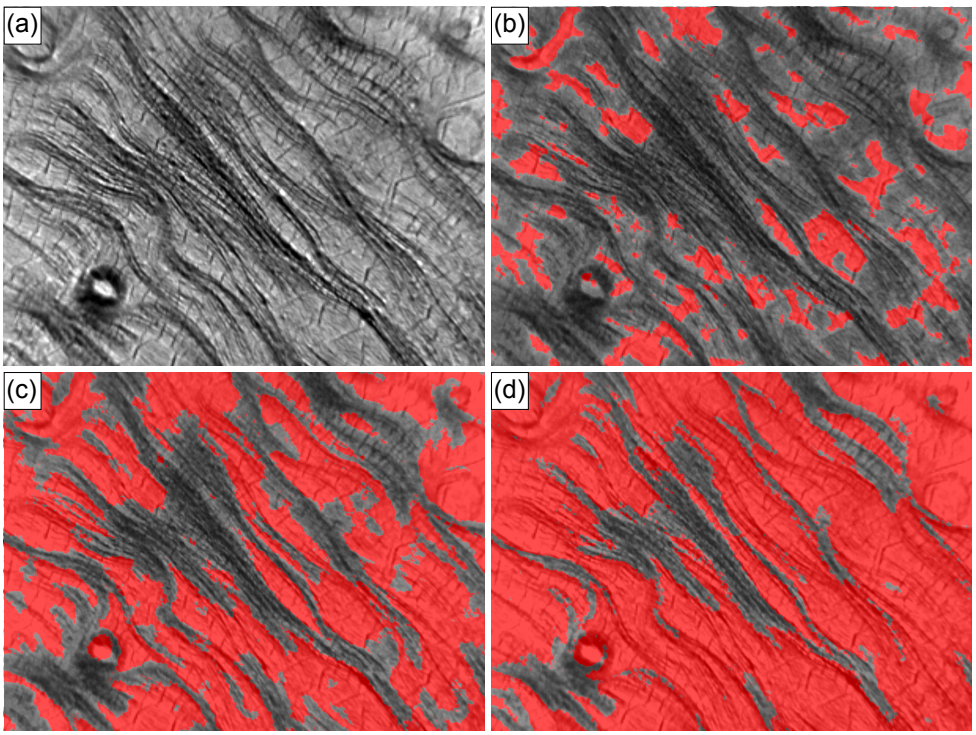

Figure 5.23: (a) Mirror mode LEEM image (15 µm × 10 µm) of the region indicated in Fig. 5.22. Several step bunches and terraces with wrinkles are visible. (b) - (d) Zooms of the PEEM images in Figs. 5.22(c), (d), and (f) overlayed to the LEEM image in (a). The intercalated regions are colored in red. Extended terraces are intercalated first, and step bunches last.

In Fig. 5.23(a), a LEEM image of the region indicated by the boxes in Fig. 5.22 is shown. By decelerating the incoming electrons to 0 eV (mirror mode) a strong step contrast is achieved, revealing several step bunches that separate extended terraces. When overlaying in Figs. 5.23(b) to (d) the PEEM images, it becomes apparent that the intercalation starts on the extended terraces, which get progressively intercalated during further deposition, whereas the step bunches are filled only in the very late stage of intercalation.

In Fig. 5.23(a), also wrinkles are slightly visible on the extended terraces. To make them better visible, the objective lens was slightly defocused as shown in Fig. 5.24(a). Since wrinkles are substantially higher than the average surface this results in a pronounced contrast of the wrinkle network. Although it is tricky to overlay the PEEM images exactly to the defocused LEEM image, it becomes apparent in Fig. 5.23(b) that the intercalated areas always nucleate at wrinkles. As visible in Figs. 5.23(c) and (d), the intercalation proceeds along the wrinkle network upon further Eu deposition.

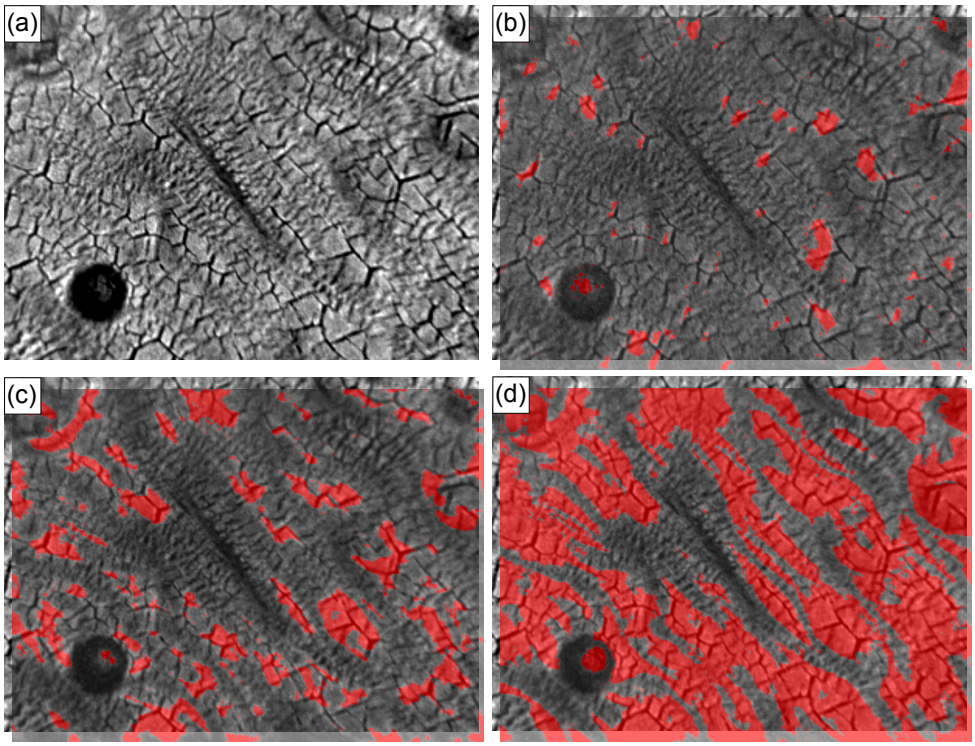

Figure 5.24: (a) Defocused mirror mode LEEM image (15 µm × 10 µm) of the region indicated in Fig. 5.22. The wrinkle network is well visible. (b) - (d) Zooms of the PEEM images in Figs. 5.22(c), (d), and (e) overlayed to the LEEM image in (a). The slight shift roughly compensates the defocus aberration. Intercalated regions are colored in red.

The observations show that the intercalation mechanism of Eu is very similar to the one of Cs described in Ref. [284]: The intercalation starts at wrinkles, which allow the Eu to penetrate probably via small cracks. Since the wrinkle density is highest on extended terraces (here, strain relaxation cannot be achieved as easily as on step bunches), the intercalation starts there. Upon progressing Eu deposition, the intercalation propagates along the wrinkle network, as it is easy to transport Eu along wrinkles. Similar to the Cs case, step edges act as diffusion barriers so that step bunches are intercalated last.

The similar behavior of Cs and Eu is expected, since both elements have similar ionic and atomic radii, thus making similar requirements on the entrance points for intercalation plausible. Furthermore, both bind ionically to the substrate (see Chap. 6), indicating a similar sticking and mobility behavior.

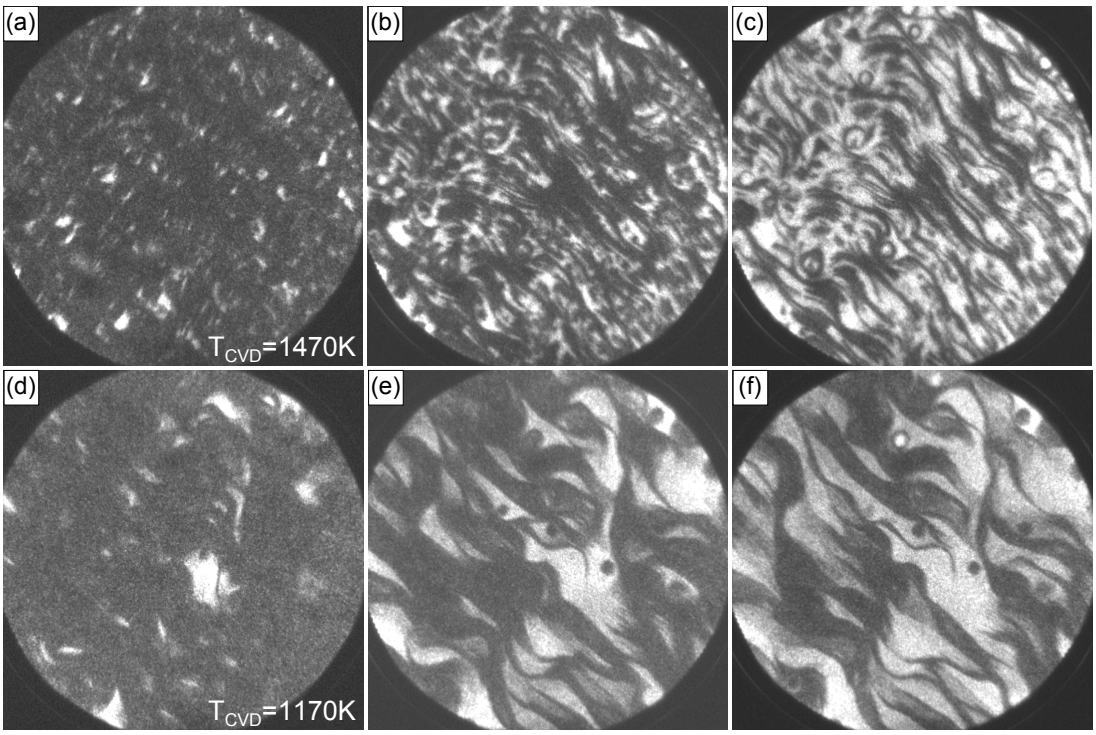

Figure 5.25: (a) - (c) PEEM series of Eu intercalation underneath Gr grown at 1470 K (same data as in Figs. 5.22(b) to (d)). (d) - (f) PEEM series of Eu intercalation underneath Gr grown at a lower CVD temperature of 1170 K. The field of view is always 25 µm.

To underline the relevance of wrinkles, Eu was also intercalated underneath Gr grown at a lower CVD temperature of 1170 K instead of 1470 K. As visible in Figs. 5.25(d) to (f), in the early stage of intercalation the size of the coherently intercalated areas is substantially larger than for the higher Gr growth temperature in Figs. 5.25(a) to (c). This is consistent with the fact that at a lower CVD temperature less wrinkles are present, which reduces the nucleation density for intercalation. Unfortunately, it was not possible to achieve wrinkle contrast for this sample, which could directly proof the interpretation.
Although wrinkles seem to be the dominating pathway of intercalation, it cannot be excluded that penetration via defects additionally takes place. Evidence for this comes from STM images for very low Eu coverage as shown in Fig.5.26: The intercalated material is found only at five-seven defects, which are always present at small-angle grain boundaries between differently rotated Gr domains [92]. Typically, the Eu decorates the defects from

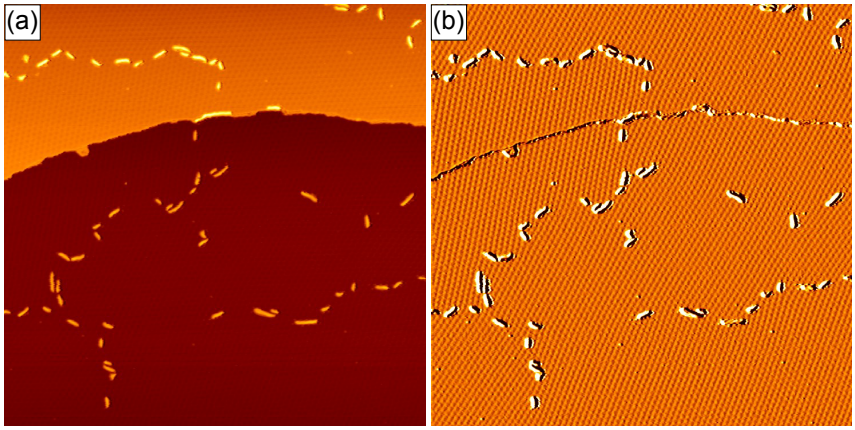

Figure 5.26: (a) STM topograph (160 nm × 160 nm) of a small intercalated Eu amount decorating the five-seven defects at small-angle grain boundaries in Gr. (b) Different area on the same sample with a higher local intercalation amount (160 nm × 160 nm).

both sides, leading to double stripes in STM. However, I note that this observation is not a rigorous proof as it may also be possible that the Eu has penetrated the Gr layer somewhere else and just sticks to the five-seven defects when diffusing on the surface. To exclude this possibility experiments at the minimum intercalation temperature would be needed, provided that the mobility at this temperature is low enough to prohibit diffusion.

5.5 Summary

In this chapter, the intercalation of Eu underneath Gr on Ir(111) was investigated. In the submonolayer regime, Eu intercalates at elevated temperatures forming a (2×2) superstructure attached to the Gr lattice. DFT calculations show that a large energy gain is the driving force for intercalation. The Eu intercalation system reveals surprisingly rich and complex patterns, which can consistently be explained by the interplay of the moiré binding inhomogeneity and a change in the strain state of Gr due to intercalation. Thereby, the intercalation step density directly visualizes local variations in the initial strain distribution of Gr. During further Eu deposition the intercalated monolayer is compacted to a $(\sqrt{3} \times \sqrt{3})$R30° structure.
By means of ARPES, the band structure of Gr is found to stay largely intact upon Eu intercalation. There is no evidence for the opening of a band gap. The doping level was determined to about -1.4 eV for the (2×2) and -1.5 eV for the $(\sqrt{3} \times \sqrt{3})$R30° structure, consistent with previous results. It is furthermore observed that also the Ir surface states are doped by the intercalated Eu layer.

To get insight to the intercalation mechanism, the Eu intercalation was followed in real time by PEEM and LEEM. The dominating pathway for intercalation is penetration at wrinkles, just as in the case of Cs intercalation. With increasing deposited amount, the Eu first fills the Ir terraces before it eventually enters step bunches, indicating that the latter act as diffusion barriers. When growing Gr at lower temperatures, the intercalated structures are larger, which can be attributed to the lower amount of pre-existing wrinkles. STM images for low Eu coverages indicate that intercalation via five-seven defects at small-angle grain boundaries might be a second pathway for intercalation.

CHAPTER 6

Adsorption on Intercalated Graphene

The content of Sec. 6.1 is published in Nano Lett. ***13*** *5013 (2013) [63]. I conducted all STM and work function measurements with Eu; STM experiments with Cs have been performed by S. Runte. ARPES data were obtained by M. Petrović, D. F. Förster, and M. Kralj. DFT calculations were performed by T. O. Wehling (Eu), and P. Lazić (Cs). Sec. 6.2 contains results measured and analyzed by F. Huttmann in Ref. [273], and me.*

In this chapter, I discuss the adsorption of Eu on intercalated Gr. Eu deposition onto bare Gr has already been studied by Förster *et al.* in Ref. [28], from which Fig. 6.1 is adapted as overview: Upon depositing 3.3% ML Eu with respect to Gr (see Fig. 6.1(a)) small dispersed clusters with an average size of about 15 atoms cover the sample. In an intermediate coverage range around 12% ML, the cluster phase coexists in two-dimensional equilibrium with large Eu islands (see Fig. 6.1(b)). Both, clusters and islands, internally possess a $(\sqrt{3}\times\sqrt{3})$R30° structure with respect to Gr, which implies a saturation coverage of 33% ML for the first monolayer. When going beyond this value (see Fig. 6.1(c)) the island phase essentially covers the whole sample with a small amount of clusters left. A second $(\sqrt{3}\times\sqrt{3})$R30° Eu layer nucleates before closure of the first layer.

The related energetics are explained in detail in Ref. [28]: Electrons from the Eu atoms can lower their kinetic energy by going into Gr, but thereby a charge imbalance is built up, which costs Coulomb energy. This penalty is much lower for uniformly distributed small clusters than for large Eu islands. This leads to formation of the cluster phase. With increasing coverage the doping level in Gr rises so that the kinetic energy gain and thus also the Coulomb penalty is reduced [293]. In consequence, above a critical coverage the metallic Eu-Eu binding dominates and large $(\sqrt{3}\times\sqrt{3})$R30° islands form.

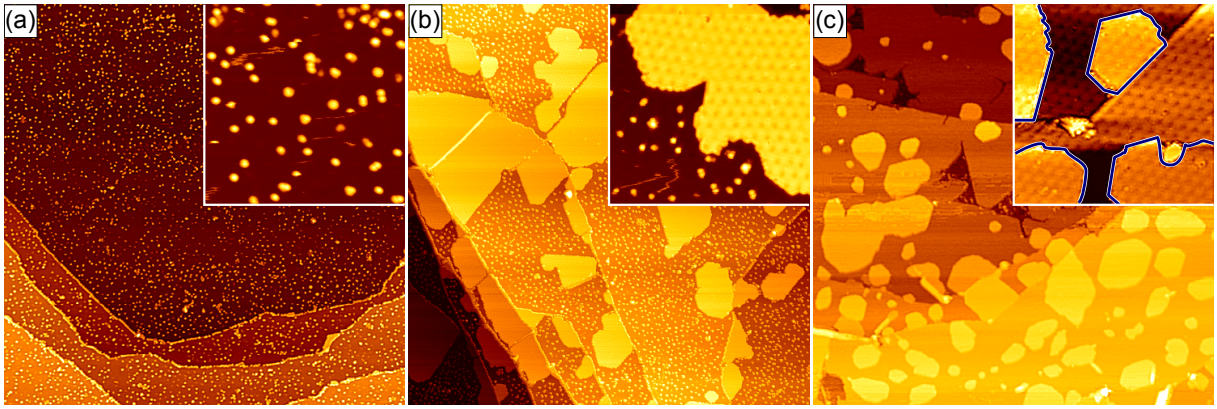

Figure 6.1: STM topographs after deposition of (a) 3.3% ML, (b) 12% ML, and (c) 40% ML Eu at 300 K onto bare Gr. In the inset of (c), second layer Eu islands are encircled by blue lines. The image sizes are (320 nm × 320 nm) and (40 nm × 40 nm) for the large images and the insets, respectively. The figure is adapted from Ref. [28].

In the following, I first demonstrate for submonolayer coverages how adsorption on Gr can be changed by an intercalated layer. Afterwards, I investigate the structural properties of fully coalesced adsorbate layers on intercalated Gr.

6.1 Manipulating Adsorption by Intercalation

The electronic properties of Gr are extremely sensitive to adsorption. Due to the marginal DOS at the Fermi edge of undoped Gr even a minor adsorption related charge transfer causes a substantial shift of the chemical potential. Schedin *et al.* [89] exploited this sensitivity to detect single NO_2 molecules on Gr: NO_2 molecule adsorption causes chemical doping of Gr and the resulting change of the charge carrier density gives rise to a measurable change in the resistivity of Gr. Furthermore, it was established in numerous experimental and theoretical investigations that even weakly binding adsorbates - not affecting the integrity of the Dirac cone - typically imply doping and thus a shift of the chemical potential within Gr [89, 294, 295].
Reciprocity implies that the adsorbate binding must also sensitively depend on the location of the chemical potential in Gr. Indeed, Brar *et al.* demonstrated this sensitivity by the observation of a gate voltage dependent ionization state of a Co adatom adsorbed to Gr [35]. Using a field effect transistor based on bilayer Gr, Sato *et al.* were able to change the rate of molecular O_2 adsorption to Gr by a gate controlled variation of the chemical potential [36]. Abanin *et al.* predicted a doping dependent ordering of covalently bound adsorbates on one sublattice of Gr through a Peierls-instability type mechanism mediated

by RKKY-like interactions [37]. Finally, Huang *et al.* found by DFT calculations a doping dependent bond strength of H to Gr, with a substantial binding energy increase through either n-doping or p-doping [38].

As discussed in Sec. 2.1.3, intercalation provides a flexible means to drastically modify the chemical potential of the Dirac electrons. The span of the shift of the Dirac point energy E_{D} measured with respect to the Fermi level E_{F} is about one order of magnitude larger than typically achieved by gating of Gr. Since intercalation leaves one side of Gr free, it enables to explore the consequences of the chemical potential shift for the interaction of Gr with the environment. The patterned intercalation of Eu demonstrated in Chap. 5 is a unique tool to provide patches of strongly n-doped Gr located above the intercalant, and marginally p-doped Gr in contact with the Ir(111) substrate side-by-side. As I will show, controlled adsorption on such a doping pattern directly visualizes large differences in the binding energy of ionic adsorbates on Gr.

All STM experiments concerning Eu were performed at ATHENE. The Cs experiments were performed at a different low temperature setup in Cologne. ARPES experiments were conducted in Zagreb (Eu intercalation), and at the APE beamline of the ELETTRA synchrotron in Trieste (Cs intercalation). A fully closed Gr layer was prepared by a TPG step at 1470 K followed by CVD at 1170K (see Sec. 4.5 for details). Intercalated and adsorbed amounts θ are specified in monolayers with respect to the Gr lattice. DFT calculations were performed as described in Sec. 4.6.

Europium Adsorption and Intercalation

Fig. 6.2(a) displays an STM topograph taken at 35 K after deposition of 10% ML Eu onto Gr at 720 K. As already discussed in Chap. 5, a pattern of intercalated stripes and islands is formed. In contrast, we find in Fig. 6.2(b) upon room temperature deposition compact islands coexisting with clusters on top of Gr as discussed before.

Fig. 6.2(c) visualizes the key experiment related to Eu adsorption: We deposited Eu at room temperature on a partly intercalated sample. Again, a phase separation of the adsorbed Eu into islands and clusters is observed. However, the Eu clusters and islands are only found on the non-intercalated (Gr/Ir) areas, but not on the intercalated (Gr/Eu/Ir) regions. The schematic cross section in Fig. 6.2(d) along the line in Fig. 6.2(c) clarifies the morphology. The arrow in Fig. 6.2(c) highlights that the large adsorbed Eu island displays a hole at the location of an intercalated Eu island. The arrangement of the intercalation stripes on the upper terrace is rather inhomogeneous, since the large area underneath the adsorbed island is free of stripes, whereas it is surrounded by a dense

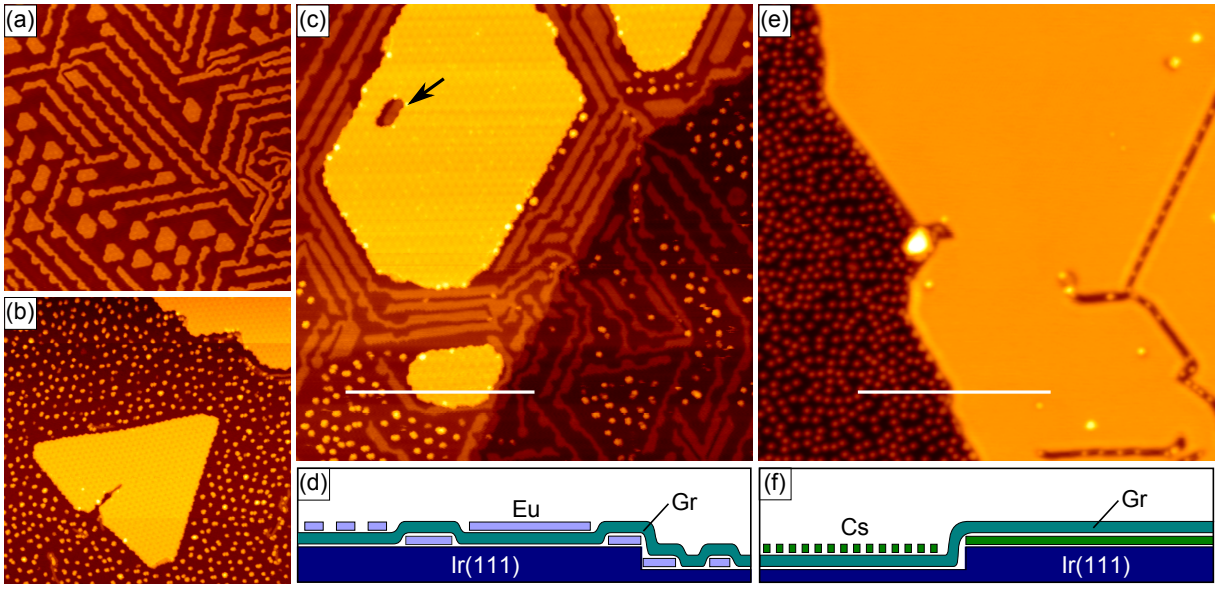

Figure 6.2: (a) STM topograph of 10% ML Eu intercalated at 720 K (120 nm × 120 nm). (b) 12% ML Eu adsorbed at 300 K (120 nm × 120 nm). (c) Intercalation of 10% ML Eu at 720 K, and subsequent adsorption of 12% ML Eu at 300 K (120 nm × 120 nm). The arrow in (c) highlights a Eu intercalation island which was not overgrown by the large adsorbed Eu island. (d) Schematic cross section along the line indicated in (c). (e) Deposition of 10% ML Cs onto bare Gr/Ir at 300 K (45 nm × 45 nm). (f) Schematic cross section along the line indicated in (e). The imaging temperature was 35 K in (a) - (c), and 6.5 K in (e).

stripe arrangement. Such an inhomogeneous distribution has never been observed for pure intercalation (compare Chap. 5). Since the intercalated Eu stripes and islands are able to fluctuate in position and shape at the deposition temperature of 300 K, one can tentatively attribute the observed stripe arrangement to be a dynamic response to the growth of the adsorbed Eu island.

At 300 K, the deposited Eu forms equilibrium structures as explicitly demonstrated in Ref. [28]. It is highly mobile, and thus scans the surface for locations of strongest binding. Upon cooling, the morphology is frozen at some unknown temperature below 300 K. Imaging at 35 K therefore represents the equilibrium situation at this freezing temperature. The absence of adsorbed Eu clusters and islands on intercalated regions immediately implies that adsorbed Eu is more strongly bound to non-intercalated areas. Upon analyzing about 30 STM images with a total scanning area of 1 µm^2 with an intercalated share of 40%, we find only one small adsorbed island of 100 nm^2 size on an intercalated region yielding a percentage of 2.5×10^{-4}. As 12% ML Eu corresponding to 36% apparent coverage in a $(\sqrt{3} \times \sqrt{3})$R30° structure were adsorbed, this fraction would be 0.36 for a random distribution. Therefore, the probability for Eu to adsorb on an intercalated area

is drastically reduced by a factor of 1500. However, without knowing the precise freezing temperature of the morphology and details on the binding energies within a cluster or island it is not straightforward to obtain a quantitative value for the binding energy difference ΔE_b between the atoms in the two different areas.

Cesium Adsorption and Intercalation

A similar binding energy difference for adsorption to intercalated and non-intercalated areas can be inferred from experiments with Cs deposition onto Gr/Ir at room temperature. As displayed in Fig. 6.2(e), for $\theta \approx 10\%$ ML a phase separation of the deposited material is observed. The morphology is clarified by the schematic cross section in Fig. 6.2(f) taken along the line in Fig. 6.2(e): An adsorbed dilute gas of ionized Cs adatoms (the only phase for $\theta \leqslant 2\%\,\mathrm{ML}$) coexists with large intercalated islands which possess a (2×2) structure with respect to Gr [284]. The intercalated structure is denoted as Gr/Cs/Ir in the following. Although the deposited amounts are similar, it is not unexpected that the material is distributed quite differently from the Eu case, since first the electronic structure, and second the atomic and ionic radii of the two elements differ. However, I will not discuss this here in more detail.
In the present context, the key observation is that the Cs adatoms are adsorbed *only* on Gr/Ir areas, despite the fact that the adsorbed ions repel each other by Coulomb interaction. This is also reflected by the presence of Cs atoms in the non-intercalated trenches of the large Gr/Cs/Ir island. Our observation again implies that adsorbates are more strongly bound to non-intercalated areas.

Local Doping and Work Function

The key to understand why Eu and Cs adsorbates preferentially bind to non-intercalated areas must be sought in local changes in the electronic structure of Gr. Therefore, we conducted ARPES and STS experiments. For reference, Fig. 6.3(a) displays the band structure of Gr on Ir(111) along the ΓKM direction showing a largely intact Dirac cone with slight p-doping and an estimated Dirac point position of $E_\mathrm{D} = 0.1\,\mathrm{eV}$ [279]. For a complete Eu intercalation layer strong n-doping is found with an estimated value of $E_\mathrm{D} = -1.38\,\mathrm{eV}$ as shown by Fig. 6.3(b).
Even more instructive are ARPES data of Cs intercalation: After deposition of about 10% ML corresponding to the situation in Fig. 6.2(e) two Dirac cones are observed in Fig. 6.3(c). The first cone is shifted just slightly below E_F with $E_\mathrm{D} = -0.12\,\mathrm{eV}$, whereas the second one is strongly shifted by $E_\mathrm{D} = -1.13\,\mathrm{eV}$. Upon further Cs deposition the

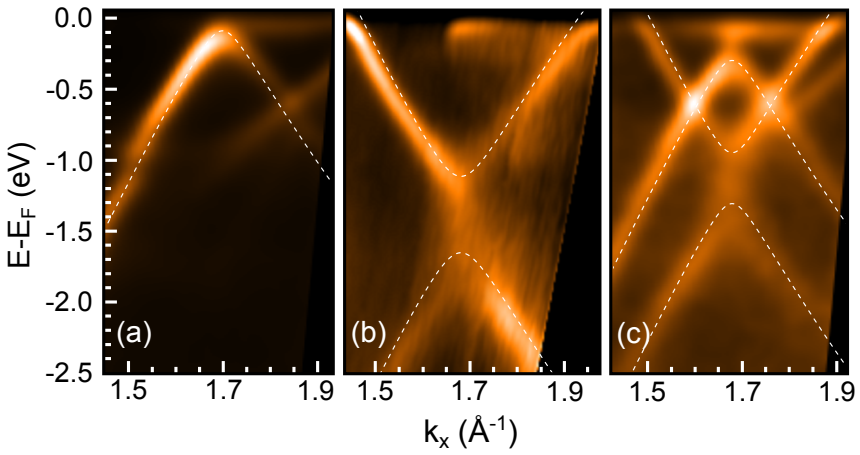

Figure 6.3: ARPES spectra along ΓKM direction with a small azimuthal offset of about 1° in (a) and (c), and about 1.5° in (b). (a) Gr/Ir. (b) 25% ML Eu deposited at 720 K resulting in a complete Gr/Eu/Ir layer. (c) 10% ML Cs deposited at 300 K. White dashed lines indicate fitted NN TBA bands taking into account the azimuthal offset. The corresponding Dirac point energies are (a) $E_D = 0.1\,\text{eV}$, (b) $E_D = -1.38\,\text{eV}$, and (c) $E_D = -0.12\,\text{eV}$ and $E_D = -1.13\,\text{eV}$.

slightly shifted cone diminishes in intensity until it vanishes for layer completion, while the strongly shifted cone gains intensity. A comparison with Fig. 6.2(e) yields a straightforward interpretation of the situation: Whereas the dilute gas of Cs ions induces just a slight local n-doping, the large intercalated Cs islands induce strong n-doping of the Gr underneath. Thus, Cs intercalation creates a doping pattern in Gr.

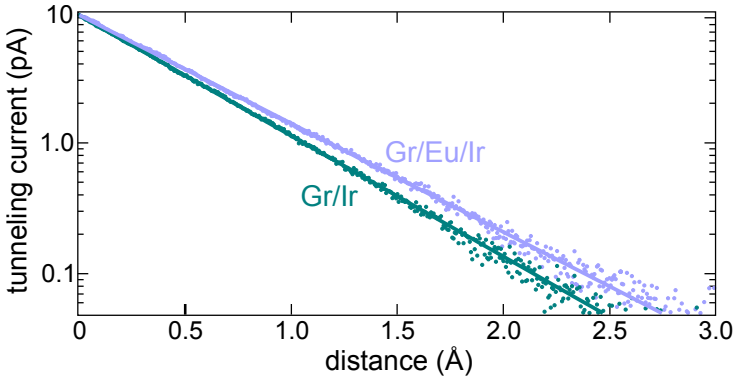

Figure 6.4: $I(z)$ spectra for Gr/Ir (green) and Gr/Eu/Ir (blue) taken at -0.5 V sample bias. Here, $z = 0$ is the start position of tip retraction. Lines indicate fits to the data.

Similar to Cs intercalation also the Eu intercalation pattern must be assumed to create a doping pattern in Gr on an even finer scale. To establish its existence we used $I(z)$ spectroscopy and measured differences in the local work function on adjacent areas of Gr/Ir and Gr/Eu/Ir (see Sec. 3.1 for details). The corresponding spectra are displayed

in Fig. 6.4. By fitting the data one finds a work function difference of $\Delta\Phi = \Phi_{\mathrm{Gr/Ir}} - \Phi_{\mathrm{Gr/Eu/Ir}} = (1.5 \pm 0.2)\,\mathrm{eV}$. This value is in remarkable agreement with the doping level difference given by $\Delta E_{\mathrm{D}} = E_{\mathrm{D,Gr/Ir}} - E_{\mathrm{D,Gr/Eu/Ir}} = 0.1\,\mathrm{eV} - (-1.38\,\mathrm{eV}) = 1.48\,\mathrm{eV}$. In view of the DFT calculations by Khomyakov *et al.* [296] this agreement is well understandable: The authors find that with an accuracy of better than 0.1 eV the difference between the work function Φ of Gr doped by its substrate and the Dirac point energy E_{D} is a constant, namely the free Gr work function Φ_{free}: $\Phi_{\mathrm{free}} = \Phi - E_{\mathrm{D}}$. This implies that for two areas $\Delta\Phi$ must be identical to ΔE_{D}, just as we observe it experimentally. Therefore, our local work function measurement also reflects the presence of a doping pattern in Gr which is related to the spatial Eu intercalation pattern.

A Model for the Binding Preference

The link between doping level and work function gives access to understand the preferred binding to the non-intercalated areas. For the morphology sketched in Fig. 6.5(a) the energy diagram of Fig. 6.5(b) shows that the work function Φ and the doping level E_{D} display a constant energetic separation irrespectively whether Gr is intercalated or not.

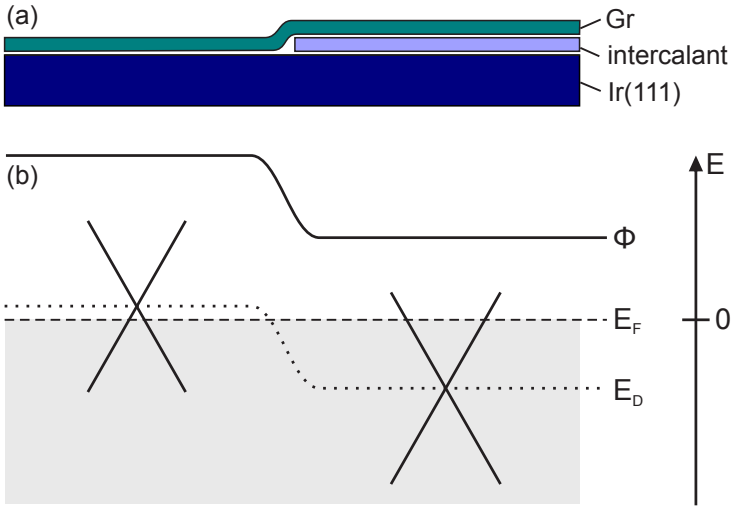

Figure 6.5: (a) Schematic cross section of a sample with Gr on Ir(111) that is partly intercalated. (b) Corresponding electron energy diagram for the case of an n-doping intercalant.

In a gedankenexperiment one may partition the adsorption process of an ionic adsorbate into three steps as sketched in Fig. 6.6. For simplicity, we focus here on a single adatom. Initially, we consider the atom to be near the substrate at a height where a well defined work function is established, but sufficiently far way to avoid wave function overlap with the substrate. This initial state is well-defined, as it does not cost energy to move a neutral atom at this height parallelly to the surface through areas of different work function.

In step (1) an electron is removed from the atom. To good approximation, the ionization energy will not depend on the electronic structure of the substrate. In step (2) the electron is moved to the substrate where it delocalizes. Thereby, it can lower its kinetic energy by a value identical to Φ, irrespective of how the charge is distributed within the substrate. A comparison between Figs. 6.5(a) and (b) tells that in this step substantially more energy is gained on the non-intercalated areas (1.48 eV more for Eu, and 1.23 eV more for Cs). In step (3), the positive ion is moved to the substrate. Assuming for the moment that the energy gain in this step does not depend on the substrate, the adsorption of the ionic adsorbate to non-intercalated areas is preferred by just $\Delta\Phi = \Delta E_{\mathrm{D}}$, i.e., the binding energy difference is given by the difference in the Gr doping level.

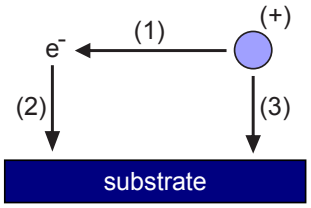

Figure 6.6: The adsorption process of an ionic adsorbate can be partitioned into three steps: (1) Ionization close to the surface, (2) transfer of the electron to the substrate, and (3) transfer of the remaining positively charged ion to the substrate.

In order to see whether and to what extent this simple picture is adequate we conducted DFT calculations. We consider Eu and Cs adatoms adsorbed to Gr/Ir (Fig. 6.7(a)) as well as to Gr/Eu/Ir and Gr/Cs/Ir (Fig. 6.7(b)). First, we analyze the 6s LDOS of Eu adatoms on Gr/Ir and Gr/Eu/Ir shown in Fig. 6.7(c), and of Cs adatoms on Gr/Ir and Gr/Cs/Ir shown in Fig. 6.7(d). For a Eu adatom the majority spin 6s orbital is in both cases below the Fermi level, while the minority spin LDOS shows spectral weight only above E_{F}. As the 6s orbital of a free Eu atom is doubly occupied, this means that there is in both cases a charge transfer of about one electron to the substrate.
For a Cs adatom adsorbed to Gr/Ir or Gr/Cs/Ir the 6s spectral weight is almost entirely above the Fermi level. As the 6s orbital of free Cs atoms is singly occupied, also the Cs adatom donates in both cases about one electron to the substrate. The major difference between the 6s LDOS of the adatoms on bare and intercalated Gr is a rigid shift. In conclusion, Eu and Cs always bind ionically to the substrate by donation of about one electron as assumed in the model above.
In qualitative agreement with ARPES, our DFT calculations show that intercalated Gr is strongly n-doped, while non-intercalated Gr is essentially undoped. The Dirac point positions are $E_{\mathrm{D}} \approx 0\,\mathrm{eV}$ for Gr/Ir, $E_{\mathrm{D}} = -1.2\,\mathrm{eV}$ for Gr/Eu/Ir and $-0.94\,\mathrm{eV}$ for Gr/Cs/Ir

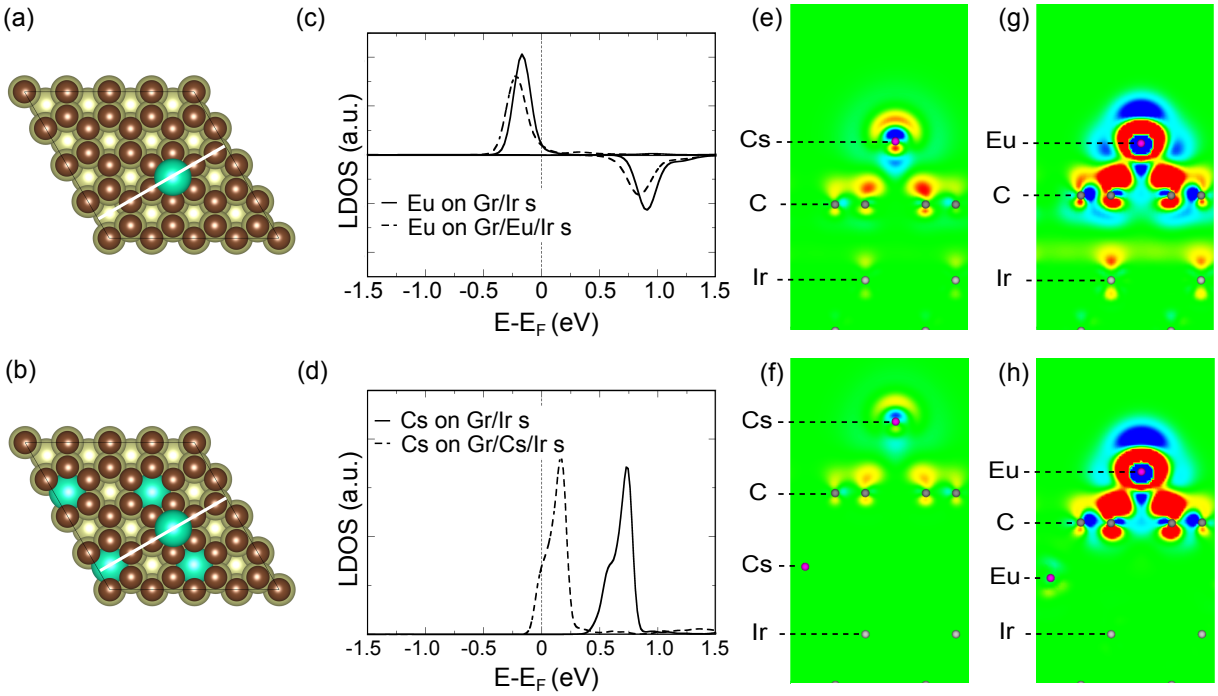

Figure 6.7: (a), (b) Unit cells for Eu or Cs adsorption on (a) Gr/Ir, and (b) Gr/Eu/Ir or Gr/Cs/Ir. (c) Spin-polarized LDOS of the 6s orbitals for Eu adatoms on Gr/Ir (full line), and Gr/Eu/Ir (dashed line). The majority (minority) spin is shown on the positive (negative) ordinate. (d) LDOS of the 6s orbitals for Cs adatoms on Gr/Ir (full line), and Gr/Cs/Ir (dashed line). (e) - (h) Charge density difference between (i) the whole system, and (ii) a free atom and the rest of the system. The cuts are taken along the white lines in (a) and (b). (e) Cs adatom on Gr/Ir, (f) Cs adatom on Gr/Cs/Ir, (g) Eu adatom on Gr/Ir, and (h) Eu adatom on Gr/Eu/Ir. The charge difference from blue to red is ± 0.03 (± 0.01) electrons per Å^3 for Cs (Eu).

deviating less than 0.2 eV from the experimental numbers given above. Based on our simple model one would thus expect that the Eu (Cs) adatoms bind more strongly to Gr/Ir compared to the intercalated substrate by $\Delta E_\mathrm{b} = 1.2\,\mathrm{eV}$ ($\Delta E_\mathrm{b} = 0.94\,\mathrm{eV}$).
To check this, we calculated the adatom binding energies for all cases. We get $E_\mathrm{b} = 1.2\,\mathrm{eV}$ and $E_\mathrm{b} = 0.6\,\mathrm{eV}$ for Eu adsorbed to Gr/Ir and Gr/Eu/Ir, respectively. For Cs the corresponding values are $E_\mathrm{b} = 1.5\,\mathrm{eV}$ and $E_\mathrm{b} = 0.8\,\mathrm{eV}$. Thus, the binding energy differences are $\Delta E_\mathrm{b} = 0.6\,\mathrm{eV}$ for Eu, and $\Delta E_\mathrm{b} = 0.7\,\mathrm{eV}$ for Cs. In sign and magnitude the values agree with our expectations from the work function model, but are quantitatively smaller by factor of 2 for the Eu case, and by 25% for the Cs case.
Apparently, the qualitative model sketched above oversimplifies the physical situation. First, in step (2) the electron gains the entire work function Φ only in the limit of infinitely dilute adsorption. Otherwise, the electron transfer itself will contribute to the doping and thereby reduce the energy gain (*quantum capacitance effect*). More important, we

assumed that the energy related to step (3) is independent of the substrate. However, the electrostatic energy after complete adsorption depends on the ability of the substrate to screen the positive ion. Considering only the Gr layer to first approximation the screening will be the better the higher the LDOS at the Fermi level. Thus, screening will be more efficient for adsorption on the intercalated, n-doped Gr areas which possess a much higher LDOS at the Fermi level. Consequently, the expected binding preference to Gr/Ir due to the larger work function (stronger lowering in kinetic energy) will be diminished by the poorer screening in this case (larger Coulomb penalty).

The charge difference plots in Figs. 6.7(e) to (h) visualize the total charge redistribution upon adsorption for the four cases under concern. For adsorption to Gr/Ir there is significantly more charge redistribution indicating a larger Coulomb penalty associated with charge transfer. The poorer screening of the cation by the Gr layer for the case of Gr/Ir is also visible as the charge transfer extends here to the Ir substrate atoms, whereas not even the intercalation layer is involved for the cases of Gr/Cs/Ir or Gr/Eu/Ir.

q (e^-/2 C atoms)	E_D (eV)	E_b (eV)
0.00	0.00	0.72
0.01	0.45	0.55
0.02	0.65	0.45
0.06	1.01	0.31

Table 6.1: Adsorption energies E_b of Eu on doped freestanding Gr as a function of the charge doping level q related to the Dirac point energy E_D before Eu adsorption.

The relevance of screening for the ionic binding energy is underlined by DFT calculations for adsorption on freestanding Gr. To model the effect of pure doping on the adsorption energy we considered freestanding Gr with adsorbed Eu and added further electrons to the supercell (together with a compensating positive jellium background). We find decreasing adsorption energies with increasing n-doping as expected (see Tab. 6.1). However, for perfectly freestanding Gr the binding energy decrease is even more than twice smaller than the related Dirac point shift. We attribute this to an even stronger variation of screening with the doping level due to the absence of the metallic substrate. A comparison of Eu adsorption on undoped freestanding Gr and metal supported undoped Gr directly illustrates the better cation screening for supported Gr: The binding energy of Eu on Gr/Ir is by 0.4 eV higher than for Eu on freestanding pristine Gr.

The Role of Rehybridization, Diffusion, and Strain

Finally, we analyze alternative hypothetical explanations for the preferential binding of adsorbates to bare Gr. As pointed out in Sec. 2.1.2 transition metals form regular cluster arrays on Gr/Ir [39] by inducing a rehybridization of Gr from sp^2 to sp^3 diamond-like C in precisely those locations where already without adsorbates a slight hybridization of Gr with the Ir substrate is present [95]. The rehybridization is accompanied by a drastic decrease of the C-metal bond distance from about 3.4 Å to about 2.1 Å [102, 103]. Therefore, one might consider that the preferential binding of the ionic adsorbates to Gr/Ir is rather due to a larger ability of the non-intercalated areas to rehybridize upon adsorption.

However, this effect is irrelevant here: (i) Even the slightest binding energy inhomogeneity within the moiré unit cell should be reflected by a lateral ordering of Cs adatoms or Eu clusters with respect to the moiré. The STM topographs in Fig. 6.2 make plain that such an ordering is absent. This is consistent with a continuous variation of the Eu cluster separation upon deposition at low temperatures [28]. (ii) Our DFT calculations show that there is no change in the height of Gr above Ir(111) upon Cs or Eu adsorption. Such a change would be expected if rehybridization was of any relevance. (iii) As evident in the LDOS plots in Figs. 6.7(c) and (d), there is no change in the width of the 6s resonances. This rules out significant changes in the hybridization when going from the bare to the intercalated substrate. (iv) As shown Tab. 6.1, the same binding preference is also observed for free standing Gr where no rehybridization can take place.

Furthermore, we note that neither differences in adatom diffusion on the bare and intercalated regions, nor variations in the local Gr strain are able to account for our observations. First, the absence of adsorbates on the intercalated areas and their homogeneous distribution on the non-intercalated areas underline that the adatom mobility at 300 K is high enough to establish a local equilibrium. Second, though slight differences between the strain in Gr/Ir and Gr/Eu/Ir might be present, they do not exceed a few per mill and extend over mesoscopic scales [62, 100], inconsistent with the sharp changes in adsorption behavior on the nanometer scale associated with intercalation.

6.2 Formation of Complete Adlayers

Up to now, I only discussed small adsorbed amounts on partially intercalated layers. Certainly, when the deposited Eu amount is increased beyond the area of acceptance provided by the non-intercalated Gr, also the Gr/Eu/Ir areas start to become overgrown

until eventually a complete Eu adsorption layer forms. This does not contradict our inferences above, but is just a consequence of the fact that Eu also binds to Gr/Eu/Ir, though weaker than to Gr/Ir. In the following, I discuss the adsorption of Eu on fully coalesced (2×2) and $(\sqrt{3} \times \sqrt{3})$R30° intercalation layers, and compare our findings to the growth of Eu on non-intercalated Gr.

Adsorption on the (2×2) Intercalation Layer

Fig. 6.8(a) shows an STM topograph after adsorption of 25% ML Eu at 300 K on an almost fully (2×2) intercalation layer. The corresponding morphology along the blue line profile is shown in Fig. 6.8(b). As there are hole stripes in the intercalation layer, one can be certain that the deposited Eu amount was low enough to prevent the formation of $(\sqrt{3} \times \sqrt{3})$R30° intercalated areas.

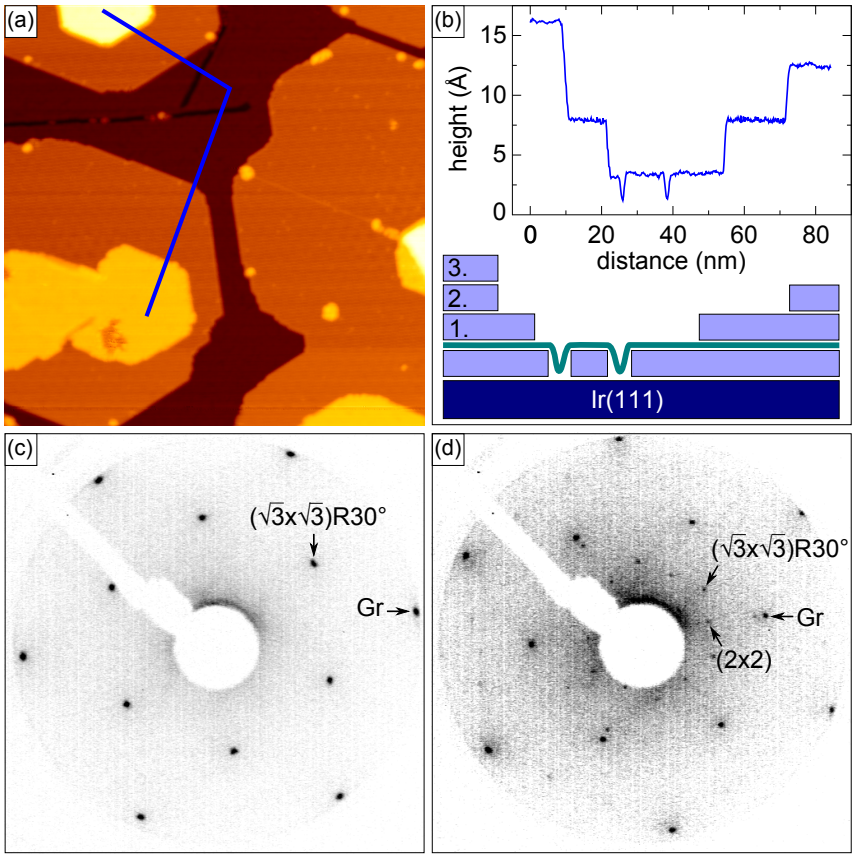

Figure 6.8: (a) STM topograph of 25% ML Eu adsorbed at 300 K to an almost fully intercalated (2×2) layer (90 nm × 90 nm). (b) Profile and schematic stacking along the blue line in (a). (c), (d) Corresponding LEED images at 70 eV and 192 eV primary electron energy, respectively. First-order Gr and superstructure spots are indicated.

The LEED pattern in Fig. 6.8(c) shows intense $(\sqrt{3}\times\sqrt{3})$R30° diffraction spots coexisting with weak (2×2) spots of the intercalation layer, which are best visible in Fig. 6.8(d). Thus, the Eu islands adsorbed on top of Gr must internally possess an $(\sqrt{3} \times \sqrt{3})$R30° structure just like Eu on non-intercalated Gr.

The Eu islands preferentially align their edges parallelly to the dense-packed Eu rows in the $(\sqrt{3}\times\sqrt{3})$R30° superstructure. The mostly threefold symmetry of the (hole) islands in the non-intercalated case (compare Fig. 6.1(c)) has been superseded by hexagonal symmetry in the intercalated case. This can be qualitatively understood to arise from decoupling of the Eu/Gr system (hexagonal symmetry) from the Ir substrate (only threefold symmetry) by the intercalated Eu layer.

As in the case of Eu on non-intercalated Gr, second layer islands nucleate before closure of the first layer. However, we observe in Fig. 6.8(a) also flat islands with a height of three layers, which have the peculiar property *not* to be surrounded by an only two layer high island. Such islands have been observed several times in different STM topographs. Their presence cannot be explained by conventional layer-by-layer growth, since the third layer cannot grow faster than the underlying second layer, which would be necessary for the third layer to cover the second one completely. Therefore, our observation might yield evidence that on the intercalated Gr layer local dewetting already takes place at the deposition temperature consistent with the lower binding energy derived above.

In contrast to the case of Eu on bare Gr, we do not observe a cluster phase between the large Eu islands. This can easily be understood if one remembers the reason for the emergence of the cluster phase [28]: Adsorbed Eu atoms donate electrons to Gr, where they can lower their kinetic energy. This is associated with a Coulomb penalty which can be reduced by formation of small size clusters. In the case of Eu adsorption on already intercalated Gr the charge transfer and thus the Coulomb penalty is much lower since Gr is already heavily n-doped from the Eu underneath. Consequently, the metallic Eu-Eu binding dominates, and causes the formation of large islands.

Adsorption on the $(\sqrt{3} \times \sqrt{3})$R30° Intercalation Layer

Next, I discuss the adsorption of Eu on a complete $(\sqrt{3} \times \sqrt{3})$R30° intercalation layer. An STM image after deposition of 25% ML Eu at 300 K is shown in Fig. 6.9(a). The corresponding morphology along the blue line profile is depicted in Fig. 6.9(b). Atomic resolution within a hole island of the adsorbed layer in Fig. 6.9(c) reveals the $(\sqrt{3} \times \sqrt{3})$R30° structure of the intercalation layer (compare Fig. 5.16). In the LEED image in

Fig. 6.9(d), the $(\sqrt{3} \times \sqrt{3})$R30° superstructure spots of the intercalation layer intensify upon Eu adsorption. Hence, also here the adsorbed layer has a $(\sqrt{3} \times \sqrt{3})$R30° structure.

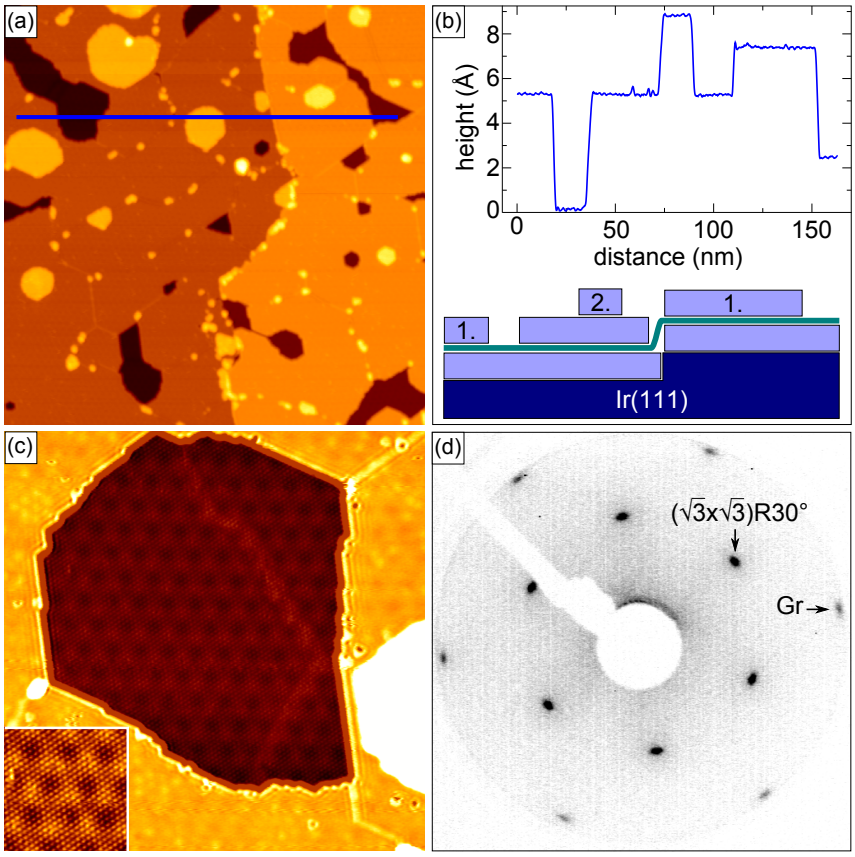

Figure 6.9: (a) STM topograph of 25% ML Eu adsorbed at 300 K to a fully intercalated $(\sqrt{3} \times \sqrt{3})$R30° layer (180 nm × 180 nm). (b) Profile and schematic stacking along the blue line in (a). (c) Hole island in the adsorbed Eu layer with atomic resolution on the intercalation layer underneath (45 nm × 45 nm). The strongly non-linear contrast results in artifacts at the steps. Inset: Zoom from the center of a hole island (9 nm × 9 nm). (d) Corresponding LEED image at 70 eV primary electron energy. The first-order Gr and $(\sqrt{3} \times \sqrt{3})$R30° spots are indicated.

Upon strongly enhancing the contrast on the adsorbed Eu layer characteristic line defects become apparent in Fig. 6.10(a), one of which is pointed by a white arrow. They were already faintly visible in Fig. 6.9(a). The lines have a corrugation of about 20pm, and are oriented parallel to the dense-packed rows of the $(\sqrt{3} \times \sqrt{3})$R30° Eu structure.
We interpret the lines to be translational domain boundaries. Since every third C ring in a $(\sqrt{3} \times \sqrt{3})$R30° superstructure is special, there are consequently three different translational domains. There are two different kinds of domain boundaries, which are shown in Fig. 6.10(b). In the following, they are denoted as a *thin* (marked in green) and *thick* (marked in orange) domain boundaries. The distance of the atomic Eu rows in a perfect

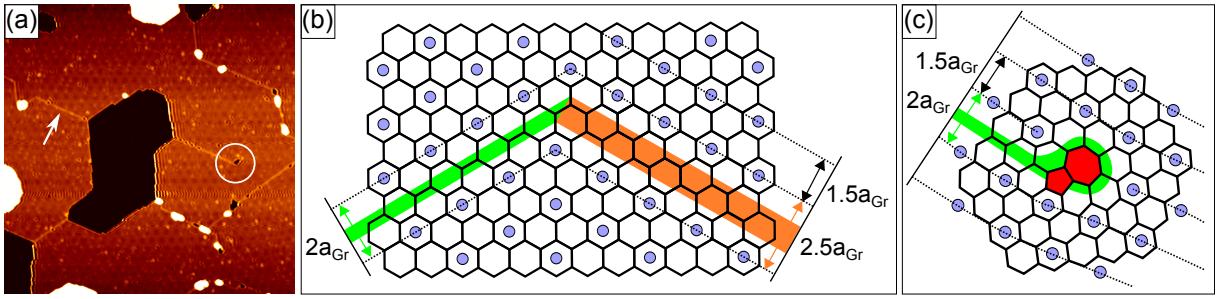

Figure 6.10: (a) STM topograph with strongly enhanced contrast to highlight line defects in the adsorbed Eu layer, one of which is pointed by a white arrow. The white circle marks a line ending in the intercalated layer. (b), (c) Schematic of possible defects in the adsorbed layer showing Eu atoms in blue and Gr honeycombs in black. a_{Gr} is the Gr lattice constant. (b) Thin (green) and thick (orange) translational domain boundaries. The boundary changes its character as it goes around a corner. (c) End of a thin translational domain boundary in a five-seven defect (red). Note that also thick lines can end in five-seven defects depending on their orientation.

islands is $1.5a_{\mathrm{Gr}}$, while it is $2a_{\mathrm{Gr}}$ between adjacent Eu rows on different sides of the domain boundary in the case of the thin boundary, and $2.5a_{\mathrm{Gr}}$ in the case of the thick boundary.

The structural model in Fig. 6.10(b) further shows that the character of the line changes whenever the domain boundary takes a turn by 60°. One would expect that this leads to lines with larger/smaller corrugation or width in STM before and after a turn has been taken. However, one has to take into account that also the tip shape and the scanning direction have an effect on the appearance of lines in different directions. Thus, one would need to image lines of both types in the same direction with the same tip in order to unambiguously demonstrate this effect, but such data have not been acquired.

There is another feature (encircled in white in Fig. 6.10(a)) that needs more explanation: a line that ends within an island. This cannot be explained by a boundary between two translational domains. However, if one assumes a five-seven defect in Gr where the line ends, the conundrum is easily resolved as shown in the schematic picture in Fig. 6.10(c). Unfortunately, the image quality of Fig. 6.10(a) is too poor to directly prove this model.

The model for domain boundaries in an adsorbed Eu layer is independent of what is underneath Gr. So, it seems surprising that there are no similar defects for Eu on non-intercalated or (2×2) intercalated Gr. We explain this as follows: Upon Eu intercalation the Gr hexagons become inequivalent; some are preferred adsorption sites for Eu on top, while others are not. If Gr is intercalated by a $(\sqrt{3} \times \sqrt{3})\mathrm{R}30°$ layer, the Eu superstructure underneath is the same as on top. Thus, the two can lock in with respect to each other, and the translational domain is hard to change by thermal diffusion. In contrast, if Gr is

not intercalated or intercalated by a (2×2) Eu layer, the $(\sqrt{3} \times \sqrt{3})$R30° superstructure on top cannot lock in with respect to the one underneath so that the translational phase will be easier to change by thermal diffusion. In consequence, we expect that domain boundaries cannot anneal as easily for adsorption on $(\sqrt{3} \times \sqrt{3})$R30° intercalated Gr as for bare or (2×2) intercalated Gr, and hence appear more often in the former case.

6.3 Summary

In this chapter, the adsorption of Eu and Cs on intercalated Gr was investigated. First, I demonstrated that intercalation underneath Gr is an efficient tool to change the binding of adsorbates on the frontside. By adsorption onto partially intercalated Gr a preferential binding of cationic adatoms, adatom clusters, and extended islands to non-intercalated regions can be directly visualized. This preference originates from a change in the work function resulting from local doping of Gr by the intercalant: We find that the work function of bare Gr is substantially higher than for intercalated Gr. Since a higher work function implies a larger lowering in kinetic energy when donating electrons from the adsorbates to Gr, the non-intercalated regions are the preferred adsorption sites.
Our DFT calculations confirm this binding preference, but yield smaller binding energy differences than estimated from the work function alone. Therefore, we conclude that the Coulomb penalty associated with charge redistribution upon adsorption as well as substrate dependent screening substantially reduce the binding energy differences below those estimated from the work function differences.
In Sec. 6.2, I discussed the adsorption of Eu on fully closed (2×2) and $(\sqrt{3} \times \sqrt{3})$R30° intercalation layers. Similar to the case of Eu adsorption onto bare Gr, the adsorbed Eu forms islands with internal $(\sqrt{3} \times \sqrt{3})$R30° structure, but the pre-existing doping by the intercalation layer prohibits the formation of an adsorbed cluster phase. For Eu adsorbed to a $(\sqrt{3} \times \sqrt{3})$R30° intercalation layer characteristic line defects are observed which we attribute to anti-phase domain boundaries.

CHAPTER 7

Rare Earth Layers on Iridium

The data presented in Sec. 7.1 were measured and analyzed by F. Huttmann in Ref. [273], and me. The experiments in Sec. 7.2 were conducted and interpreted by myself.

In the last two chapters, I discussed the intercalation and adsorption of Eu on Ir supported Gr. Here, I focus on the growth of Eu directly deposited onto the Ir(111) substrate. All experiments were conducted at the UHV chamber ATHENE. Eu and Gd were deposited from two Knudsen cells onto a clean Ir(111) surface (see Sec. 4.5 for details). In both cases, the deposited amounts are given in monolayers with respect to Ir(111).

7.1 Europium on Iridium

The growth of submonolayer coverages of Eu on Ir(111) has already been investigated previously by our group (see Ref. [204] and appendix of Ref. [29]). The system behaves similar to the well investigated deposition of alkali metals on fcc(111) surfaces (see Refs. [297] and [298] for detailed reviews): The Eu atom donates electrons to the Ir substrate, becomes positively charged, and forms a dipole with its screening cloud in the metal. In consequence, the adatom-adatom interaction is dominated by Coulomb repulsion of the parallelly oriented dipoles. In the dilute limit, this leads to a liquid-like behavior with short-range quasi-hexagonal order. When increasing the deposited amount, the Eu adatoms form successively denser phases, some of which are commensurate with respect to the Ir lattice. Above saturation of a $(\sqrt{7} \times \sqrt{7})$R19.1° structure, the metallic Eu bonding dominates over the electrostatic repulsion so that metallic islands nucleate. In the following, I characterize a full monolayer of that dense phase.

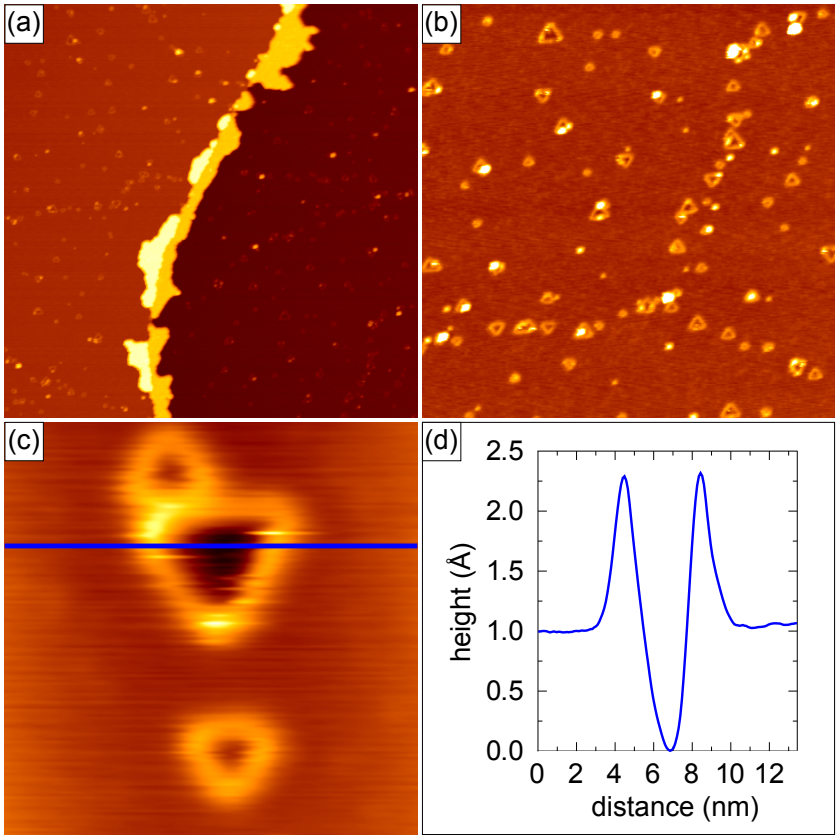

Figure 7.1: STM topographs of 50% ML Eu deposited on Ir(111) at room temperature. (a) Closed first Eu layer with nucleation of a second layer at a substrate step (270 nm × 270 nm). (b) Characteristic triangular defects often arrange along lines (130 nm × 130 nm). (c) Close-up on three triangles (14 nm × 14 nm). (d) Height profile along the blue line in (c).

By deposition of 50% ML Eu on Ir(111) at room temperature, Eu forms a closed layer as apparent by the STM topograph in Fig. 7.1(a). A small fraction of a second layer nucleates at step edges, but never appears on extended terraces. Most of the second layer is located at ascending steps, and less at descending steps. This leads to the following conclusions: The mobility of Eu at room temperature is high enough to form a closed layer. Since the second layer nucleates only after closure of the first, the Eu-Ir bond is stronger than the Eu-Eu bond. The ascending steps provide the highest coordination for Eu adatoms and are therefore the preferred nucleation sites for the second Eu layer.

The step height between the first and second Eu layer of 6.3 Å is substantially larger than the value of 3.24 Å between the dense-packed (110) terraces of bulk Eu. In general, this is not surprising since for example the *first* Eu layer on Gr also has a large apparent height of about 5 Å [28], which is probably related to the strong charging of the adsorbed Eu atoms. However, in contrast to the present case, the height of the *second* Eu layer on Gr

is close to the bulk value. A difference in the charge transfer might be responsible for the different apparent heights in the two systems.

As well visible in Fig. 7.1(b), a high density of triangular defects is characteristic for the first Eu layer on Ir. Three of these triangles are enlarged in Fig. 7.1(c): Their edges are aligned parallelly to the dense-packed Ir$\langle 1\bar{1}0\rangle$ directions and have typical lengths of 2-4 nm. The triangles point up- and downwards in about equal shares, thereby not breaking the sixfold rotational symmetry. As apparent by the line profile in Fig. 7.1(d), the triangles appear about 1 Å higher (lower) at the edges (interior) than the surrounding terrace. This is nearly independent on the applied bias voltage. As also visible in Fig. 7.1(b), the defects often arrange along lines, which are supposed to be translational domain boundaries, where defect formation is energetically cheaper. However, the atomic resolution needed to prove this hypothesis could not be obtained.

The nature of the triangular defects is puzzling. It seems implausible that they are triangular holes in the Eu layer since the mobility of Eu on Ir at room temperature is high. Alternatively, they could be electronic features related to point defects such as vacancies, interchanged Eu/Ir atoms, or adsorbates. However, in this case one would expect a characteristic size instead of a size distribution. Also a change in appearance with varying bias voltage which usually signalizes an electronic feature is missing. Therefore, the most probable explanation is that the triangles are nuclei of oxidation. Indeed, we will see in Chap. 10 that Eu easily reacts with O to a EuO(111) bilayer that appears lower than surrounding Eu, just as observed here.

To establish the atomic structure of the Eu layer, LEED measurements as shown in Fig. 7.2 were performed. The first-order spots of Ir(111) are marked in dark blue, whereas the ones belonging to Eu are highlighted in light blue. The dense-packed rows are parallelly aligned and the structure is close to a 2:3 relation between the lattice constants of Eu and Ir. However, the lattice parameter belonging to Eu was determined to (3.85 ± 0.02) Å, which is smaller than the 4.07 Å expected for an ideal 2:3 relation. This deviation is also evident in the splitting of the superstructure spots encircled in red, which originate from vector sums of reciprocal lattice vectors pointing to Eu and Ir spots; for an ideal 2:3 ratio the three spots would merge into one.

Within the accuracy of the measurements, it is not possible to decide whether the structure is commensurate or not. Therefore, in the following a structure of (7×7) Eu atoms on (10×10) Ir atoms is used as the most simple rational approximation that reproduces the superstructure spot splitting. Furthermore, the 7:10 ratio yields a Eu lattice constant of 3.88 Å in reasonable agreement with the measured value. At a first glance, it seems

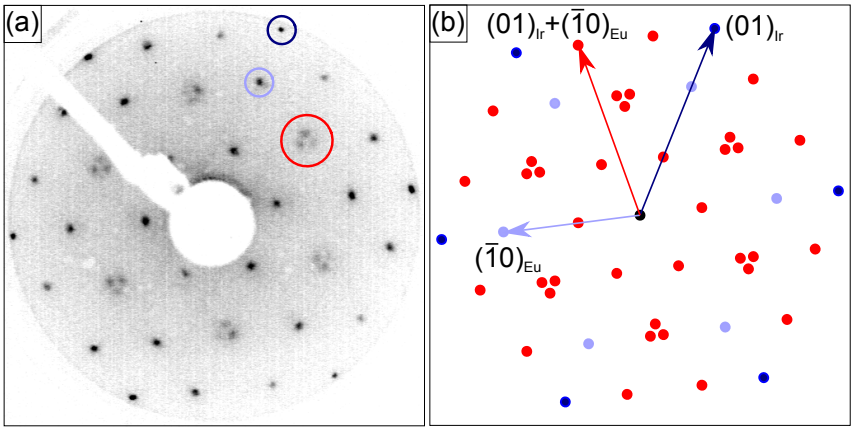

Figure 7.2: (a) LEED pattern of 50% ML Eu on Ir(111) at a primary electron energy of 59 eV. One of the first-order Ir and Eu spots is encircled in dark and light blue, respectively. Additional superstructure reflections are visible. Three adjacent of them are encircled in red. (b) Corresponding model for a 7:10 ratio between the Eu and Ir lattice constants. The occurrence of the superstructure spots (red) by adding reciprocal lattice vectors of Ir (dark blue) and Eu (light blue) is clarified for one particular spot.

surprising that the Eu does not lock in to the more simple 2:3 relation although the Eu-Ir interaction is stronger than the Eu-Eu interaction. A plausible reason might be that the lattice constant in the 7:10 structure is closer to the NN distance of 3.96 Å in bulk Eu. Furthermore, the deviation follows the general trend that the reduced coordination in a thin layer leads to shortened bonds [299].

7.2 Gadolinium on Iridium

Besides Eu, also Gd is an interesting rare earth metal in respect of its magnetic properties. Since Gd has the same $4f^7$ configuration as Eu, it also carries a magnetic moment of $7\,\mu_B$ per atom. The only electronic difference to Eu is an additional electron in the 5d shell. In contrast to the bulk antiferromagnet Eu with a low Néel temperature of 90 K, Gd orders ferromagnetically close to room temperature [300].

With this in view, nominally 7% ML Gd were deposited at 370 K on a clean Ir(111) surface. The slightly elevated deposition temperature was chosen to ensure enough mobility to form a flat Gd layer. Indeed, the corresponding STM image in Fig. 7.3(a) shows that the surface is covered by a flat layer. The high amount of scratches within the layer shows that the atoms easily become mobile under the STM tip. The high mobility is consistent with the absence of any spots in LEED except for the Ir ones (not shown here).

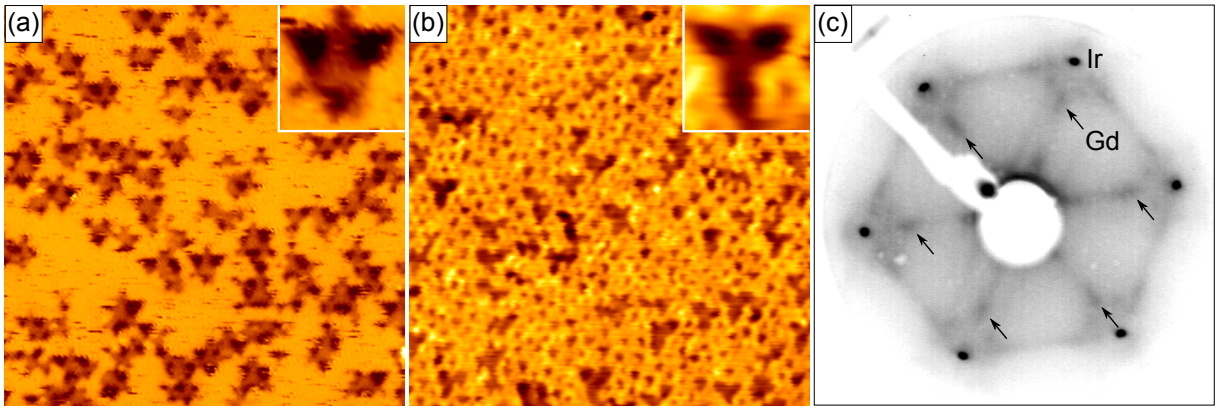

Figure 7.3: (a) STM topograph of Gd on Ir(111) deposited and imaged at 370 K. (b) Same preparation as (a), but imaged at 100 K. The insets are zooms on the triangular depressions. The image sizes are 40 nm × 40 nm and 4.4 nm × 4.4 nm, respectively. (c) LEED image at 100 K and 78 eV primary electron energy corresponding to (b). First-order Ir and Gd spots are indicated.

I note that the coverage observed in STM is substantially larger than expected from the microbalance rate (θ = 7% ML), even in the case of a very dilute adsorbate phase. I cannot give a sound explanation for this deviation, but argue that the microbalance rate might be affected by radiation heat from the Gd evaporator. This was never a problem for Eu, which is evaporated at much lower temperatures.

The flat adsorbed layer shows a high density of characteristic triangular depressions. One triangle with common size and appearance is enlarged in the inset of Fig. 7.3(a). It consists of three smaller triangles in its corners with a depth of about 2 Å with respect to the flat layer. In the middle of the large triangle, there is an intermediate height level about 1 Å below the flat layer or above the dark triangles, respectively.

To reduce the mobility, the sample was cooled down to 100 K. Because of technical problems with the liquid He cooling, the typical temperature of 35 K could not be achieved in this experiment. Similar to Fig. 7.3(a), again a flat layer with triangular depressions is found. Although the triangles have slightly changed their appearance upon cooling, they still show the two different height levels 1 Å and 2 Å below the flat layer. The most prominent difference between room- and low-temperature imaging is an additional dot pattern on the flat layer. The dots have a low corrugation of less than 50 pm and are typically separated by 10 - 15 Å, but there is no long-range order.

The low temperature LEED pattern in Fig. 7.3(c) shows in addition to the first-order Ir substrate spots also reflections with a lattice constant of (3.80 ± 0.06) Å. Furthermore, weak moiré spots around the Ir reflections are visible. All spots are rather diffuse and appear more like a distribution of spots with similar lattice constant.

The previous observations yield evidence that the flat layer consists of Gd adsorbed to Ir(111). Whereas the layer is too mobile at room temperature to determine its lattice parameter, the lattice constant of (3.80 ± 0.06) Å measured at 100 K is close to the NN distance of 3.64 Å in bulk Gd. Supported by the moiré spots in LEED, the dot pattern on the Gd layer observed at low temperatures can be interpreted as a moiré with the Ir(111) surface. For $a_{\mathrm{Gd}} = 3.80$ Å one would expect a moiré periodicity of $a_{\mathrm{m}} = (a_{\mathrm{Ir}}^{-1} - a_{\mathrm{Gd}}^{-1})^{-1} \approx 9.5$ Å. The observed periodicity of 10 - 15 Å is slightly larger, but on the right order of magnitude. The diffuse spots in LEED and the hardly ordered moiré pattern in STM, show that there is a substantial variation in the Gd lattice parameter.

Next, I discuss the triangular depressions. The intermediate height level of 1 Å is surprisingly low, since typical step edges are on the order of 2 Å. Therefore, I argue that Gd atoms have been incorporated in the Ir surface, whereby they slightly protrude out of it. In other words, there is evidence for the onset of surface alloying. The small dark triangles show the bare Ir surface around the incorporated Gd. The fact that the adsorbed Gd layer leaves a characteristic distance to the incorporated Gd probably originates from lattice distortions in the Ir surface induced by the incorporated atoms. However, a better resolution would be required to develop an atomistic model for this interpretation.

It is tempting to compare the growth of Gd on Ir(111) with the one of Pb on Cu(111) investigated by Nagl *et al.* in Ref. [301]: First, the atomic radii are identical (135 pm for Ir/Cu, and 180 pm for Gd/Pb [302]). Second, the lattice mismatch is similar (34%/37% between Ir(111)/Cu(111) and Gd(0001)). Upon room temperature deposition, Pb forms a flat layer with a frizzy appearance and a weak moiré corrugation on Cu(111), similar to our case. Additionally, Pb atoms are incorporated in the Cu(111) surface and protrude 0.7 Å out of it. Since all Pb is incorporated in the Cu(111) surface after annealing to 570 K, the surface alloy is stated to be the thermodynamically stable structure.

To prevent the formation of a surface alloy between Gd and Ir(111), Gd was also deposited at a lower temperature of 130 K. Fig. 7.4(a) shows an STM topograph of the corresponding preparation. The surface looks qualitatively similar to the one in Fig. 7.3(b), but there are neither well defined triangular depressions nor a moiré pattern visible. This indicates that at the lower deposition temperature the mobility is not sufficient to form long range order. Most interesting for our purposes, the depressions in the Gd layer do not show an intermediate height level at 1 Å in their middle, but are just holes in the Gd layer. This yields evidence that alloying can be prevented by deposition at 130 K.

In Fig. 7.4(b), the sample was again annealed to 370 K. The result is very similar to Gd deposition at 370 K (compare Fig. 7.3(b)), but with a less ordered moiré pattern.

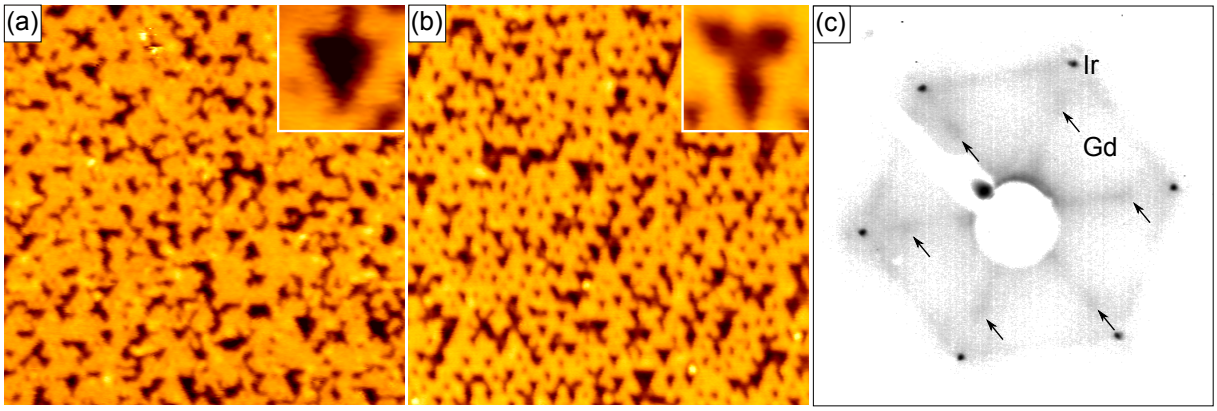

Figure 7.4: (a) STM topograph of Gd on Ir(111) deposited at 130 K and imaged at 100 K. (b) After annealing to 370 K for 60 s. The insets show zooms on the triangular depressions. The image sizes are 40 nm × 40 nm and 4.4 nm × 4.4 nm, respectively. (c) LEED image at 78 eV primary electron energy corresponding to (b). First-order Ir and Gd spots are indicated.

Consistently, the LEED image in Fig. 7.4(c) shows the same spots as Fig. 7.3(c), but with less intensity. When looking at the triangular depressions, again the intermediate height level is found, which proves that alloying has taken place during annealing.

To learn more about the alloying process, the sample was annealed in Fig. 7.5 to stepwise higher temperatures. Fig. 7.5(a) shows again the Gd layer deposited at 370 K with incipient alloying. After annealing to 470 K in Fig. 7.5(b), the coverage of the Gd layer has decreased, while more Gd has been incorporated into the Ir surface. During further annealing to 570 - 670 K, the adsorbed Gd layer becomes rough and shows two different height levels, indicating that now also here intermixing of Gd and Ir takes place. At the same time, the incorporated Gd dewets the surface to form triangular structures.

The corresponding LEED pattern in Fig. 7.5(d) shows $(\sqrt{3} \times \sqrt{3})$R30° superstructure with respect to Ir (slightly compressed by 3%). This leads to the conclusion that the incorporated Gd atoms form a surface alloy as shown in Fig. 7.6(a). This type of surface alloy with $GdIr_2$ stoichiometry also occurs for epitaxial alloy systems such as Sn on Pt(111) [303], or Al on Ru(0001) [304]. Also annealing of co-deposited Fe and Au on Ru(0001) leads to formation of an $FeAu_2$ alloy with the same superstructure [305].

Upon further annealing to 770 - 870 K in Figs. 7.5(f) and (g), the surface morphology again drastically changes. First, the triangles of embedded Gd disappear to a great extent, which probably indicates that the Gd partially diffuses into the Ir bulk. Second, the rough adsorbed layer becomes again flat, while the corresponding LEED pattern in Fig. 7.5(h) shows a (2×2) superstructure (slightly compressed by 3%). We interpret this as formation of a Gd-Ir alloy with a (2×2) superstructure on top of Ir(111).

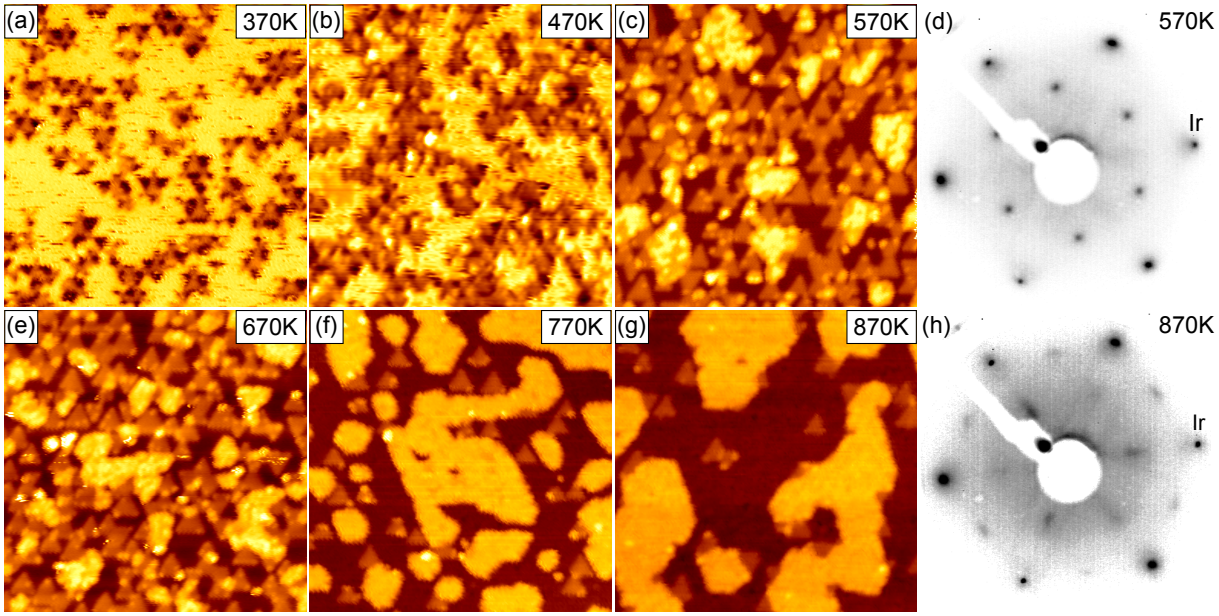

Figure 7.5: (a) Gd on Ir(111) deposited at 370 K. (b) - (g) Annealing series to the indicated temperatures. The image size is always 35 nm × 35 nm. (d), (h) LEED at 78 eV primary electron energy corresponding to (c) and (g). The first-order Ir substrate spots are indicated.

Since it was not possible to achieve atomic resolution on the surface alloy, the arrangement of the basis atoms within the (2×2) unit cell is not known and can be only speculated. Three possibilities are shown in Figs. 7.6(b) to (d). Fig. 7.6(b) shows the most simple surface alloy with a (2×2) superstructure, which occurs for example for Cu_3Au or Pt_3Sn surface alloys [306, 307]. However, in the present case an alloy with higher Gd content is expected since it is formed from an initially pure Gd layer. Nevertheless, also the Gd rich Gd_3Ir alloy shown in Fig. 7.6(b) appears improbable since here the NN Gd distance of 2.715 Å is substantially lower than the 3.64 Å in bulk Gd.

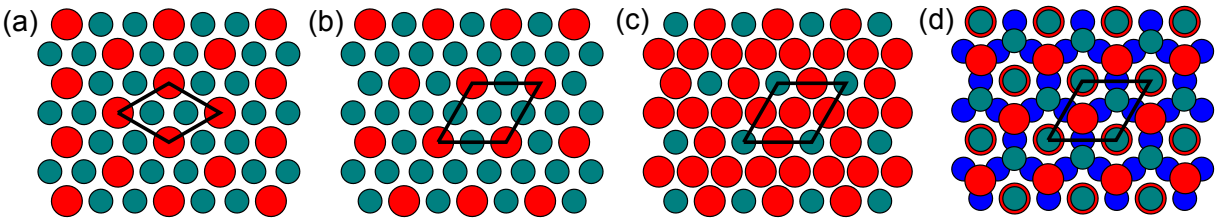

Figure 7.6: Ball models for different types of surface alloys (Gd: red, topmost Ir layer: green, second Ir layer: blue). (a) $GdIr_2$ with $(\sqrt{3} \times \sqrt{3})R30°$ superstructure with respect to the Ir(111) substrate. (b) $GdIr_3$. (c) Gd_3Ir. (d) Bilayer alloy with $GdIr_2$ stoichiometry. (b) - (d) all form a (2×2) superstructure with respect to the Ir(111) substrate.

Therefore, it seems reasonable that the structure is of the type shown in Fig. 7.6(d). The corresponding alloy involves two layers: Gd atoms on top of Ir surface atoms are exchanged by each other, while each one Ir and one Gd atom per (2×2) unit cell adsorb on fcc and hcp sites of the Ir(111) substrate. Note that the alloy type has the same stoichiometry as the one in Fig. 7.6(a) found for surface-embedded alloy.
The surface alloy shown in Fig. 7.6(d) has also been observed for Gd deposition on Au(111) [308–310]. However, one should be careful to compare Gd on Ir(111) with Gd on Au(111), since (i) the Au(111) is reconstructed in contrast to Ir(111) [311], (ii) the vacancy formation energy for Au is much lower than for Ir [312], and (iii) the lattice mismatch is smaller (26% between Au(111) and Gd(0001) instead of 34% between Ir(111) and Gd(0001)). The comparison with Pb on Cu(111) drawn already above might be more reasonable. However, for this system no long-range ordered alloy is found, but only typical Pb separations in (2×2) and $(\sqrt{3} \times \sqrt{3})$R30° distances with respect to Cu(111) are found [301].

7.3 Summary

In this chapter, I presented results on the growth of different rare earth metals on Ir(111). For a coverage of 50% ML with respect to Ir(111), Eu forms a flat metallic layer covering the whole Ir surface. The unit cell can be approximated by about (7×7) Eu atoms on (10×10) Ir atoms. The layer shows a high density of triangular defects, which are presumably nuclei of oxidation.
Also Gd forms at 370 K a flat layer on Ir(111). Low temperature LEED reveals a lattice parameter slightly larger than in bulk Gd. The incommensurability with respect to the substrate results in a moiré pattern visible in LEED and STM. In addition to the adsorbed Gd layer, there is a substantial amount of Gd atoms incorporated into the Ir surface, i.e., surface alloying takes place. The alloying can be prevented by low temperature deposition, but at the cost of less order in the Gd layer.
By annealing the Gd layer to higher temperatures, the process of alloying can be followed: Up to 470 K more Gd atoms are incorporated into the surface. Above 570 K the incorporated Gd atoms form a well-ordered surface alloy with a $(\sqrt{3} \times \sqrt{3})$R30° superstructure with respect to Ir(111). At the same temperature, the adsorbed Gd layer starts to intermix with Ir atoms from the substrate. The intermixing results above 770 K in formation of a different surface alloy with a (2×2) superstructure.

CHAPTER 8

Magnetism of Europium Layers

The XMCD data presented in this chapter were taken during a beamtime at the ESRF. I was responsible for the sample preparation together with F. Huttmann and C. Vo-Van, and heavily involved in the XMCD measurements together with P. Ohresser. Additionally, V. Sessi, J. Coraux, N. Rougemaille, and T. Michely took part in the measurements. The data were analyzed by F. Huttmann in Ref. [273] (in particular, he invented the shape anisotropy model) and me, with advice of P. Ohresser.

In Chap. 5, I discussed the structure and electronic properties of intercalated Eu layers. In this context, the DFT calculations presented in Fig. 5.17 predicted a spin-splitting of the Dirac cone. However, for the calculations spontaneous ferromagnetic ordering of the Eu atoms was assumed, which needs to be confirmed by experiments. Therefore, in this chapter the magnetic properties of Eu intercalation layers are investigated. Furthermore, I address the magnetism of Eu/Gr/Eu sandwich structures and of Eu on bare Ir(111). The corresponding structure has already been discussed in Secs. 6.2 and 7.1.

8.1 Intercalated Structures

To investigate the magnetism of Eu intercalation layers in (2×2) and $(\sqrt{3} \times \sqrt{3})$R30° structure, first a fully closed Gr layer was prepared by TPG + CVD each at 1470 K (see Sec. 4.5). Eu was intercalated at 720 K till an intense $(\sqrt{3} \times \sqrt{3})$R30° LEED pattern was visible indicating saturation of the layer. The (2×2) structure was prepared by annealing the same sample several times to temperatures of $1200 - 1240$ K till a clear (2×2) pattern was visible in LEED. The quality of both samples did not deteriorate upon several hours of XMCD measurements as checked afterwards by LEED.

In the following, I first present the method for analysis of the XMCD data in general, and afterwards discuss the magnetic properties characteristic for the (2×2) and $(\sqrt{3}\times\sqrt{3})$R30° intercalation structures separately. Furthermore, I address the strong anisotropy present in the $(\sqrt{3}\times\sqrt{3})$R30° structure in more detail, and draw a comparison to the magnetism of the first stage Eu GIC EuC_6.

Since the magnetism of Eu originates from its 4f electrons, transitions from $3d_{5/2}$ and $3d_{3/2}$ to 4f ($M_{5,4}$ edges) were investigated. Fig. 8.1(a) exemplarily shows the XAS signal across those edges for a fully intercalated $(\sqrt{3}\times\sqrt{3})$R30° Eu layer. The measurement was conducted at $T = 10\,\mathrm{K}$ and $B = 5\,\mathrm{T}$ with left (μ^-) and right (μ^+) circularly polarized X-rays entering under normal incidence. The spectra have been normalized to the average intensity in the pre-edge region between 1100 eV and 1120 eV. Since the spectra for grazing incidence and the (2×2) intercalation structure qualitatively look very similar to the ones in Fig. 8.1(a), they are not shown here.

Fig. 8.1(b) shows the XCMD signal $\mu^+ - \mu^-$ which results from subtraction of the two absorption spectra. In order to deduce the orbital (m_L) and spin (m_S) magnetic moments from the XMCD data, the sum rules of Thole and Carra were applied (compare Sec. 3.2.3). As a reminder, they are given for the Eu $M_{4,5}$ edges by

$$\frac{m_L}{n_\mathrm{h}\mu_\mathrm{B}} = \frac{q}{r} \tag{8.1}$$

$$\frac{m_S}{n_\mathrm{h}\mu_\mathrm{B}} = \frac{5p-3q}{2r} - 6\frac{\langle T_z\rangle}{n_\mathrm{h}} \approx \frac{5p-3q}{2r}. \tag{8.2}$$

As pointed out in Sec. 3.2.3, the dipolar term $\langle T_z\rangle$ is usually neglected for cubic symmetry and vanishing orbital moment. Since both is expected to be the case for Eu in $4f^7$ configuration, I will not distinguish between real and effective spin moments in the following. Nevertheless, I emphasize that this is only an approximation and small contributions from this term cannot be excluded.

For normalization, the integral r over the polarization-averaged absorption cross section $\frac{1}{2}(\mu^+ + \mu^-)$ was used. The corresponding spectrum is shown in Fig. 8.1(c). As discussed in Sec. 3.2.3, in general for rare earths the isotropic XAS spectrum has to be taken into account, too [244]. Therefore, also data at room temperature without magnetic field were recorded to ensure a non-magnetic state. However, in contrast to Ho discussed in Ref. [244], the isotropic spectrum does not differ from the polarization-averaged one in the case of Eu. Therefore, it has been neglected here in order to avoid possible systematic errors that result from averaging spectra taken under different conditions.

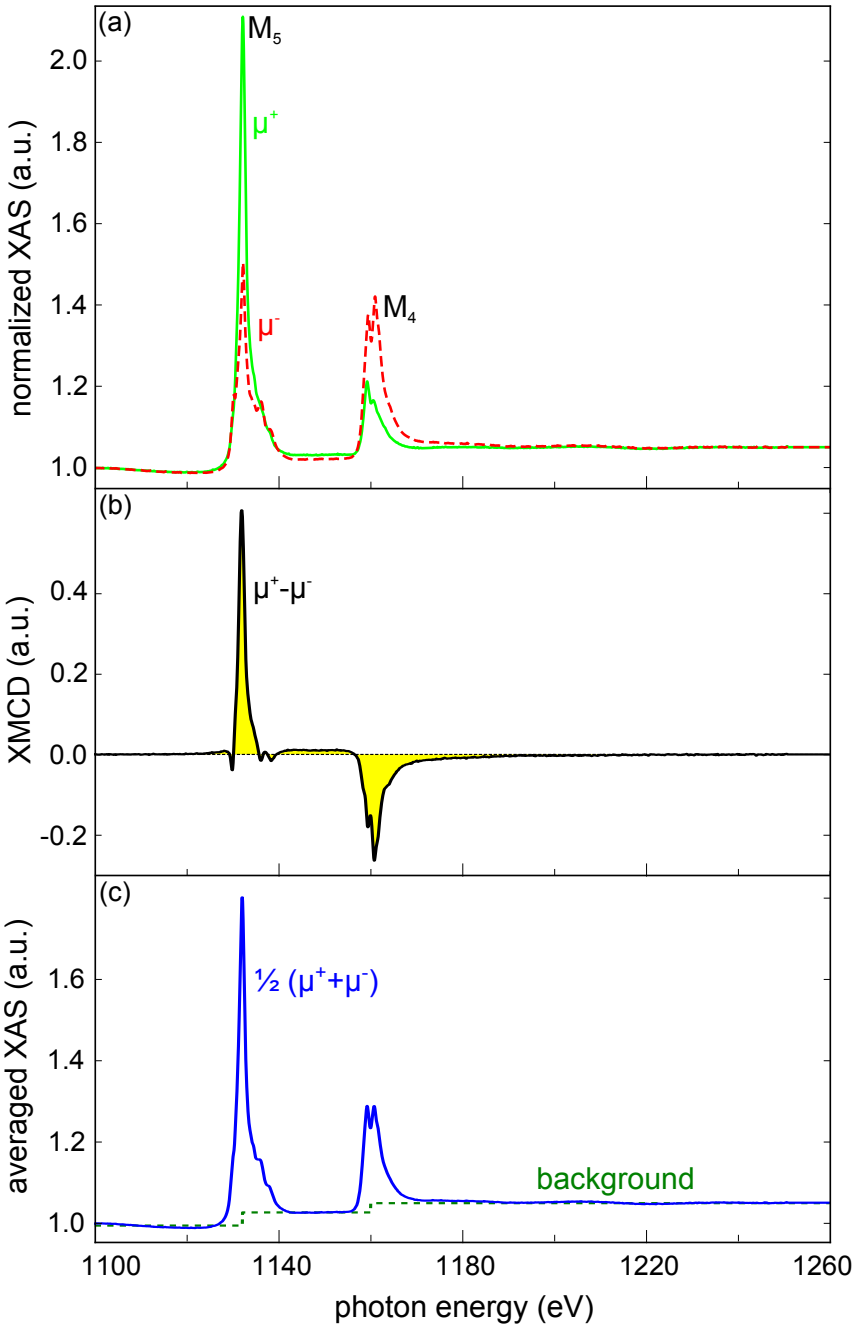

Figure 8.1: (a) Normalized XAS signal at 10 K and 5 T for right (μ^+, solid green line) and left (μ^-, dashed red line) circularly polarized X-rays entering under normal incidence. (b) Corresponding XMCD signal $\mu^+ - \mu^-$. (c) Polarization-averaged XAS spectrum $\frac{1}{2}(\mu^+ + \mu^-)$ (blue solid line) with a step-like continuum background (green dashed line).

The polarization-averaged spectrum is close to the expected one for divalent Eu shown in Ref. [313], but clearly distinguishable from the one of Eu^{3+} in the same reference. Hence, the higher oxidation state can be excluded in the present case.

In order to separate the $M_{4,5}$ contributions from the continuum, a step-like function as depicted in Fig. 8.1(c) has been subtracted. The height of the plateaus was fitted in the regions before, between and after the edges. For the $(\sqrt{3} \times \sqrt{3})$R30° structure the ratio of the step heights at the M_5 and M_4 edges (*branching ratio*) agrees within 10% with the theoretically expected value of 3:2 resulting from the degeneracy of the $3d_{5/2}$ and $3d_{3/2}$ orbitals. However, the branching ratio varies for unknown reasons between 1.0 and 2.8 for other structures investigated here. I only note that also the $L_{2,3}$ branching ratio in transition metals clusters has been found to vary depending on the cluster size, which has been attributed to a size dependent screening of Coulomb interactions [314].

	$m_S(\mu_B)$		$\chi(\mu_B/T)$	
sample	0°	60°	0°	60°
(2×2)	4.9	5.3	1.2	1.5
$(\sqrt{3} \times \sqrt{3})$R30°	6.3	6.8	6.2	24

Table 8.1: Spin moment m_S per Eu atom derived from the sum rules with $n_h = 7$, and zero-field susceptibilities χ for intercalated layers of different density. The data were taken under normal (0°) and grazing (60°) incidence at 10 K and 5 T. The relative errors were estimated to 10%.

By applying the orbital sum rule to the XMCD spectra for normal and grazing incidence, m_L is found to be zero for both structures within the experimental errors. This implies that Eu is present in the same half-filled $4f^7$ configuration as in bulk. Knowing that, the spin moments listed in Tab. 8.1 are specified per Eu atom using $n_h = 7$. I note that data for incidence angles of 20° and 40° (not shown here) yield consistent results.

To learn more about the magnetic behavior, magnetization *versus* field loops were measured. They are obtained by normalizing the XAS signal measured at the Eu M_5 edge to a pre-edge value in dependence on the magnetic field. The loops for normal and grazing incidence are shown in Fig. 8.2 for a fully intercalated $(\sqrt{3} \times \sqrt{3})$R30° Eu layer (squares) and a saturated (2×2) Eu layer (circles). As there is no hysteresis, the loops were averaged over increasing and decreasing field direction. Furthermore, the data were symmetrized, i.e., the magnetization $M(B)$ was replaced by $\frac{1}{2}[M(B) - M(-B)]$, since $M(-B) = -M(B)$ should be applicable. Each curve is scaled using the corresponding spin moment per Eu atom at 5 T from Tab. 8.1.

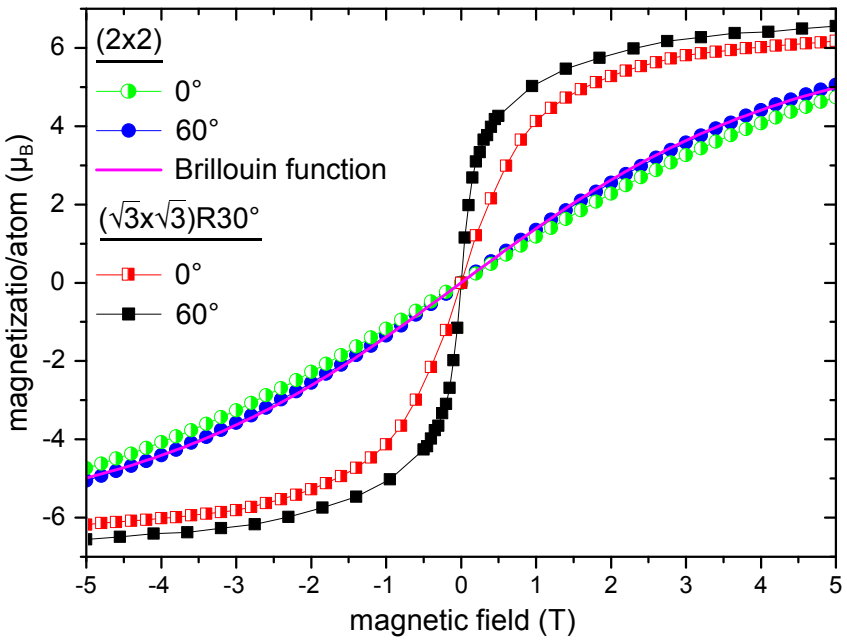

Figure 8.2: Magnetization loops for a fully intercalated $(\sqrt{3} \times \sqrt{3})$R30° Eu layer (squares) and a (2×2) Eu layer (circles) at 10 K for different normal (half filled) and grazing (solid) incidence. Each curve is scaled to the corresponding spin moment per Eu atom at 5 T. The magenta line is a Brillouin function for $J = \frac{7}{2}$ at $T = 10\,\mathrm{K}$ describing paramagnetic behavior.

As a characteristic quantity the zero-field susceptibility was determined by fitting the curves linearly around $B = 0$. I note that this method presumably underestimates the susceptibility due to the limited field resolution. Therefore, the values listed in Tab. 8.1 should be interpreted as lower limits for the zero-field susceptibility.

Magnetism of the (2×2) Intercalation Structure

First, I address the measurements concerning the intercalated (2×2) structure. The magnetization curves show an almost linear behavior with a low zero-field susceptibility of about $1.4\,\mu_\mathrm{B}/\mathrm{T}$ and do not saturate at 5 T. The slightly flatter magnetization curve for normal compared to grazing incidence points to a weak in-plane anisotropy. The flat and rather isotropic magnetization behavior is indicative for a paramagnetic system. To confirm this hypothesis, I recall that the field dependent magnetization $M(B)$ per atom for a paramagnet at a temperature T is given by the Brillouin function

$$M(B) = g\mu_\mathrm{B} J \left(\frac{2J+1}{2J} \coth\left(\frac{2J+1}{2J} x \right) - \frac{1}{2J} \coth\left(\frac{1}{2J} x \right) \right) \tag{8.3}$$

with $x = \frac{g\mu_B JB}{k_B T}$. J denotes the total angular momentum ($J = \frac{7}{2}$ for $S = \frac{7}{2}$ and $L = 0$) and g is the Landé factor ($g = 2$ for a pure spin moment). The function $M(B)$ is plotted in Fig. 8.2 as magenta line. Comparing the curve to the measured data yields an excellent agreement except for the very slight in-plane anisotropy. This proofs that the intercalated (2×2) structure behaves like an ordinary paramagnet.

To explain this observation, a first idea is that the interatomic Eu distance of 4.92 Å in the (2×2) structure is too large for an effective exchange interaction. However, this consideration is not applicable here, since the magnetic coupling is expected to be mediated by an indirect RKKY interaction, just as for the GIC EuC_6 (compare Sec. 2.2.2). The RKKY interaction is long-range with an oscillatory nature, i.e., it can be ferro- or antiferromagnetic depending on the distance. For reference, we consider the coupling constants for several atomic distances occurring in EuC_6 [31], which are listed in Tab. 8.2. For that system, the transition between ferro- and antiferromagnetic coupling indeed occurs around the interatomic distance present in the (2×2) structure.

distance	d (Å)	J (K)
$(\sqrt{3} \times \sqrt{3})$R30° NN	4.26	-0.5
(2×2) NN	4.92	?
interlayer NN	5.47	+0.1
$(\sqrt{3} \times \sqrt{3})$R30° NNN	7.38	+0.4

Table 8.2: Coupling constants J for different distances d occurring in the Eu GIC EuC_6. Positive (negative) values correspond to ferromagnetic (antiferromagnetic) coupling.

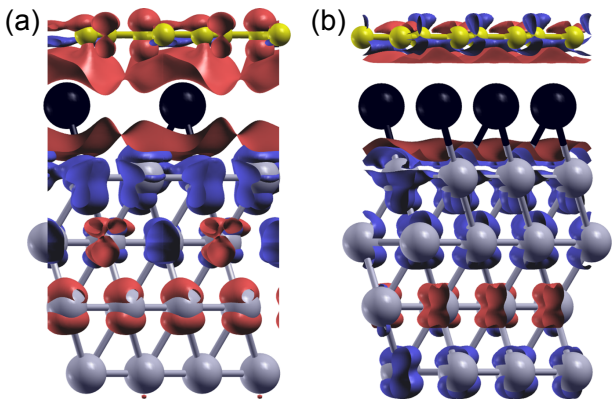

Figure 8.3: Spin densities $m_S(r)$ for Eu intercalated Gr on Ir(111). (a) (2×2) structure. (b) $(\sqrt{3} \times \sqrt{3})$R30° structure. Isosurfaces with $|m_S(r)| = 0.001\,\mathrm{e/Å^3}$ are shown. The majority spin isosurface ($m_S > 0$) is shown in red, the minority one ($m_S < 0$) in blue.

However, such a comparison neglects the Ir substrate, through which also a coupling could be mediated. To determine the relevance of the substrate we calculated the spin densities shown in Fig. 8.3 by DFT. For the (2×2) structure in Fig. 8.3(a), a substantial polarization of the surface Ir atoms is evident (blue isosurfaces). The moments are coupled antiferromagnetically to the intercalated Eu atoms (red isosurfaces). The induced moment per Ir atom exceeds the one per C atom by one order of magnitude (compare Tab. 8.3). In the second Ir layer, an alternating spin moment is induced, which averages over the whole layer to a small value of $-0.003\,\mu_B$ per atom.

layer	(2×2)	$(\sqrt{3} \times \sqrt{3})$R30°
Gr	0.001	-0.001
1^{st} Ir	-0.010	-0.017
2^{nd} Ir	-0.003	-0.012

Table 8.3: Magnetic moments (in units of μ_B per atom) induced in the indicated layers. The values are derived from DFT for both intercalation structures.

The fact that the induced moments in the Ir layer are substantially larger than in the Gr layer leads to the conclusion that the RKKY interaction is predominantly mediated by the Ir substrate. Thus, the present situation strongly differs from the one in EuC_6 so that a simple comparison between both systems cannot be drawn. In order to determine the oscillation period of the RKKY interaction mediated by the Ir substrate, one would need to establish a well defined Fermi wave vector, but this is out of scope of the present DFT calculations.

Magnetism of the $(\sqrt{3} \times \sqrt{3})$R30° Intercalation Structure

In contrast to the (2×2) intercalation structure, the $(\sqrt{3} \times \sqrt{3})$R30° layer is almost saturated at 5 T. The saturation value is close to the $7\,\mu_B$ expected for the $4f^7$ configuration. Moreover, the zero-field susceptibility of $6.2\,\mu_B$/T ($24\,\mu_B$/T) for normal (grazing) incidence is substantially higher than for the paramagnetic (2×2) structure. These observations yield evidence for a significant ferromagnetic coupling.

When looking once more at Tab. 8.3, it becomes obvious that the Ir moments induced by the $(\sqrt{3} \times \sqrt{3})$R30° structure are larger by a factor of about 3 than for the (2×2) case. This originates especially from the homogeneous polarization of the second Ir layer visible in Fig. 8.3(b). From the larger induced moments one can conclude on a stronger RKKY coupling. However, a prediction for the type of RKKY coupling (ferro- or antiferromagnetic) cannot be made on the basis of the present calculations.

As already mentioned above, there is no spontaneous magnetization or hysteresis for the $(\sqrt{3} \times \sqrt{3})$R30° layer. To explain this, we assume that the layer in principle shows long-range ferromagnetic coupling, but the lowest temperature of 10 K attainable at the beamline is still above the Curie temperature T_C. According to the Curie-Weiss law [315]

$$\chi = \frac{C}{T - T_C} \qquad \text{with} \qquad C = \frac{\mu_0 \mu_B^2}{3k_B} g^2 J(J+1) \tag{8.4}$$

the susceptibility of a ferromagnet diverges as T approaches T_C from above, which could explain the high susceptibility without hysteresis if measuring close to, but above T_C. To estimate how far above T_C one has to measure to get the observed susceptibility χ, we calculated the Curie constant C for $J = \frac{7}{2}$. With that, one gets $T - T_C = 0.63\,\mathrm{K}$, i.e., a difference of only 6% at the measurement temperature of $T = 10\,\mathrm{K}$. Although it seems improbable to measure so close to T_C by chance, this explanation is not excluded.

One might argue that according to the Mermin-Wagner theorem there cannot be ferromagnetic order in two dimensions at any temperature [316]. However, it has been shown that a long-range dipolar interaction as observed here is sufficient to change the magnon dispersion such that the Mermin-Wagner theorem is violated [317].

In contrast to the fluctuation dominated scenario of a ferromagnet above T_C, one might also assume fixed units of N ferromagnetically coupled atoms with moments m, whereby adjacent units do not couple (except for a small dipolar interaction always present). This would lead to superparamagnetic behavior, which is described in the isotropic case by the classical Langevin function

$$M(B) = m \left(\coth\left(\frac{NmB}{k_B T}\right) - \frac{k_B T}{NmB} \right). \tag{8.5}$$

Within this model, the zero-field susceptibility $\chi = Nm^2/3k_BT$ is higher by a factor N compared to a paramagnet with isolated moments m. In the present case, the most natural choice for the superparamagnetic entities are the moiré unit cells with $N = 10.32^2/3 \approx 36$ Eu atoms, which would yield a zero-field susceptibility of about $39\,\mu_B/\mathrm{T}$. The value is of the same order as the measured $24\,\mu_B/\mathrm{T}$ as visualized in Fig. 8.4, where the corresponding Langevin function is plotted to the data. Note that the shape of the experimental curve is not reproduced, but this is not surprising, since the Langevin function only describes isotropic superparamagnetism and does not take into account the in-plane anisotropy. Although the model could explain the high zero-field susceptibility, it appears improbable since there is no evidence why the moiré cells should be decoupled from each other.

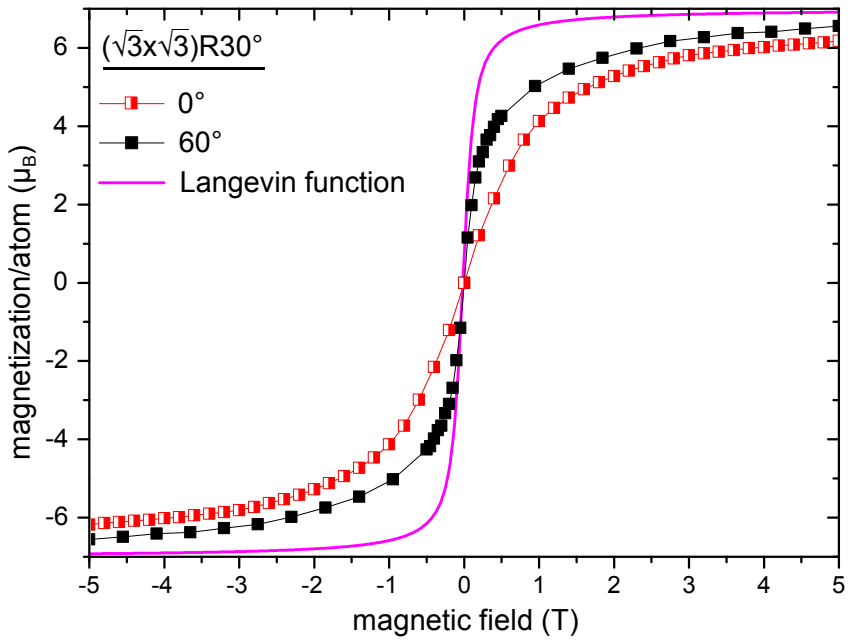

Figure 8.4: Magnetization loops for an intercalated $(\sqrt{3} \times \sqrt{3})$R30° Eu layer under normal (red) and grazing (black) incidence (same data as in Fig. 8.2). The magenta line is a Langevin function for $T = 10\,\mathrm{K}$ with one moiré cell of Eu atoms as magnetic unit (see text).

Anisotropy of the $(\sqrt{3} \times \sqrt{3})$R30° Intercalation Structure

Next, I address the strong anisotropy of the $(\sqrt{3} \times \sqrt{3})$R30° structure visible in the magnetization loops of Fig. 8.2: The higher zero-field susceptibility for grazing incidence points to a preferred in-plane direction of the magnetization. Since m_L and thus also $\vec{L}$ are zero, one can exclude the presence of magnetocrystalline anisotropy, which is caused by spin-orbit coupling and thus proportional to $\vec{L} \cdot \vec{S}$.

In contrast, a monoatomic layer is so exceptionally thin that a strong shape anisotropy can be expected. In the following, its magnitude is estimated by calculating the shape anisotropy energy per Eu atom, from which the response of the magnetization to small external fields can be derived. The corresponding geometry is depicted in Fig. 8.5.

According to basic magnetostatics, the dipole-dipole interaction Hamiltonian of two magnetic moments $\vec{m}_i$, $\vec{m}_j$ separated by a distance vector $\vec{r}_{ij}$ is given by

$$\mathcal{H} = -\frac{\mu_0}{4\pi|\vec{r}_{ij}|^3}\left(3(\vec{m}_i \cdot \vec{e}_{ij})(\vec{m}_j \cdot \vec{e}_{ij}) - \vec{m}_i \cdot \vec{m}_j\right), \tag{8.6}$$

where $\vec{e}_{ij}$ denotes the unit vector $\vec{e}_{ij} = \vec{r}_{ij}/|\vec{r}_{ij}|$. In the following, for simplification ferromagnetic order of the spins is assumed, i.e., all spins are parallelly oriented. With that, one gets $\vec{m}_i = \vec{m}_j = 7\,\mu_\mathrm{B} \cdot \vec{e}_{\vec{M}}$ with the unit vector $\vec{e}_{\vec{M}}$ in the direction of magnetization

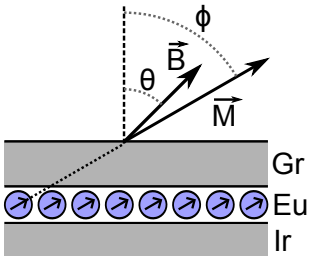

Figure 8.5: Sketch of the situation assumed in the calculation of the shape anisotropy of the $(\sqrt{3} \times \sqrt{3})$R30° intercalation structure. The magnetic field $\vec{B}$ and the magnetization $\vec{M}$ form angles θ and ϕ with the surface normal, respectively.

$\vec{M}$. With that one can calculate the dipole-dipole interaction energy of one Eu atom with all others as a function of the magnetization direction:

$$E_{\text{dipole}} = -\frac{1}{2} \sum_{\vec{r}_{ij} \neq \vec{0}} \frac{\mu_0}{4\pi |\vec{r}_{ij}|^3} (7\,\mu_{\text{B}})^2 \left(3(\vec{e}_{\vec{M}} \cdot \vec{e}_{ij})^2 - 1\right) \tag{8.7}$$

The sum runs over all position vectors of Eu atoms

$$\vec{r}_{ij} = i \begin{pmatrix} 1 \\ 0 \\ 0 \end{pmatrix} + j \begin{pmatrix} -\frac{1}{2} \\ \sqrt{3} \\ 0 \end{pmatrix} \cdot \sqrt{3} \cdot 2.46\,\text{Å}. \tag{8.8}$$

In Eq. 8.7, a factor one half has been added to avoid double counting of pairwise interactions so that E_{dipole} can be properly understood as an anisotropy energy per Eu atom. E_{dipole} has been calculated by F. Huttmann for several magnetization directions using a python script making a numerical summation over about 4×10^6 neighbors. From this one can conclude on the following dependence of E_{dipole} on the angle ϕ between magnetization and surface normal:

$$E_{\text{dipole}} = E_{\text{aniso}} \cdot \left(-\frac{1}{3} + \cos^2 \phi\right) \tag{8.9}$$

with $E_{\text{aniso}} = 281.3\,\mu\text{eV}$ per Eu atom. For comparison, this value lies in the typical range of magnetocrystalline anisotropy energies (for example, 60 µeV for hcp Co [318], or 3000 µeV for $L1_0$ FePt [319]). The total energy in an external magnetic field of modulus B oriented along an angle θ with respect to the surface normal is now given by

$$E_{\text{total}} = E_{\text{aniso}}(-\frac{1}{3} + \cos^2 \phi) - MB\cos(\phi - \theta) \tag{8.10}$$

The intuition of this equation is as follows: To minimize the anisotropy energy resulting from dipolar interactions, the magnetization would prefer to be in-plane ($\phi = 90°$); this is captured by the anisotropy energy (first summand). However, the external field is able to pull the magnetization out of the plane by means of the additional Zeeman energy (second summand). By minimizing E_{total} via setting its derivative to zero, one can calculate ϕ as a function of the magnitude B and the angle θ of the external field:

$$\frac{\partial E_{\text{total}}}{\partial \phi} = -2E_{\text{aniso}} \sin\phi \cos\phi + MB \sin(\phi - \theta) \stackrel{!}{=} 0 \tag{8.11}$$

Within the simple model of an ideal ferromagnet with easy-plane anisotropy, the zero-field susceptibility is always infinite for a non-vanishing in-plane component of the magnetic field ($\theta \neq 0$) since there is no barrier for rotating the spin within the plane. In contrast, for $\theta = 0$ the zero-field susceptibility is finite and can be matched to the normal incidence measurement. One obtains the simple relation

$$\cos\phi = \frac{MB}{2E_{\text{aniso}}}. \tag{8.12}$$

The experimentally observable quantity is the projection of the magnetization on the beam, i.e., $M\cos\phi$ for $\theta = 0$. So, one can calculate the theoretical expectation for the zero-field susceptibility to be

$$\chi_{\text{theo}} = \frac{\partial}{\partial B} M\cos\phi = \frac{M^2}{2E_{\text{aniso}}} = 5.04\,\mu_{\text{B}}/\text{T}. \tag{8.13}$$

This value is close to the experimentally determined zero-field susceptibility under normal incidence of $\chi_{\text{exp}} = 6.2\,\mu_{\text{B}}/\text{T}$, which demonstrates the relevance of the previous calculation. Furthermore, we remember that for simplicity ideal ferromagnetic order was assumed. The model predicts a susceptibility which is *lower* than the experimental value, corresponding to a *higher* anisotropy. If one takes into account that the system is only almost ferromagnetic, this would reduce the expected shape anisotropy and yield an even better agreement with the experiment.

Comparison with the Graphite Intercalation Compound EuC_6

It is tempting to compare the magnetic properties of the $(\sqrt{3} \times \sqrt{3})$R30° intercalation structure with those of the first stage Eu GIC EuC_6 since both have the same in-plane structure (compare Sec. 2.2.2). Therefore, in Fig. 8.6 the first quadrant of the magnetization loops from Fig. 8.2 is shown together with data for EuC_6 adapted from Ref. [159]. Unfortunately, no directly comparable data are available since XMCD measurements can

be performed only up to 60° incidence angle, whereas bulk measurements allow fields exactly in-plane. Furthermore, for normal incidence only data at $T = 16\,\mathrm{K}$ are available.

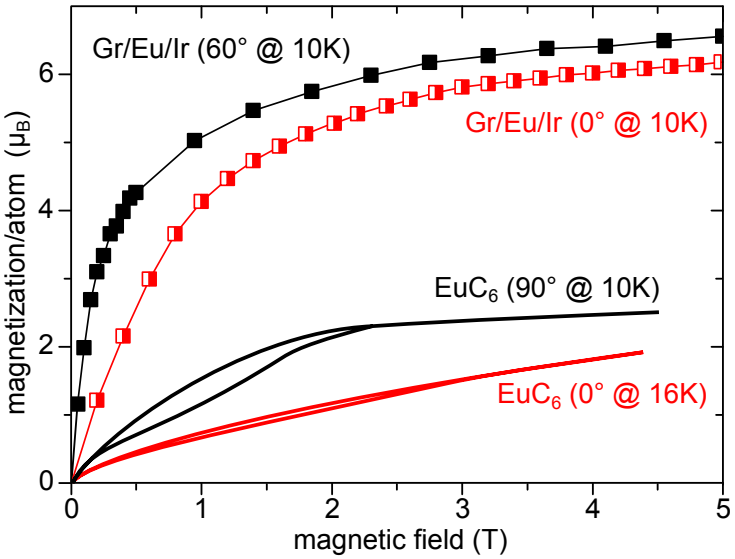

Figure 8.6: Magnetization loops for a fully intercalated $(\sqrt{3}\times\sqrt{3})$R30° Eu layer at the indicated temperatures and incidence angles with respect to the surface normal (same data as in Fig. 8.2). Additionally, corresponding data for EuC_6 taken from Ref. [159] are shown.

Both systems show a pronounced in-plane anisotropy, but beside this similarity the magnetic behavior is very different: Whereas the initial magnetization steeply rises and goes into saturation close to $7\,\mu_B$ for the intercalated monolayer, the magnetization curve of EuC_6 has a much lower zero-field susceptibility and already saturates at about $2.5\,\mu_B$. As described in Sec. 2.2.2, the low zero-field susceptibility is due to an antiferromagnetic 120° spin order, and the saturation corresponds to a ferrimagnetic state at higher fields.
There are two reasons to explain the different magnetic behavior: First, as shown before, the Ir substrate mediates the main part of the RKKY interaction. Second, it has been shown that a small coupling between adjacent Eu layers is an important ingredient to explain the metamagnetic behavior of EuC_6 [31]. This coupling is of course absent in the present system, since it is restricted to a single Eu layer.

8.2 Europium Sandwich Structures

After discussing the magnetism of solely intercalated Eu structures, I now turn over to structures with additional Eu adsorbed on top of Gr. The structural properties of such sandwich layers have already been discussed in Sec. 6.2. For adsorption on the (2×2)

intercalation layer the sample investigated in the previous section was reused, whereas for the $(\sqrt{3} \times \sqrt{3})$R30° a new sample was prepared. On top of both samples an amount of Eu corresponding to a saturated $(\sqrt{3} \times \sqrt{3})$R30° layer (i.e., 33% ML with respect to Gr) was adsorbed at room temperature. LEED shows in both cases intense $(\sqrt{3} \times \sqrt{3})$R30° superstructure spots. To establish the influence of the intercalation layer, moreover a sample with a Eu layer adsorbed to bare Gr was investigated.
During the beamtime, we noticed that for all systems with adsorbed Eu the sharp and intense $(\sqrt{3} \times \sqrt{3})$R30° spots in LEED present after preparation became faint or even invisible after the XMCD measurements, which suggests a contamination of the sample. Since the magnetic properties of the samples did not change during their stay in the XMCD chamber, the degradation must already have taken place during the transport from the preparation chamber. Indeed, the transfer tube between preparation and XMCD chamber only has a pressure of about 2×10^{-9} mbar. The high pressure is due to the fact that samples are transferred from air into the tube using a load-lock without a subsequent bakeout. Thus, the worse pressure is expected to arise mainly from water.
In order to find out which kind of contamination could have happened we have a look at the magnetic properties of the sample. The XAS spectra of all three samples (one is exemplarily shown in Fig. 8.7(a)) are qualitatively identical to the one in Fig. 8.1(a) indicating that Eu is present in a $4f^7$ configuration also after contamination. This is supported by the fact that the orbital moments again vanish within the error of the measurement. The corresponding spin moments and the magnetization curves are shown in Tab. 8.4 and Figs. 8.7(b) - (d), respectively. Since there is no hysteresis, the curves were again averaged over both field ramping directions and are symmetrized with respect to the sign of the magnetic field.

	$m_S(\mu_B)$		$\chi(\mu_B/T)$	
sample	0°	60°	0°	60°
Eu on bare Gr	6.7	7.0	12	77
Eu on (2×2)	6.3	6.5	9.3	69
Eu on $(\sqrt{3} \times \sqrt{3})$R30°	6.3	6.9	9.3	62

Table 8.4: Spin moment m_S per Eu atom derived from the sum rules with $n_h = 7$ and zero-field susceptibilities χ for different Eu sandwich structures. The data were taken under normal and grazing incidence at 10 K and 5 T. The relative errors were estimated to 10%.

First, it is surprising that all three samples show a very similar magnetic behavior independently whether Eu is intercalated or not. This leads to the conclusion that the

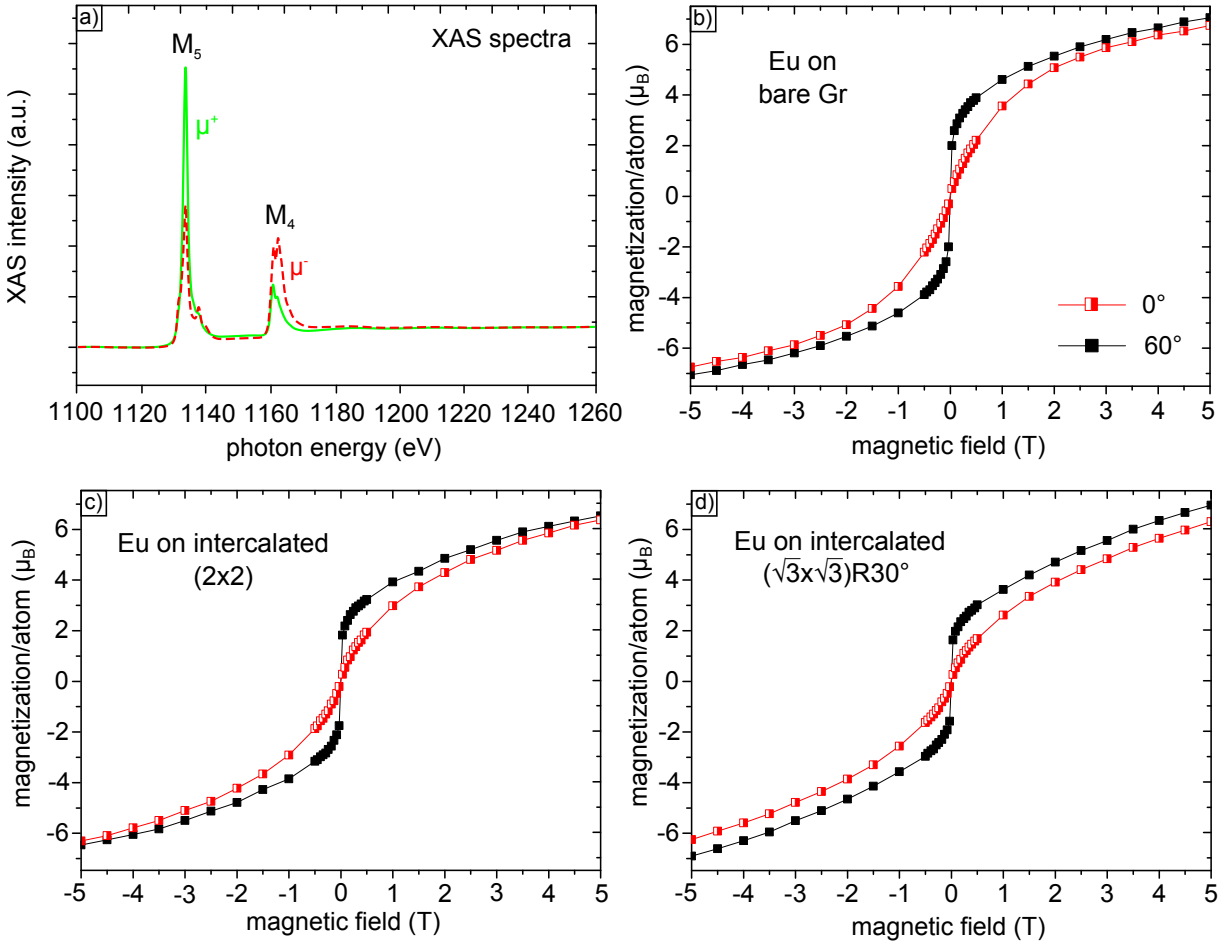

Figure 8.7: (a) (a) Normalized XAS signal at 10 K and 5 T for right (μ^+, solid green line) and left (μ^-, dashed red line) circular polarized X-rays in normal incidence for a saturated Eu layer adsorbed to Gr. (b)-(c) Magnetization loop for Eu adsorbed to bare Gr and two different Eu sandwich structures under normal (red) and grazing (black) incidence.

magnetism is determined by the adsorbed layer, whereas the intercalation layer simply couples to it. Second, all curves go to a saturation value on the order of 7 μ_B demonstrating a substantial magnetic coupling since the saturation in the paramagnetic case was only around 5 μ_B. The only known ferromagnetic Eu compound is EuO, in which Eu also has a $4f^7$ configuration consistent with the XAS spectra discussed above.

In the following, I discuss how a degradation of the adsorbed Eu to EuO might have taken place without the presence of O, which is not a common residual gas in UHV systems because it does not form a wetting layer on the chamber walls. Therefore, I recall that the high pressure in the transfer tube is expected to arise essentially from water. It is known that Eu reacts with water to Eu(III)-hydroxide, which can be thermally decomposed in two steps to dehydrated Eu(III)-oxide [320] according to the equations

$$
\begin{aligned}
2\,\mathrm{Eu} + 6\mathrm{H_2O} &\longrightarrow 2\,\mathrm{Eu(OH)_3} + 3\mathrm{H_2} \\
\mathrm{Eu(OH)_3} &\longrightarrow \mathrm{EuOOH} + \mathrm{H_2O} \quad \text{at } 563\,\mathrm{K} \text{ in air} \\
2\mathrm{EuOOH} &\longrightarrow \mathrm{Eu_2O_3} + \mathrm{H_2O} \quad \text{at } 738\,\mathrm{K} \text{ in air.}
\end{aligned}
$$

However, the sesquioxide Eu_2O_3 does not carry magnetic moments due to the 3+ valence state of Eu ($J = 0$). Unfortunately, there are no data in the literature on the decomposition of Eu(II)-hydroxide, which one would expect to be present here. Nevertheless, it is known that Ba, which is isoelectronic to Eu except for the highly localized 4f electrons, forms Ba(II)-hydroxide upon reaction with water that already decomposes at 373 K in vacuum [321] according to the equations

$$
\begin{aligned}
\mathrm{Ba} + 2\,\mathrm{H_2O} &\longrightarrow \mathrm{Ba(OH)_2} + \mathrm{H_2} \\
\mathrm{Ba(OH)_2} &\longrightarrow 2\mathrm{BaO} + \mathrm{H_2O} \quad \text{at } 373\,\mathrm{K} \text{ in vacuum.}
\end{aligned}
$$

For a single monolayer under UHV conditions, one would expect such a decomposition to occur at much lower temperatures. To get a feeling for this effect, we consider that bulk water boils at atmospheric pressure at 373 K while monolayers of water in UHV evaporate already at 100 K. Therefore, it is likely that Eu got oxidized before the XMCD measurements according to the net reaction

$$\mathrm{Eu} + \mathrm{H_2O} \longrightarrow \mathrm{EuO} + \mathrm{H_2}.$$

In order to estimate the water fluence F to which the Eu layer was exposed, we consider that the samples spent about 10 minutes in a pressure of $p = 2 \cdot 10^{-9}$ mbar, and get

$$F = \frac{10\,\mathrm{min} \cdot 2 \cdot 10^{-9}\,\mathrm{mbar}}{\sqrt{2\pi \cdot 18\,\mathrm{u} \cdot k_\mathrm{B} \cdot 300\,\mathrm{K}}} \cdot (2.46\,\text{Å})^2 \cdot \frac{2}{\sqrt{3}} \approx 30\%\ \text{ML Gr.} \tag{8.14}$$

Considering that a saturated $(\sqrt{3} \times \sqrt{3})\mathrm{R}30°$ corresponds only to 33% ML with respect to Gr, it is plausible that a substantial part of the Eu on top has been oxidized. Since the structure of the contaminated samples was not investigated, it is speculative to discuss the magnetic properties in more detail. However, I address some general observations: As shown by Klinkhammer *et al.*, EuO can be grown on Gr by reactive MBE resulting in ferromagnetic grains that saturate at around 100 mT at 44 K [50]. The presence of such EuO grains could explain the high zero-field susceptibilities listed in Tab. 8.4, which appear as jumps of about one quarter of the saturation value in Figs. 8.7(b) - (d). For the comparably low coverages investigated here the grains are expected to be very small, which presumably results in superparamagnetic behavior. This would explain the lack

of any hysteresis. The in-plane anisotropy can easily be interpreted as shape anisotropy, since the grains grown in Ref. [50] have a very flat aspect ratio.

Nevertheless, the shape of the magnetization curves is not yet understood. Although the zero-field susceptibility is substantially higher for the sandwich structures than for the $(\sqrt{3} \times \sqrt{3})$R30° intercalation layer in Fig. 8.2, the magnetization saturates at higher fields. An explanation could be that the system possesses a non-collinear spin structure - for example, a spin spiral like in bulk Eu (compare Sec. 2.2.1). Such a structure has a component that can be easily aligned in small magnetic fields, whereas the spins become parallel only upon applying high fields. A non-collinear spin structure is actually not expected for the ferromagnet EuO, but it could be related to the remaining non-oxidized parts of the sample.

8.3 Europium on Iridium

In the last part of this chapter, I discuss the magnetism of a single monolayer of Eu adsorbed to Ir(111). Therefore, 50% ML Eu with respect to Ir(111) corresponding to the saturation coverage determined in Sec. 7.1 were deposited on a bare Ir substrate at room temperature. While the LEED pattern was identical to the one shown in Fig. 7.1 after preparation, it has substantially changed after the XMCD measurements and resembled more the one of EuO(111) on Ir(111) (see Chap. 10). Therefore, it is probable that the same surface contamination as in the previous section has happened.

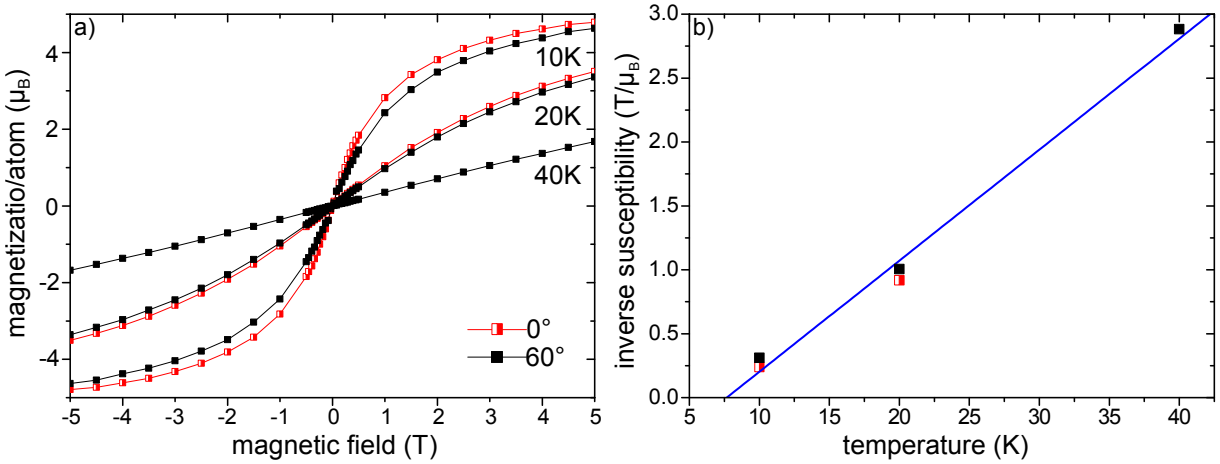

Figure 8.8: (a) Magnetization loops for a monolayer of Eu on Ir(111) at the indicated temperatures under normal (red, not measured at 40 K) and grazing (black) incidence. (b) Inverse zero-field susceptibility for the curves in (a). The blue line is a linear fit to the data.

The spin moment of about $4.7\,\mu_B$ derived from the sum rules is much smaller than for a saturated $4f^7$ state and close to the $5\,\mu_B$ for a $J = 7/2$ paramagnet at 5T and 10 K. However, the zero-field susceptibility of about $4\mu_B/T$ is substantially higher than the $1.4\,\mu_B$/T for a $J = 7/2$ paramagnet at 10 K. This could be explained by ferrimagnetic contributions, causing a higher zero-field susceptibility than a paramagnet, but a lower saturation value. However, there is no further evidence for this explanation.
For this sample, also temperature-dependent magnetization loops have been measured showing that the zero-field susceptibility declines with increasing temperature. If one considers the system to be a ferro- or ferrimagnet above its Curie temperature following the Curie-Weiss law $\chi \propto \frac{1}{T-T_C}$, plotting of $\chi^{-1}(T)$ should yield a linear dependence. Indeed, this is approximately the case and fitting yields a Curie temperature of $T_C \approx 8$ K. Even though, the result should be taken with care without knowing the structure and composition of the sample in detail.
In contrast to all other systems investigated up to now, Eu on Ir(111) shows a slight out-of-plane anisotropy. This means that other anisotropies have to overcompensate the shape anisotropy, but for an analysis more structural details would be needed.

8.4 Summary

In this chapter, first the magnetic properties of two intercalation layers with different density were investigated. They show fundamentally different magnetic behaviors: Whereas the (2×2) layer is paramagnetic, the $(\sqrt{3} \times \sqrt{3})$R30° layer shows a substantial magnetic coupling and is interpreted to be a ferromagnet slightly above its Curie temperature. Its strong in-plane anisotropy is shown to arise essentially from the extremely low aspect ratio of the Eu layer. The magnetic behavior of the $(\sqrt{3} \times \sqrt{3})$R30° layer strongly deviates from its bulk counterpart EuC_6, indicating the importance of the Ir substrate and the restriction to a single layer.
All samples with Eu adsorbed on top of Gr and with(out) an additional intercalation layer were deteriorated by contamination during the sample transfer to the XMCD chamber. The magnetism of those samples is dominated by the adsorbed layer, which shows a notable magnetic coupling. This is probably related to the presence of ferromagnetic EuO originating from the reaction of Eu with the water background pressure. However, since neither the extent of the contamination nor the film morphology is known, an interpretation of the magnetic properties stays speculative. The same holds for the magnetism of a Eu layer adsorbed to Ir(111).

CHAPTER 9

Magnetism of Metal Clusters on Graphene

Parts of Secs. 9.1 and 9.2 are published in Appl. Phys. Lett. ***99*** *142504 (2011) [322]. The XMCD data were taken during two beamtimes at the ESRF. I was responsible for the sample preparation together with F. Huttmann and C. Vo-Van, and heavily involved in the XMCD measurements together with P. Ohresser. Additionally, V. Sessi, J. Coraux, O. Fruchart, N. Rougemaille, and T. Michely took part in the measurements. The data were analyzed by F. Huttmann in Ref. [273], P. Ohresser, C. Vo-Van, and me.*

In this chapter, the magnetic properties of metal clusters on Gr are investigated. First, I analyze Co clusters with different sizes. Afterwards, I figure out whether also Rh clusters show ferromagnetism, and conclude with the growth of Eu clusters.
Deposited amounts are given in monolayers with respect to Ir(111). Thereby, 0.1ML correspond to well-ordered clusters with an average size of about 9 atoms. The clusters are termed as X_N with the chemical element X and the cluster size N in atoms.

9.1 Moiré-Templated Cobalt Clusters

First, I investigate the magnetism of Co clusters seeded by small Pt nuclei. Therefore, 0.13 ML Pt followed by 0.25 ML Co were deposited onto a fully coalesced Gr sheet which was prepared by a TPG step at 1470 K followed by CVD at 1170 K (see Sec. 4.5 for details). The deposited amount corresponds to well-ordered $Pt_{11}Co_{22}$ clusters. An STM image of the same sample prepared at ATHENE is shown in Fig. 9.1(a). Besides the well-ordered cluster lattice, a significant amount of coalesced clusters is present. Counting the clusters in a larger STM image (not shown here) reveals that on average 28% of the clusters are coalesced. This results in a mean cluster size of $Pt_{15}Co_{28}$.

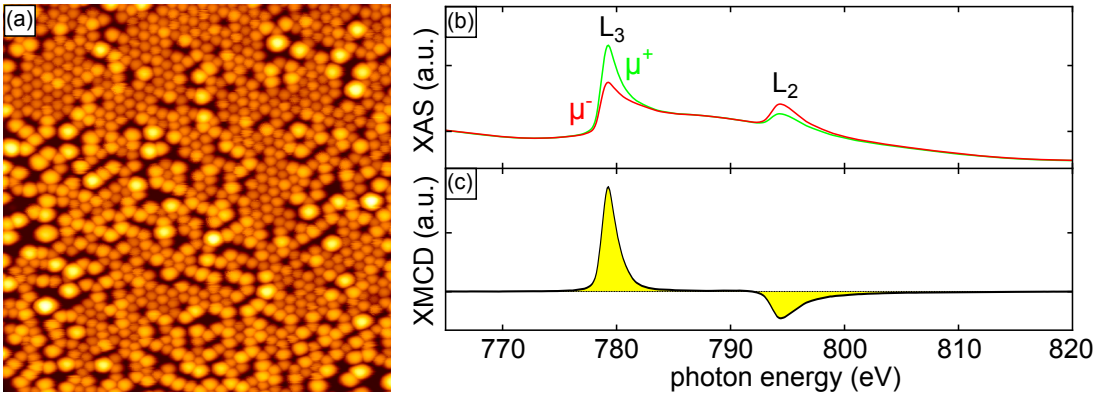

Figure 9.1: (a) STM topograph (80 nm × 80 nm) of $Pt_{15}Co_{28}$ clusters on Gr. (b) XAS signal at 10 K and 5 T under normal incidence across the Co $L_{2,3}$ edges for left (μ^-) and right (μ^+) circularly polarized light. (c) Corresponding XMCD spectrum.

Fig. 9.1(b) shows two XAS spectra measured at 10 K and 5 T under normal incidence across the Co $L_{2,3}$ edges for left (μ^-) and right (μ^+) circularly polarized light. The spectra look as expected for Co [182] and do not show any sign of oxidation or other contaminations. Subtracting the XAS signals measured for opposite magnetic fields or polarizations yields the XMCD signal shown in Fig. 9.1(c).

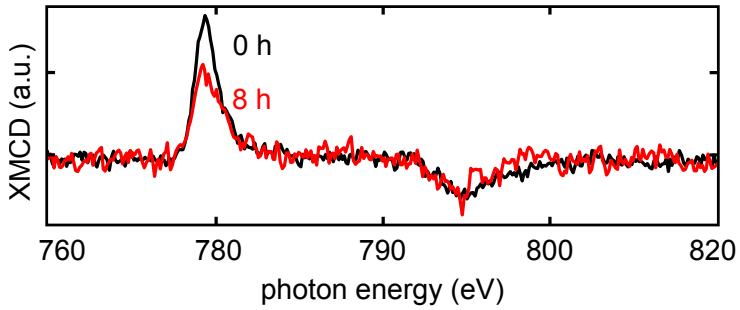

Figure 9.2: Loss of the initial XMCD intensity (black) after 8 h X-irradation (red), here exemplarily shown for a sample with Ir_4Co_8 clusters.

At this point, I remark that we have noticed a decrease of the XMCD signal over time during the measurements. As illustrated in Fig. 9.2, the XMCD signal dropped during 8 h irradiation by about 40%. Surfaces measured after the same waiting time, but not exposed to the beam, did not show any reduction of intensity, which excludes surface contaminations. Consequently, the damage has to be induced by the beam. Such a degradation is common for fragile magnetic species [323, 324], but usually not observed for metallic clusters. We surmise that the X-ray beam promotes a decomposition of Gr

by the clusters, similar to what happens at elevated temperatures [325]. A resulting C enrichment of the clusters might be liable for the reduction of the XMCD signal. To prevent this effect, we reduced the exposure time, changed the beam position on the sample during the measurements, and shuttered the beam if not used.
From the data in Fig. 9.1(b) and (c), the magnetic moments of the $Pt_{15}Co_{28}$ clusters can be determined by applying the sum rules of Thole and Carra [240, 241] for the Co $L_{2,3}$ edges (compare Sec. 3.2.3), which are in the present case

$$\frac{m_L}{n_\mathrm{h}\mu_\mathrm{B}} = \frac{2}{3}\frac{q}{r} \tag{9.1}$$

$$\frac{m_S}{n_\mathrm{h}\mu_\mathrm{B}} = \frac{3p-2q}{r} - 7\frac{\langle T_z\rangle}{n_\mathrm{h}} \approx \frac{3p-2q}{r}. \tag{9.2}$$

The dipolar term $\langle T_z\rangle$ is neglected in the following, since it has been shown to be small for bulk Co [326]. For the number of holes in the 3d shell $n_\mathrm{h} = 2.5$ is used, just a for bulk Co [182]. For normalization, the integral over the polarization averaged absorption cross section is used. From the sum rules we derive a spin moment of $m_S = (1.5 \pm 0.2)\,\mu_\mathrm{B}$ per atom which is comparable to the bulk value of $1.62\,\mu_\mathrm{B}$ [182]. The good agreement indicates that (i) neglecting $\langle T_z\rangle$ is reasonable, (ii) the number of 3d holes is close to the bulk value, and (iii) a possible charge transfer between Co, Pt, and Gr does not significantly affect the magnetism of Co. On the contrary, the ratio between orbital and spin moment of $m_L/m_S = 0.15 \pm 0.04$ is larger than the bulk value of 0.095 [182]. Such an enhancement is typical for small-size objects, and arises from the local loss of symmetry as described in Sec. 2.3. The results are independent on the incident angle, indicating the absence of magnetic anisotropy in the clusters.

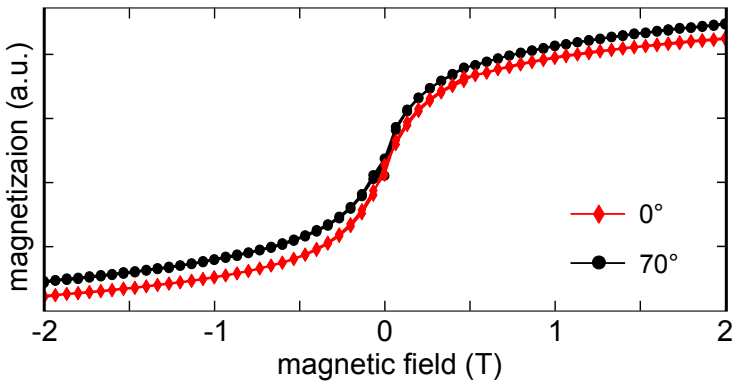

Figure 9.3: Magnetization loops for $Pt_{15}Co_{28}$ clusters at 10 K under normal (red rhomboids) and grazing (black dots) incidence. The curves are vertically shifted for better visibility.

To investigate this in more detail, the magnetization loops under normal and grazing incidence shown in Fig. 9.3 were measured. The curves do not show any hysteresis, have a high zero-field susceptibility, and are almost saturated at 5 T, all hinting at superparamagnetic behavior. Furthermore, the curves are almost isotropic. Within the Bruno model [327], that links the magnetic anisotropy energy with the anisotropy of the orbital moment, this is consistent with the negligible anisotropy of m_L found above.

The lack of anisotropy contrasts with other low-dimensional magnetic systems on metal surfaces [328–330]. Consequently, it has to be a peculiarity of the Gr substrate. Indeed, it is known that the interaction between clusters and Gr is weak, since they can be easily picked up with an STM tip during imaging. Furthermore, the clusters become mobile and Smoluchowski ripen during annealing at temperatures which are low compared to the typical onset of bulk mobility [40]. Thus, it is plausible that the Gr substrate does not induce a shape or interface anisotropy because of the weak interaction.

To establish whether the previous findings depend on the choice of the magnetic material, also $Pt_{12}Fe_{22}$ clusters were investigated. To apply the sum rules, $n_h = 3.39$ was used as in bulk Fe [182]. Again, the dipolar term $\langle T_z \rangle$ is neglected. We find a spin moment of $(2.0 \pm 0.2)\,\mu_B$ in excellent agreement with the Fe bulk value of $1.98\,\mu_B$ [182]. Just as for $Pt_{15}Co_{28}$ clusters, also here the ratio m_L/m_S has an enhanced value of 0.13 ± 0.04 compared to the 0.043 in bulk Fe [182].

Moreover, $Ir_{13}Co_{26}$ clusters were investigated to figure out the influence of the seeding material. We again find a high value of 0.20 ± 0.03 for m_L/m_S, but a reduced spin moment of only $(1.0 \pm 0.2)\,\mu_B$. However, since this measurement was performed before we noticed the cluster damage by the beam mentioned above, it cannot be excluded that the low moment arises from that degradation. Consistently with the $Pt_{15}Co_{28}$ clusters, both $Pt_{12}Fe_{22}$ and $Ir_{13}Co_{26}$ clusters show almost no anisotropy. To summarize, the magnetic properties of seeded clusters on Gr seem to depend neither strongly on the seeding material nor the magnetic material.

The Superparamagnetic Entity

To get more insight to the magnetization process, magnetization loops for $Pt_{15}Co_{28}$ clusters were measured at different temperatures. The corresponding data are shown in Fig. 9.4. Consistent with the previous results, there is no hysteresis at all temperatures. A decrease of the zero-field susceptibility with increasing temperature is found as expected for superparamagnetic behavior. Given the close-to-isotropic magnetic properties, the magnetization loops were fitted by a modified Langevin function

$$M(B) = M_\mathrm{s}\left(\coth\left(\frac{mB}{k_\mathrm{B}T}\right) - \frac{k_\mathrm{B}T}{mB}\right) + \frac{\chi_\mathrm{add}}{\mu_0}B \tag{9.3}$$

with the saturation moment M_s and the moment m of the magnetic entity (compare Eq. 8.3). In principle, a sum of Langevin functions would have to be used due to different particle sizes, but since the size distribution is Poisson-like and thus very narrow, a single Langevin function is appropriate. The non-vanishing susceptibility (linear slope) dominating the magnetization loops above $\pm 2\,\mathrm{T}$ was taken into account by the additional field-proportional term $\frac{\chi_\mathrm{add}}{\mu_0}$, which will be discussed below.

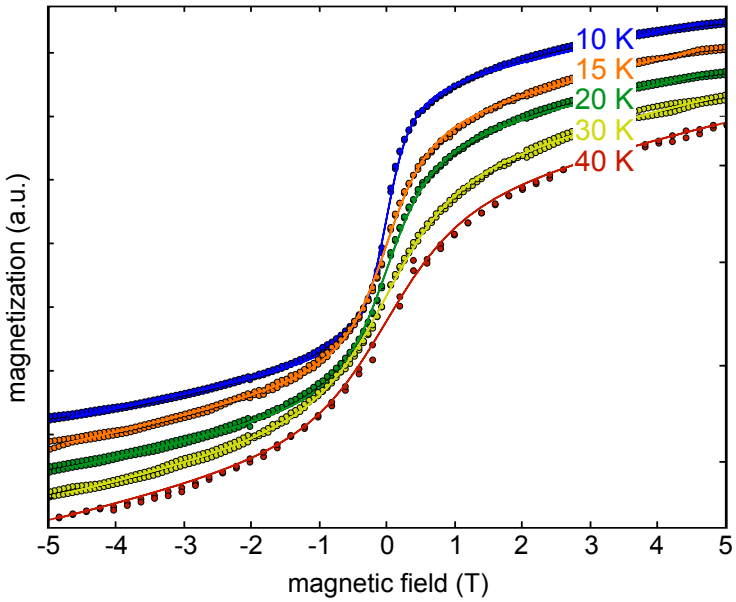

Figure 9.4: Magnetization loops under normal incidence for $Pt_{15}Co_{28}$ clusters at the indicated temperatures. The solid lines are modified Langevin fits according to Eq. 9.3. The curves are vertically shifted for better visibility.

The parameters resulting from the Langevin fits are listed in Tab. 9.1. Since we did not take full XMCD spectra for each temperature, the magnetization is given in arbitrary units. Consequently, the absolute values of M_s and χ_add/μ_0 do not contain physical information. Nevertheless, the low scattering of both shows that (i) the pure Langevin part is always saturated at 5 T, and (ii) the additional slope does not depend on temperature hinting at an origin different from superparamagnetism. A probable explanation is that the spins within the clusters are not ideally ferromagnetically coupled, but favor a non-collinear arrangement. Consequently, the magnetization process occurs in two steps: First, the superspin of each cluster gets aligned with the field, and second, the canted spins within the clusters become collinear. Such effects are known from the literature. For

T (K)	M_s (a.u.)	χ_{add}/μ_0 (a.u./T)	m (μ_B)
10	0.722	0.066	107.5
15	0.709	0.072	87.9
20	0.740	0.065	109.7
30	0.750	0.068	103.8
40	0.725	0.072	125.6
mean	0.73	0.069	107
error	0.01	0.001	6

Table 9.1: Saturation magnetization M_s, additional slope χ_{add}/μ_0, and moment of the magnetic entity m derived from modified Langevin fits of the magnetization loops shown in Fig. 9.3.

example, a hedgehog-like spin structure has been found for nanometer-sized Co particles dispersed a polymer [331, 332], consistent with micromagnetic calculations [333].

The moment of the magnetic entity m was found to be independent of the temperature within errors, confirming the relevance of the fitting function. We determine an average value of $m = (107 \pm 6)\,\mu_B$. Dividing this by the number of Co atoms per cluster (N=28) yields a magnetic moment of $(3.8 \pm 0.2)\,\mu_B$ per atom. This value is unphysically high for Co, even in low coordination [329], and largely exceeds that derived from the sum rules. Therefore, it indicates that the magnetic entity is substantially larger than a single cluster. There are two different approaches to an explanation: First, one could imagine that there are correlated blocks of clusters, i.e., coupling between the clusters is present. Such a coupling could be either direct dipolar exchange between neighboring clusters, or indirectly mediated by the Gr charge carriers via RKKY interaction. However, this explanation seems questionable since an in-plane coupling should be accompanied by an in-plane shape anisotropy (compare Sec. 8.1), which is not observed here.

Therefore, I turn to the second hypothesis that the large magnetic entity results from a larger average cluster size than expected. Since the evaporator calibration by STM has only a small error and the deposition rate is highly stable, we trust in the deposited amounts. However, it might be possible that the effect of coalescence was underestimated. Although the cluster size of $Pt_{15}Co_{28}$ already includes coalescence, I note that it was determined from an STM picture taken at ATHENE. It is known that small Pt clusters on Gr/Ir(111) become mobile and coalesce upon exposure to CO [334]. Since the UHV chamber at ID08 is less efficiently pumped than the one at ATHENE, the CO background pressure is expected to be higher at ID08. Therefore, a larger degree of coalescence is likely. Furthermore, also for the sample investigated at ATHENE it cannot be excluded

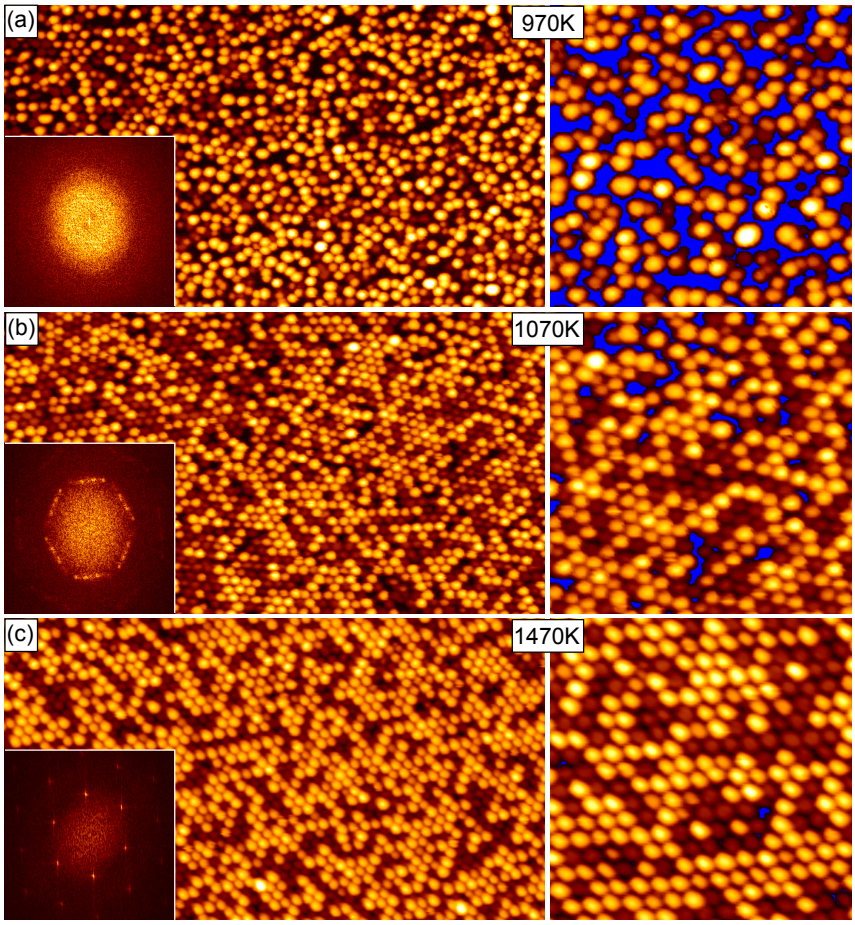

Figure 9.5: Deposition of 0.30 ML Ir on Gr grown using different CVD temperatures of (a) 970 K, (b) 1070 K, and (c) 1470 K. The image sizes are (130 nm × 75 nm) and (45 nm × 45 nm) for the left and right images, respectively. The Fourier transforms of the left images are shown as insets. Vacancies in the cluster lattice are marked blue in the right images.

that sample regions with a larger amount of coalescence are present. Unfortunately, the quality of the cluster preparation at ID08 could not checked by STM due to technical problems. So, the puzzle of the large magnetic entity cannot be solved for this preparation.

Optimization of the Cluster Lattice

To reduce the uncertainties caused by an unknown amount of coalescence, we performed during a second beamtime three changes to enhance the quality of the cluster lattice:

(i) The CVD step of the Gr growth was performed at 1470 K instead of 1170 K.

(ii) The size of the seeds was increased from 0.13 ML to 0.20 ML.

(iii) The seeding material was changed from Pt to Ir.

The increase of the CVD temperature T_{CVD} was made to improve the regularity of the seeding cluster lattice. To illustrate this effect, we have a look at Fig. 9.5. It is obvious that the quaility of the cluster lattice substantially improves with increasing T_{CVD}: For the lowest temperature in Fig. 9.5(a) there is almost no rotational order as seen best in the corresponding Fourier transform. The lattice contains many coalesced clusters as well as vacancies (highlighted in blue). At $T_{\mathrm{CVD}} = 1070\,\mathrm{K}$, the clusters are well-oriented along different rotational domains of the moiré pattern, but still a substantial amount of vacancies is present. Only at the highest growth temperature of $T_{\mathrm{CVD}} = 1470\,\mathrm{K}$ the cluster lattice becomes nearly perfect.

Without performing a detailed analysis, we briefly discuss this relation: It is well known that the orientational alignment of Gr with respect to Ir becomes worse at lower T_{CVD} [335]. To connect this effect to the cluster lattice, I recall that the moiré unit cell reaches its maximum size for parallel alignment between Gr and Ir, and shrinks for increasing misorientation angles. Accordingly, also the hcp regions, in which the clusters bind to the substrate, shrink with decreasing T_{CVD}, which presumably leads to worse sticking of the clusters. With that, the larger share of coalescence and vacancies at lower T_{CVD} can be explained. In addition, also the higher density of defects and rotational domain boundaries at lower growth temperatures disturbs the cluster lattice.

The size of the seeds was increased and the seeding material changed because it is known that larger clusters as well as clusters made from Ir instead of Pt are more stable against annealing at elevated temperatures [40]. Therefore, it is reasonable that they are also more resistant towards ripening upon Co deposition.

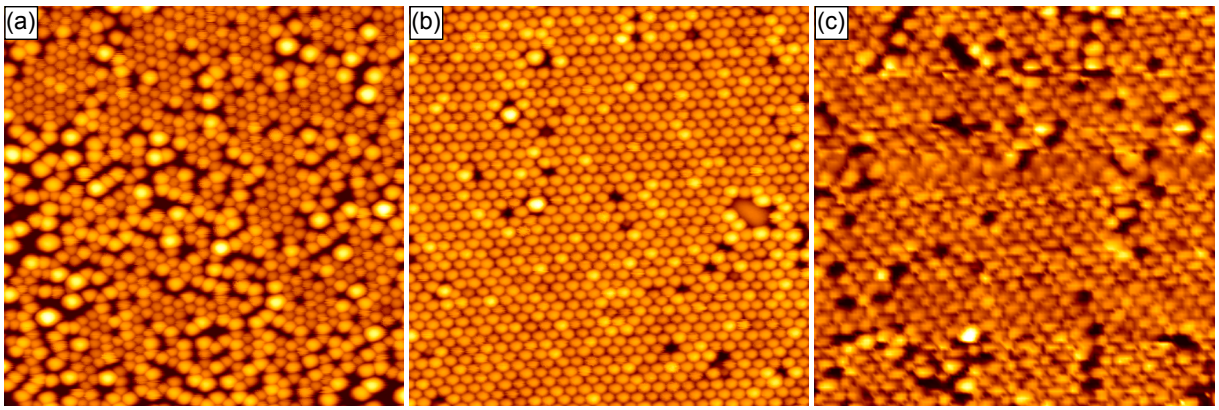

Figure 9.6: (a) $Pt_{12}Co_{22}$ clusters with 28% coalescence imaged at ATHENE. (b) and (c) Optimized $Ir_{18}Co_{27}$ cluster lattice imaged at ATHENE with 4% coalescence (b), and at ID08 with 14% coalescence (c). The image size is always $80\,\mathrm{nm} \times 80\,\mathrm{nm}$.

By comparing the STM topographs of both preparations in Figs. 9.6(a) and (b) it becomes evident that a strong reduction in coalescence has been achieved. Since all three changes were made at one go, it is impossible to tell how each of them contributed to the overall large improvement. Compared to the share of 28% of the clusters coalesced in the previous preparation the new preparation yields only 4% coalescence (both measured at ATHENE). This time, also STM measurements at ID08 were possible (see Fig. 9.6(c)) and yield a larger coalesced share of 14%. However, this is still a factor of 2 better than in the original preparation. All revalant data are summarized in Tab. 9.2.

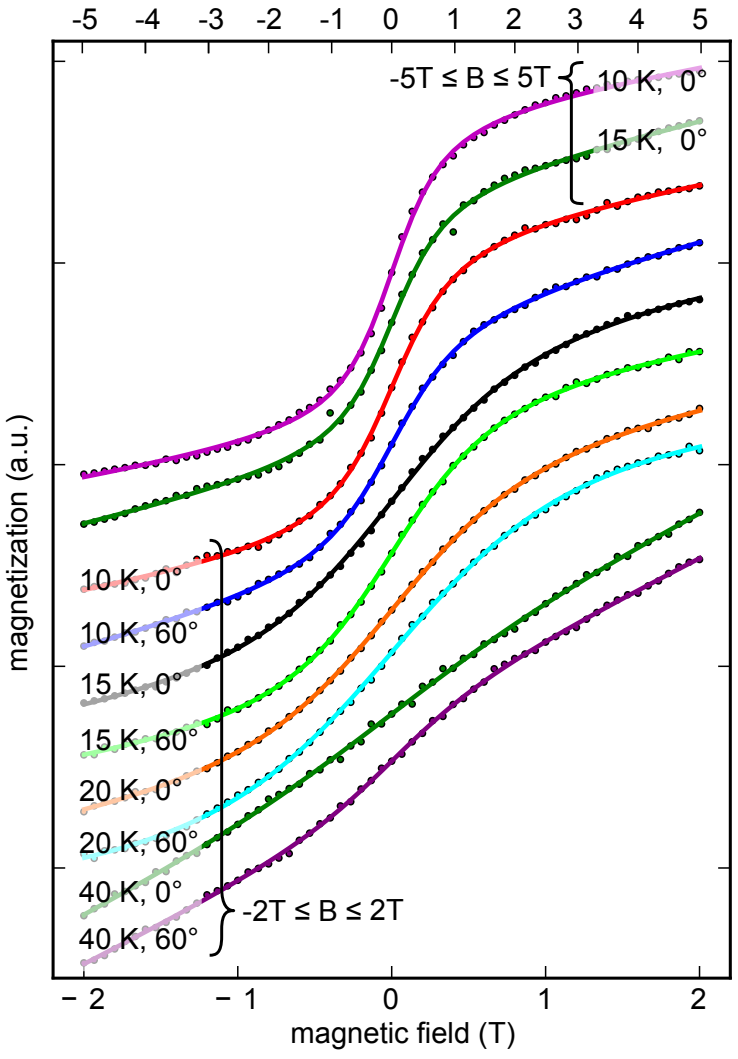

Figure 9.7: Magnetization loops under normal incidence for $Ir_{20}Co_{30}$ clusters at the indicated temperatures. The top axis belongs to the first two curves, the bottom axis to the rest. The lines are modified Langevin fits (see Eq. 9.3). The data are vertically shifted for better visibility.

deposited amount	nominal size	chamber	coalescence	mean size
0.13 ML Pt	$Pt_{12}Co_{22}$	ATHENE	28%	$Pt_{15}Co_{28}$
+ 0.25 ML Co		ID08	-	-
0.20 ML Pt	$Ir_{18}Co_{27}$	ATHENE	4%	$Ir_{19}Co_{28}$
+ 0.30 ML Co		ID08	14%	$Ir_{20}Co_{30}$

Table 9.2: Deposited metal amounts and coalescence yields determined by STM at ATHENE and ID08. The corresponding average cluster sizes are given, too.

$\theta(^\circ)$	T (K)	M_s (a.u.)	χ_{add}/μ_0 (a.u./T)	m (μ_B)
		$-5\,T \leqslant B \leqslant +5\,T$		
0	10	0.813	0.051	45.6
0	15	0.700	0.069	63.9
		$-2\,T \leqslant B \leqslant +2\,T$		
0	10	0.815	0.128	89.8
60	10	0.680	0.192	80.2
0	15	0.983	0.106	59.2
60	15	0.939	0.097	78.5
0	20	0.953	0.111	76.2
60	20	1.312	0.017	59.4
0	40	0.356	0.369	107.1
60	40	0.296	0.375	221.9
	mean	0.90	0.10	69
	error	0.07	0.02	5

Table 9.3: Saturation magnetization M_s, additional slope χ_{add}/μ_0, and moment m of the magnetic entity derived from modified Langevin fits of the magnetization loops at different temperatures T shown in Fig. 9.7. The data at 40 K were not used for averaging.

As for the previous preparation, magnetization loops have been measured under normal and grazing incidence at various temperatures (see Fig. 9.7). Unfortunately, most of the curves were measured only up to ± 2 T and just two curves are available up to ± 5 T. Furthermore, the quality of the measured data in terms of drift and noise was significantly worse than in the previous beamtime. This problem is not related to the sample preparation, but probably arises from aging of the beamline. Consequently, upon fitting the data with Eq. 9.3 the parameters scattered much more. To reduce the noise, the data were symmetrized and averaged over increasing and decreasing field ramping direction, as

already applied for the magnetization loops of intercalated Eu in Sec. 8.1. Furthermore, knowing from the previous results that the clusters do not show magnetic anisotropy, the data set for grazing incidence was used as well.

The parameters resulting from the Langevin fits are listed in Tab. 9.3. Still, the values of M_s and χ_{add}/μ_0 scatter substantially more than the ones in Tab. 9.1, but the average of $m = (69 \pm 5)\,\mu_B$ is rather well-defined. For averaging, the curves taken at 40 K were discarded, since they are almost straight and thus do not carry reliable information for the purpose of this fit. Furthermore, they are obviously outliers.

Dividing again the average magnetic moment per entity of $(69 \pm 5)\,\mu_B$ by the number of Co atoms per cluster (N=30), we obtain $(2.3 \pm 0.2)\,\mu_B$ per Co atom. This value is much lower than the $(3.8 \pm 0.2)\,\mu_B$ previously obtained, and closer to the $1.6\,\mu_B$ derived from the sum rules. If one considers only the curves measured up to ± 5 T , which should be most reliable since they allow the fit to distinguish best between the contributions of χ_{add}/μ_0 and m, one obtains $m = (1.8 \pm 0.2)\,\mu_B$ which is even closer to $1.6\,\mu_B$. Since there is still some scatter in the coalescence yield, the results are consistent with the magnetic entities being single clusters which are not coupled to each other.

9.2 Larger Cobalt Clusters

After discussing small moiré-templated Co clusters, I focus on the magnetic properties of larger clusters. For comparison, Fig. 9.8(a) again shows an STM topograph of the $Pt_{15}Co_{28}$ clusters investigated before. In Fig. 9.8(b), 1.70 ML Co were deposited on Ir_{15} seeds. Since the amount of Co is too large to fit in one moiré unit cell, coalescence takes place and leads to a dense array of Co clusters anchored by several Ir seeds. The average cluster size was determined by STM to $Ir_{50}Co_{500}$. As shown in Fig. 9.8(c), deposition of 0.25 ML Co without previous seeding leads to the formation of even larger Co clusters which are sparsely and disorderedly distributed over the sample. They possess either a spherical or a triangular shape, and have a mean size of 2700 atoms.

From the sum rules one gets the magnetic moments listed in Tab. 9.4. As already discussed for the smallest clusters, the spin moment is close to the bulk value in all cases. This indicates that neither the occupation of the 3d bands nor the charge transfer strongly depends on the cluster size. The enhanced ratio m_L/m_S found for $Pt_{15}Co_{28}$ clusters gradually decreases with increasing cluster size towards the bulk value of 0.095.

Magnetization loops taken under normal and grazing incidence are shown in Fig. 9.9 for all three samples. In line with smallest clusters, also $Ir_{50}Co_{500}$ and Co_{2700} clusters show almost

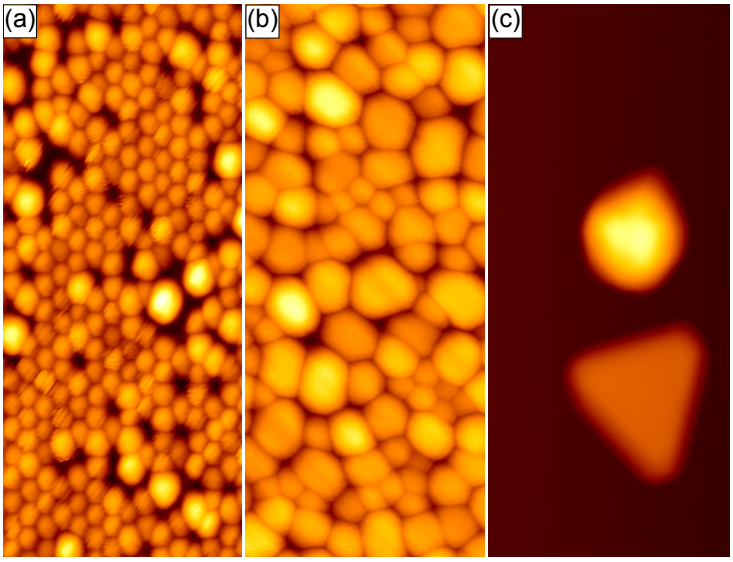

Figure 9.8: STM topopgraphs of $Pt_{15}Co_{28}$ (a), $Ir_{50}Co_{500}$ (b), and Co_{2700} (c) clusters. The sizes are average values determined by STM. The image size is always 25 nm × 60 nm.

cluster	θ (ML)	d (nm)	$m_S(\mu_B)$	$m_L(\mu_B)$	m_L/m_S
$Pt_{15}Co_{28}$	0.13/0.25	2.5	1.5 ± 0.2	0.22 ± 0.02	0.15 ± 0.04
$Ir_{50}Co_{500}$	0.17/1.70	4.8	1.7 ± 0.2	0.20 ± 0.02	0.12 ± 0.03
Co_{2700}	- /0.25	30	1.7 ± 0.2	0.18 ± 0.02	0.11 ± 0.03

Table 9.4: Spin (m_S) and orbital (m_L) magnetic moments and their ratio m_L/m_S measured at 10 K and 5 T under normal incidence for different cluster sizes. The samples were prepared by depositing different amounts θ of the seeding/magnetic material. The average cluster distance d was determined by STM (except for $Pt_{15}Co_{28}$, where d is the moiré pitch).

no anisotropy. However, in contrast to the $Pt_{15}Co_{28}$ clusters, the larger clusters exhibit a pronounced hysteresis with a coercive field of about 250 mT. This yields evidence that the clusters are in the blocked state, which is reasonable since the blocking temperature T_B generally increases with the particle size.

Since hysteresis in single domain particles can only arise from anisotropy (for larger particles also domain pinning can lead to hysteresis), a loop opening in the spatially isotropic magnetization curves appears surprising. We reason that the anisotropy causing the hysteresis is too small to be observable within the resolution of the angular-dependent magnetization loops. Another hypothetical explanation would be that indeed each clusters has a non-vanishing anisotropy, but it is zero in average because of a random orientation of the clusters. However, this can be excluded since the clusters are known to possess a well-defined orientation with respect to the Gr layer [102].

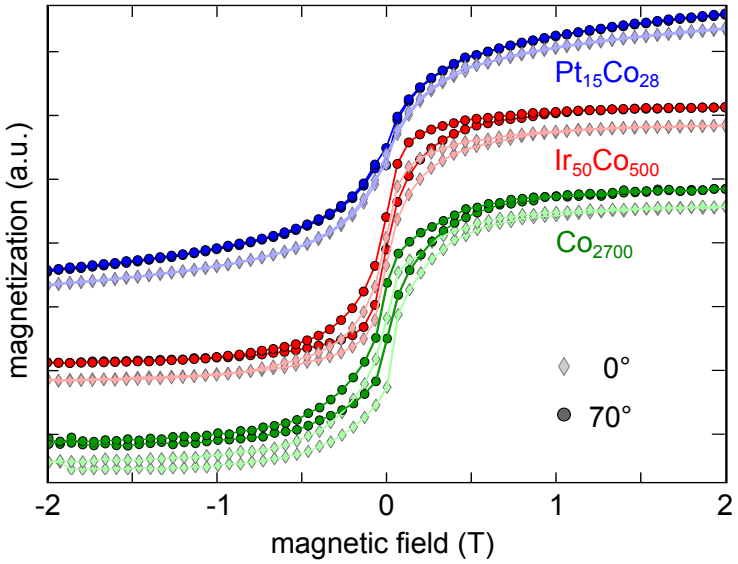

Figure 9.9: Magnetization loops for clusters of indicated size at 10 K under normal (rhomboids) and grazing (dots) incidence. The curves are vertically shifted for better visibility.

To get an estimate for the blocking temperature, in Fig. 9.10 temperature dependent hysteresis loops were measured for $Ir_{50}Co_{500}$ and Co_{2700} clusters. For the $Ir_{50}Co_{500}$ clusters the hysteresis disappears at around 30 K, whereas it vanishes for the larger Co_{2700} clusters only at around 40 K. A comparison to theoretical expectations cannot be drawn here, since the structure of the clusters is not known in detail.

9.3 Rhodium Clusters

Unlike elements of the 3d series such as Fe, Co and Ni, none of the elements of the 4d series exhibits ferromagnetism. This is understood to arise from the 4d orbitals being more extended compared to the 3d ones, which results in broader bands and therefore a lower density of states at the Fermi edge. Consequently, the Stoner criterion for ferromagnetism is violated (compare Sec. 2.3). However, the criterion is almost fulfilled by some of the 4d elements such as Rh. In this case, a band narrowing by formation of small clusters can be sufficient to push the system beyond the limit towards ferromagnetism.

In this context, Cox *et al.* investigated the magnetism of free mass-selected Rh clusters using a Stern-Gerlach type experiment [336]. They find ferromagnetic behavior with a magnetic moment per atom that strongly depends on the cluster size N in atoms. The maximum of about $1\,\mu_B$/atom occurs for $N = 15$. Beside this study on free Rh clusters, several XMCD studies on Rh clusters supported by various substrates have been

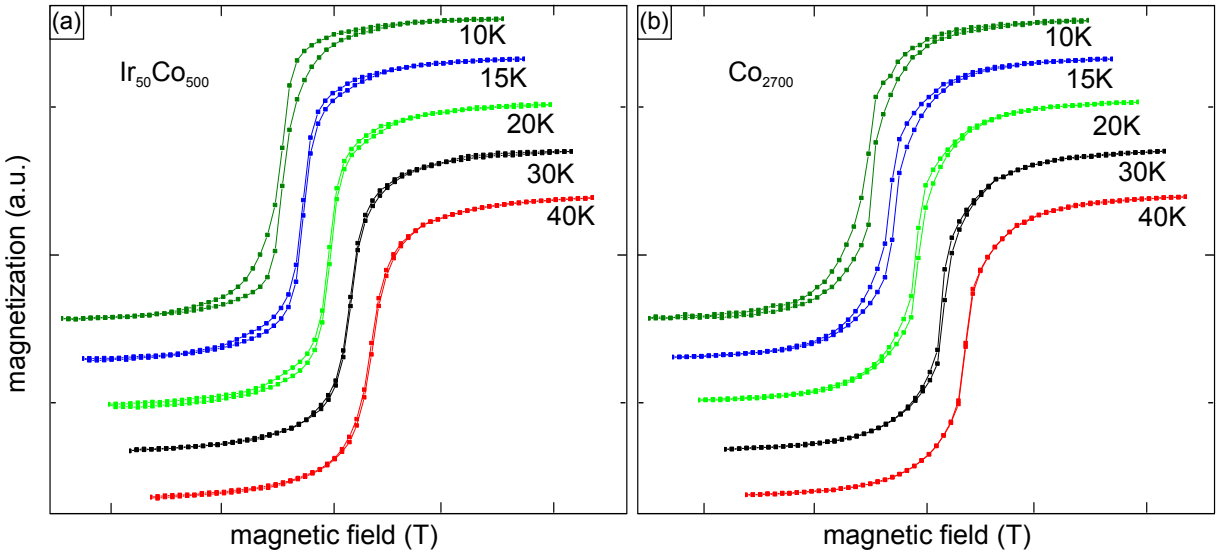

Figure 9.10: Temperature dependent hysteresis loops from -2 T to 2 T for (a) seeded $Ir_{50}Co_{500}$ clusters and (b) pure Co_{2700} clusters showing a decrease of coercivity with increasing temperature. The curves are horizontally and vertically shifted for better visibility.

performed. Sessi *et al.* measured Rh clusters on an inert Xe buffer layer, and obtained moments as large as $0.4\,\mu_B$/atom at 10 K and 5 T [337]. Barthem *et al.* observed Rh clusters with sizes of about 150 atoms embedded in an Al_2O_3 matrix to have a magnetization of $0.067\,\mu_B$/atom at 2.3 K and 17 T [338]. In contrast, XMCD measurements on Rh clusters in contact with Ag(100) or Pt(997) revealed that the clusters do not exhibit sizable magnetic moments [339].

It has thus been reasoned that the undercoordination of Rh atoms in small clusters is the crucial point: On weakly interacting substrates such as Xe, the undercoordination of the free cluster is preserved, whereas it is broken by the strong interaction with a metallic substrate. In terms of binding to the substrate, clusters on Gr/Ir(111) represent an intermediate case: On the one hand, the binding mechanism is clearly chemical since it is mediated by sp^3 rehybridization of C atoms underneath the clusters. On the other hand, the easy manipulation by an STM tip and the low temperature onset of Smoluchowski ripening indicate a weak binding, which is confirmed by the isotropic magnetic behavior found in the previous sections. Thus, it is interesting to determine whether Rh clusters on Gr behave quasi-free or not in the context of magnetism.

It has previously been shown that Rh does not form regular cluster lattices for deposition at 300 K, but at a lower temperature of 90 K [340, 341]. Compared to the preparations by Sessi *et al.*[337] or Barthem *et al.*[338], the size distribution of Rh clusters on Gr is narrow

and well-defined by a Poission distribution. For the present experiment an amount of 0.18 ML Rh is used corresponding to Rh_{16} clusters, which is close to the size exhibiting the maximum moment per atom in the free beam [336].

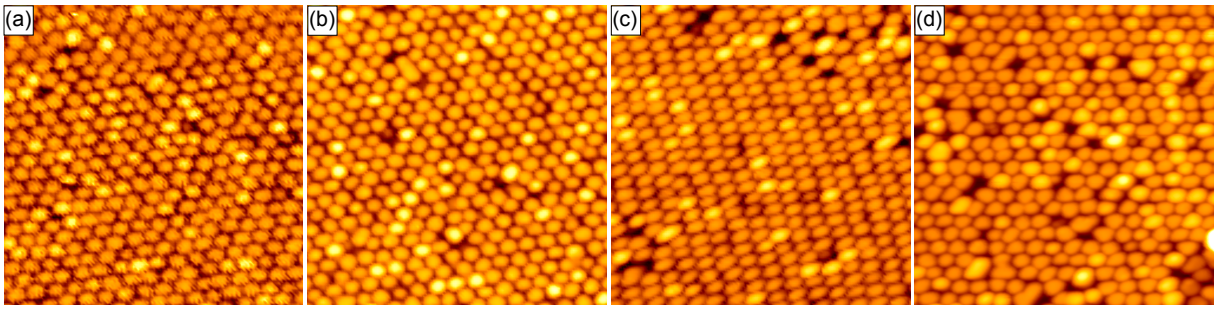

Figure 9.11: STM images of Rh_{16} clusters after growth at 130 K (a), after annealing to 300 K (b), and after annealing to 400 K (c), always imaged at 130 K. (d) Seeded Ir_9Rh_{18} clusters grown and imaged at 300 K. The image size is always 80 nm × 80 nm.

Fig. 9.11(a) shows an STM topograph of 0.18 ML Rh deposited onto Gr at 120 K, which is the lowest temperature attainable at ATHENE with liquid N_2 cooling. The image reveals a cluster lattice of high perfection. To assess the temperature stability the sample was subsequently annealed to 300 K (see Fig. 9.11(b)), where no significant ripening occurs. Also upon annealing to 400 K (see Fig. 9.11(c)) ripening just sets in.

Since it was not sure in advance whether the required cooling during Rh deposition would be accessible at ID08, we also prepared Rh_{16} clusters seeded by Ir_9 (0.10 ML Ir) at room temperature. The corresponding STM topograph in Fig. 9.11(d) shows that the quality the cluster lattice is still good, though noticeably lower than in the low temperature, non-seeded case. The quality determined by STM at ID08 (not shown here) turned out to be not much worse than at ATHENE for both preparations.

An XAS spectrum and the corresponding XMCD signal are shown in Fig. 9.12. The XMCD signal is zero except for noise and drift at the Rh $M_{2,3}$ energies. This means that there is no net magnetization. In the following, I derive an upper limit for the magnetic moment to quantify this statement. Therefore, it is first necessary to determine the XAS intensity of the Rh M_3 edge. This is difficult since the Rh edges do not stand out in the XAS spectra which seem to be rather dominated by background. The background should contain the Ir N_2 and N_3 edges (577.8 eV and 495.8 eV) from the substrate as well as the O K edge (543.1 eV) since O is always present in the beamline optics. However, we cannot unambiguously match the expected edges to the features in the spectra.

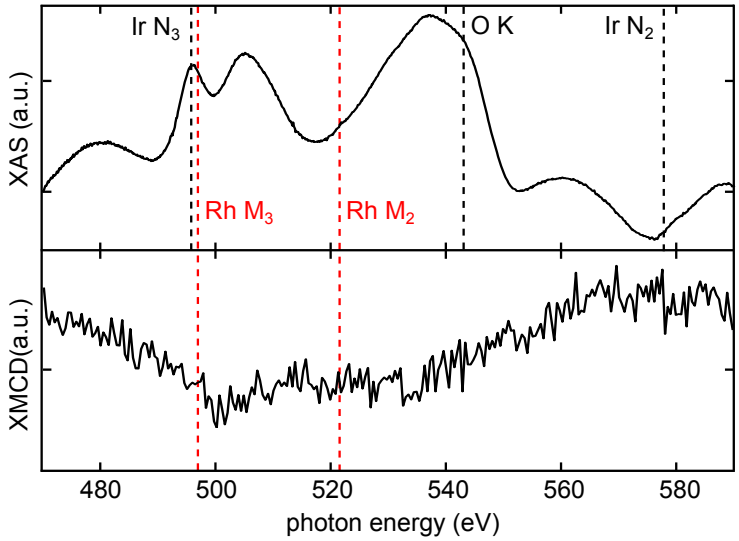

Figure 9.12: XAS spectrum (top) and corresponding XMCD signal (bottom) for Rh_{16} clusters at 10 K and 5 T. Literature values for the relevant absorption edges are indicated.

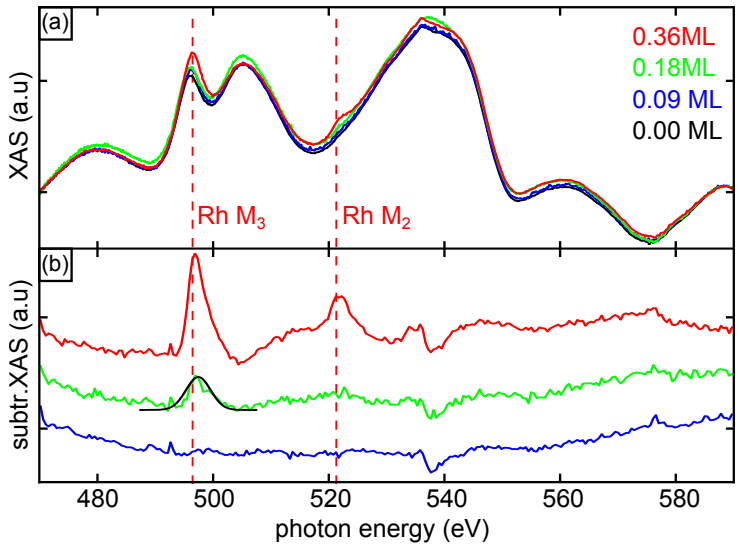

Figure 9.13: XAS spectra for increasing Rh coverages. (b) Spectra after subtracting the zero-coverage spectrum. For 0.18 ML coverage a Gaussian is fitted to the Rh M_3 edge.

In order to separate the Rh edges from the background, on a second sample a series of XAS spectra with increasing Rh coverage from 0 ML, via 0.09 ML and 0.18 ML, to 0.36 ML was measured as shown in Fig. 9.13(a). Since the intensity drifted during data acquisition, the spectra were normalized by subtracting a linear background such that they coincide at 470 eV and 590 eV. I note that all these spectra also exhibit vanishing dichroism (not shown here). By subtracting the zero-coverage spectrum from the non-zero ones, the pure

Rh part is obtained as shown in Fig. 9.13(b). The increase in intensity of the Rh M_3 edge at 496.5 eV with increasing coverage is clear (although not quite proportional to the deposited amount), whereas the Rh M_2 edge is not clearly observed. This is in line with the observations of Sessi *et al.* [337]. By fitting the M_3 edge for 0.18 ML coverage with a Gaussian peak one gets the required XAS intensity of the M_3 edge.
Because of the low signal-to-noise ratio it is not possible to get an upper estimate for the magnetic moment by applying the sum rules. Therefore, here a different approach is used: According to Refs. [337] and [238] a magnetization of $1\,\mu_B$ per atom leads to an XMCD signal at the Rh M_3 edge which is of 13% of the corresponding XAS signal. Hence, by adding $0.2 \cdot 13\% = 2.6\%$ of the Gaussian-fitted M_3 intensity onto the XMCD signal, one obtains the XMCD signal expected for a magnetization of $0.2\,\mu_B$ per atom. The corresponding spectrum shown in Fig. 9.14 (blue curve) demonstrates that $0.2\,\mu_B$/atom are a reasonable estimate for the detection limit. By adding $0.4 \cdot 13\% = 5.2\%$ of the M_3 intensity corresponding to $0.4\,\mu_B$ per atom (green curve) already a pronounced peak in the XMCD spectra should be visible.

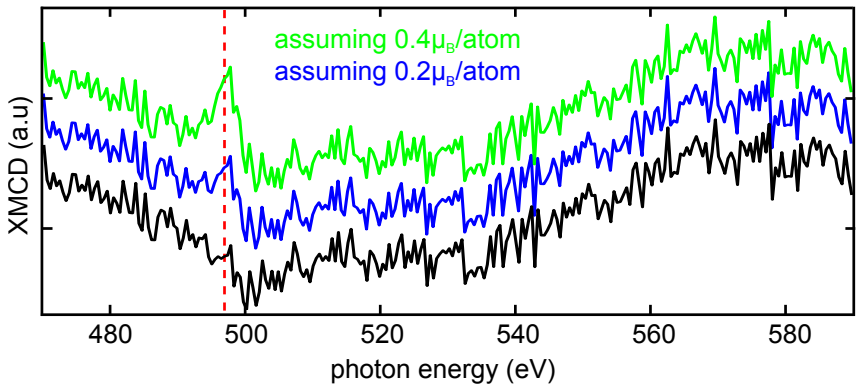

Figure 9.14: Black: XMCD spectrum of Rh_{16} clusters at 10 K and 5 T (same data as in Fig. 9.12). Blue and green: Adding 2.6% and 5.2% of the fitted Rh M_3 XAS intensity from Fig. 9.12, i.e., assuming a magnetic moment of $0.2\,\mu_B$ and $0.4\,\mu_B$ per atom, respectively. The position of the Rh M_3 edge is marked by a red dashed line.

To summarize, I have shown that the magnetic moments per atom in Rh clusters on Gr are clearly lower than in the free beam. On the other hand, the moments of Rh clusters on Xe found by Sessi *et al.* at the same magnetic field and temperature are typically below our detection limit [337]. In other words, we would not be able to find magnetism in the present clusters, even if they were as magnetic as on a Xe substrate.
The fact that Sessi *et al.* used the same beamline begs the question why the quality of the present data is much worse. Two explanations come to mind: First, it is known that

beamline optics are subject to a certain aging resulting in instabilities and significant drift. Second, Sessi *et al.* used Ag and Xe as substrate and therefore avoided the Ir $N_{2,3}$ edges which make background large and complex in the present case. In principle, it is possible to avoid those also here by using the Rh $L_{2,3}$ edges instead of the Rh $M_{2,3}$ ones (as done by Barthem *et al.* in Ref. [338]), but they are energetically not accessible at ID08.
Finally, I remark that we also investigated seeded Ir_9Rh_{18} clusters. Since they also exhibit vanishing dichroism, they are not further discussed here.

9.4 Europium Clusters

Since the magnetism of intercalated and adsorbed Eu discussed in Secs. 8.1 and 8.2 turned out to be interesting, we also tried to grow Eu clusters. As already shown in Chap. 6, Eu on top of Gr does not lead to templated cluster growth. Therefore, we tried to use well-ordered Ir_{18} clusters as seeds for subsequent deposition of 0.30 ML Eu.

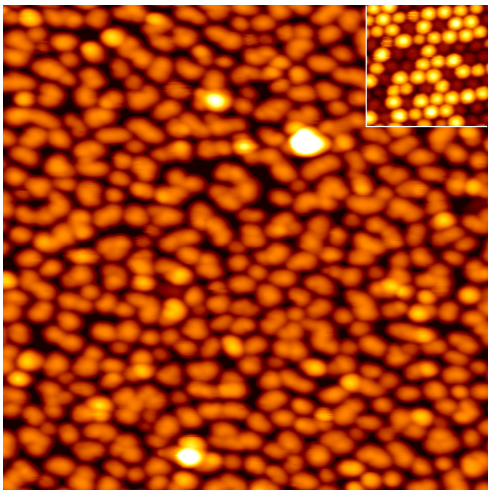

Figure 9.15: STM image (90 nm × 60 nm) after deposition of 0.30 ML Eu on Ir_{18} clusters. Inset: Ir_{27} clusters with identical lateral (though not vertical) scale for an intuitive size comparison.

In contrast to the case of Co, the STM topograph in Fig. 9.15 reveals that the deposition of Eu destroys the order of the seeding cluster lattice, and the number of clusters is strongly reduced by coalescence. Consequently, the size distribution is very broad, although the apparent height of about 10 Å is rather homogeneous.
This can be explained as follows: The NN distance in bulk Eu and all Eu structures presented in this thesis is always on the order of 4 Å. Therefore, only a small amount of Eu can directly bind to the Ir seeds. The excess Eu may either bind on top of the clusters

only to Eu, or at the side of the cluster both to Eu and Gr. Since Eu forms flat layers on top of Gr [28], the Eu-Eu and Eu-Gr binding strengths have to be of similar magnitude. Therefore, binding at the side of the clusters is probably energetically more favorable due to the higher coordination. This leads to coalescence with increasing Eu amount.
Since we were not able to achieve well-ordered seeded Eu clusters, the magnetism of this preparation was not investigated by XMCD. It might be possible to achieve a better Eu cluster lattice by using less Eu, but this would also involve a loss of XMCD intensity.

9.5 Summary

In this chapter, first the magnetic properties of Co clusters on Gr were investigated. Small moiré-templated $Pt_{15}Co_{28}$ clusters show a Langevin magnetization behavior as expected for superparamagnetism. For larger $Ir_{50}Co_{500}$ and Co_{2700} clusters a hysteresis opens due to the higher blocking temperature of about 30 K and 40 K, respectively. The ratio of orbital to spin moment is enhanced for the smallest clusters and gradually decreases towards the bulk value with increasing cluster size. All clusters show a vanishing anisotropy which probably originates from a weak interaction with the supporting Gr layer.
For $Pt_{15}Co_{28}$ clusters, Langevin fits indicate that the size of the magnetic entity is much larger than a single cluster. Since this effect might result from an underestimated amount of coalesced clusters, the quality of the cluster lattice was optimized by increasing the Gr growth temperature and changing the seeding clusters from Pt_{12} to Ir_{18}. With this recipe, the amount of coalescence is substantially reduced, and the moment of the magnetic entity is in good agreement with the one of a single cluster.
Besides Co clusters, also Rh clusters were investigated to find out whether they are magnetic as in the free beam and on weakly interacting substrates, or non-magnetic as on metal substrates. The XMCD data do not show any sign of ferromagnetism. We estimate an upper limit of $0.2\,\mu_B$ per atom for the magnetic moment. This limit is substantially lower than the moments found for free clusters, but the presence of magnetic moments as small as found on weakly interacting substrates cannot be excluded.
Finally, Eu clusters have been grown on Gr, but since they do not order well and have a broad size distribution, their magnetic properties were not investigated by XMCD.

CHAPTER 10

Polar Europium Oxide on Ir(111)

The content of this chapter is published in Phys. Rev. B ***89*** *115410 (2014) [64]. Furthermore, it is partially contained in Ref. [29]. I conducted all STM and work function measurements, partially together with D. F. Förster. DFT calculations were performed by T. O. Wehling and F. Hu. I performed the MOKE measurements together with J. Klinkhammer.*

In this chapter, the growth of polar EuO(111) is investigated. In order to promote high quality growth, Ir(111) was chosen as substrate. Ir is a noble metal and therefore cannot be oxidized under the EuO growth conditions. The high cohesion of Ir implies marginal substrate atom diffusion at the oxide growth temperature, and thus reduces the probability of mass transport as observed for EuO growth on Ni [49]. Hence, together with the low (electronic) corrugation of the dense-packed (111) surface, the influence of the substrate on EuO growth is minimized, prohibiting the formation of complicated surface oxide phases as observed in the initial growth state of EuO(100) on Ni(100) [49].

All experiments were performed at the UHV system ATHENE. The Ir(111) crystal was prepared as described in Sec. 4.5. Directly before EuO growth it was flash annealed to 1530 K, and then cooled to the actual growth temperature T_{growth}. EuO was grown by reactive MBE as described in Sec. 4.5. The amount θ of EuO grown is specified in EuO(111) bilayers (BL), where 1 (or 100%) BL is defined as 1 ML of O ions plus 1 ML of Eu ions, each with the bulk atomic surface density of 8.7×10^{18} atoms m^{-2}.

As under O excess all Eu is expected to react to EuO, in this case the coverage is calculated by the Eu fluence. On the contrary, under Eu excess the growth is limited by the O amount so that the O fluence is used for calculating the coverage. Together, the coverage θ, the flux ratio $f_{\mathrm{Eu}}/f_{\mathrm{O}}$ and the growth temperature T_{growth} fully define the film properties.

Magneto optical Kerr effect (MOKE) measurements were conducted *in situ* in a different UHV chamber using a home-built setup in longitudinal geometry with a red HeNe laser. DFT calculations have been performed as described in Sec. 4.6.
In the following, I first investigate the structural and electronic properties of a EuO(111) bilayer on Ir(111) using DFT. Afterwards, structure and growth, including rotational misalignments, defects, and the influence of the Eu rich growth conditions, will be analyzed by STM and LEED. I focus on the apparent height and the work function of the bilayer, discuss the temperature stability, and conclude with the magnetic properties.

10.1 DFT Calculations

As outlined in the next section, a EuO(111) bilayer is experimentally found to be the only oxide structure on Ir(111). The bilayer displays a slightly expanded lattice parameter of 3.67 Å compared to the bulk value, and therefore deviates from a perfect 3:4 registry with the substrate. Furthermore, a slight orientation scatter between the dense-packed EuO and Ir rows is observed. As an approximation which is accessible to *ab initio* calculations, a (3×3) EuO(111) unit cell with an in-plane lattice constant of 3.67 Å resting on a (4×4) four layer Ir(111) slab with a slightly expanded lattice constant of 2.75 Å is used.
First, I address the question whether O or Eu ions terminate the bilayer to the vacuum. Therefore, both configurations were used as starting point of the calculations. It was impossible to stabilize a Eu terminated bilayer on Ir(111). Thus, the bilayer is O terminated as also invariably found for other polar bilayer oxides on metals [54, 58, 342].

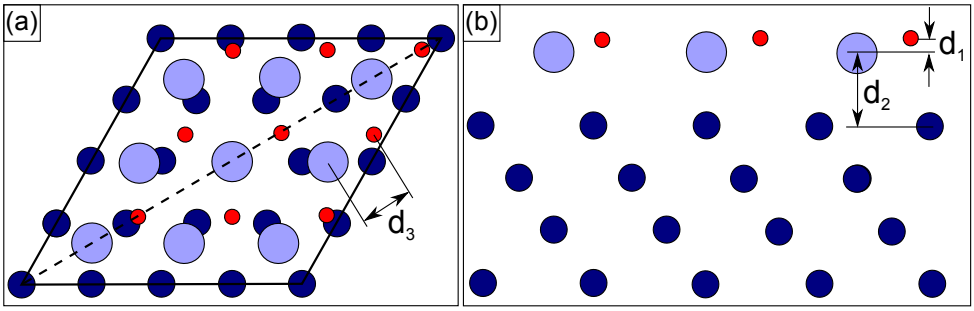

Figure 10.1: (a) Top view ball model and (b) cut along the dashed line in (a) of the DFT optimization for a EuO(111) bilayer in 3:4 registry with the Ir(111) substrate. Color scheme: Ir dark blue, Eu light blue, O red. $d_1 = 0.51$ Å, $d_2 = 3.07$ Å, and $d_3 = 2.18$ Å denote the thickness of the EuO bilayer, the height of Eu above Ir, and the Eu-O bond length, respectively.

Ball models representing the optimized O terminated EuO(111) bilayer on Ir(111) are shown in Fig. 10.1. As most important result, the interlayer distance d_1 is found to be only

0.51 Å. This value is reduced by a factor of 3 compared the bulk value of 1.49 Å. The finding is stable upon relaxing the first substrate layer, and upon varying the number of Ir layers in the slab. As a counter-check, the distance of the (111) planes in bulk EuO was calculated, yielding 1.49 Å consistent with the literature value, which confirms the reliability of the *ab initio* approach. The reduction in the bilayer thickness is much stronger than expected from the lowered coordination in a thin layer which is often thought to cause strengthened and thereby shortened bonds [299, 343]. Note that the layer contraction also implies a reduction in the Eu-O bond length d_3 from 2.57 Å to 2.18 Å.

The driving force for the drastic reduction in the distance between the oppositely charged Eu and O layers is straightforwardly to understand in a simple capacitor model of the polar bilayer. The difference in electrostatic potential $\Delta\Phi_{\mathrm{BL}}$ between the planes, separated by the interlayer distance d_1 and each having a surface charge density σ, is given by

$$\Delta\Phi_{\mathrm{BL}} = \sigma \cdot \frac{d_1}{\epsilon_0}, \tag{10.1}$$

where ϵ_0 is the vacuum permittivity. A reduction in the interlayer distance by a factor of 3 from 1.49 Å to 0.51 Å therefore reduces $\Delta\Phi_{\mathrm{BL}}$ and consequently the polarity of the film by the same factor. Also for FeO(111) on Pt(111) a strong reduction in the layer spacing by almost 50% was observed by X-ray photoelectron diffraction [215, 344], and has been interpreted to relieve the dipole moment [216].

In order to investigate the coupling between EuO and the Ir substrate, it is instructive to compare the height d_2 of Eu above Ir for (i) the EuO bilayer, and (ii) Eu adatoms on Ir. For EuO, d_2 is found to be 3.07 Å (see Fig. 10.1(b)). This is substantially larger than the distance between Eu adatoms and Ir, which the DFT calculations find to be 2.36 Å. Thus, the coupling of EuO to Ir is much weaker than the one of Eu adatoms to Ir. The weak coupling also manifests in the energy required to shift the EuO bilayer laterally out of the minimum position shown in Fig. 10.1(b). Shifting the bilayer to a configuration where none of the Eu atoms occupies a high symmetry site requires less than 5 meV per atom. This energy difference is as small as stacking energy differences for Gr on BN [345], a system, which is dominated by weak vdW forces.

To obtain further insight to the bonding and the electronic structure, in Fig. 10.2 the LDOS of the EuO(111) bilayer on Ir(111) and of bulk EuO was calculated. In the latter case, the Fermi level lies inside the band gap as expected for an insulator. To study the EuO bilayer, the corresponding total DOS which includes the Ir substrate was projected on the local orbitals of the Eu and O atoms. Despite the strong structural distortions in the bilayer, the EuO LDOS is still qualitatively similar to bulk EuO, but in contrast

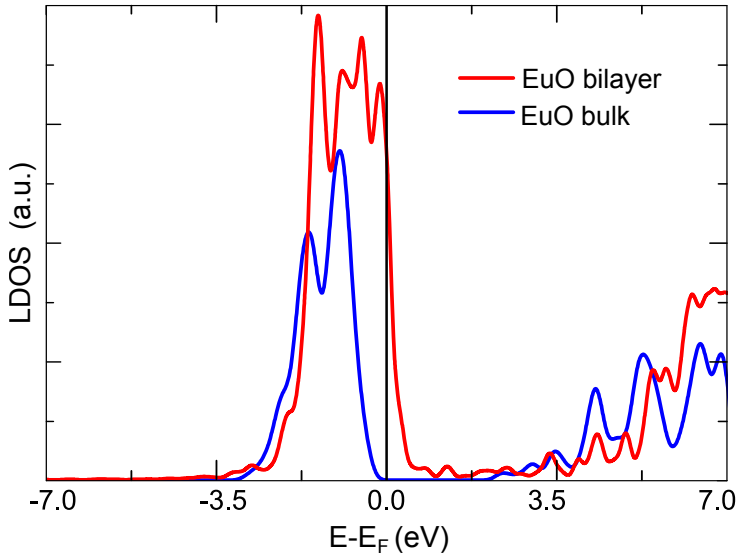

Figure 10.2: LDOS of a EuO(111) bilayer on Ir(111) (red), and of bulk EuO (blue).

to the bulk material, the Fermi level is located here in the valance band of EuO. Thus, electrons are transferred from the EuO bilayer to Ir indicating a weak ionic bonding. Such a charge transfer is energetically favorable as it further reduces the surface dipole. A similar surface metalization has also been observed for MgO(111) on Ag(111) [54]. Furthermore, it it supported by the experimental finding that the samples can be imaged at very low voltages of several millivolts, which is not expected for an insulating layer.

10.2 Structure and Growth

Fig. 10.3(a) shows a large scale STM topograph after EuO growth at $T_{\mathrm{growth}} = 720\,\mathrm{K}$ with a flux ratio of $f_{\mathrm{Eu}}/f_{\mathrm{O}} = 1.7$. The flux ratio $f_{\mathrm{Eu}}/f_{\mathrm{O}}$ was varied over a range from 0.85 to 1.7, which does not essentially influence the structure. This is in contrast to the case of EuO growth on a Ni(100) substrate, where already small changes in the flux ratio cause a variety of surface oxide phases [49]. The Ir terraces labeled with (i) - (iv) are almost fully covered by extended flat EuO(111) islands. The islands on terraces (i), (ii), and (iv) carry a few second layer islands which I disregard in the following discussion.
Surprisingly, the large bilayer EuO(111) islands are imaged as depressions in the Ir terraces; the decrease in apparent height is considerable as demonstrated by the line profile in Fig. 10.3(c) taken along the path indicated in Fig. 10.3(b). The step height between the Ir terraces (blue arrow) is 2.2 Å as expected from the Ir crystal structure. However, the step height along the green arrow is 1.5 Å with EuO being lower than Ir. Although the specific value of the height difference depends on the tunneling parameters, the EuO(111)

bilayer always has an apparent *negative* thickness under the applied growth conditions. This puzzle will be resolved later by the analysis in Sec. 10.2.2.

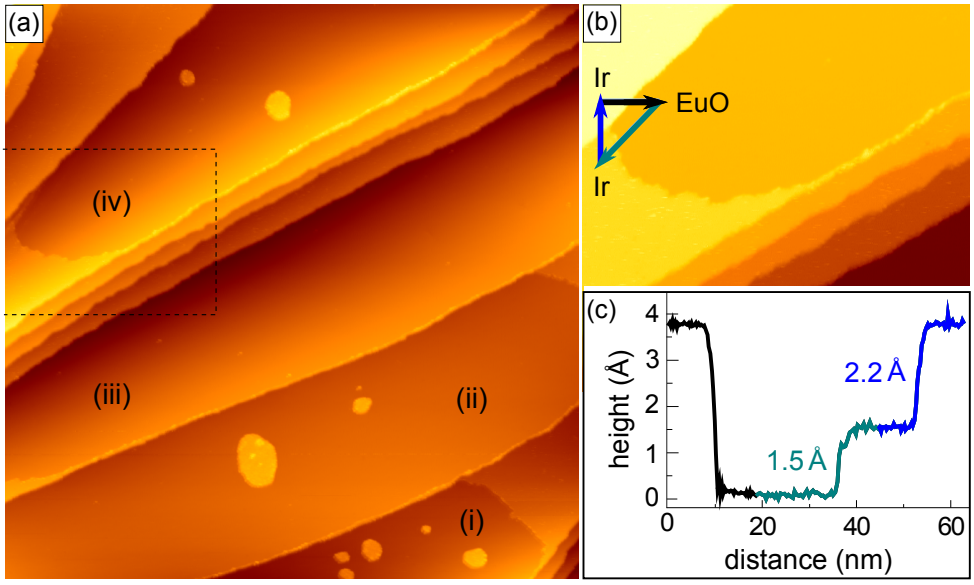

Figure 10.3: (a) STM topograph of a 23% BL EuO(111) film grown on Ir(111) with $f_{\mathrm{Eu}}/f_{\mathrm{O}} = 1.7$ at $T_{\mathrm{growth}} = 720\,\mathrm{K}$ ($320\,\mathrm{nm} \times 320\,\mathrm{nm}$). Terraces partially covered by EuO are labeled with (i) - (iv). (b) Zoom on the area surrounded by the dotted line in (a). A local plane subtraction has been applied to align the terraces horizontally. (c) Height profile taken along the path indicated by differently colored arrows in (b).

Since the O_2 exposure is only sufficient to create on average 23% BL EuO coverage, one can conclude from the substantially larger coverage in Fig. 10.3(a) on considerable local variations due to diffusion during growth, which is consistent with the large size of the islands. Moreover, the large substrate coverage confirms that the islands consist of a single bilayer only.

The O termination found in the DFT calculations is supported by an interesting morphological feature: The apparent height difference between the EuO(111) islands (depressions) and the Ir(111) terraces (elevations) enables one to see that the islands always grow in contact to ascending steps, but stay away a few nanometers from descending steps, thereby leaving a characteristic rim (compare Fig. 10.3(a)). The corresponding situation is schematically depicted in Fig. 10.4: Step edge dipoles are formed on metal surfaces due to smoothening of the electron distribution which is associated with an excess of negative charge at the step bottom, and a lack of negative charge at the step top [346]. The step edge dipole must be assumed to interact with the EuO dipole. A bilayer terminated by negatively charged O ions consistent with DFT explains the observed EuO island repul-

sion from descending steps and attraction to ascending steps. A terminating Eu layer would cause the opposite effect, which is not observed here.

Figure 10.4: Schematic side view of EuO(111) bilayer islands at a substrate step edge (Eu light blue, O red). The indicated charges correspond to the idealized oxidation states in bulk EuO. The electron density of the substrate (indicated in blue) is smoothed at the step edge, leading to a step edge dipole which attracts the polar EuO bilayer at the ascending step edge, and repels it at the descending step edge.

In Fig. 10.5(a) the LEED image corresponding to the sample presented in Fig. 10.3 is shown. One of the six first-order Ir substrate spots is marked by a blue circle. Additional intense spots, one of which is encircled in green, are aligned with the substrate reflections, but closer to the central spot. They belong to the EuO(111) bilayer with a surface lattice constant of (3.67 ± 0.03) Å, and are surrounded by hexagons of weak reflections as indicated by the black lines. A hexagon of spots with identical dimension is also surrounding the central spot (partly hidden by the electron source). The weak reflections are located at positions corresponding to vector sums of reciprocal vectors pointing to Ir(111) and EuO(111) spots, and may thus be interpreted to arise from multiple diffraction or diffraction at the unit cell of a buckled overlayer (compare Sec. 3.3).

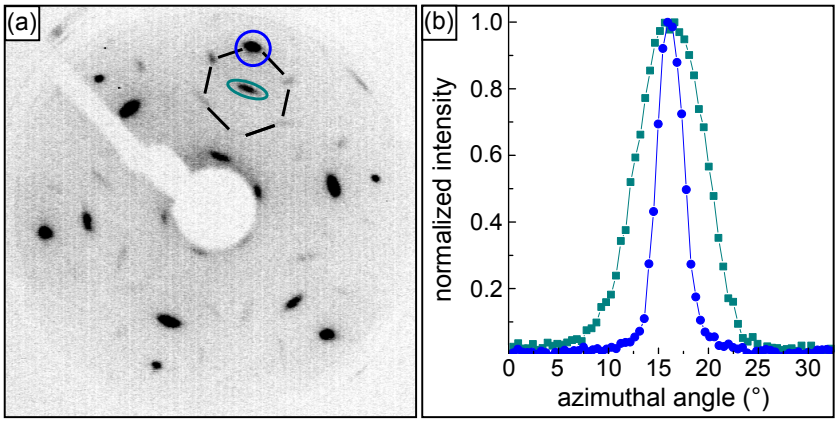

Figure 10.5: (a) LEED image (76 eV primary electron energy) corresponding to the sample in Fig. 10.3. First-order Ir(111) and EuO(111) spots are encircled in blue and green. Additional weak superstructure spots are connected by black lines. (b) Averaged intensity profiles taken in azimuthal direction over three equivalent spots of Ir (blue dots) and EuO (green squares).

A closer look reveals that all spots, except the Ir ones, are elongated. In order to quantify the elongation, intensity profiles in azimuthal direction were taken and averaged over three equivalent spots. The results are presented in Fig. 10.5(b). The blue dots show the intensity distribution of the first-order Ir(111) spots with a FWHM of $(3.1 \pm 0.3)^\circ$ for the polar angle ϕ. The green squares show the intensity of the first-order EuO(111) bilayer islands. The FWHM of $(7.9 \pm 0.9)^\circ$ is considerably larger, indicating an azimuthal scatter of the EuO(111) bilayer islands around the high symmetry substrate directions. I note that the magnitude of this scatter sensitively depends on the growth conditions.

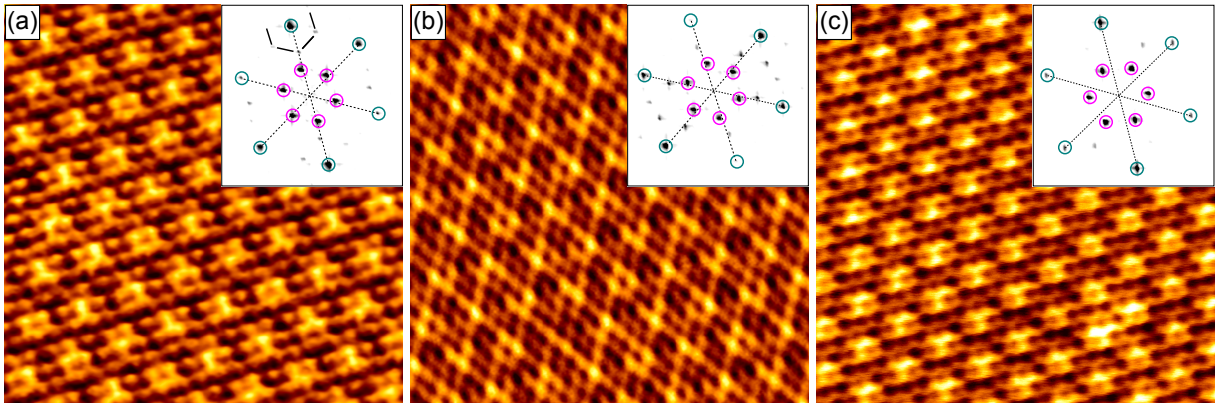

Figure 10.6: Atomically resolved STM topographs (8 nm × 8 nm) showing EuO bilayer films of different orientation with respect to the substrate. (a) $f_{\mathrm{Eu}}/f_{\mathrm{O}} = 1.7$, $T_{\mathrm{growth}} = 620\,\mathrm{K}$. (b) $f_{\mathrm{Eu}}/f_{\mathrm{O}} = 1.7$, $T_{\mathrm{growth}} = 720\,\mathrm{K}$. (c) $f_{\mathrm{Eu}}/f_{\mathrm{O}} = 0.85$, $T_{\mathrm{growth}} = 720\,\mathrm{K}$. The insets show the corresponding Fourier transforms. Spots belonging to the atomic lattice are indicated by green circles and connected by dashed lines, whereas the spots highlighted in magenta belong to the superstructure. The partial hexagon in (a) connects the higher-order superstructure spots.

Additional insight to the structure of the EuO(111) bilayer islands is obtained from atomically resolved STM topographs such as Fig. 10.6(a). It displays the hexagonal atomic arrangement of one ion species of the EuO(111) bilayer - presumably the terminating O ions - together with a periodic height modulation of 0.3 Å amplitude, hexagonal symmetry, and a periodicity of approximately three in-plane NN spacings. In the corresponding Fourier transform shown in the inset of Fig. 10.6(a), the fundamental periodicity is marked by green circles. The additional superstructure periodicity gives rise to a hexagonal spot arrangement surrounding the fundamental spots (indicated by a black hexagon) and the origin (magenta circles). Thus, the Fourier transform is similar to the LEED pattern in Fig. 10.5(a), but without the first-order Ir(111) reflections, which are intense in LEED due to uncovered substrate areas.

At first sight, it may be surprising that invariably a slight expansion of the EuO(111) lattice parallel to the surface is observed, although just a compression of 0.5% would be necessary for a perfect 4:3 epitaxial relation. This deviation of the EuO(111) from an ideal (3×3) superstructure is also visible by close inspection of Fig. 10.6(a). The expansion of 0.8% can be interpreted to be a response to the strongly reduced interlayer distance found by DFT (*Poisson effect*). Such a relation also occurs for FeO(111) on Pt(111) (1.6% in-plane expansion [216], and 50% reduction in the interlayer spacing [215, 344]), and has been proposed for CoO(111) on Pt(111) (2.7% in-plane expansion [58]). For MgO(111) on Ag(111) up to now the strongest expansion for the in-plane lattice parameter of a bilayer polar oxide has been observed, amounting to about 10% [54]. Also here, the expansion is likely related to a reduced interlayer distance, as the MgO(111) bilayer on Ag(111) has been theoretically predicted to adopt even a planar crystal structure by reducing the layer separation to zero [347].

The omission of an epitaxial relation is in line with the weak interaction of the EuO(111) bilayer with the Ir substrate found by the DFT calculation. Furthermore, it is consistent with the orientation scatter between EuO and Ir apparent in the LEED pattern of Fig. 10.5, which will be the topic of the next section.

10.2.1 Rotational Misalignment

Based on the findings above, the EuO(111) islands can be imagined to good approximation as rigid, independent lattice, not matched to the substrate, but with a preferred orientation. Consequently, the EuO(111) lattice is not commensurate to the substrate lattice, but forms a moiré with it. Figs. 10.6(a) - (c) display EuO(111) bilayer islands with different degrees of rotational misalignment. As straightforwardly deduced from the topographs and their Fourier transforms, the superstructures are rotated with respect to the dense-packed EuO(111) rows by angles $\phi_{\mathrm{EuO,s}} = (3.5 \pm 0.5)^\circ$ in Fig. 10.6(a), $\phi_{\mathrm{EuO,s}} = (5 \pm 1)^\circ$ in Fig. 10.6(b), and $\phi_{\mathrm{EuO,s}} = (19 \pm 2)^\circ$ in Fig. 10.6(c). Note that the latter is close to a $(\sqrt{7} \times \sqrt{7})$R19.1° superstructure, but a change in the local atomic arrangement at the moiré maxima over the extension of the topograph indicates the incommensurability between EuO(111) and Ir(111) also for this case.

Formally, the moiré reciprocal lattice vector $\vec{k}_{\mathrm{s}}$ is generated by the vector difference of the reciprocal lattice vectors $\vec{k}_{\mathrm{Ir}}$ of Ir and $\vec{k}_{\mathrm{EuO}}$ of EuO: $\vec{k}_{\mathrm{s}} = \vec{k}_{\mathrm{Ir}} - \vec{k}_{\mathrm{EuO}}$. If the atomic lattices include an angle $\phi_{\mathrm{EuO,Ir}}$, the superstructure is rotated by an angle $\phi_{\mathrm{EuO,s}}$ with respect to the EuO lattice as shown in Fig. 10.7. Both angles are connected via

$$\phi_{\mathrm{EuO,s}} = \tan^{-1}\left(\frac{\sin\phi_{\mathrm{EuO,Ir}}}{\frac{k_{\mathrm{Ir}}}{k_{\mathrm{EuO}}} - \cos\phi_{\mathrm{EuO,Ir}}}\right) + \phi_{\mathrm{EuO,Ir}} \tag{10.2}$$

$$\approx \frac{k_{\mathrm{Ir}}}{k_{\mathrm{Ir}} - k_{\mathrm{EuO}}}\phi_{\mathrm{EuO,Ir}} \quad \text{for} \quad \phi_{\mathrm{EuO,Ir}} \ll 1\,, \tag{10.3}$$

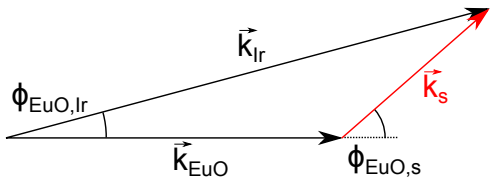

Figure 10.7: Superposing the lattices of EuO and Ir with reciprocal lattice vectors $\vec{k}_{\mathrm{EuO}}$ and $\vec{k}_{\mathrm{Ir}}$ under an angle $\phi_{\mathrm{EuO,Ir}}$ results in a superstructure with reciprocal lattice vector $\vec{k}_{\mathrm{s}} = \vec{k}_{\mathrm{Ir}} - \vec{k}_{\mathrm{EuO}}$ which is rotated by $\phi_{\mathrm{EuO,s}}$ with respect to $\vec{k}_{\mathrm{EuO}}$.

whereby Eq. 10.3 is an approximation for small angles. By inserting the bulk value k_{Ir} =0.368 Å^{-1} and k_{EuO} =0.272 Å^{-1} from the LEED measurement, one obtains a rotation of the EuO lattice with respect to the Ir one of $\phi_{\mathrm{EuO,Ir}} = (0.9 \pm 0.2)°$ for Fig. 10.6(a), $\phi_{\mathrm{EuO,Ir}} = (1.3 \pm 0.3)°$ for Fig. 10.6(b), and $\phi_{\mathrm{EuO,Ir}} = (5.2 \pm 0.5)°$ for Fig. 10.6(c). By comparing these values of $\phi_{\mathrm{EuO,Ir}}$ to the corresponding $\phi_{\mathrm{EuO,s}}$ ones, it becomes obvious that the moiré amplifies the atomic misalignment. In the small angle approximation of Eq. 10.3 the amplification factor $k_{\mathrm{Ir}}/(k_{\mathrm{Ir}} - k_{\mathrm{EuO}})$ has a value of about 3.84.

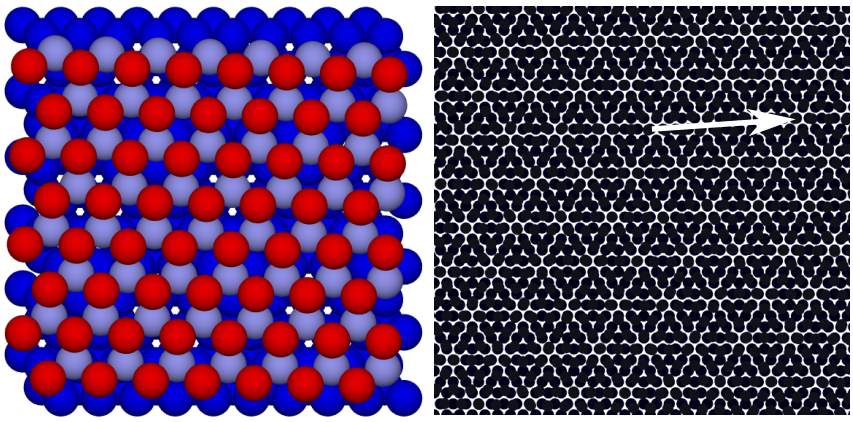

Figure 10.8: Top view ball model for a EuO(111) bilayer island on Ir(111) rotationally misaligned by $\phi_{\mathrm{EuO,Ir}} = 1.3°$ (compare Fig. 10.6(b)). The experimentally determined lattice parameter of $a_{\mathrm{EuO}} = 3.67$ Å is used. Color scheme: Ir dark blue, Eu light blue, O red. In the right part, the resulting moiré is emphasized on a larger scale by overlaying the Eu and Ir lattices as black dots. The white arrow shows the dense-packed direction of the moiré superstructure.

The situation is visualized by the ball models in Fig. 10.8 for the example of Fig. 10.6(b). In the left part, the EuO(111) bilayer is superimposed to the Ir(111) substrate with the measured lattice parameter of 3.67 Å and $\phi_{\mathrm{EuO,Ir}} = 1.3°$ as derived above from the measured $\phi_{\mathrm{EuO,s}}$. In order to illustrate the resulting moiré, in the right part of Fig. 10.8 both the EuO and Ir lattice are formed by black dots resulting in an enhanced contrast. The moiré and the rotational magnification are well visible.
Moiré structures with similar orientation scatter are also known also for other thin polar oxide films on metal substrates such as, e.g., FeO(111) on Pt(111) [251, 342, 348]. They occur for incommensurate layers with weak and unspecific coupling to the substrate as found in the present case. Such a rotational epitaxy has been theoretically analyzed in the past [349, 350], and was experimentally observed, e.g., for incommensurate physisorbed noble gas monolayers on graphite [351].

10.2.2 Apparent Height and Work Function

As discussed in Sec. 10.2, the EuO(111) bilayer islands appear as depressions in the surrounding Ir terraces under Eu rich growth conditions (compare Fig. 10.3). The reduction in apparent height is substantial, since for the EuO(111) bilayer on Ir(111) a *positive* geometric height of 3.58 Å was calculated in Sec. 10.1. In this section, I demonstrate that the apparent height of the EuO islands changes with the growth conditions. Depending on whether they are Eu or O rich, either Eu or O is adsorbed to the bare Ir(111) terraces next to the EuO islands, which does not only affect the *topographic* height difference, but also the tunneling process via its influence on the work function.
Fig. 10.9 displays an STM topograph of EuO grown under the same conditions as used for Fig. 10.3 ($f_{\mathrm{Eu}}/f_{\mathrm{O}} = 1.7$, $T_{\mathrm{growth}} = 720\,\mathrm{K}$), but imaged at 35 K instead of room temperature. The lower substrate terrace in the upper left corner of Fig. 10.9(a) is partially covered by EuO(111), whereas on the remaining terrace a complex variety of incommensurable Eu adatom phases is found, as better visible in Fig. 10.9(b). Thereby, areas with higher adatom density appear brighter than areas with lower density. The average NN adatom distance is (8.0 ± 0.5) Å. Assuming an ideal hexagonal arrangement this distance corresponds to a coverage of 11.5% ML with respect to Ir(111). When depositing 23% BL EuO(111) with a flux ratio of $f_{\mathrm{Eu}}/f_{\mathrm{O}} = 1.7$, the Eu excess is expected to cover 12% of the remaining Ir(111) surface atoms, in excellent agreement with the observation. The excess Eu is distributed as single adatoms rather than islands on Ir(111), since the positively charged ions are subject to Coulomb repulsion [28]. At 300 K imaging temperature the Eu adatoms are highly mobile and form a structureless background, at first glance indis-

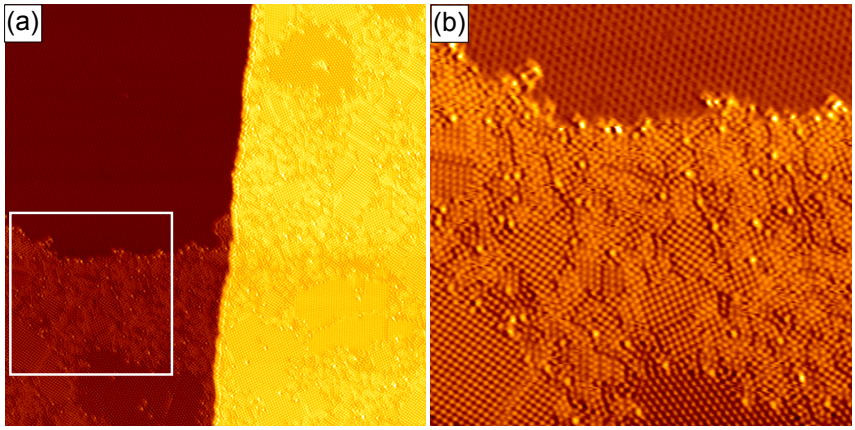

Figure 10.9: (a) STM topograph taken at 35 K of a partial EuO(111) bilayer grown under 70% Eu excess (130 nm × 130 nm). The upper left corner consists of EuO(111), whereas the rest of the image is Ir(111) covered by Eu adatom phases of different density. (b) Zoom into the area marked by a white square in (a) (50 nm × 50 nm).

tinguishable from a bare Ir(111) terrace. The adsorbed Eu adatom phase thereby creates in STM an additional topographic height on the Ir(111) terrace that contributes to the impression of an apparent negative height of the EuO(111) bilayer islands as previously observed in Fig. 10.3.

To confirm the influence of the dilute Eu adatom phase on the apparent height, the sample was exposed to additional O_2 in order to remove the mobile Eu adatoms. The corresponding experiment is shown in Fig. 10.10. The initial film shown in Fig. 10.10(a) was grown under Eu rich conditions ($f_{Eu}/f_O = 1.7$). The schematic profile in Fig. 10.10(g) along the black line illustrates the morphology of the sample: On the lower Ir terrace, there is a triangular area not covered by EuO, whereas on the upper terrace only a rim adjacent to the step edge is uncovered. In the initial stage EuO appears 0.4 Å lower than the surroundings, as expected under these growth conditions.

During exposure of the sample to a total amount of 10 L O_2 at 300 K, the sequence of images shown in Figs. 10.10(b) - (f) was taken. During O_2 exposure, there is no sign of adsorbed O or structural changes on the EuO islands. The invariable appearance of the EuO islands once more confirms that the bilayer is terminated by a layer of O ions, since a topmost Eu layer would be expected to react with the supplied O.

In contrast, the apparent height of the Ir terrace decreases substantially during O_2 dosing such that it appears 1.8 Å lower than the EuO islands after exposure to 10 L O_2. At the same time, the noise level on the Ir terrace initially increases, reaches a maximum in Figs. 10.10(d) and (e), until it eventually vanishes in Fig. 10.10(f), while new EuO(111) has formed at pre-existing EuO edges and on the bare Ir(111).

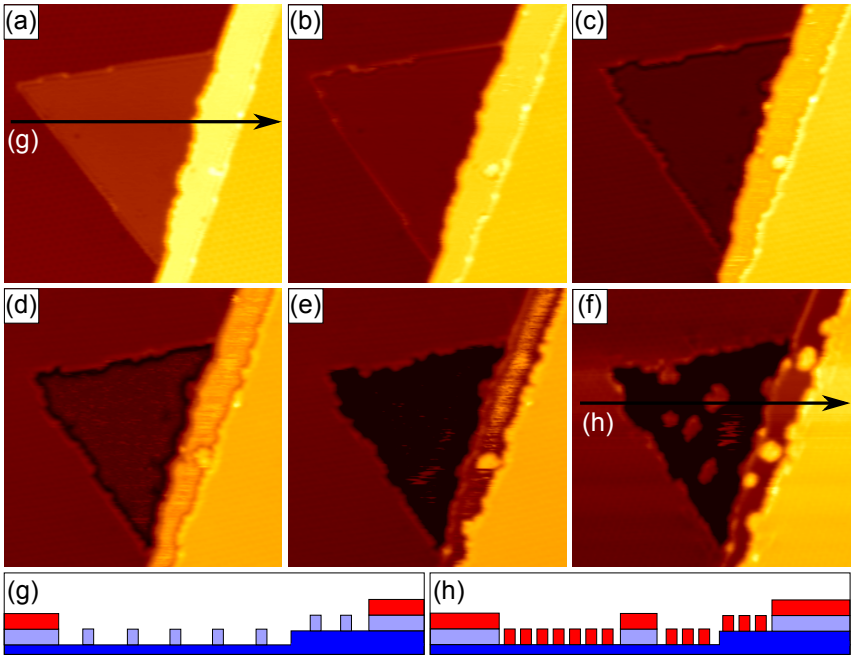

Figure 10.10: (a) - (f) STM topographs of a partial EuO(111) film grown under Eu excess (40 nm × 40 nm). The brightness of the EuO layers is kept constant. During tunneling the sample was exposed to 1×10^{-8} mbar O_2 at 300 K. The O_2 exposure increases from 0 L (a) via 2 L (b), 4 L (c), 6 L (d) and 8 L (e) to 10 L (f). The apparent height of Ir continuously decreases from +0.4 Å to -1.8 Å with respect to the EuO level. (g) and (h) show schematic profiles taken along the lines in (a) and (f). Color scheme: Ir dark blue, Eu light blue, O red.

The observations can be explained as follows: During O_2 exposure, O adsorbs and dissociates on the surface reacting with the Eu adatoms to EuO. The mobile EuO species incorporate into existing EuO island edges. Due to the increasing amount of mobile O the noise level increases. When a certain O amount is reached, O forms a dense saturation layer and loses its mobility resulting in disappearance of the noise. EuO species created in this late state of oxidation have a reduced mobility due to the O adlayer, and thus nucleate in new small islands. This corresponds to the situation shown in Fig. 10.10(f), which is also sketched in the line profile in Fig. 10.10(h).

Knowing that the apparent height of the EuO(111) bilayer islands must be referenced at room temperature to the level of the adsorbate layer and not to the bare Ir(111) certainly helps to understand why the EuO islands are initially imaged as depressions. However, the change in apparent height during O_2 exposure cannot be of geometric origin, since Eu and O adsorbate layers have similar topographic heights. Therefore, this effect is must be attributed to a change in the work function of the areas free of EuO(111), which is caused by the oxidation induced replacement of the Eu adatom phase by an O layer. Indeed, I

have shown in Sec. 3.1 that the tunneling current I through a one-dimensional barrier of width z is given by

$$I(z) \propto \exp\left(-k\sqrt{\bar{\Phi}}z\right) \tag{10.4}$$

with the constant $k = 2\frac{\sqrt{2m}}{\hbar} \approx 1.025\,\mathrm{eV}^{-\frac{1}{2}}\mathrm{\AA}^{-1}$ and the apparent barrier height $\bar{\Phi}$ which is proportional to the work function [352]. Thus, the work function directly influences the apparent height in constant current mode. Since it turned out to be successful for intercalated Eu, again $I(z)$ spectroscopy is used to measure work function differences (compare Sec. 3.1). As a quick reminder, the apparent barrier height difference $\Delta\bar{\Phi} = \bar{\Phi}_\mathrm{A} - \bar{\Phi}_\mathrm{B}$ can be determined by measuring the decay of the tunneling current with increasing tip distance above sample positions A and B. For a simple trapezoidal barrier the work function difference $\Delta\Phi$ is just twice the apparent barrier height difference $\Delta\bar{\Phi}$.
Fig. 10.11 shows the distance dependent tunneling current decay in logarithmic scale. All measurements were performed using a bias voltage of $U_\mathrm{s} = 0.5\,\mathrm{V}$ and a stabilization current of $I_0 = 0.35\,\mathrm{nA}$. After opening the feedback loop, the tip was retracted by 3 Å within 0.5 s while a small z-piezo drift was actively compensated. The data were averaged over several measurements and fitted with an exponential function to yield values for the apparent barrier height.

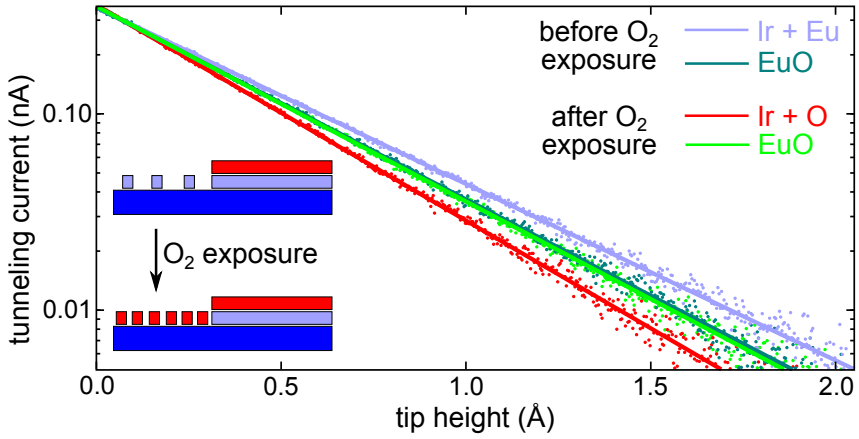

Figure 10.11: $I(z)$ measurements on Eu covered Ir (light blue) and EuO (dark green) for a 23% BL EuO(111) film grown with $f_\mathrm{Eu}/f_\mathrm{O} = 1.7$ at $T_\mathrm{growth} = 720\,\mathrm{K}$. The additional data for O covered Ir (red) and EuO (light green) are measured on the same sample after 10 L O_2 exposure. The lines are exponential fits to the data points.

The first set of measurements was performed on the surface shown in Fig. 10.10(a) before O_2 exposure. For the EuO(111) bilayer we obtain an apparent barrier height of $\bar{\Phi}_\mathrm{EuO} = (4.89 \pm 0.02)\,\mathrm{eV}$ (dark green), and for the Eu covered Ir(111) substrate $\bar{\Phi}_\mathrm{Ir+Eu} = (4.09 \pm$

0.02) eV. This results in a work function difference of $\Delta\Phi = (1.60 \pm 0.06)$ eV, with the work function of EuO(111) being higher than the one of Eu covered Ir(111).

In order to confirm the work functions achieved by $I(z)$ spectroscopy, additional measurements by means of Gundlach oscillations were performed (see Sec. 3.1 for details). To recall the basic concept, Gundlach oscillations shift by a constant energy value when measuring on sample areas of different work function, whereby the value of the shift is equal to the work function difference [224].

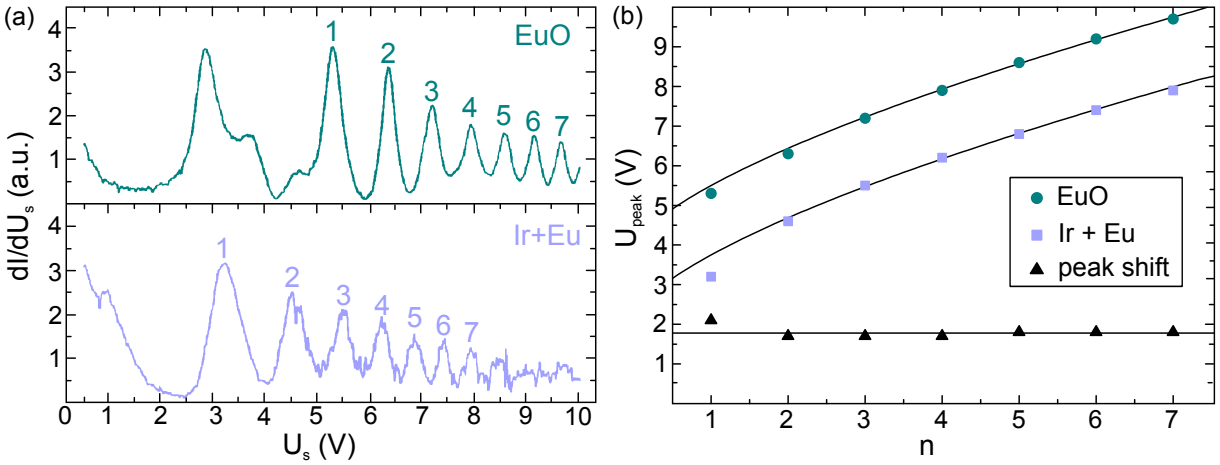

Figure 10.12: (a) STS spectrum measured above EuO (green) and Eu covered Ir (blue) showing Gundlach oscillations; their order n is indicated at the corresponding maximum. (b) Peak positions in dependence of n for EuO (green dots) and Ir+Eu (blue squares). The black lines are fits using Eq. 10.5 with $U_0 = 3.9\,\mathrm{V}$ (EuO) and $U_0 = 2.1\,\mathrm{V}$ (Ir+Eu), respectively, and $U_1 = 1.6\,\mathrm{V}$. Black triangles represent the shifts between EuO and Ir+Eu peak positions of the same order. For $n \geqslant 1$ the shift is constant as given by the red line.

Fig. 10.12(a) shows two STS measurements conducted on a sample grown under the same conditions as before ($f_{\mathrm{Eu}}/f_{\mathrm{O}} = 1.7$, $T_{\mathrm{growth}} = 720\,\mathrm{K}$). The spectra were taken between $0.5\,\mathrm{V} < U_{\mathrm{s}} < 10\,\mathrm{V}$, whereby U_{s} was modulated by 50 mV with a frequency of 433 Hz. The feedback loop was tuned to slow response, keeping the average tunneling current constant at $\bar{I} = 1.0\,\mathrm{nA}$. The recording time for each spectrum was 100 s. One observes pronounced oscillations, which are indicated by their order n in Fig. 10.12(a). The spectrum on the Ir surface is noisy because of the mobile Eu adatoms on the surface. In Fig. 10.12(b) the peak positions are shown in dependence of their order n, following in good agreement the expected relation

$$U_{\mathrm{peak}} = U_0 + U_1 \cdot n^{\frac{2}{3}}, \tag{10.5}$$

where U_0 and U_1 are offset and slope constants [353]. Only the first peak deviates from this dependence as it is most strongly influenced by the image potential of the surface. Furthermore, the peak at about 3 eV on the EuO(111) surface is not a Gundlach oscillation as it does not fit into the expected series of relative positions. Instead, it might be an interface state, as for example observed for MgO on Ag(111) [353].

In the lower part of Fig. 10.12(b) the shift between EuO and Ir+Eu peaks of the same order is shown. Except for the first order, the shift is quite constant with an average value of (1.77 ± 0.02) eV, whereby the EuO peaks lie at higher energies than the corresponding Ir+Eu peaks. Hence, Gundlach oscillations and $I(z)$ spectroscopy yield comparable values for the work function difference between Eu covered Ir and EuO of (1.77 ± 0.02) eV and (1.60 ± 0.06) eV, respectively. The deviation of the values obtained by the two entirely different methods provides an estimate for systematic error involved in the approach.

After 10 L O_2 exposure corresponding to the situation in Fig. 10.10(f) the apparent barrier height of the EuO(111) bilayer stays almost unchanged at $\bar{\Phi}_{\mathrm{EuO}} = (5.07 \pm 0.03)$ eV (light green). The slight difference of 4% most likely results from minor tip changes during gas exposure. In contrast, for the now O covered Ir(111) terrace a strong increase in the apparent barrier height to $\bar{\Phi}_{\mathrm{Ir+O}} = (6.13 \pm 0.04)$ eV is observed. Hence, the work function difference is $\Delta\Phi = (2.14 \pm 0.10)$ eV, with the work function of the EuO(111) bilayer being lower than the one of O covered Ir(111). A comparative measurement by means of Gundlach oscillations was not possible due to an increased interaction between tip and sample at higher voltages due to the adsorbed O.

In order to get quantitative estimates for the work functions of the different structures, one can use the O saturated Ir(111) surface as a reference. As known from literature, O adsorbed on Ir(111) gives rise to a work function increase of 0.56 eV at saturation coverage [354]. Adding this value to the work function of pristine Ir(111) ($\Phi_{\mathrm{Ir}} = 5.76$ eV [355]) yields $\Phi_{\mathrm{Ir+O}} = 6.32$ eV. On the basis of this reference, one can estimate the work function of Eu covered Ir(111) to be $\Phi_{\mathrm{Ir+Eu}} = (2.58 \pm 0.12)$ eV, consistent with the first-order peak of the Gundlach oscillations appearing at slightly higher energies. The value is 3.8 eV lower than for O covered Ir(111), and thus explains the considerable change in apparent height of the EuO(111) islands during O_2 exposure. The low work function of Eu covered Ir(111) is close to the value for bulk Eu of 2.5 eV [356] showing that it is mainly determined by the dilute Eu adatom phase.

Using again the O covered Ir(111) surface as reference, one obtains for the EuO work function $\Phi_{\mathrm{EuO}} = (4.18 \pm 0.10)$ eV , also consistent with the first-order peak of the Gundlach oscillations appearing at slightly higher energies. Compared to bulk EuO(100) with a work

function reported to be only 0.6 eV [357, 358] this value is remarkably high. Based on the expectation of a substantial surface dipole, one might have expected an even larger work function, but as pointed out in Sec. 10.1, the metalization of the bilayer implies a charge transfer to the substrate that tends to reduce the surface dipole and thus the work function. Furthermore, the compression of the electron density tail of the substrate by the oxide film may additionally lower the work function [57, 359]. Although local variations in the surface potential for polar oxide films as well as local barrier heights have already been reported several times [57, 360, 361], never experimental estimates for absolute values of the work function of polar oxide films were made.

We also calculated the work function of a bilayer EuO(111) on Ir(111) using DFT. Based on the optimized structures from Sec. 10.1 and using a vacuum length of about 50 Å between the periodic images of the slabs, a self-consistent calculation was carried out to obtain the Fermi energy E_{F} and the vacuum energy E_{vac}; the work function Φ is then equal to $E_{\mathrm{vac}} - E_{\mathrm{F}}$. For the work function of bare Ir(111) a value of 5.52 eV is found. The slight deviation from the literature value of 5.76 eV gives the systematic error of the approach. Next, the work function for 12.5% ML Eu on Ir(111) was calculated employing a dipole correction. The Eu coverage is close to the experimentally observed one of 11.5% ML Ir(111). The calculated result of $\Phi_{\mathrm{Ir+Eu}} = 2.51$ eV is in excellent agreement with the experimental value of 2.58 eV.

Finally, for the EuO bilayer on Ir(111) a work function of $\Phi_{\mathrm{EuO}} = 6.06$ eV is found. Consistent with the experiments, this value is substantially larger than the EuO(100) work function, but considerably deviates from the experimental result of about 4.2 eV. I cannot offer a sound explanation for this deviation. Although the experimental and calculated work functions agree well for Eu covered Ir(111) ($\Phi_{\mathrm{Ir+Eu}}$) and a number of cases investigated by us in the past [28, 63], certainly the assumption of a simple trapezoidal tunneling barrier is a severe simplification and might give rise to a substantial error in the experimental estimates under specific conditions.

10.2.3 Defects in the Bilayer

In the previous STM images already several types of defects in the EuO layer were visible, which I now analyze in more detail. In Fig. 10.13(a), arrows highlight a few of many defects that appear as missing superstructure protrusions. They have a much higher areal density for $T_{\mathrm{growth}} = 620$ K than for $T_{\mathrm{growth}} = 720$ K. In the inset of Fig. 10.13(a), two adjacent defects are enclosed by hexagons. The atomic rows run unaffectedly through the defects,

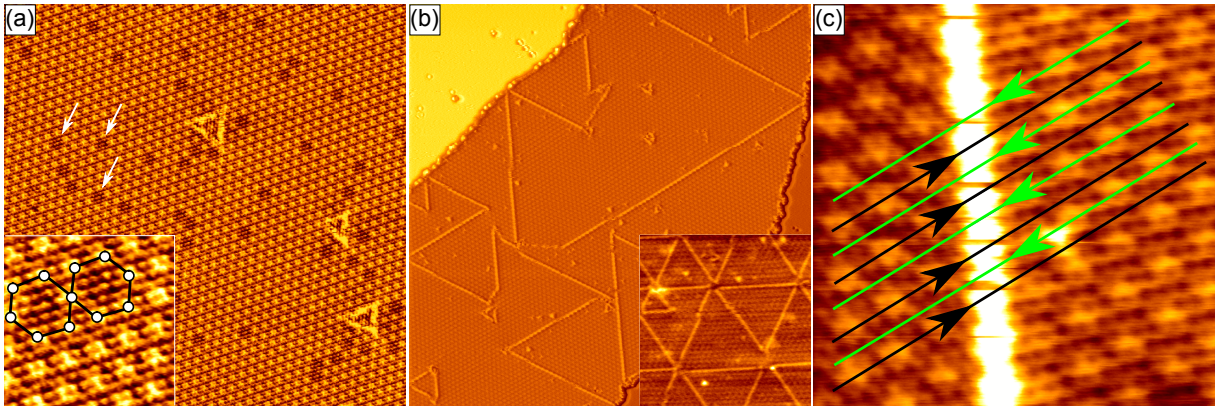

Figure 10.13: STM topographs showing different types of defects in EuO bilayer films. (a) $f_{Eu}/f_O = 1.7$, $T_{growth} = 620\,K$ ($37\,nm \times 37\,nm$). Inset: Point defects (indicated by arrows in the large scale image) appear as missing superstructure protrusions ($5\,nm \times 5\,nm$). (b) $f_{Eu}/f_O = 0.85$, $T_{growth} = 720\,K$ ($79\,nm \times 79\,nm$). Inset: Zoom on a EuO island with a network of line defects ($29\,nm \times 29\,nm$). (c) Same growth conditions as for (b). Black (green) lines indicate dense-packed superstructure rows on the left (right) side of the bright stripe ($8\,nm \times 8\,nm$).

i.e., there seem to be no missing or shifted atoms. Therefore, such superstructure defects likely mark missing atoms below the top layer, which would be Eu vacancies.

In Fig. 10.13(b), bright stripe defects are visible. They follow the directions given by the superstructure, and often form triangular networks, as especially well visible in the inset of Fig. 10.13(b). The smallest version of such a triangle is also present in Fig. 10.13(a). The bright stripes are due to anti-phase domain boundaries: When two EuO(111) islands grow together, it is improbable that their superstructures fit together as there are different translational domains due to the large size of the moiré unit cell. In such a case, a line type defect is expected where a registry shift of the superstructures occurs.

Evidence for this comes from Fig. 10.13(c), which shows the superstructure lattice well resolved on both sides of a stripe defect. The black (green) lines follow the dense-packed rows of the superstructure protrusions on the left (right) side. The lines are shifted with respect to each other confirming the presence of an anti-phase domain boundary. Similar line defects forming triangular structures also appear for thin layers of FeO(111) [362] and CoO(111) [58], and have been interpreted as dislocation loops of O vacancies. Here, this can be ruled out as the defects do not change during O_2 exposure, and are mostly observed under O rich growth conditions. The latter can be interpreted as follows: The higher O chemical potential apparently drives the growth kinetics towards formation of smaller domains by reducing the mobility of the initial oxide species. A similar effect has been previously observed for FeO(111) nanoislands on Pt(111) [363].

10.2.4 Influence of the Europium Excess

As shown before, under Eu rich conditions surplus Eu remains on the Ir surface during EuO growth. Increasing the deposited amount while maintaining the Eu rich growth conditions will cause a larger surface fraction to be covered by EuO(111) bilayer islands. The question arises, whether the increasing Eu excess is still accommodated on the decreasing area of Ir(111) terraces as a Eu adatom phase, or squeezed on the EuO(111) bilayer islands. In order to answer this question, a larger coverage of $\theta = 51\%$ BL was deposited at 720 K with a flux ratio of $f_{\mathrm{Eu}}/f_{\mathrm{O}} = 1.7$. Fig. 10.14(a) shows that the surface is afterwards fully covered by two different structures: (i) A flat surface labeled as Eu with hexagonal lattice symmetry as shown in Fig. 10.14(b). (ii) A structure labeled as EuO(111) with a rough appearance consisting of triangularly shaped objects (see Figs. 10.14(c) and (d)).

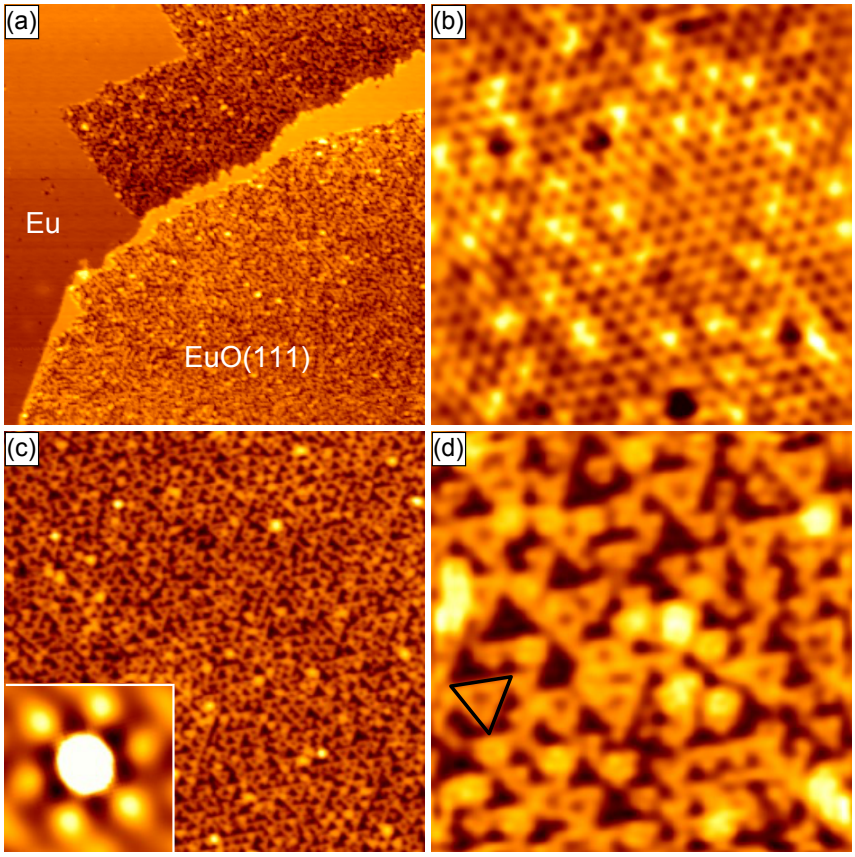

Figure 10.14: STM topographs showing a EuO film with 51% BL nominal coverage grown under $f_{\mathrm{Eu}}/f_{\mathrm{O}} = 1.7$ at $T_{\mathrm{growth}} = 720\,\mathrm{K}$. (a) Overview over the occurring structures (160 nm × 160 nm). (b) Eu structure (20 nm × 20 nm). (c) EuO(111) structure (70 nm × 70 nm). Inset: Self-correlation. (d) Same as (c) (20 nm × 20 nm). One of the most common triangles is indicated.

We interpret the structure labeled as Eu in Fig. 10.14(a) to arise from Eu adsorbed to Ir(111). Due to the higher coverage it forms a dense Eu layer instead of a dilute adatom phase. In LEED (not shown here), a hexagonal spot arrangement corresponding to a lattice constant of 4.2 Å is visible. This value is just in between the two Eu-Eu distances for an (110) plane of bulk Eu, which is quasi-hexagonal with atomic distances of 3.97 Å and 4.58 Å along and across the $\langle 001 \rangle$ chains, respectively. The structure visible in Fig. 10.14(b) has a NN distance of about 10 Å and therefore has to be a superstructure. Consistent with the assignment as Eu layer, the structure appears defective, which can be attributed to the high reactivity of metallic Eu.

Next, I address the structure labeled as EuO(111) in Fig. 10.14(a). From the higher resolved topographs in Figs. 10.14(c) and (d) one can see that it consists of either triangular depressions or protrusions on an otherwise flat surface. The edges of the triangles are aligned with the EuO$\langle 1\bar{1}0 \rangle$ directions. In the self-correlation shown in the inset of Fig. 10.14(c), a characteristic hexagonal order with a separation of about 2.2 nm was found, but as the size of the triangles is obviously not homogeneous there exists no long range order. The 2.2 nm are slightly more than the length of the largest triangles, one of which is indicated in Fig. 10.14(d). These show a depression at their center giving the impression that they consist of three smaller triangles at their corners. Thus, the large triangles probably appear when three small triangles have formed in the closest possible distance to each other. Hence, the 2.2 nm should be the shortest repetition distance of the small triangles.

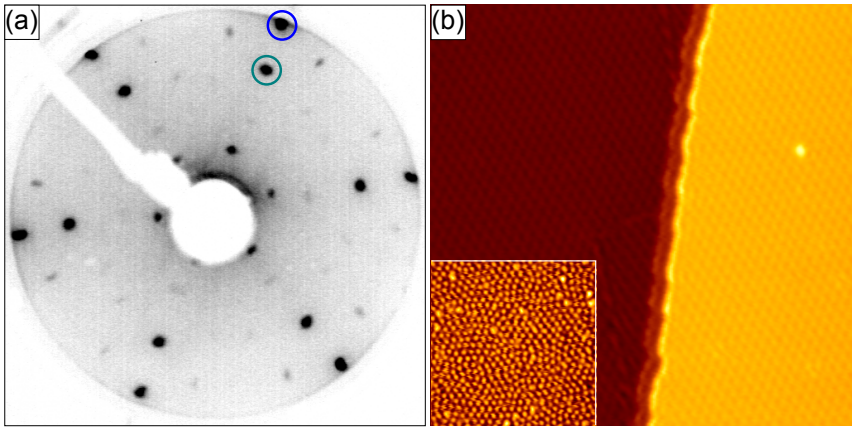

Figure 10.15: (a) LEED image (54 eV primary electron energy) of a EuO film (23% BL, $f_{\mathrm{Eu}}/f_{\mathrm{O}} = 1.7$, $T_{\mathrm{growth}} = 720\,\mathrm{K}$) after annealing to 1420 K for 60 s. Ir and EuO first-order spots are highlighted in blue and green, respectively. (b) Corresponding STM topograph (40 nm × 40 nm). The whole image is covered by EuO except for the small rim close to the descending substrate step. The inset (30 nm × 30 nm) shows the dilute Eu adatom phase on Ir at 35 K.

Triangular motifs as observed here are often found in reconstructions of polar surfaces. Especially the appearance of the polar (0001)-Zn surface of ZnO looks qualitatively very similar in STM [364]. Thus, we tentatively attribute the structure to consist of a EuO(111) bilayer where a reconstructed, partial third Eu layer has grown on top. The material for the partial layer stems from Eu that could not be accommodated anymore in the dense Eu layer on the Ir(111) substrate.

Further evidence for the polarity compensating effect of the Eu adlayer comes from the structure of the underlying bilayer: LEED displays a EuO(111) phase with a lattice parameter of 3.62 Å, i.e., there seems to be no further need for an expanded lattice constant. With the reduced lattice parameter the EuO(111) perfectly fits in a 3:4 registry with the Ir(111) substrate resulting in a lack of rotational misalignment.

10.3 Temperature Stability

Although the term *polar surface* bears the connotation of instability, I show here that the EuO(111) bilayer on Ir(111) is surprisingly stable. As demonstrated by the LEED pattern in Fig. 10.15(a), annealing of the EuO(111) bilayer up to 1420 K does not show any structural degradation of the material. To the contrary, the rotational misalignment of the film and the diffuse background are considerably lowered. Both effects can be attributed to annealing of defects in the film and the ensuing increase in the domain size. The lattice constant of (3.67 ± 0.03) Å is still slightly expanded compared to the bulk value, and therefore prohibits an ideal epitaxial 3:4 relation of EuO(111) and Ir(111). The STM image in Fig. 10.15(b) taken after annealing to 1420 K confirms the excellent film quality and the reduced defect density. Although the island size has substantially increased, the characteristic rim of uncovered Ir close to the descending step edge is still present. Since the rim is considered to be an effect of the bilayer dipole, one can conclude that polarity in the film remains also after annealing.

As visible on the upper terrace in Fig. 10.15(b), the apparent height of the EuO islands with respect to the substrate has changed during annealing to 1420 K, as they now appear higher than the surroundings. To explain this, we have once more a look at the Eu adatoms on Ir(111) at 35 K, and find that the phase has been diluted during annealing to 1420 K, either through re-evaporation to the vacuum or diffusion into the bulk. Compared to the situation before annealing, the Eu NN distance increased from (8.0±0.5) Å to (13.0±0.5) Å corresponding to a coverage decrease from 11.5% to 4.4% ML Ir(111). The reduced adatom density gives rise to a higher work function and therefore to an increase in the apparent

EuO height with respect to the surroundings. The findings above are consistent with the observation in Fig. 10.9 that the apparent height depends on the adatom density. As an additional remark, for annealing to even higher temperatures the spots belonging to EuO become gradually weaker, but are still visible till 1520 K, before they eventually vanish at a temperature of 1570 K.
Since bulk EuO has a high formation enthalpy of 5.85 eV/atom [365] attesting a strong Eu to O binding, while there is only a weak interaction between the oxide and the substrate, one might have expected a phase transformation to the more stable Eu_2O_3, or a transformation of the two-dimensional material to three-dimensional crystallites. The absence of such structural and morphological transformations indicates a deep energetic minimum of the EuO(111) bilayer on Ir(111). Its robustness makes it an interesting candidate for the toolbox of surface engineering with two-dimensional materials.

10.4 Magnetic Properties

Since EuO is a ferromagnetic semiconductor, it is of interest to explore whether the EuO(111) bilayer displays magnetic order at accessible temperatures. Whereas Kondo lattice model calculations predict a substantially decreased T_C for ultrathin EuO films with respect to the bulk value of 69 K [366], recently EuO(100) films with thicknesses of a few nanometers were demonstrated to display even an enhanced T_C [50].

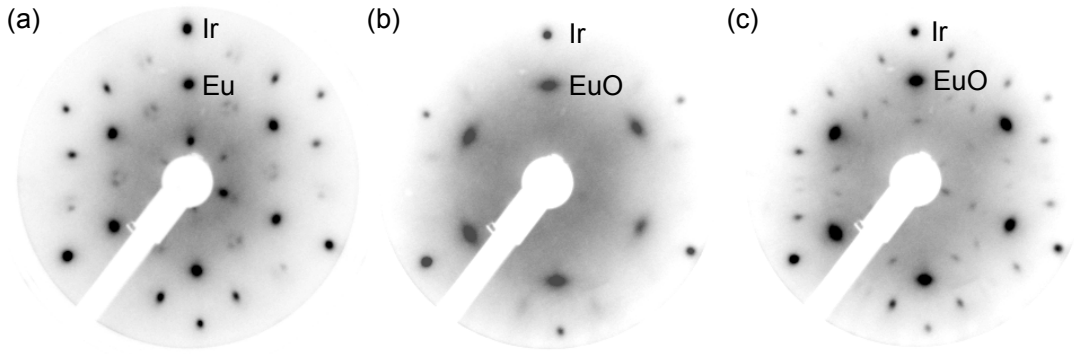

Figure 10.16: LEED images after (a) deposition of 49% ML Eu with respect to Ir(111) at 300 K, (b) subsequent exposure to 2 L O_2 at 300 K, and (c) annealing to 720 K for 60 s. At the end, the EuO(111) diffraction pattern with the characteristic superstructure spots is visible. All images are taken at 91 eV primary electron energy with a micro-channel plate LEED. Note that the planar screen slightly distorts the reciprocal lattice.

Since reactive MBE under Eu rich growth conditions prohibits the completion of the EuO(111) bilayer without a reconstructed Eu layer on top, an alternative approach was

tried here: First, a full monolayer of Eu was deposited onto Ir(111) at room temperature, which produces the LEED pattern shown in Fig. 10.16(a) (compare also Fig. 7.2). Afterwards, the Eu layer was reacted to EuO by exposure to 2 L O_2 at room temperature (see Fig. 10.16(b)), and subsequent annealing to 720 K. The resulting LEED pattern in Fig. 10.16(c) shows intense EuO(111) diffraction spots. Since the polar bilayer is slightly denser than the saturated Eu layer, the surface is covered by about 90% BL EuO(111), i.e., an almost complete polar bilayer can be realized by this method.

In order to explore the magnetic properties of the EuO(111) bilayer, MOKE measurements were conducted. Within the accessible resolution of 10 µrad in Kerr angle, no ferromagnetic behavior was detected down to 45 K sample temperature. Certainly, this observation does not exclude a coupling of the bilayer at even lower temperatures.

10.5 Summary

In this chapter, it has been shown that high quality bilayers of polar EuO(111) can be grown on Ir(111) by reactive MBE over a broad flux ratio and temperature range. Alternatively, Eu pre-deposition with subsequent oxidation and annealing yields films of the same quality. DFT calculations show that the EuO(111) bilayer is O terminated, which is experimentally backed up by *in vivo* exposure to O_2.

The EuO(111) bilayer does not obey a strict epitaxial relation with respect to the substrate, although therefore just a compression of 0.5 % would be needed. Instead, the in-plane lattice parameter is expanded by about 0.8%, resulting in rotational epitaxy with a scatter of up to 5°, and signifying a weak coupling to the substrate. The in-plane lattice parameter expansion results from a drastic contraction of the bilayer thickness from 1.49 Å in bulk EuO to 0.51 Å on Ir(111), which must be considered as the prime mechanism to reduce the electrostatic potential within the film. Furthermore, DFT shows that the bilayer is metallic, providing an additional contribution to reduce the polarity. The residual dipole moment of the EuO(111) bilayer implies a electrostatic interaction with the step dipoles of the Ir(111) substrate. Despite the remaining polarity, the EuO(111) bilayer is thermally highly stable up to 1420 K.

For larger coverages and Eu rich growth conditions an additional mechanism of polarity reduction can be identified: Eu is squeezed onto the EuO(111) bilayer where it creates a partial adlayer consisting of triangular patches that lifts the in-plane lattice parameter reduction (and presumably also the bilayer contraction), brings the islands into perfect epitaxy with the substrate, and lifts the rotational misalignment.

Depending on the growth conditions either Eu or O is adsorbed on the bare Ir(111) between the EuO islands, whose apparent height strikingly depends on the co-adsorbed species. Extensive work function measurements show that the variation of the apparent EuO bilayer island thickness is predominantly caused by work function variations in their surroundings. Experimentally, the work function of EuO(111) on Ir(111) is estimated to $\Phi_{\mathrm{EuO}} \approx 4.2\,\mathrm{eV}$. This value is substantially larger than for the (100) surface of a EuO single crystal, consistent with the DFT calculations.
Finally, two specific defects in the EuO(111) bilayer are identified: Subsurface vacancies, and antiphase domain boundaries resulting from island coalescence during growth. MOKE measurements at 45 K reveal that the EuO(111) bilayer does not exhibit ferromagnetism down to this temperature.

CHAPTER 11

Summary and Outlook

In this thesis, I studied in detail the structural, magnetic and binding properties of novel two-dimensional materials. To conclude, I summarize in this chapter the most important results and give perspectives for future investigations.

Intercalated Europium

Eu intercalates at elevated temperatures underneath Gr on Ir(111), thereby forming a (2×2) superstructure with respect to the Gr lattice. The layer can be compacted to a $(\sqrt{3} \times \sqrt{3})$R30° structure by further Eu deposition. DFT calculations showed that a large energy gain is the driving force for intercalation. The intercalated material forms complex patterns, which can be consistently explained by the interplay of binding inhomogeneities within the moiré unit cell and a change in the strain state of Gr during intercalation. The intercalation step density directly visualizes local variations in the initial strain distribution of Gr. Since binding inhomogeneities and pre-existing strain are present for epitaxial Gr on a variety of substrates, it is probable that the observed pattern formation is a more general phenomenon and might be present also for other systems.
By means of ARPES, a rigid shift of the Gr band structure by about -1.5 eV due to strong n-doping is found. Future work should aim to assign the additionally observed features in the spectra to band structures calculated by DFT including the Ir substrate. Experimentally, it would be of special interest to perform in addition spin-resolved ARPES measurements on intercalated Eu. Provided that the energy resolution is high enough, a potential spin splitting of the Dirac cone could so be directly detected.
To get insight to the intercalation mechanism, the Eu intercalation was monitored in real time by PEEM and LEEM. Thereby, the dominating pathway for intercalation was found

to be penetration at wrinkles, just as in the case of Cs intercalation. It would be desirable to find imaging conditions under which the intercalation and the wrinkle network can be imaged at the same time, since the relaxation of strain during intercalation should be reflected also in the amount and size of the wrinkles.

STM experiments with low Eu coverages indicated that intercalation via five-seven defects at small-angle grain boundaries might be an additional pathway for intercalation. To corroborate this interpretation, it would be desirable to find out the minimum temperature at which Eu can intercalate (somewhere between 400 K [28] and 620 K [this thesis]). STM experiments at this temperature could prove that the Eu atoms indeed penetrate at the five-seven defects and not just bind there upon diffusion under the Gr sheet.

Adsorption on Intercalated Graphene

Intercalation on the backside of Gr is an efficient tool to change the binding of adsorbates on its frontside. I have shown that the binding of cationic adsorbates is weaker to intercalated Gr than to pristine Gr. This preference is linked to a change in the local work function by doping from the intercalant. DFT calculations reveal that the Coulomb penalty associated with charge redistributions and a substrate-dependent screening reduce the binding energy difference estimated from the work function difference.

The concept of manipulating adsorption by intercalation is envisioned to be applicable also for other types of adsorbates. In this context, Huttmann *et al.* have meanwhile shown that the vdW binding of polyaromatic molecules (such as naphthalene or benzene) to Gr is strengthened by the n-doping from intercalated Eu, and weakened by the p-doping from intercalated O [273, 367]. The results are supported by vdW-DFT calculations and thermodesorption spectroscopy (TDS) [367]. The underlying mechanism is a change in the polarizability of the π/π^* Gr orbitals as a function of their doping-dependent filling. Moreover, radicals that form covalent bonds with Gr might show a preferred adsorption. By using a doping pattern, this would allow to imprint a chemical pattern to Gr, which might have far reaching practical consequences for lithography.

The adsorption of Eu on fully closed (2×2) and $(\sqrt{3} \times \sqrt{3})$R30° intercalation layers was shown to be similar to Eu adsorption on pristine Gr. Large adsorbed Eu islands with $(\sqrt{3} \times \sqrt{3})$R30° structure are formed, but the doping from the intercalant prohibits the formation of a cluster phase. In Eu $(\sqrt{3} \times \sqrt{3})$R30° intercalation layers, characteristic line defects were observed. Supplemental atomically resolved STM images could prove that these lines are related to anti-phase domain boundaries.

Rare Earth Layers on Ir(111)

Around the saturation coverage of a single monolayer, Eu forms a dense layer on Ir(111). Its large unit cell can be approximated by (7×7) Eu atoms on (10×10) Ir atoms. The layer shows a high density of triangular defects, which are presumably be nuclei of oxidation. This might be proven by intended exposure to O_2. For future investigations, it would be interesting to image the system at low temperatures with spin-polarized STM. Since already bulk Eu has an unusual helical spin structure, peculiar magnetic arrangements such as skyrmion lattices [368] might also occur for the monolayer.

Besides Eu, also Gd forms at 370 K a flat layer on Ir(111) with a slightly expanded lattice parameter compared to the bulk. In addition to the adsorbed layer, Gd atoms are incorporated into the Ir surface. The surface alloying can be prevented by low temperature deposition, but at the cost of less order. By annealing the Gd layer to higher temperatures, two different types of alloys are observed: One embedded in the Ir surface with a $(\sqrt{3}\times\sqrt{3})$R30° superstructure, and one adsorbed to Ir(111) with a (2×2) superstructure, both revealed by LEED. Since LEED does not allow to draw inferences on the atomic arrangement within the superstructure unit cell, atomically resolved STM imaging on the two alloy surfaces is highly desirable. Moreover, experiments with lower Gd coverages might give insight to the processes in the submonolayer regime.

It is certainly of interest to study the magnetic properties of the Gd surface alloy. It has been previously shown that there is a strong correlation between structure and magnetism for many surface alloys [369, 370]. Furthermore, interesting physical phenomena such as enhanced magnetic moments [371], giant Rashba splitting [372], and unconventional spin topologies [373] have been observed for various two-dimensional alloys.

Magnetism of Intercalated and Adsorbed Europium Layers

The two intercalated Eu layers have fundamentally different magnetic properties: Whereas the (2×2) layer is paramagnetic, the $(\sqrt{3}\times\sqrt{3})$R30° layer shows a substantial magnetic coupling without hysteresis. It is reasonable that the layer is ferromagnetic, but was measured slightly above the Curie temperature. However, a more complex behavior cannot be excluded. A better understanding might be obtained by future measurements of temperature-dependent magnetization loops.

A strong in-plane anisotropy was shown to arise essentially from the two-dimensionality of the Eu layer. Interestingly, the magnetic behavior of the $(\sqrt{3}\times\sqrt{3})$R30° layer strongly deviates from its bulk counterpart EuC_6 indicating the importance of the Ir substrate, which is supported by DFT calculations of the spin density. The Eu intercalation system

might serve as a playground for theoretical investigations of two-dimensional magnetic layers in general, which are not yet comprehensively understood.

At first sight, the lack of spontaneous magnetization darkens the hopes of a spin split Dirac cone in Gr, which was predicted by DFT only under the assumption of ferromagnetic order. Nevertheless, the measurements have shown that the Eu spins can be be easily aligned in an external field. A possible way to create such an external field is a hybrid 3d/4f structure: A ferromagnetic Co or Ni multilayer film (Fe is not suitable since it might prefer the non-magnetic fcc stacking [374]) separated from the Gr sheet by an intercalated Eu layer. For such a Gr/Eu/FM/Ir(111) system, the ferromagnet might induce a stable magnetization in the Eu layer, which in turn induces a spin-split Dirac cone in Gr and prevents hybridization between the transition metal film and Gr.

An alternative to Eu might be Nd with its more extended 4f orbitals, which might induce an even larger spin-splitting by a mild hybridization. Furthermore, Nd atoms carry an even higher magnetic moment of $10\,\mu_B$ ($S = \frac{4}{2}$, $L = 6$). As preliminary work, STM and LEED experiments should determine the optimum conditions for Nd intercalation. Subsequent XMCD measurements could then reveal the magnetic properties. Also intercalation of Gd might be of interest, since Gd is a bulk ferromagnet with a Curie temperature close to 300 K. However, alloying with the Ir(111) substrate might be a problem at the elevated temperatures needed for intercalation. On the other hand, this would not matter if the surface alloy also shows magnetic order and preserves the band structure of Gr.

Since one motivation of this thesis was to induce magnetism in Gr, the reader might ask why the magnetic properties of the Gr layer itself have not been investigated. The simple answer is that the C K adsorption edge at about 284 eV [18] is energetically not accessible at the ID08 beamline. Thus, XMCD measurements at a different synchrotron beamline would be the next step to find out whether also magnetic moments are induced to. However, one should be careful with the expectations since the magnetic moments are probably very small (compare Tab. 8.3). Furthermore, only the orbital moment can be measured since the C 1s level is not spin-orbit split.

All samples investigated with Eu adsorbed on top of Gr were deteriorated by contamination during the sample transfer to the XMCD chamber. The same holds for the magnetism of a Eu layer directly adsorbed to Ir(111). The contamination is assumed to result from the reaction of Eu with water to EuO. However, the amount of contamination and the resulting structure is not known. Nevertheless, all samples show a substantial magnetic coupling. Thus, it might be fruitful to investigate the magnetic properties of well-defined EuO films on Gr or Ir(111) by XMCD.

Magnetism of Metal Clusters on Graphene

Small moiré-templated $Pt_{15}Co_{28}$ clusters show a Langevin magnetization behavior as expected for superparamagnetism. For larger $Ir_{50}Co_{500}$ and Co_{2700} clusters a hysteresis opens due to the higher blocking temperature of about 30 - 40 K. An enhanced ratio of orbital to spin moment was found for the smallest clusters. It gradually decreases towards the bulk value with increasing cluster size. All clusters show vanishing anisotropy which indicates a weak interaction with the underlying Gr substrate.

For $Pt_{15}Co_{28}$ clusters, the size of the magnetic entity appeared much larger than a single cluster. It was speculated that this arises from an underestimation of the share of coalesced clusters. By enhancing the quality of the cluster lattice via increasing the Gr growth temperature and changing the seeding clusters from Pt_{12} to Ir_{18}, the amount of coalescence was substantially reduced. In consequence, a moment of the magnetic entity in agreement with the one of a single cluster was found.

Besides Co clusters, also Rh clusters were investigated in order to find out whether they are magnetic as in the free beam and on weakly interacting substrates, or non-magnetic as on metal substrates. The corresponding XMCD data did not show any sign of magnetism for Rh clusters on Gr. However, because of the low signal-to-noise ratio of the measurements, the presence of magnetic moments as small as found on weakly interacting substrates cannot be excluded. Looking forward, the large background around the Rh $M_{2,3}$ edges making an analysis complicated might be avoided by investigating the $L_{2,3}$ edges. This would require measurements at a different beamline. I note that the ID08 beamline has meanwhile been rebuilt as beamline ID32, providing higher magnetic fields up to ± 9 T and lower temperatures down to 7 K. Furthermore, the new beamline optics might result in a lower signal-to-noise ratio and thus a lower detection limit.

Polar Europium Oxide on Ir(111)

A EuO(111) bilayer was grown on Ir(111) by reactive MBE. Alternatively, Eu deposition with subsequent oxidation and annealing yielded films of the same quality. DFT calculations showed that the EuO(111) bilayer is O terminated. It has a strongly reduced layer distance compared to the bulk compound, which results in a slightly expanded in-plane lattice parameter and rotational epitaxy. The strong layer contraction together with a metalization of the naturally insulating material reduces the electrostatic potential of the film. The residual dipole moment implies a electrostatic interaction with the step dipoles of the Ir(111) substrate. Under Eu rich growth conditions the polarity can be additionally

reduced by formation of a partial Eu adlayer. A further STM investigation might yield an atomistic model for the triangular structures within the adlayer.
Depending on the growth conditions, either Eu or O is adsorbed on the bare Ir(111) between the EuO islands, whose apparent height strikingly depends on the type of the co-adsorbed species. Extensive work function measurements showed that the apparent EuO bilayer island thickness is predominantly influenced by the work function in the surroundings. Two specific defects in the EuO(111) bilayer were identified, which are subsurface vacancies and antiphase domain boundaries. Concerning the magnetic properties, the EuO(111) bilayer does not exhibit ferromagnetism down to 45 K.
The EuO(111) bilayer on Ir(111) is the first example of a polar bilayer of a rare earth metal. Although its properties are in several respects similar to the more frequently described polar bilayers of transition metals, it is unique in its quality and thermal stability. These properties make the EuO(111) bilayer an interesting candidate for the toolbox of surface engineering with two-dimensional materials. Moreover, it is a promising candidate for further investigation by XMCD, ARPES, and STS. In this context, a spin-polarized surface state has recently been observed on EuO(100) on Gr [51]. It is certainly of interest to investigate, whether such a surface state is also present for the EuO(111) bilayer on Ir(111). Finally, I hope that the present thesis triggers future work to explore the properties of other polar bilayers based on rare earth metals.

APPENDIX A

Appendix

In this appendix, I show results which have not yet been analyzed in detail, or are not completely understood since they require additional experiments. Nevertheless, they might be of interest for further investigations.

A.1 Band Structure of Graphene at the M Point

In this thesis, I discussed only ARPES spectra of Gr taken at the K point of the Brillouin zone. In addition, also data at the M point (see Fig. 2.1) were recorded. The results before and after intercalation of Eu in (2×2) and $(\sqrt{3} \times \sqrt{3})$R30° structure are shown in Fig. A.1. Note that the spectra are not converted from angle- to k-space.

For pristine Gr (see Fig. A.1(a)), the van Hove singularity of the π band is clearly visible -2.3 eV below the Fermi edge. After Eu intercalation, the bottom of the π band shifts down to about -4.3 eV and becomes substantially broader (see Figs. A.1(b) and (c)). The shift is related to the strong n-doping by the intercalated Eu layer, though larger than the expected -1.5 eV derived from the shift of the Dirac point.

In addition to the π band of Gr, several weak bands are visible. To enhance their visibility, they are indicated by black lines and arrows. For pristine Gr shown in Fig. A.1(a), there is a weakly dispersing band close to the Fermi edge. For the (2×2) intercalation structure in Fig. A.1(b), a flat band appears at a higher binding energy of about -1.0 eV. Most interesting, two bands cross below the Fermi edge for the $(\sqrt{3} \times \sqrt{3})$R30° structure in Fig. A.1(c). Such a band structure is typically observed for Rashba-split surface states. To find out more about the origin of the bands in all three cases, a comparison to DFT band structure calculations including the Ir substrate would be needed.

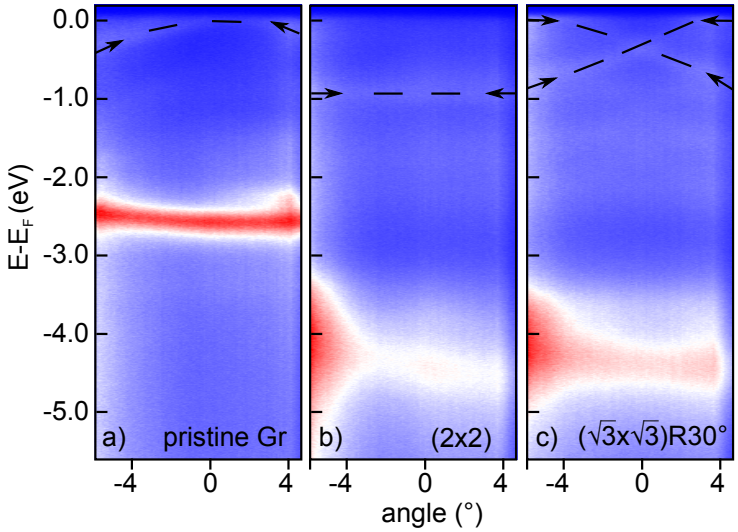

Figure A.1: (a) ARPES spectrum of pristine Gr on Ir(111) at the M point along KK' direction. (b) Spectrum after intercalation of a complete (2×2) Eu intercalation layer. (c) Spectrum after intercalation of a complete $(\sqrt{3} \times \sqrt{3})$R30° Eu intercalation layer.

A.2 Higher Gadolinium Coverages on Ir(111)

In Sec. 7.2, I discussed the growth of Gd on Ir(111) only for one particular coverage. In addition, I also investigated higher Gd coverages, which turned out to be even more complex. Nevertheless, here a short overview about the results shall be given.

In Fig. A.2(a), the double amount of Gd compared to Fig. 7.3(a) was deposited at 370 K. According to the quartz microbalance, this means 14% ML with respect to Ir(111), but as already discussed in Sec. 7.2, the real coverage is substantially higher. Just as in Fig. 7.3(a), a flat layer covers almost the whole surface in Fig. A.2(a). Since the double amount was deposited, one might argue that a second Gd layer was grown. However, the Ir spots are still intense in LEED (see Fig. A.2(c)), which disagrees with the interpretation that the substrate is covered by two layers of Gd. In addition to the Ir spots, there are spots at a lattice constant of (2.94 ± 0.02) Å. The value is close to the Ir lattice constant, resulting in a moiré pattern visible in LEED. Since the structure is $(3.80\,\text{Å}/2.94\,\text{Å})^2 - 1 = 67\%$ denser than the one in Fig. 7.3(a) and the double amount was deposited, the lattice constant is roughly consistent with both structures forming a complete monolayer. However, it is surprising how the Gd atoms might have been compressed to a distance of 2.94 Å, whereas the bulk NN distance is 3.64 Å.

After annealing the sample in Fig. A.2(b) to 870 K, a (2×2) superstructure is found in the corresponding LEED image in Fig. A.2(e). The same pattern was already observed for the

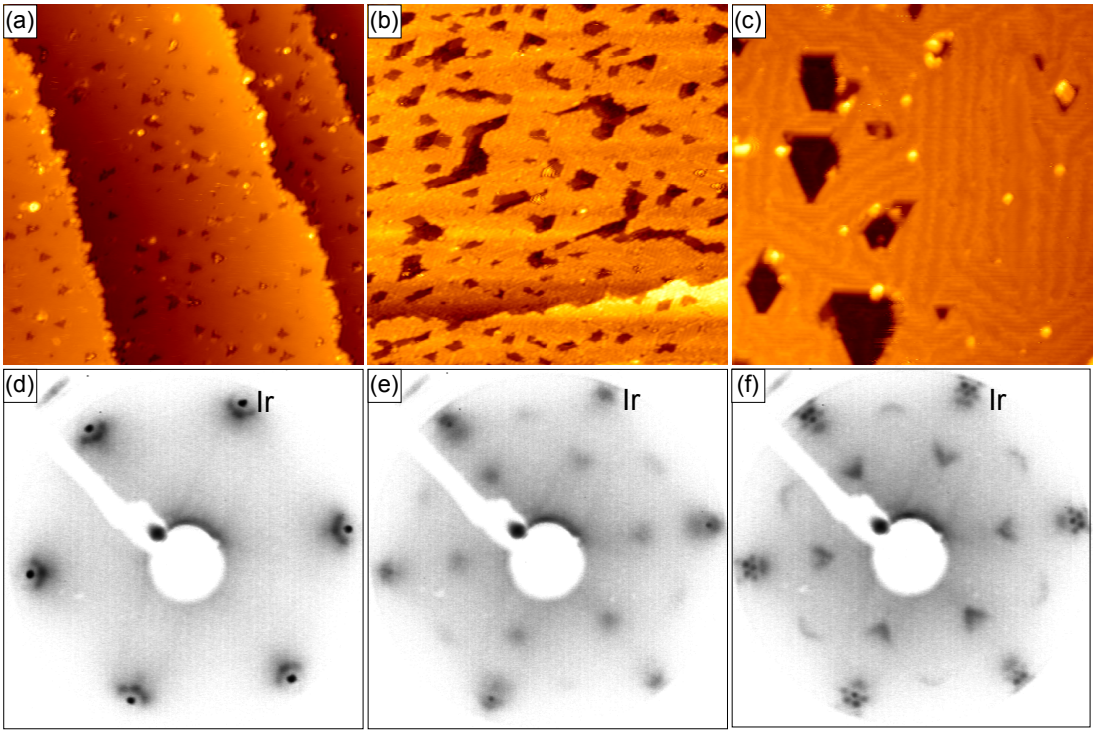

Figure A.2: STM images (45 nm × 45 nm) of an intermediate coverage of Gd on Ir(111). (a) After deposition at 370 K. (b) After annealing to 870 K. (c) After annealing to 1070 K. (d) - (e) Corresponding LEED images at 78 eV primary electron energy.

lower Gd coverage in Fig. 7.5(h), indicating that the same surface alloy is formed. Consistent with the double deposited amount, the coverage in Fig. A.2(b) is approximately twice as large as in Fig. 7.5(h). When annealing the sample to an even higher temperature of 1070 K (see Fig. A.2(c)), the holes in the layer coalesce and an additional stripe pattern with low corrugation evolves. The latter might be a reconstruction related to strain relaxation. The corresponding LEED pattern in Fig. 7.5(f) still shows the (2×2) superstructure, but with a complex, winglike fine structure. Around the first-order Ir spots, a moiré-like spot arrangement is observed, but note that it is rotated by 30° compared to ordinary moiré patterns, such as the one for Gr on Ir(111).

Finally, also a Gd coverage of 41% ML Ir(111) according to the quartz microbalance, i.e., the triple Gd amount of the one in Fig. A.2 was deposited. The results are shown in Fig. A.3. At 370 K, the Gd forms rough, three-dimensional structures, presumably on top of the flat layer shown in Fig. A.2(a). Consequently, the corresponding LEED image does not reveal any order (not shown here). When annealing the sample to 870 K or 1070 K as shown in Figs. A.3(b) and (c), the three-dimensional structures form flat islands. They possess a further unknown atomic structure as apparent by the LEED

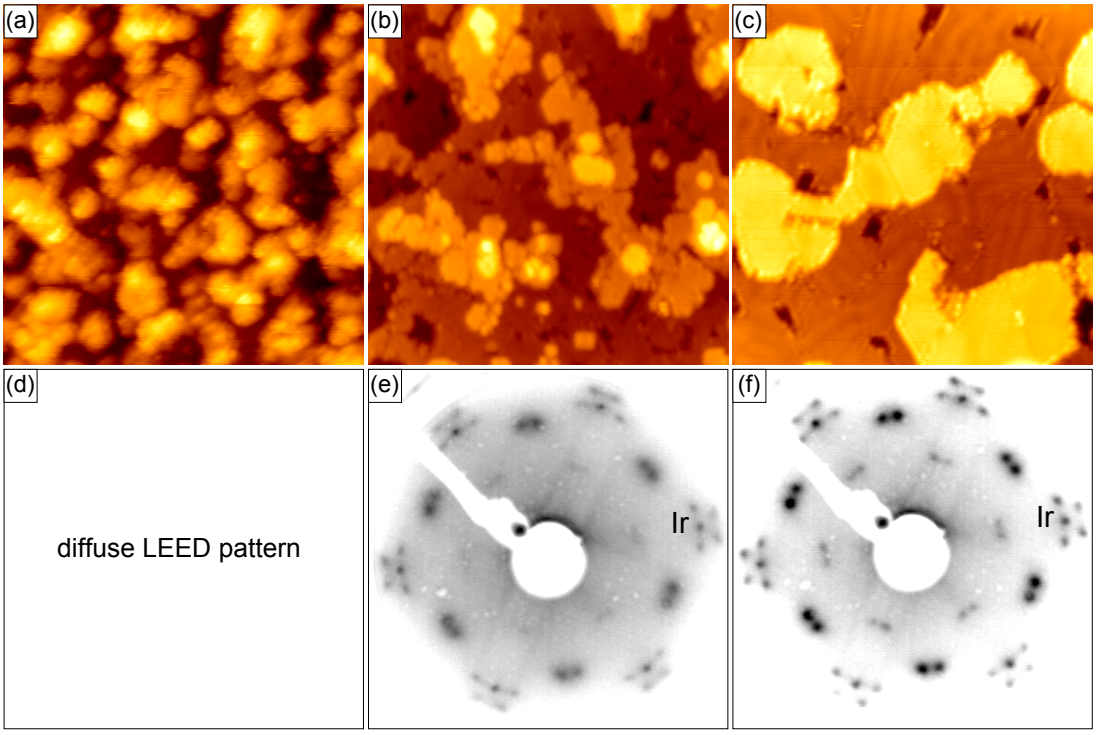

Figure A.3: STM images (45 nm × 45 nm) of a high coverage of Gd on Ir(111). (a) After deposition at 370 K. (b) After annealing to 870 K. (c) After annealing to 1070 K. (d) - (e) Corresponding LEED images at 68 eV primary electron energy.

images in Figs. A.3(e) and (f). Although the LEED pattern is intense and highly ordered, up to now a model for the observed structure is missing.

Due to the strong dependence on coverage and temperature, the incommensurable structures, and the tendency to form surface alloys, the epitaxial growth of Gd on Ir(111) is highly complex. Thus, a full analysis of the system is out of the scope of the present thesis, but might be a challenging task for future investigations.

A.3 Magnetic Properties of Cobalt on Ir(111)

In order to illustrate that the magnetic properties of Co clusters on Gr are peculiar, it is instructive to deposit the same amount of Co on the bare Ir(111) surface. This was done for a coverage of 50% ML with respect to Ir(111) at room temperature, which results in the growth of pseudomorphic monolayer islands (not shown here). The corresponding magnetization loops under normal and grazing incidence are shown in Fig. A.4. In contrast to the isotropic Co_{2700} clusters in Fig. 9.9, here a pronounced out-of-plane anisotropy is found. In consequence, the magnetization cannot be saturated within the plane even at

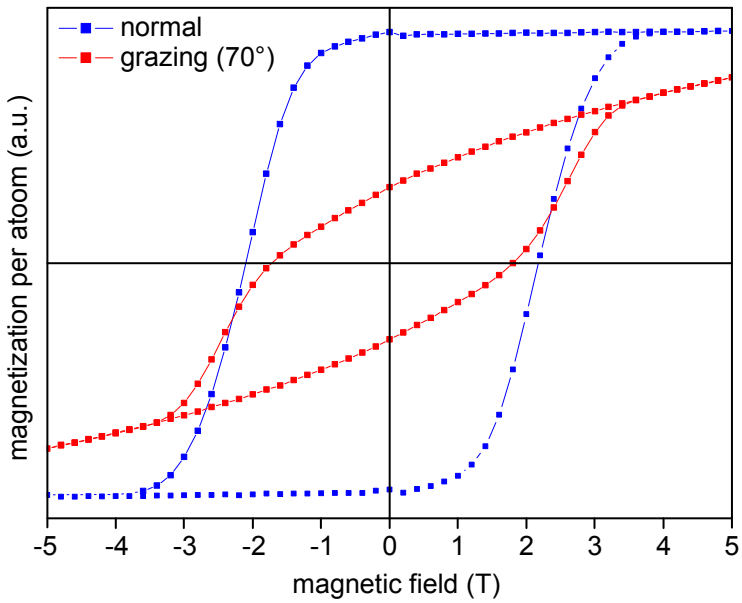

Figure A.4: Normal and grazing hysteresis loops of 50% ML Co on Ir(111) at 10 K.

5 T. This shows that other anisotropies than the one originating from the two-dimensional shape have to be of importance in the present case.

The hysteresis with a large coercive field of about 2 T shows that the Co monolayer is ferromagnetic. The effective spin moment at 5 T of about 1.3 μ_B is reduced by 20% compared to the bulk value. This could be an effect of the dipolar term $\langle T_z \rangle$, which might not vanish for the strong anisotropy. The ratio m_L/m_S adopts a value of 0.15. Just as observed for the smallest clusters on Gr, the ratio is enhanced compared to the bulk value, which can be attributed to the low coordination of the Co atoms.

A.4 Magnetism of Gadolinium Layers

Besides intercalated Eu layers, also the magnetic properties of Gd layers were investigated by XMCD. However, there was no experience with the intercalation of Gd in advance. In a first attempt, Gd was deposited at room temperature onto Gr and then stepwise annealed to a maximum temperature of about 1000 K, until a (2×2) superstructure was visible in LEED. However, STM reveals a flat film with three different height levels (not shown here), which leads to the conclusion that presumably a Gd film on top of Gr was grown. The corresponding XAS spectra reveal a pronounced XMCD effect as shown in Fig. A.5(a). The sum rules yield a spin moment around 7 μ_B in agreement with the expectations. The

orbital moment vanishes just as in the case of Eu, indicating a $4f^7$ configuration. The magnetization loops in Fig. A.5(b) show an in-plane anisotropy of the film. The high zero-field susceptibility without hysteresis is indicative for superparamagnetic behavior.

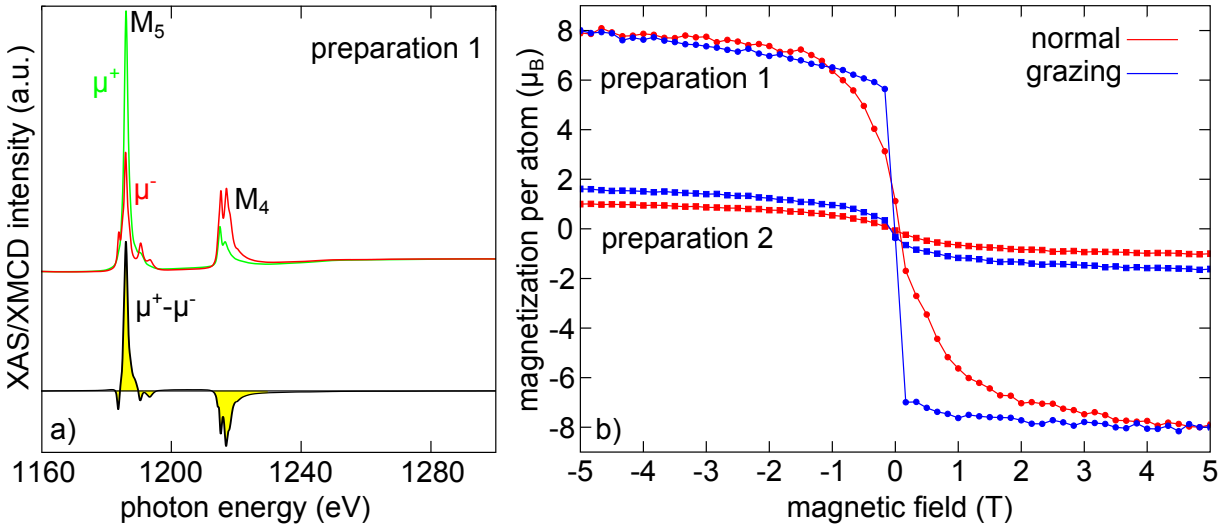

Figure A.5: a) XAS and XMCD signal at 5 T and 10 K for Gd on Ir(111) according to the first preparation (see text). (b) Magnetization loops at 10 K under normal and grazing incidence for both Gd preparations (see text). The curves are averaged over both field ramping directions.

In a second preparation, Gd was deposited onto Gr at an elevated temperature of 970 K. LEED reveals again a (2×2) superstructure, but of much higher quality than before. Unfortunately, the LEED pattern could not be photographed. The structure might be related to intercalated Gd, but there is no further proof. The corresponding XMCD spectra (not shown here) yield only a small spin moment on the order of $1\,\mu_B$ and a slight in-plane anisotropy (see Fig. A.5(b)). Note that the saturation magnetization is much less than expected than for paramagnetism (compare Fig. 8.2). Therefore, the observations might be an indication for ferri- or antiferromagnetic coupling. Looking forward, it would desirable to investigate the intercalation of Gd underneath Gr by STM and LEED to get more insight to the structures investigated by XMCD.

Bibliography

[1] A. P. Guimarães: *Principles of Nanomagnetism*. Springer, Berlin (2009). (Cit. on pp. 1, 23).

[2] R. Blakemore: "Magnetotactic bacteria". *Science* **190** 377 (1975). DOI: 10.1126/science.170679. (Cit. on p. 1).

[3] R. Wiltschko and W. Wiltschko: *Magnetic Orientation in Animals*. Springer, Berlin (1995). (Cit. on p. 1).

[4] R. E. Kopp and J. L. Kirschvink: "The identification and biogeochemical interpretation of fossil magnetotactic bacteria". *Earth.-Sci. Rev.* **86** 42 (2008). DOI: 10.1016/j.earscirev.2007.08.001. (Cit. on p. 1).

[5] M. Evans and F. Heller: *Environmental magnetism: principles and applications of enviromagnetics*. Academic Press, San Diego (2003). (Cit. on p. 1).

[6] V. V. Mody et al.: "Magnetic nanoparticle drug delivery systems for targeting tumor". English. *Appl. Nanosci.* 1 (2013). DOI: 10.1007/s13204-013-0216-y. (Cit. on p. 1).

[7] R. Hergt et al.: "Magnetic particle hyperthermia: nanoparticle magnetism and materials development for cancer therapy". *J. Phys. D: Condens. Matter* **18** S2919 (2006). DOI: 10.1088/0953-8984/18/38/S26. (Cit. on p. 1).

[8] M. Colombo et al.: "Biological applications of magnetic nanoparticles". *Chem. Soc. Rev.* **41** 4306 (2012). DOI: 10.1039/C2CS15337H. (Cit. on p. 1).

[9] M. N. Baibich et al.: "Giant Magnetoresistance of (001)Fe/(001)Cr Magnetic Superlattices". *Phys. Rev. Lett.* **61** 2472 (1988). DOI: 10.1103/PhysRevLett.61.2472. (Cit. on p. 1).

[10] G. Binasch et al.: "Enhanced magnetoresistance in layered magnetic structures with antiferromagnetic interlayer exchange". *Phys. Rev. B* **39** 4828 (1989). DOI: 10.1103/PhysRevB.39.4828. (Cit. on p. 1).

[11] P. A. Grünberg: "Nobel Lecture: From spin waves to giant magnetoresistance and beyond". *Rev. Mod. Phys.* **80** 1531 (2008). DOI: 10.1103/RevModPhys.80.1531. (Cit. on p. 1).

[12] I. McFadyen, E. Fullerton, and M. Carey: "State-of-the-Art Magnetic Hard Disk Drives". *MRS Bull.* **31** 379 (2006). DOI: 10.1557/mrs2006.97. (Cit. on p. 1).

[13] S. A. Wolf et al.: "Spintronics: A Spin-Based Electronics Vision for the Future". *Science* **294** 1488 (2001). DOI: 10.1126/science.1065389. (Cit. on p. 1).

[14] I. Zutić, J. Fabian, and S. Das Sarma: "Spintronics: Fundamentals and applications". *Rev. Mod. Phys.* **76** 323 (2004). DOI: 10.1103/RevModPhys.76.323. (Cit. on pp. 1, 15, 16).

[15] A. H. Castro Neto et al.: "The electronic properties of graphene". *Rev. Mod. Phys.* **81** 109 (2009). DOI: 10.1103/RevModPhys.81.109. (Cit. on pp. 2, 6, 7, 70).

[16] N. Tombros et al.: "Electronic spin transport and spin precession in single graphene layers at room temperature". *Nature* **448** 571 (2007). DOI: 10.1038/nature06037. (Cit. on pp. 2, 13).

[17] A. Varykhalov and O. Rader: "Graphene grown on Co(0001) films and islands: Electronic structure and its precise magnetization dependence". *Phys. Rev. B* **80** 035437 (2009). DOI: 10.1103/PhysRevB.80.035437. (Cit. on p. 2).

[18] M. Weser et al.: "Electronic structure and magnetic properties of the graphene/Fe/Ni(111) intercalation-like system". *Phys. Chem. Chem. Phys.* **13** 7534 (2011). DOI: 10.1039/C1CP00014D. (Cit. on pp. 2, 172).

[19] E. V. Rut'kov and N. R. Gall': *Intercalation of Graphene Films on Metals with Atoms and Molecules*. InTech, Rijeka (2011). DOI: 10.5772/15362. (Cit. on pp. 2, 12).

[20] A. Varykhalov et al.: "Electronic and Magnetic Properties of Quasifreestanding Graphene on Ni". *Phys. Rev. Lett.* **101** 157601 (2008). DOI: 10.1103/PhysRevLett.101.157601. (Cit. on pp. 2, 12, 16).

[21] C. Riedl et al.: "Quasi-free-standing epitaxial graphene on SiC obtained by hydrogen intercalation". *Phys. Rev. Lett.* **103** 246804 (2009). DOI: 10.1103/PhysRevLett.103.246804. (Cit. on pp. 2, 12, 73).

[22] P. Sutter, J. T. Sadowski, and E. A. Sutter: "Chemistry under cover: tuning metal- graphene interaction by reactive intercalation". *J. Am. Chem. Soc.* **132** 8175 (2010). DOI: 10.1021/ja102398n. (Cit. on pp. 2, 12, 58, 72).

[23] A. L. Walter et al.: "Highly p-doped epitaxial graphene obtained by fluorine intercalation". *Appl. Phys. Lett.* **98** 184102 (2011). DOI: 10.1063/1.3586256. (Cit. on pp. 2, 12).

[24] Y. S. Dedkov et al.: "Graphene protected iron layer on Ni(111)". *Appl. Phys. Lett.* **93** 022509 (2008). DOI: 10.1063/1.2953972. (Cit. on pp. 2, 12).

[25] C. E. Olsen, N. G. Nereson, and G. P. Arnold: "Neutron Diffraction Studies on Europium Metal". *J. Appl. Phys.* **33** 1135 (1962). DOI: 10.1063/1.1728632. (Cit. on pp. 2, 16).

[26] N. G. Nereson, C. E. Olsen, and G. P. Arnold: "Magnetic Structure of Europium". *Phys. Rev.* **135** 176 (1964). DOI: 10.1103/PhysRev.135.A176. (Cit. on pp. 2, 16).

[27] G. P. Arnold, C. E. Olsen, and N. G. Nereson: "Magnetic Properties of Eu". *J. Appl. Phys.* **35** 1031 (1964). DOI: 10.1063/1.1713365. (Cit. on pp. 2, 16).

[28] D. F. Förster et al.: "Phase coexistence of clusters and islands: europium on graphene". *New J. Phys.* **14** 23022 (2012). DOI: 10.1088/1367-2630/14/2/023022. (Cit. on pp. 2, 49, 62, 72, 81, 82, 84, 91, 93, 98, 143, 154, 160, 170, 213).

[29] D. F. Förster: "EuO and Eu on metal crystals and graphene: interface effects and epitaxial films". PhD thesis. Universität zu Köln (2011). (Cit. on pp. 2, 21, 43, 48, 51, 67–70, 97, 145).

[30] H. Suematsu et al.: "Magnetic properties of europium-graphite intercalation compound C_6Eu". *Synthetic Met.* **8** 23 (1983). DOI: 10.1016/0038-1098(81)90966-2. (Cit. on pp. 2, 19, 20).

[31] S. T. Chen et al.: "Magnetoresistivity and Monte Carlo studies of magnetic phase transitions in C_6Eu". *Phys. Rev. B* **34** 423 (1986). DOI: 10.1103/PhysRevB.34.423. (Cit. on pp. 2, 18–20, 112, 118).

[32] G. Binnig et al.: "Revisiting the (7x7) reconstruction of Si(111)". *Surf. Sci.* **157** L373 (1985). DOI: 10.1016/0039-6028(85)90666-1. (Cit. on p. 2).

[33] R. Plass et al.: "Self-assembled domain patterns". *Nature* **412** 875 (2001). DOI: 10.1038/35091143. (Cit. on pp. 2, 58).

[34] S. Macko et al.: "Phenomenology of iron-assisted ion beam pattern formation on Si (001)". *New J. Phys.* **13** 073017 (2011). DOI: 10.1088/1367-2630/13/7/073017. (Cit. on p. 2).

[35] V. W. Brar et al.: "Gate controlled ionization and screening of cobalt adatoms on a graphene surface". *Nature Phys.* **7** 43 (2011). DOI: 10.1038/nphys1807. (Cit. on pp. 2, 82).

[36] Y. Sato, K. Takai, and T. Enoki: "Electrically Controlled Adsorption of Oxygen in Bilayer Graphene Devices". *Nano Lett.* **11** 3468 (2011). DOI: 10.1021/nl202002p. (Cit. on pp. 2, 12, 82).

[37] D. A. Abanin, A. V. Shytov, and L. S. Levitov: "Peierls-Type Instability and Tunable Band Gap in Functionalized Graphene". *Phys. Rev. Lett.* **105** 086802 (2010). DOI: 10.1103/physrevlett.105.086802. (Cit. on pp. 2, 83).

[38] L. F. Huang et al.: "Modulation of the thermodynamic, kinetic, and magnetic properties of the hydrogen monomer on graphene by charge doping". *J. Chem. Phys.* **135** 064705 (2011). DOI: 10.1063/1.3624657. (Cit. on pp. 2, 24, 83).

[39] A. T. N'Diaye et al.: "Two-dimensional Ir cluster lattice on a graphene moire on Ir(111)". *Phys. Rev. Lett.* **97** 215501 (2006). DOI: 10.1103/PhysRevLett.97.215501. (Cit. on pp. 2, 7, 10, 47, 91).

[40] A. T. N'Diaye et al.: "A versatile fabrication method for cluster superlattices". *New J. Phys.* **11** 103045 (2009). DOI: 10.1088/1367-2630/11/10/103045. (Cit. on pp. 2, 10, 11, 128, 132).

[41] N. A. Frey and S. Sun: *Magnetic Nanoparticle for Information Storage Applications*. CRC Press, Boca Raton (2010). (Cit. on p. 3).

[42] R. Xiao et al.: "Co Dimers on Hexagonal Carbon Rings Proposed as Subnanometer Magnetic Storage Bits". *Phys. Rev. Lett.* **103** 187201 (2009). DOI: 10.1103/PhysRevLett.103.187201. (Cit. on p. 3).

[43] C. Vo-Van et al.: "Ultrathin epitaxial cobalt films on graphene for spintronic investigations and applications". *New J. Phys.* **12** 103040 (2010). DOI: 10.1088/1367-2630/12/10/103040. (Cit. on p. 3).

[44] J. Coraux et al.: "Air-protected epitaxial graphene/ferromagnet hybrids prepared by chemical vapor deposition and intercalation". *J. Phys. Chem. Lett.* **3** 2059 (2012). DOI: 10.1021/jz3007222. (Cit. on p. 3).

[45] V. Kumar and Y. Kawazoe: "Magnetism in clusters of non-magnetic elements: Pd, Rh, and Ru". English. *Eur. Phys. J. D* **24** 81 (2003). DOI: 10.1140/epjd/e2003-00193-6. (Cit. on p. 3).

[46] A. J. Cox et al.: "Magnetism in 4d-transition metal clusters". *Phys. Rev. B* **49** 1190236 (1994). DOI: 10.1103/PhysRevB.49.12295. (Cit. on p. 3).

[47] P. G. Steeneken et al.: "Exchange Splitting and Charge Carrier Spin Polarization in EuO". *Phys. Rev. Lett.* **88** 047201 (2002). DOI: 10.1103/PhysRevLett.88.047201. (Cit. on pp. 3, 20).

[48] D. F. Förster et al.: "Epitaxial europium oxide on Ni(100) with single-crystal quality". *Phys. Rev. B* **83** 045424 (2011). DOI: 10.1103/PhysRevB.83.045424. (Cit. on pp. 3, 48).

[49] D. F. Förster, J. Klinkhammer, and T. Michely: "Eu oxides on Ni(100): Polar surfaces, magic clusters and structures with large lattice dilation". *Surf. Sci.* **606** 1019 (2012). DOI: 10.1016/j.susc.2012.02.021. (Cit. on pp. 3, 145, 148).

[50] J. Klinkhammer et al.: "Structure and magnetic properties of ultra thin textured EuO films on graphene". *Appl. Phys. Lett.* **103** 131601 (2013). DOI: 10.1063/1.4821953. (Cit. on pp. 3, 121, 122, 165, 214).

[51] J. Klinkhammer et al.: "Spin-Polarized Surface State in EuO(100)". *Phys. Rev. Lett.* **112** 016803 (2014). DOI: 10.1103/PhysRevLett.112.016803. (Cit. on pp. 3, 174).

[52] P. W. Tasker: "The stability of ionic crystal surfaces". *J. Phys. C* **12** 4977 (1979). DOI: 10.1088/0022-3719/12/22/036. (Cit. on pp. 3, 26).

[53] J. Goniakowski, F. Finocchi, and C. Noguera: "Polarity of oxide surfaces and nanostructures". *Rep. Prog. Phys.* **71** 016501 (2008). DOI: 10.1088/0034-4885/71/1/016501. (Cit. on pp. 3, 26).

[54] M. Kiguchi et al.: "Atomic and electronic structure of an unreconstructed polar MgO(111) thin film on Ag(111)". *Phys. Rev. B* **68** 115402 (2003). DOI: 10.1103/PhysRevB.68.115402. (Cit. on pp. 3, 27, 146, 148, 152).

[55] K. Koike and T. Furukawa: "Evidence for Ferromagnetic Order at the FeO(111) Surface". *Phys. Rev. Lett.* **77** 3921 (1996). DOI: 10.1103/PhysRevLett.77.3921. (Cit. on p. 3).

[56] J. Yang et al.: "Effect of polar and non-polar surfaces of ZnO nanostructures on photocatalytic properties". *J. Alloys Comp.* **528** 28 (2012). DOI: 10.1016/j.jallcom.2012.02.162. (Cit. on p. 3).

[57] L. Giordano et al.: "Interplay between structural, magnetic, and electronic properties in a FeO/Pt(111) ultrathin film". *Phys. Rev. B* **76** 075416 (2007). DOI: 10.1103/PhysRevB.76.075416. (Cit. on pp. 3, 160).

[58] M. De Santis et al.: "Growth of ultrathin cobalt oxide films on Pt(111)". *Phys. Rev. B* **84** 125430 (2011). DOI: 10.1103/PhysRevB.84.125430. (Cit. on pp. 3, 146, 152, 161).

[59] F. Sedona et al.: "Ultrathin TiO_x Films on Pt(111): A LEED, XPS, and STM Investigation". *J. Phys. Chem. C* **109** 24411 (2005). DOI: 10.1021/jp0543173. (Cit. on p. 3).

[60] C. Tusche, H. L. Meyerheim, and J. Kirschner: "Observation of Depolarized ZnO(0001) Monolayers: Formation of Unreconstructed Planar Sheets". *Phys. Rev. Lett.* **99** 026102 (2007). DOI: 10.1103/PhysRevLett.99.026102. (Cit. on p. 3).

[61] Y. Pan et al.: "Compensating Edge Polarity: A Means To Alter the Growth Orientation of MgO Nanostructures on Au(111)". *J. Phys. Chem. C* **116** 11126 (2012). DOI: 10.1021/jp302302v. (Cit. on p. 3).

[62] S. Schumacher et al.: "Strain in Epitaxial Graphene Visualized by Intercalation". *Phys. Rev. Lett.* **110** 086111 (2013). DOI: 10.1103/PhysRevLett.110.086111. (Cit. on pp. 5, 43, 51, 91, 213).

[63] S. Schumacher et al.: "The Backside of Graphene: Manipulating Adsorption by Intercalation". *Nano Lett.* **13** 5013 (2013). DOI: 10.1021/nl402797j. (Cit. on pp. 5, 12, 43, 81, 160, 213).

[64] S. Schumacher et al.: "Polar EuO(111) on Ir(111): A two-dimensional oxide". *Phys. Rev. B* **89** 115410 (2014). DOI: 10.1103/PhysRevB.89.115410. (Cit. on pp. 5, 43, 145, 213).

[65] K. S. Novoselov et al.: "Electric Field Effect in Atomically Thin Carbon Films". *Science* **306** 666 (2004). DOI: 10.1126/science.1102896. (Cit. on p. 5).

[66] K. V. Emtsev et al.: "Interaction, growth, and ordering of epitaxial graphene on SiC{0001} surfaces: A comparative photoelectron spectroscopy study". *Phys. Rev. B* **77** 155303 (2008). DOI: 10.1103/PhysRevB.77.155303. (Cit. on p. 5).

[67] T. Ohta et al.: "Morphology of graphene thin film growth on SiC(0001)". *New J. Phys.* **10** 023034 (2008). DOI: 10.1088/1367-2630/10/2/023034. (Cit. on p. 5).

[68] J. Wintterlin and M.-L. Bocquet: "Graphene on metal surfaces". *Surf. Sci.* **603** 1841 (2009). DOI: 10.1016/j.susc.2008.08.037. (Cit. on p. 5).

[69] Y. Gamo et al.: "Atomic structure of monolayer graphite formed on Ni(111)". *Surf. Sci.* **374** 61 (1997). DOI: 10.1016/S0039-6028(96)00785-6. (Cit. on p. 5).

[70] H. Ueta et al.: "Highly oriented monolayer graphite formation on Pt(111) by a supersonic methane beam". *Surf. Sci.* **560** 183 (2004). DOI: 10.1016/j.susc.2004.04.039. (Cit. on p. 5).

[71] J. Coraux et al.: "Growth of graphene on Ir(111)". *New J. Phys.* **11** 023006 (2009). DOI: 10.1088/1367-2630/11/2/023006. (Cit. on pp. 5, 7, 47).

[72] P. W. Sutter, J.-I. Flege, and E. A. Sutter: "Epitaxial graphene on ruthenium". *Nature Mat.* **7** 406 (2008). DOI: 10.1038/nmat2166. (Cit. on p. 5).

[73] E. N. Voloshina et al.: "Graphene on Rh(111): Scanning tunneling and atomic force microscopies studies". *Appl. Phys. Lett.* **100** 241606 (2012). DOI: 10.1063/1.4729549. (Cit. on p. 5).

[74] L. Gao, J. R. Guest, and N. P. Guisinger: "Epitaxial Graphene on Cu(111)". *Nano Lett.* **10** 3512 (2010). DOI: 10.1021/nl1016706. (Cit. on p. 5).

[75] P. R. Wallace: "The Band Theory of Graphite". *Phys. Rev.* **71** 622 (1947). DOI: 10.1103/PhysRev.71.622. (Cit. on p. 6).

[76] A. K. Geim and K. S. Novoselov: "The rise of graphene". *Nature Mat.* **6** 183 (2007). DOI: 10.1038/nmat1849. (Cit. on pp. 6, 7).

[77] J.-H. Chen et al.: "Intrinsic and extrinsic performance limits of graphene devices on SiO_2". *Nature Nanotech.* **3** 206 (2008). DOI: 10.1038/nnano.2008.58. (Cit. on p. 6).

[78] Y. Zhang et al.: "Experimental observation of the quantum Hall effect and Berry's phase in graphene". *Nature* **438** 201 (2005). DOI: 10.1038/nature04235. (Cit. on p. 6).

[79] M. I. Katsnelson, K. S. Novoselov, and A. K. Geim: "Chiral tunnelling and the Klein paradox in graphene". *Nature Phys.* **2** 620 (2006). DOI: 10.1038/nphys384. (Cit. on p. 6).

[80] A. K. Geim: "Nobel Lecture: Random walk to graphene". *Rev. Mod. Phys.* **83** 851 (2011). DOI: 10.1103/RevModPhys.83.851. (Cit. on p. 6).

[81] R. R. Nair et al.: "Fine Structure Constant Defines Visual Transparency of Graphene". *Science* **320** 1308 (2008). DOI: 10.1126/science.1156965. (Cit. on p. 6).

[82] S. Bae et al.: "Roll-to-roll production of 30-inch graphene films for transparent electrodes". *Nature Nanotech.* **5** 574 (2010). DOI: 10.1038/nnano.2010.132. (Cit. on p. 6).

[83] X. Li et al.: "Graphene-On-Silicon Schottky Junction Solar Cells". *Adv. Mater.* **22** 2743 (2010). DOI: 10.1002/adma.200904383. (Cit. on p. 6).

[84] F. Schwierz: "Graphene transistors". *Nature Nanotech.* **5** 487 (2010). DOI: 10.1038/nnano.2010.89. (Cit. on p. 6).

[85] M. Y. Han et al.: "Energy Band-Gap Engineering of Graphene Nanoribbons". *Phys. Rev. Lett.* **98** 206805 (2007). DOI: 10.1103/PhysRevLett.98.206805. (Cit. on p. 6).

[86] F. Xia et al.: "Graphene Field-Effect Transistors with High On/Off Current Ratio and Large Transport Band Gap at Room Temperature". *Nano Lett.* **10** 715 (2010). DOI: 10.1021/nl9039636. (Cit. on p. 6).

[87] V. M. Pereira, A. H. Castro Neto, and N. M. R. Peres: "Tight-binding approach to uniaxial strain in graphene". *Phys. Rev. B* **80** 045401 (2009). DOI: 10.1103/PhysRevB.80.045401. (Cit. on p. 6).

[88] Y.-M. Lin et al.: "100-GHz transistors from wafer-scale epitaxial graphene". *Science* **327** 662 (2010). DOI: 10.1126/science.1184289. (Cit. on p. 6).

[89] F. Schedin et al.: "Detection of individual gas molecules adsorbed on graphene". *Nature Mat.* **6** 652 (2007). DOI: 10.1038/nmat1967. (Cit. on pp. 7, 82).

[90] J. H. Seol et al.: "Two-dimensional phonon transport in supported graphene". *Science* **328** 213 (2010). DOI: 10.1126/science.1184014. (Cit. on p. 7).

[91] M. I. Katsnelson: "Graphene: carbon in two dimensions". *Mater. Today* **10** 20 (2007). DOI: 10.1016/S1369-7021(06)71788-6. (Cit. on p. 7).

[92] J. Coraux et al.: "Structural Coherency of Graphene on Ir(111)". *Nano Lett.* **8** 565 (2008). DOI: 10.1021/nl0728874. (Cit. on pp. 7, 47, 61, 64, 77).

[93] A. T. N'Diaye et al.: "Structure of epitaxial graphene on Ir(111)". *New J. Phys.* **10** 043033 (2008). DOI: 10.1088/1367-2630/10/4/043033. (Cit. on pp. 7, 8, 47, 57).

[94] J. Knudsen et al.: "Clusters binding to the graphene moiré on Ir(111): x-ray photoemission compared to density functional calculations". *Phys. Rev. B* **85** 035407 (2012). DOI: 10.1103/PhysRevB.85.035407. (Cit. on pp. 8, 11).

[95] C. Busse et al.: "Graphene on Ir(111): Physisorption with Chemical Modulation". *Phys. Rev. Lett.* **107** 036101 (2011). DOI: 10.1103/PhysRevLett.107.036101. (Cit. on pp. 7, 8, 59, 61, 91).

[96] P. Trucano and R. Chen: "Structure of graphite by neutron diffraction". *Nature* **258** 136 (1975). DOI: 10.1038/258136a0. (Cit. on p. 8).

[97] A. B. Preobrajenski et al.: "Controlling graphene corrugation on lattice mismatched substrates". *Phys. Rev. B* **78** 073401 (2008). DOI: 10.1103/PhysRevB.78.073401. (Cit. on p. 8).

[98] E. Starodub et al.: "In-plane orientation effects on the electronic structure, stability and Raman scattering of monolayer graphene on Ir(111)". *Phys. Rev. B* **83** 125428 (2011). DOI: 10.1103/PhysRevB.83.125428. (Cit. on p. 8).

[99] M. J. Rost, T. Michely, and G. Comsa: "Comment on "Self-diffusion and dynamic behavior of atoms at step edges on iridium surfaces"". *Phys. Rev. B* **57** 1992 (1998). DOI: 10.1103/PhysRevB.57.1992. (Cit. on p. 8).

[100] A. T. N'Diaye et al.: "In situ observation of stress relaxation in epitaxial graphene". *New J. Phys.* **11** 113056 (2009). DOI: 10.1088/1367-2630/11/11/113056. (Cit. on pp. 9, 62, 64, 91).

[101] H. Hattab et al.: "Interplay of wrinkles, strain, and lattice parameter in graphene on iridium". *Nano Lett.* **12** 678 (2012). DOI: 10.1021/nl203530t. (Cit. on pp. 9, 10, 64).

[102] D. Franz et al.: "Atomic Structure and Crystalline Order of Graphene-Supported Ir Nanoparticle Lattices". *Phys. Rev. Lett.* **110** 065503 (2013). DOI: 10.1103/PhysRevLett.110.065503. (Cit. on pp. 10, 91, 136, 214).

[103] P. J. Feibelman: "Pinning of graphene to Ir(111) by flat Ir dots". *Phys. Rev. B* **77** 165419 (2008). DOI: 10.1103/PhysRevB.77.165419. (Cit. on pp. 10, 91).

[104] P. J. Feibelman: "Onset of three-dimensional Ir islands on a graphene/Ir(111) template". *Phys. Rev. B* **80** 085412 (2009). DOI: 10.1103/PhysRevB.80.085412. (Cit. on p. 10).

[105] Z. Zhou, F. Gao, and D. W. Goodman: "Deposition of metal clusters on single-layer graphene/Ru(0001): Factors that govern cluster growth". *Surf. Sci.* **604** L31 (2010). DOI: 10.1016/j.susc.2010.03.008. (Cit. on p. 11).

[106] M. S. Dresselhaus and G. Dresselhaus: "Intercalation compounds of graphite". *Adv. Phys.* **30** 139 (1981). DOI: 10.1080/00018738100101367. (Cit. on pp. 11, 12).

[107] G. Foley et al.: "Room temperature electrical conductivity of a highly two dimensional synthetic metal: AsF_5-graphite". *Solid State Commun.* **24** 371 (1977). DOI: 10.1016/0038-1098(77)90985-1. (Cit. on p. 12).

[108] N. Emery et al.: "Superconducting graphite intercalation compounds with calcium". *Solid State Sci.* **10** 466 (2008). DOI: 10.1016/j.solidstatesciences.2007.11.034. (Cit. on p. 12).

[109] A. M. Shikin et al.: "Surface intercalation of gold underneath a graphite monolayer on Ni(111) studied by angle-resolved photoemission and high-resolution electron-energy-loss spectroscopy". *Phys. Rev. B* **62** 13202 (2000). DOI: 10.1103/PhysRevB.62.13202. (Cit. on p. 12).

[110] Y. S. Dedkov et al.: "Intercalation of copper underneath a monolayer of graphite on Ni(111)". *Phys. Rev. B* **64** 035405 (2001). DOI: 10.1103/PhysRevB.64.035405. (Cit. on p. 12).

[111] S. Forti et al.: "Large-area homogeneous quasifree standing epitaxial graphene on SiC(0001): Electronic and structural characterization". *Phys. Rev. B* **84** 125449 (2011). DOI: 10.1103/PhysRevB.84.125449. (Cit. on pp. 12, 58).

[112] J. A. Robinson et al.: "Epitaxial graphene transistors: enhancing performance via hydrogen intercalation". *Nano Lett.* **11** 3875 (2011). DOI: 10.1021/nl2019855. (Cit. on p. 12).

[113] E. Widenkvist et al.: "Mild sonochemical exfoliation of bromine intercalated graphite: a new route towards graphene". *J. Phys. D: Appl. Phys.* **42** 112003 (2009). DOI: 10.1088/0022-3727/42/11/112003. (Cit. on p. 12).

[114] C. Herbig et al.: "Mechanical exfoliation of epitaxial graphene on Ir(111) enabled by Br_2 intercalation". *J. Phys.: Condens. Matter* **24** 314208 (2012). DOI: 10.1088/0953-8984/24/31/314208. (Cit. on pp. 12, 73, 214).

[115] E. E. Santiso et al.: "Effect of confinement on chemical reactions". *Adsorption* **11** 349 (2005). DOI: 10.1007/s10450-005-5949-9. (Cit. on p. 12).

[116] E. Starodub, N. C. Bartelt, and K. F. McCarty: "Oxidation of graphene on metals". *J. Phys. Chem. C* **114** 5134 (2010). DOI: 10.1021/jp912139e. (Cit. on pp. 12, 58).

[117] R. Mu et al.: "Visualizing Chemical Reactions Confined under Graphene". *Angew. Chem. Int. Ed.* **51** 4856 (2012). DOI: 10.1002/anie.201200413. (Cit. on p. 12).

[118] M. Sepioni et al.: "Limits on Intrinsic Magnetism in Graphene". *Phys. Rev. Lett.* **105** 207205 (2010). DOI: 10.1103/PhysRevLett.105.207205. (Cit. on p. 13).

[119] P. Esquinazi et al.: "Induced Magnetic Ordering by Proton Irradiation in Graphite". *Phys. Rev. Lett.* **91** 227201 (2003). DOI: 10.1103/PhysRevLett.91.227201. (Cit. on p. 13).

[120] V. M. Pereira et al.: "Disorder Induced Localized States in Graphene". *Phys. Rev. Lett.* **96** 036801 (2006). DOI: 10.1103/PhysRevLett.96.036801. (Cit. on p. 13).

[121] O. V. Yazyev and L. Helm: "Defect-induced magnetism in graphene". *Phys. Rev. B* **75** 125408 (2007). DOI: 10.1103/PhysRevB.75.125408. (Cit. on p. 13).

[122] P. O. Lehtinen et al.: "Irradiation-Induced Magnetism in Graphite: A Density Functional Study". *Phys. Rev. Lett.* **93** 187202 (2004). DOI: 10.1103/PhysRevLett.93.187202. (Cit. on p. 13).

[123] Y. Zhang et al.: "First-Principles Study of Defect-Induced Magnetism in Carbon". *Phys. Rev. Lett.* **99** 107201 (2007). DOI: 10.1103/PhysRevLett.99.107201. (Cit. on p. 13).

[124] S. Okada and A. Oshiyama: "Magnetic Ordering in Hexagonally Bonded Sheets with First-Row Elements". *Phys. Rev. Lett.* **87** 146803 (2001). DOI: 10.1103/PhysRevLett.87.146803. (Cit. on p. 13).

[125] D. W. Boukhvalov, M. I. Katsnelson, and A. I. Lichtenstein: "Hydrogen on graphene: Electronic structure, total energy, structural distortions and magnetism from first-principles calculations". *Phys. Rev. B* **77** 035427 (2008). DOI: 10.1103/PhysRevB.77.035427. (Cit. on p. 13).

[126] P. O. Lehtinen et al.: "Magnetic Properties and Diffusion of Adatoms on a Graphene Sheet". *Phys. Rev. Lett.* **91** 017202 (2003). DOI: 10.1103/PhysRevLett.91.017202. (Cit. on p. 13).

[127] Y. Ma et al.: "Nitrogen in graphite and carbon nanotubes: Magnetism and mobility". *Phys. Rev. B* **72** 205416 (2005). DOI: 10.1103/PhysRevB.72.205416. (Cit. on p. 13).

[128] H. Min et al.: "Intrinsic and Rashba spin-orbit interactions in graphene sheets". *Phys. Rev. B* **74** 165310 (2006). DOI: 10.1103/PhysRevB.74.165310. (Cit. on p. 13).

[129] B. Trauzettel et al.: "Spin qubits in graphene quantum dots". *Nature Phys.* **3** 192 (2007). DOI: 10.1038/nphys544. (Cit. on p. 13).

[130] O. V. Yazyev: "Hyperfine Interactions in Graphene and Related Carbon Nanostructures". *Nano Lett.* **8** 1011 (2008). DOI: 10.1021/nl072667q. (Cit. on p. 13).

[131] J. Fischer, B. Trauzettel, and D. Loss: "Hyperfine interaction and electron-spin decoherence in graphene and carbon nanotube quantum dots". *Phys. Rev. B* **80** 155401 (2009). DOI: 10.1103/PhysRevB.80.155401. (Cit. on p. 13).

[132] P. J. Zomer et al.: "Long-distance spin transport in high-mobility graphene on hexagonal boron nitride". *Phys. Rev. B* **86** 161416 (2012). DOI: 10.1103/PhysRevB.86.161416. (Cit. on p. 13).

[133] M. H. D. Guimarães et al.: "Spin Transport in High-Quality Suspended Graphene Devices". *Nano Lett.* **12** 3512 (2012). DOI: 10.1021/nl301050a. (Cit. on p. 13).

[134] B. Dlubak et al.: "Highly efficient spin transport in epitaxial graphene on SiC". *Nature Phys.* **8** 557 (2012). DOI: 10.1038/nphys2331. (Cit. on p. 13).

[135] O. V. Yazyev: "Emergence of magnetism in graphene materials and nanostructures". *Rep. Prog. Phys.* **73** 056501 (2010). DOI: 10.1088/0034-4885/73/5/056501. (Cit. on pp. 14, 16).

[136] M. Fujita et al.: "Peculiar Localized State at Zigzag Graphite Edge". *J. Phys. Soc. Jpn.* **65** 1920 (1996). DOI: 10.1143/JPSJ.65.1920. (Cit. on p. 13).

[137] Y.-W. Son, M. L. Cohen, and S. G. Louie: "Half-metallic graphene nanoribbons". *Nature* **444** 347 (2006). DOI: 10.1038/nature05180. (Cit. on p. 13).

[138] C. Heiliger, P. Zahn, and I. Mertig: "Microscopic origin of magnetoresistance". *Mater. Today* **9** 46 (2006). DOI: 10.1016/S1369-7021(06)71694-7. (Cit. on p. 14).

[139] W. Y. Kim and K. S. Kim: "Prediction of very large values of magnetoresistance in a graphene nanoribbon device". *Nature Nanotech.* **3** 408 (2008). DOI: 10.1038/nnano.2008.163. (Cit. on p. 14).

[140] H. Haugen, D. Huertas-Hernando, and A. Brataas: "Spin transport in proximity-induced ferromagnetic graphene". *Phys. Rev. B* **77** 115406 (2008). DOI: 10.1103/PhysRevB.77.115406. (Cit. on p. 14).

[141] V. M. Karpan et al.: "Graphite and graphene as perfect spin filters". *Phys. Rev. Lett.* **99** 176602 (2007). DOI: 10.1103/PhysRevLett.99.176602. (Cit. on p. 15).

[142] R. Winkler: *Spin–Orbit Coupling Effects in Two-Dimensional Electron and Hole Systems*. Springer, Berlin (2003). (Cit. on p. 15).

[143] D. Marchenko et al.: "Giant Rashba splitting in graphene due to hybridization with gold". *Nature Comm.* **3** 1232 (2012). DOI: 10.1038/ncomms2227. (Cit. on p. 16).

[144] P. D. C. King et al.: "Large Tunable Rashba Spin Splitting of a Two-Dimensional Electron Gas in Bi_2Se_3". *Phys. Rev. Lett.* **107** 096802 (2011). DOI: 10.1103/PhysRevLett.107.096802. (Cit. on p. 16).

[145] S. Datta and B. Das: "Electronic analog of the electro-optic modulator". *Appl. Phys. Lett.* **56** 665 (1990). DOI: 10.1063/1.102730. (Cit. on p. 16).

[146] Y. G. Semenov, K. W. Kim, and J. M. Zavada: "Spin field effect transistor with a graphene channel". *Appl. Phys. Lett.* **91** 153105 (2007). DOI: 10.1063/1.2798596. (Cit. on p. 16).

[147] I. R. Harris and G. V. Raynor: "Some observations on the crystal structures of the rare-earth metals and alloys". *J. Less Common Met.* **17** 336 (1969). DOI: 10.1016/0022-5088(69)90154-4. (Cit. on p. 16).

[148] R. L. Cohen, S. Hüfner, and K. W. West: "First-Order Phase Transition in Europium Metal". *Phys. Rev.* **184** 263 (1969). DOI: 10.1103/PhysRev.184.263. (Cit. on p. 16).

[149] R. M. Bozorth and J. H. Van Vleck: "Magnetic Susceptibility of Metallic Europium". *Phys. Rev.* **118** 1493 (1960). DOI: 10.1103/PhysRev.118.1493. (Cit. on p. 16).

[150] M. A. Curry, S. Legvold, and F. H. Spedding: "Electrical Resistivity of Europium and Ytterbium". *Phys. Rev.* **117** 953 (1960). DOI: 10.1103/PhysRev.117.953. (Cit. on p. 16).

[151] B. C. Gerstein et al.: "Heat Capacity of Europium from 5K-300K". *J. Chem. Phys.* **47** 5194 (1967). DOI: 10.1063/1.1701779. (Cit. on p. 16).

[152] M. A. Ruderman and C. Kittel: "Indirect Exchange Coupling of Nuclear Magnetic Moments by Conduction Electrons". *Phys. Rev.* **96** 99 (1954). DOI: 10.1103/PhysRev.96.99. (Cit. on p. 17).

[153] T. Kasuya: "A Theory of Metallic Ferro- and Antiferromagnetism on Zener's Model". *Prog. Theor. Phys.* **16** 45 (1956). DOI: 10.1143/PTP.16.45. (Cit. on p. 17).

[154] K. Yosida: "Magnetic Properties of Cu-Mn Alloys". *Phys. Rev.* **106** 893 (1957). DOI: 10.1103/PhysRev.106.893. (Cit. on p. 17).

[155] O. K. Andersen and T. L. Loucks: "Fermi Surface and Antiferromagnetism in Europium Metal". *Phys. Rev.* **167** 551 (1968). DOI: 10.1103/PhysRev.167.551. (Cit. on p. 17).

[156] C. Herring: *Magnetism*. Academic Press Inc., New York (1966). (Cit. on p. 17).

[157] J. Kuneš and R. Laskowski: "Magnetic ground state and Fermi surface of bcc Eu". *Phys. Rev. B* **70** 174415 (2004). DOI: 10.1103/PhysRevB.70.174415. (Cit. on p. 17).

[158] M. El Makrini et al.: "Intercalation of rare earth metals in graphite". *Physica B* **99** 481 (1980). DOI: 10.1016/0378-4363(80)90282-X. (Cit. on pp. 17, 18).

[159] H. Suematsu, K. Ohmatsu, and R. Yoshizaki: "Magnetic properties of Europium-graphite intercalation compound C_6Eu". *Solid State Commun.* **38** 1103 (1981). DOI: 10.1016/0038-1098(81)90966-2. (Cit. on pp. 18, 117, 118).

[160] N. Emery, C. Hérold, and P. Lagrange: "The synthesis of binary metal-graphite intercalation compounds using molten lithium alloys". *Carbon* **46** 72 (2008). DOI: 10.1016/j.carbon.2007.10.039. (Cit. on p. 18).

[161] G. Lamura et al.: "The zero-field magnetic ground state of EuC_6 investigated by muon spectroscopy". *Carbon* **50** 3995 (2012). DOI: 10.1016/j.carbon.2012.04.028. (Cit. on pp. 18, 20).

[162] H. Suematsu et al.: "High field magnetization of europium-graphite intercalation compound C_6Eu". *Solid State Commun.* **40** 241 (1981). DOI: 10.1016/0038-1098(81)90749-3. (Cit. on p. 18).

[163] R. Deutscher and H. U. Everts: "The $S = \frac{1}{2}$ Heisenberg antiferromagnet on the triangular lattice: Exact results and spin-wave theory for finite cells". *Z. Phys. B: Condens. Matter* **93** 77 (1993). DOI: 10.1007/BF01308811. (Cit. on p. 19).

[164] H. Akera and H. Kamimura: "A new mechanism of magnetic anisotropy due to π-f exchange in graphite intercalation compound C_6Eu". *Solid State Commun.* **48** 467 (1983). DOI: 10.1016/0038-1098(83)90855-4. (Cit. on p. 20).

[165] T. Sakakibara et al.: "Four-spin exchange in the europium-graphite intercalation compound C_6Eu". *Synthetic Met.* **6** 165 (1983). DOI: 10.1016/0379-6779(83)90151-0. (Cit. on p. 20).

[166] T. Sakakibara and M. Date: "Magnetism of C_6Eu. I. Existence of the Four-Spin Exchange Interactions". *J. Phys. Soc. Jpn.* **53** 3599 (1984). DOI: 10.1143/JPSJ.53.3599. (Cit. on p. 20).

[167] T. Sakakibara: "Magnetism of C_6Eu. II. Instability of the triangular spin structure in the hcp-like antiferromagnet". *J. Phys. Soc. Jpn.* **53** 3607 (1984). DOI: 10.1143/JPSJ.53.3607. (Cit. on p. 20).

[168] B. Predel: *Eu-O (Europium-Oxygen)*. SpringerMaterials - The Landolt-Börnstein Database (1995). DOI: 10.1007/10474837_1262. (Cit. on p. 20).

[169] P. Wachter: "The optical electrical and magnetic properties of the europium chalcogenides and the rare earth pnictides". *Crit. Rev. Solid State Mater. Sci.* **3** 189 (1972). DOI: 10.1080/10408437208244865. (Cit. on p. 20).

[170] M. R. Oliver et al.: "Pressure Dependence of the Electrical Resistivity of EuO". *Phys. Rev. Lett.* **24** 1064 (1970). DOI: 10.1103/PhysRevLett.24.1064. (Cit. on p. 20).

[171] T. S. Santos and J. S. Moodera: "Observation of spin filtering with a ferromagnetic EuO tunnel barrier". *Phys. Rev. B* **69** 241203 (2004). DOI: 10.1103/PhysRevB.69.241203. (Cit. on p. 20).

[172] M. Müller, G.-X. Miao, and J. S. Moodera: "Exchange splitting and bias-dependent transport in EuO spin filter tunnel barriers". *Europhys. Lett.* **88** 47006 (2009). DOI: 10.1209/0295-5075/88/47006. (Cit. on p. 20).

[173] Y. Shapira et al.: "EuO. II. Dependence of the Insulator-Metal Transition on Magnetic Order". *Phys. Rev. B* **8** 2316 (1973). DOI: 10.1103/PhysRevB.8.2316. (Cit. on p. 20).

[174] R. Bachmann and P. Wachter: "Magnetic effects on the low temperature photoconductivity of EuO and EuS". *Solid State Commun.* **6** 711 (1968). DOI: 10.1016/0038-1098(68)90570-X. (Cit. on p. 20).

[175] J. H. Greiner and G. J. Fan: "Longitudinal Magneto-Optical Kerr Effect in EuO". *Appl. Phys. Lett.* **9** 27 (1966). DOI: 10.1063/1.1754584. (Cit. on p. 20).

[176] J. C. Suits and K. Lee: "Giant Magneto-Optical Kerr Effect in EuO". *J. Appl. Phys.* **42** 3258 (1971). DOI: 10.1063/1.1660721. (Cit. on p. 20).

[177] A. Mauger and C. Godart: "The magnetic, optical, and transport properties of representatives of a class of magnetic semiconductors: the europium chalcogenides". *Phys. Rep.* **141** 51 (1986). DOI: 10.1016/0370-1573(86)90139-0. (Cit. on p. 21).

[178] X. Wan, J. Dong, and S. Y. Savrasov: "Mechanism of magnetic exchange interactions in europium monochalcogenides". *Phys. Rev. B* **83** 205201 (2011). DOI: 10.1103/PhysRevB.83.205201. (Cit. on p. 21).

[179] H. A. Mook: "Temperature Dependence of the Spin Dynamics of EuO". *Phys. Rev. Lett.* **46** 508 (1981). DOI: 10.1103/PhysRevLett.46.508. (Cit. on p. 21).

[180] J. Klinkhammer: "Electronic Structure and Magnetism of EuO Films on the Nanometer Scale". PhD thesis. Universität zu Köln (2013). (Cit. on p. 21).

[181] B. Odom et al.: "New Measurement of the Electron Magnetic Moment Using a One-Electron Quantum Cyclotron". *Phys. Rev. Lett.* **97** 030801 (2006). DOI: 10.1103/PhysRevLett.97.030801. (Cit. on p. 21).

[182] C. T. Chen et al.: "Experimental confirmation of the x-ray magnetic circular dichroism sum rules for iron and cobalt". *Phys. Rev. Lett.* **75** 152 (1995). DOI: 10.1103/PhysRevLett.75.152. (Cit. on pp. 22, 35, 36, 126–128).

[183] J. H. Van Vleck: "Theory of the Variations in Paramagnetic Anisotropy Among Different Salts of the Iron Group". *Phys. Rev.* **41** 208 (1932). DOI: 10.1103/PhysRev.41.208. (Cit. on p. 22).

[184] E. C. Stoner: "Collective electron ferromagnetism". *Proc. Roy. Soc. A* **165** 372 (1938). DOI: 10.1098/rspa.1938.0066. (Cit. on p. 22).

[185] M. Tischer et al.: "Enhancement of Orbital Magnetism at Surfaces: Co on Cu(100)". *Phys. Rev. Lett.* **75** 1602 (1995). DOI: 10.1103/PhysRevLett.75.1602. (Cit. on p. 23).

[186] R. A. Guirado-López, J. Dorantes-Dávila, and G. M. Pastor: "Orbital Magnetism in Transition-Metal Clusters: From Hund's Rules to Bulk Quenching". *Phys. Rev. Lett.* **90** 226402 (2003). DOI: 10.1103/PhysRevLett.90.226402. (Cit. on p. 23).

[187] I. M. L. Billas, A. Chatelain, and W. A. De Heer: "Magnetism from the atom to the bulk in iron, cobalt, and nickel clusters". *Science* **265** 1682 (1994). DOI: 10.1126/science.265.5179.1682. (Cit. on p. 23).

[188] D. Sander: "The magnetic anisotropy and spin reorientation of nanostructures and nanoscale films". *J. Phys.: Condens. Matter* **16** R603 (2004). DOI: 10.1088/0953-8984/16/20/R01. (Cit. on p. 23).

[189] O. Fruchart and A. Thiaville: "Magnetism in reduced dimensions". *Comp. Rend. Phys.* **6** 921 (2005). DOI: 10.1016/j.crhy.2005.10.011. (Cit. on p. 23).

[190] H. Brooks: "Ferromagnetic Anisotropy and the Itinerant Electron Model". *Phys. Rev.* **58** 909 (1940). DOI: 10.1103/PhysRev.58.909. (Cit. on p. 23).

[191] L. Néel: "Anisotropie magnétique superficielle et surstructures d'orientation". *J. Phys. Rad.* **15** 225 (1954). DOI: 10.1051/jphysrad:01954001504022500. (Cit. on p. 23).

[192] P. Bruno and J.-P. Renard: "Magnetic surface anisotropy of transition metal ultrathin films". *Appl. Phys. A* **49** 499 (1989). DOI: 10.1007/BF00617016. (Cit. on p. 23).

[193] C. Chappert and P. Bruno: "Magnetic anisotropy in metallic ultrathin films and related experiments on cobalt films". *J. Appl. Phys.* **64** 5736 (1988). DOI: 10.1063/1.342243. (Cit. on p. 24).

[194] A. Bettac et al.: "Structure and magnetism of hcp(0001) and fcc(001) thin cobalt films on a clean and carbon-reconstructed W(110) surface". *Surf. Sci.* **454** 936 (2000). DOI: 10.1016/S0039-6028(00)00184-9. (Cit. on p. 24).

[195] F. den Broeder, W. Hoving, and P. Bloemen: "Magnetic anisotropy of multilayers". *J. Magn. Magn. Mater.* **93** 562 (1991). DOI: 10.1016/0304-8853(91)90404-X. (Cit. on p. 24).

[196] L. Ranno et al.: "Strain-induced magnetic anisotropy in epitaxial manganite films". *Appl. Surf. Sci.* **188** 170 (2002). DOI: 10.1016/S0169-4332(01)00730-9. (Cit. on p. 24).

[197] S Blundell: *Magnetism in Condensed Matter*. Oxford University Press, USA (2001). (Cit. on p. 24).

[198] E. C. Stoner and E. P. Wohlfarth: "A mechanism of magnetic hysteresis in heterogeneous alloys". *Phil. Trans. R. Soc. A* **240** 599 (1948). DOI: 10.1098/rsta.1948.0007. (Cit. on p. 24).

[199] E. C. Stoner and E. P. Wohlfarth: "A mechanism of magnetic hysteresis in heterogeneous alloys". *IEEE Trans. Magn.* **27** 3475 (1991). DOI: 10.1109/TMAG.1991.1183750. (Cit. on p. 24).

[200] C. Tannous and J. Gieraltowski: "The Stoner-Wohlfarth model of ferromagnetism". *Eur. Phys. J.* **29** 475 (2008). DOI: 10.1088/0143-0807/29/3/008. (Cit. on p. 24).

[201] L. Néel: "Théorie du traînage magnétique des ferromagnétiques en grains fins avec applications aux terres cuites". *Ann. géophys.* **5** 99 (1949). (Cit. on p. 25).

[202] C. Noguera: "Polar oxide surfaces". *J. Phys.: Condens. Matter* **12** R367 (2000). DOI: 10.1088/0953-8984/12/31/201. (Cit. on pp. 26, 27).

[203] C. Noguera and J. Goniakowski: "Polarity in Oxide Nano-objects". *Chem. Rev.* **113** 4073 (2013). DOI: 10.1021/cr3003032. (Cit. on p. 26).

[204] S. Schumacher: "Wachstum von Europium und Europiumoxid auf Iridiumoberflächen und Graphen". Diploma thesis. Universität zu Köln (2010). (Cit. on pp. 27, 30, 31, 37, 97).

[205] D. Wolf: "Reconstruction of NaCl surfaces from a dipolar solution to the Madelung problem". *Phys. Rev. Lett.* **68** 3315 (1992). DOI: 10.1103/PhysRevLett.68.3315. (Cit. on p. 27).

[206] F. Finocchi et al.: "Stability of Rocksalt (111) Polar Surfaces: Beyond the Octopole". *Phys. Rev. Lett.* **92** 136101 (2004). DOI: 10.1103/PhysRevLett.92.136101. (Cit. on p. 27).

[207] C. A. Ventrice et al.: "Stable reconstruction of the polar (111) surface of NiO on Au(111)". *Phys. Rev. B* **49** 5773 (1994). DOI: 10.1103/PhysRevB.49.5773. (Cit. on p. 27).

[208] A. Barbier et al.: "Atomic Structure of the Polar NiO(111)-p(2x2) Surface". *Phys. Rev. Lett.* **84** 2897 (2000). DOI: 10.1103/PhysRevLett.84.2897. (Cit. on p. 27).

[209] M. Bowker et al.: "The surface structure of BaO on Pt(111): (2x2)-reconstructed BaO(111)". *Surf. Sci.* **600** 1973 (2006). DOI: 10.1016/j.susc.2006.02.041. (Cit. on p. 27).

[210] R. Plass et al.: "Cyclic ozone identified in magnesium oxide (111) surface reconstructions". *Phys. Rev. Lett.* **81** 4891 (1998). DOI: 10.1103/PhysRevLett.81.4891. (Cit. on p. 27).

[211] A. Barbier: "The NiO(111)-(1x1) surface". *Surf. Sci.* **402** 757 (1998). DOI: 10.1016/S0039-6028(97)01020-0. (Cit. on p. 27).

[212] F. Rohr et al.: "Hydroxyl driven reconstruction of the polar NiO(111) surface". *Surf. Sci.* **315** L977 (1994). DOI: 10.1016/0039-6028(94)90529-0. (Cit. on p. 27).

[213] S. Sindhu et al.: "A photoemission study of CoO-films on Au(111)". *Surf. Sci.* **541** 197 (2003). DOI: 10.1016/S0039-6028(03)00917-8. (Cit. on p. 27).

[214] J. Goniakowski, C. Noguera, and L. Giordano: "Prediction of Uncompensated Polarity in Ultrathin Films". *Phys. Rev. Lett.* **98** 205701 (2007). DOI: 10.1103/PhysRevLett.98.205701. (Cit. on p. 27).

[215] Y. J. Kim et al.: "Interlayer interactions in epitaxial oxide growth: FeO on Pt(111)". *Phys. Rev. B* **55** R13448 (1997). DOI: 10.1103/PhysRevB.55.R13448. (Cit. on pp. 27, 147, 152).

[216] W. Ranke, M. Ritter, and W. Weiss: "Crystal structures and growth mechanism for ultrathin films of ionic compound materials: FeO(111) on Pt(111)". *Phys. Rev. B* **60** 1527 (1999). DOI: 10.1103/PhysRevB.60.1527. (Cit. on pp. 27, 147, 152).

[217] W. Hebenstreit et al.: "Bulk Terminated NaCl(111) on Aluminum: A Polar Surface of an Ionic Crystal?" *Phys. Rev. Lett.* **85** 5376 (2000). DOI: 10.1103/PhysRevLett.85.5376. (Cit. on p. 27).

[218] G. Binnig et al.: "Tunneling through a controllable vacuum gap". *Appl. Phys. Lett.* **40** 178 (1982). DOI: 10.1063/1.92999. (Cit. on p. 29).

[219] C. J. Chen: *Introduction to Scanning Tunneling Microscopy.* Oxford University Press, New York (1993). (Cit. on pp. 29, 31).

[220] G. Binnig and H. Rohrer: "Scanning tunneling microscopy". *Surf. Sci.* **126** 236 (1982). DOI: 10.1016/0039-6028(83)90716-1. (Cit. on p. 29).

[221] J. G. Simmons: "Generalized Formula for the Electric Tunnel Effect between Similar Electrodes Separated by a Thin Insulating Film". *J. Appl. Phys.* **34** 1793 (1963). DOI: 10.1063/1.1702682. (Cit. on p. 30).

[222] K. H. Gundlach: "Zur Berechnung des Tunnelstroms durch eine trapezförmige Potentialstufe". *Solid State Electron.* **9** 949 (1966). DOI: 10.1016/0038-1101(66)90071-2. (Cit. on p. 31).

[223] Y. Suganuma and M. Tomitori: "Tunneling condition dependence of electron standing waves in vacuum gaps on Au(111) and Si(001) observed by scanning tunneling microscopy". *Surf. Sci.* **438** 311 (1999). DOI: 10.1016/S0039-6028(99)00596-8. (Cit. on p. 32).

[224] C. L. Lin et al.: "Manifestation of Work Function Difference in High Order Gundlach Oscillation". *Phys. Rev. Lett.* **99** 216103 (2007). DOI: 10.1103/PhysRevLett.99.216103. (Cit. on pp. 32, 158).

[225] J. L. Erskine and E. A. Stern: "Calculation of the M_{23} magneto-optical absorption spectrum of ferromagnetic nickel". *Phys. Rev. B* **12** 5016 (1975). DOI: 10.1103/PhysRevB.12.5016. (Cit. on p. 32).

[226] G. Schütz et al.: "Absorption of circularly polarized x-rays in iron". *Phys. Rev. Lett.* **58** 737 (1987). DOI: 10.1103/PhysRevLett.58.737. (Cit. on p. 32).

[227] J. Stöhr: "X-ray magnetic circular dichroism spectroscopy of transition metal thin films". *J. Electron. Spectrosc. Relat. Phenom.* **75** 253 (1995). DOI: 10.1016/0368-2048(95)02537-5. (Cit. on p. 32).

[228] T. Funk et al.: "X-ray magnetic circular dichroism - a high energy probe of magnetic properties". *Coord. Chem. Rev.* **249** 3 (2005). DOI: 10.1016/j.ccr.2004.05.017. (Cit. on p. 32).

[229] L. Mino et al.: "Low-dimensional systems investigated by x-ray absorption spectroscopy: a selection of 2D, 1D and 0D cases". *J. Phys. D: Appl. Phys.* **46** 423001 (2013). DOI: 10.1088/0022-3727/46/42/423001. (Cit. on p. 32).

[230] L. Tröger et al.: "Full correction of the self-absorption in soft-fluorescence extended x-ray-absorption fine structure". *Phys. Rev. B* **46** 3283 (1992). DOI: 10.1103/PhysRevB.46.3283. (Cit. on p. 33).

[231] E. Goering et al.: "Element specific x-ray magnetic circular dichroism magnetization curves using total electron yield". *J. Appl. Phys.* **88** 5920 (2000). DOI: 10.1063/1.1308095. (Cit. on p. 33).

[232] M. P. Seah and W. A. Dench: "Quantitative electron spectroscopy of surfaces: a standard data base for electron inelastic mean free paths in solids". *Surf. Interface Anal.* **1** 2 (1979). DOI: 10.1002/sia.740010103. (Cit. on p. 33).

[233] G. Schütz, M. Knülle, and H. Ebert: "Magnetic circular x-ray dichroism and its relation to local moments". *Phys. Scripta* **1993** 302 (1993). DOI: 10.1088/0031-8949/1993/T49A/053. (Cit. on p. 33).

[234] U. Fano: "Spin orientation of photoelectrons ejected by circularly polarized light". *Phys. Rev.* **178** 131 (1969). DOI: 10.1103/PhysRev.178.131. (Cit. on p. 33).

[235] U. Fano: "Spin orientation of photoelectrons: erratum and addendum". *Phys. Rev.* **184** 250 (1969). DOI: 10.1103/PhysRev.184.250. (Cit. on p. 33).

[236] J. Stöhr: "Exploring the microscopic origin of magnetic anisotropies with X-ray magnetic circular dichroism (XMCD) spectroscopy". *J. Magn. Magn. Mater.* **200** 470 (1999). DOI: 10.1016/S0304-8853(99)00407-2. (Cit. on p. 34).

[237] H. Ebert et al.: "L-edge x-ray absorption in fcc and bcc Cu metal: Comparison of experimental and first-principles theoretical results". *Phys. Rev. B* **53** 16067 (1996). DOI: 10.1103/PhysRevB.53.16067. (Cit. on pp. 34, 36).

[238] M. A. Tomaz et al.: "Comparison of x-ray magnetic circular dichroism at the L and M edges of Mo, Ru, Rh, and Pd". *J. Vac. Sci. Technol. A* **16** 1359 (1998). DOI: 10.1116/1.581151. (Cit. on pp. 34, 141).

[239] H. Ebert: "Magneto-optical effects in transition metal systems". *Rep. Prog. Phys.* **59** 1665 (1996). DOI: 10.1088/0034-4885/59/12/003. (Cit. on p. 34).

[240] B. T. Thole et al.: "X-ray circular dichroism as a probe of orbital magnetization". *Phys. Rev. Lett.* **68** 1943 (1992). DOI: 10.1103/PhysRevLett.68.1943. (Cit. on pp. 35, 127).

[241] P. Carra et al.: "X-ray circular dichroism and local magnetic fields". *Phys. Rev. Lett.* **70** 694 (1993). DOI: 10.1103/PhysRevLett.70.694. (Cit. on pp. 35, 36, 127).

[242] R. Wu, D. Wang, and A. J. Freeman: "First principles investigation of the validity and range of applicability of the x-ray magnetic circular dichroism sum rule". *Phys. Rev. Lett.* **71** 3581 (1993). DOI: 10.1103/PhysRevLett.71.3581. (Cit. on p. 36).

[243] J. P. Crocombette, B. T. Thole, and F. Jollet: "The importance of the magnetic dipole term in magneto-circular x-ray absorption dichroism for 3d transition metal compounds". *J. Phys.: Condens. Matter* **8** 4095 (1996). DOI: 10.1088/0953-8984/8/22/013. (Cit. on p. 36).

[244] J. P. Schillé et al.: "Experimental and calculated magnetic dichroism in the Ho 3d x-ray-absorption spectra of intermetallic $HoCo_2$". *Phys. Rev. B* **48** 9491 (1993). DOI: 10.1103/PhysRevB.48.9491. (Cit. on pp. 36, 108).

[245] W. L. O'Brien and B. P. Tonner: "Orbital and spin sum rules in x-ray magnetic circular dichroism". *Phys. Rev. B* **50** 12672 (1994). DOI: 10.1103/PhysRevB.50.12672. (Cit. on p. 36).

[246] S. Abdelouahed, N. Baadji, and M. Alouani: "Electronic structure and x-ray magnetic circular dichroism of gadolinium beyond the local spin density approximation". *Phys. Rev. B* **75** 094428 (2007). DOI: 10.1103/PhysRevB.75.094428. (Cit. on p. 36).

[247] V. V. Krishnamurthy et al.: "Temperature dependence of Eu 4f and Eu 5d magnetizations in the filled skutterudite $EuFe_4Sb_12$". *Phys. Rev. B* **79** 014426 (2009). DOI: 10.1103/PhysRevB.79.014426. (Cit. on p. 36).

[248] G. Ertl and J. Küppers: *Low Energy Electrons and Surface Chemistry.* VCH, Weinheim (1985). (Cit. on p. 36).

[249] M. A. van Hove, W. H. Weinberg, and C.-M. Chan: *Low-Energy Electron Diffraction.* Springer, Berlin (1986). (Cit. on pp. 36, 37).

[250] P. J. Rous et al.: "Tensor LEED: A Technique for High-Speed Surface-Structure Determination". *Phys. Rev. Lett.* **57** 2951 (1986). DOI: 10.1103/PhysRevLett.57.2951. (Cit. on p. 37).

[251] M. Ritter, W. Ranke, and W. Weiss: "Growth and structure of ultrathin FeO films on Pt(111) studied by STM and LEED". *Phys. Rev. B* **57** 7240 (1998). DOI: 10.1103/PhysRevB.57.7240. (Cit. on pp. 37, 154).

[252] L. H. Veneklasen: "The continuing development of low-energy electron microscopy for characterizing surfaces". *Rev. Sci. Instrum.* **63** 5513 (1992). DOI: 10.1063/1.1143377. (Cit. on pp. 38, 40).

[253] E. Bauer: "Low energy electron microscopy". *Rep. Prog. Phys.* **57** 895 (1994). DOI: 10.1088/0034-4885/57/9/002. (Cit. on pp. 38, 40).

[254] F.-J. Meyer zu Heringdorf: "Goldinduzierte Nanostrukturierung vicinaler Si(001) Oberflächen". PhD thesis. Universität Hannover (1999). (Cit. on pp. 38, 39).

[255] T. Schmidt et al.: "SPELEEM: Combining LEEM and Spectroscopic Imaging". *Surf. Rev. Lett.* **05** 1287 (1998). DOI: 10.1142/S0218625X98001626. (Cit. on pp. 39, 40, 47).

[256] H. Hertz: "Über einen Einfluss des ultravioletten Lichtes auf die electrische Entladung". *Ann. Phys.* **267** 983 (1887). DOI: 10.1002/andp.18872670827. (Cit. on p. 40).

[257] A. Einstein: "Über einen die Erzeugung und Verwandlung des Lichtes betreffenden heuristischen Gesichtspunkt". *Ann. Phys.* **322** 132 (1905). DOI: 10.1002/andp.19053220607. (Cit. on p. 40).

[258] L. I. Chelaru et al.: "Fringe fields in nonlinear photoemission microscopy". *Phys. Rev. B* **73** 115416 (2006). DOI: 10.1103/PhysRevB.73.115416. (Cit. on p. 40).

[259] A. Damascelli, Z. Hussain, and Z.-X. Shen: "Angle-resolved photoemission studies of the cuprate superconductors". *Rev. Mod. Phys.* **75** 473 (2003). DOI: 10.1103/RevModPhys.75.473. (Cit. on p. 41).

[260] T. Michely, M. Kaiser, and M. J. Rost: "Plug 'n' play scanning probe microscopy". *Rev. Sci. Instrum.* **71** 4461 (2000). DOI: 10.1063/1.1322587. (Cit. on p. 44).

[261] I. Horcas et al.: "WSxM: A software for scanning probe microscopy and a tool for nanotechnology". *Rev. Sci. Instrum.* **78** 013705 (2007). DOI: 10.1063/1.2432410. (Cit. on p. 44).

[262] I. Pletikosić: "Electronic states of epitaxial graphene on iridium". PhD thesis. University of Zagreb (2012). (Cit. on pp. 45, 46).

[263] J. D. Rameau, H.-B. Yang, and P. D. Johnson: "Application of the Lucy-Richardson deconvolution procedure to high resolution photoemission spectra". *J. Electron. Spectrosc. Relat. Phenom.* **181** 35 (2010). DOI: 10.1016/j.elspec.2010.05.025. (Cit. on p. 46).

[264] R. van Gastel et al.: "Selecting a single orientation for millimeter sized graphene sheets". *Appl. Phys. Lett.* **95** 121901 (2009). DOI: 10.1063/1.3225554. (Cit. on p. 47).

[265] P. Hohenberg and W. Kohn: "Inhomogeneous Electron Gas". *Phys. Rev.* **136** B864 (1964). DOI: 10.1103/PhysRev.136.B864. (Cit. on p. 48).

[266] W. Kohn and L. J. Sham: "Self-Consistent Equations Including Exchange and Correlation Effects". *Phys. Rev.* **140** A1133 (1965). DOI: 10.1103/PhysRev.140.A1133. (Cit. on p. 48).

[267] J. P. Perdew, K. Burke, and M. Ernzerhof: "Generalized Gradient Approximation Made Simple". *Phys. Rev. Lett.* **77** 3865 (1996). DOI: 10.1103/PhysRevLett.77.3865. (Cit. on p. 49).

[268] P. E. Blöchl: "Projector augmented-wave method". *Phys. Rev. B* **50** 17953 (1994). DOI: 10.1103/PhysRevB.50.17953. (Cit. on p. 49).

[269] G. Kresse and J. Hafner: "*Ab initio* molecular dynamics for liquid metals". *Phys. Rev. B* **47** 558 (1993). DOI: 10.1103/PhysRevB.47.558. (Cit. on p. 49).

[270] G. Kresse and J. Hafner: "Norm-conserving and ultrasoft pseudopotentials for first-row and transition elements". *J. Phys.: Condens. Matter* **6** 8245 (1994). DOI: 10.1088/0953-8984/6/40/015. (Cit. on p. 49).

[271] V. I. Anisimov, F. Aryasetiawan, and A. I. Lichtenstein: "First-principles calculations of the electronic structure and spectra of strongly correlated systems: the LDA+U method". *J. Phys.: Condens. Matter* **9** 767 (1997). DOI: 10.1088/0953-8984/9/4/002. (Cit. on p. 49).

[272] P. Larson et al.: "Electronic structure of rare-earth nitrides using the LSDA+U approach: Importance of allowing $4f$ orbitals to break the cubic crystal symmetry". *Phys. Rev. B* **75** 045114 (2007). DOI: 10.1103/PhysRevB.75.045114. (Cit. on p. 49).

[273] F. Huttmann: "Adsorption on and Intercalation under Gr/Ir(111): Magnetism and Binding". Master thesis. Universität zu Köln (2013). (Cit. on pp. 51, 74, 81, 97, 107, 125, 170).

[274] H. Zhang et al.: "Growth mechanism of graphene on Ru(0001) and O_2 adsorption on the graphene/Ru(0001) surface". *J. Phys. Chem. C* **113** 8296 (2009). DOI: 10.1021/jp810514u. (Cit. on p. 58).

[275] M. Sicot et al.: "Size-Selected Epitaxial Nanoislands Underneath Graphene Moiré on Rh(111)". *ACS Nano* **114** 151 (2012). DOI: 10.1021/nn203169j. (Cit. on pp. 58, 73).

[276] K. V. Emtsev et al.: "Ambiploar doping in quasifree epitaxial graphene on SiC(0001) controlled by Ge intercalation". *Phys. Rev. B* **84** 125423 (2011). DOI: 10.1103/PhysRevB.84.125423. (Cit. on p. 58).

[277] K.-O. Ng and D. Vanderbilt: "Stability of periodic domain structures in a two-dimensional dipolar model". *Phys. Rev. B* **52** 2177 (1995). DOI: 10.1103/PhysRevB.52.2177. (Cit. on p. 58).

[278] M. Mucha-Kruczyński et al.: "Characterization of graphene through anisotropy of constant-energy maps in angle-resolved photoemission". *Phys. Rev. B* **77** 195403 (2008). DOI: 10.1103/PhysRevB.77.195403. (Cit. on p. 69).

[279] I. Pletikosić et al.: "Dirac Cones and Minigaps for Graphene on Ir(111)". *Phys. Rev. Lett.* **102** 056808 (2009). DOI: 10.1103/PhysRevLett.102.056808. (Cit. on pp. 69, 71, 72, 85).

[280] M. Kralj et al.: "Graphene on Ir(111) characterized by angle-resolved photoemission". *Phys. Rev. B* **84** 075427 (2011). DOI: 10.1103/PhysRevB.84.075427. (Cit. on p. 70).

[281] A. Bostwick et al.: "Renormalization of graphene bands by many-body interactions". *Solid State Commun.* **143** 63 (2007). DOI: 10.1016/j.ssc.2007.04.034. (Cit. on p. 71).

[282] W.-K. Tse and S. Das Sarma: "Phonon-Induced Many-Body Renormalization of the Electronic Properties of Graphene". *Phys. Rev. Lett.* **99** 236802 (2007). DOI: 10.1103/PhysRevLett.99.236802. (Cit. on p. 71).

[283] E. Grånäs et al.: "Oxygen Intercalation under Graphene on Ir(111): Energetics, Kinetics, and the Role of Graphene Edges". *ACS Nano* **6** 9951 (2012). DOI: 10.1021/nn303548z. (Cit. on p. 72).

[284] M. Petrović et al.: "The mechanism of caesium intercalation of graphene". *Nature Comm.* **4** 2772 (2013). DOI: 10.1038/ncomms3772. (Cit. on pp. 73, 76, 85).

[285] A. Kimouche et al.: "Modulating charge density and inelastic optical response in graphene by atmospheric pressure localized intercalation through wrinkles". *Carbon* **68** 73 (2014). DOI: 10.1016/j.carbon.2013.10.033. (Cit. on p. 73).

[286] A. Markevich et al.: "First-principles study of hydrogen and fluorine intercalation into graphene-SiC(0001) interface". *Phys. Rev. B* **86** 045453 (2012). DOI: 10.1103/PhysRevB.86.045453. (Cit. on p. 73).

[287] T. P. Kaloni et al.: "Mechanism of Si intercalation in defective graphene on SiC". *J. Mater. Chem.* **22** 23340–23343 (2012). DOI: 10.1039/C2JM35127G. (Cit. on p. 73).

[288] C. Xia et al.: "Si intercalation/deintercalation of graphene on 6H-SiC(0001)". *Phys. Rev. B* **85** 045418 (2012). DOI: 10.1103/PhysRevB.85.045418. (Cit. on p. 73).

[289] J. Song, B. Ouyang, and N. V. Medhekar: "Energetics and Kinetics of Li Intercalation in Irradiated Graphene Scaffolds". *ACS Appl. Mater. Inter.* **5** 12968 (2013). DOI: 10.1021/am403685w. (Cit. on p. 73).

[290] D. L. Duong et al.: "Probing graphene grain boundaries with optical microscopy". *Nature* **490** 235 (2012). DOI: 10.1038/nature11562. (Cit. on p. 73).

[291] D. W. Boukhvalov and M. I. Katsnelson: "Destruction of graphene by metal adatoms". *Appl. Phys. Lett.* **95** 023109 (2009). DOI: 10.1063/1.3160551. (Cit. on p. 73).

[292] C. Virojanadara et al.: "Epitaxial graphene on 6H-SiC and Li intercalation". *Phys. Rev. B* **82** 205402 (2010). DOI: 10.1103/PhysRevB.82.205402. (Cit. on p. 73).

[293] H. Ishida and R. E. Palmer: "Electronic structure and phase transitions of submonolayer potassium on graphite". *Phys. Rev. B* **46** 15484 (1992). DOI: 10.1103/PhysRevB.46.15484. (Cit. on p. 81).

[294] T. O. Wehling, M. I. Katsnelson, and A. I. Lichtenstein: "Adsorbates on graphene: Impurity states and electron scattering". *Chem. Phys. Lett.* **476** 125 (2009). DOI: 10.1016/j.cplett.2009.06.005. (Cit. on p. 82).

[295] H. Liu, Y. Liu, and D. Zhu: "Chemical doping of graphene". *J. Mater. Chem.* **21** 3335 (2011). DOI: 10.1039/C0JM02922J. (Cit. on p. 82).

[296] P. A. Khomyakov et al.: "First-principles study of the interaction and charge transfer between graphene and metals". *Phys. Rev. B* **79** 195425 (2009). DOI: 10.1103/PhysRevB.79.195425. (Cit. on p. 87).

[297] R. D. Diehl and R. McGrath: "Structural studies of alkali metal adsorption and coadsorption on metal surfaces". *Surf. Sci. Rep.* **23** 43 (1996). DOI: 10.1016/0167-5729(95)00010-0. (Cit. on p. 97).

[298] H. P. Bonzel, A. M. Bradshaw, and G. Ertl: *Physics and chemistry of alkali metal adsorption.* Elsevier, Amsterdam (1989). (Cit. on p. 97).

[299] L. Pauling: *The nature of the chemical bond.* Cornell University Press, New York (1960). (Cit. on pp. 100, 147).

[300] J. F. Elliott, S. Legvold, and F. H. Spedding: "Some Magnetic Properties of Gadolinium Metal". *Phys. Rev.* **91** 28 (1953). DOI: 10.1103/PhysRev.91.28. (Cit. on p. 100).

[301] C. Nagl et al.: "Submonolayer growth of Pb on Cu(111): surface alloying and de-alloying". *Surf. Sci.* **321** 237 (1994). DOI: 10.1016/0039-6028(94)90189-9. (Cit. on pp. 102, 105).

[302] J. C. Slater: "Atomic Radii in Crystals". *J. Chem. Phys.* **41** 3199 (1964). DOI: 10.1063/1.1725697. (Cit. on p. 102).

[303] A. Atrei et al.: "LEED crystallographic investigation of ultrathin films formed by deposition of Sn on the Pt(111) surface". *Surf. Sci.* **290** 286 (1993). DOI: 10.1016/0039-6028(93)90712-S. (Cit. on p. 103).

[304] C. T. Campbell and D. W. Goodman: "The interaction of aluminum with the ruthenium(0001) surface and its influence upon carbon monoxide chemisorption". *J. Phys. Chem.* **92** 2569 (1988). DOI: 10.1021/j100320a034. (Cit. on p. 103).

[305] S. Mehendale et al.: "Ordered Surface Alloy of Bulk-Immiscible Components Stabilized by Magnetism". *Phys. Rev. Lett.* **105** 056101 (2010). DOI: 10.1103/PhysRevLett.105.056101. (Cit. on p. 103).

[306] Y. Fujinaga: "Surface structures of Cu-Au and Cu-Pd alloys as observed by leed". *Surf. Sci.* **86** 581 (1979). DOI: 10.1016/0039-6028(79)90437-0. (Cit. on p. 104).

[307] A. Atrei et al.: "Structure of the (001)- and (111)-oriented surfaces of the ordered fcc Pt_3Sn alloy by low-energy-electron-diffraction intensity analysis". *Phys. Rev. B* **46** 1649 (1992). DOI: 10.1103/PhysRevB.46.1649. (Cit. on p. 104).

[308] M. Corso et al.: "Rare-Earth Surface Alloying: A New Phase for $GdAu_2$". *Phys. Rev. Lett.* **105** 016101 (2010). DOI: 10.1103/PhysRevLett.105.016101. (Cit. on p. 105).

[309] M. Corso et al.: "Au(111)-Based Nanotemplates by Gd Alloying". *ACS Nano* **4** 1603 (2010). DOI: 10.1021/nn901345s. (Cit. on p. 105).

[310] L. Fernández et al.: "Self-organized growth of high density magnetic Co nanodot arrays on a Moiré template". *Appl. Phys. Lett.* **96** 013107 (2010). DOI: 10.1063/1.3280900. (Cit. on p. 105).

[311] S. Narasimhan and D. Vanderbilt: "Elastic stress domains and the herringbone reconstruction on Au(111)". *Phys. Rev. Lett.* **69** 1564 (1992). DOI: 10.1103/PhysRevLett.69.1564. (Cit. on p. 105).

[312] P. A. Korzhavyi et al.: "First-principles calculations of the vacancy formation energy in transition and noble metals". *Phys. Rev. B* **59** 11693 (1999). DOI: 10.1103/PhysRevB.59.11693. (Cit. on p. 105).

[313] B. T. Thole et al.: "3d x-ray-absorption lines and the $3d^9 4f^{n+1}$ multiplets of the lanthanides". *Phys. Rev. B* **32** 5107 (1985). DOI: 10.1103/PhysRevB.32.5107. (Cit. on p. 110).

[314] J. T. Lau et al.: "Size Dependence of $L_{2,3}$ Branching Ratio and $2p$ Core-Hole Screening in X-Ray Absorption of Metal Clusters". *Phys. Rev. Lett.* **101** 153401 (2008). DOI: 10.1103/PhysRevLett.101.153401. (Cit. on p. 110).

[315] C. Kittel: *Introduction to solid state physics.* Wiley & Sons, New York (1976). (Cit. on p. 114).

[316] N. D. Mermin and H. Wagner: "Absence of Ferromagnetism or Antiferromagnetism in One- or Two-Dimensional Isotropic Heisenberg Models". *Phys. Rev. Lett.* **17** 1133 (1966). DOI: 10.1103/PhysRevLett.17.1133. (Cit. on p. 114).

[317] A. Grechnev et al.: "Thermodynamics of a two-dimensional Heisenberg ferromagnet with dipolar interaction". *Phys. Rev. B* **71** 024427 (2005). DOI: 10.1103/PhysRevB.71.024427. (Cit. on p. 114).

[318] G. H. O. Daalderop, P. J. Kelly, and M. F. H. Schuurmans: "First-principles calculation of the magnetocrystalline anisotropy energy of iron, cobalt, and nickel". *Phys. Rev. B* **41** 11919 (1990). DOI: 10.1103/PhysRevB.41.11919. (Cit. on p. 116).

[319] K. Barmak et al.: "On the relationship of magnetocrystalline anisotropy and stoichiometry in epitaxial $L1_0$ CoPt(001) and FePt(001) thin films". *J. Appl. Phys.* **98** 033904 (2005). DOI: 10.1063/1.1991968. (Cit. on p. 116).

[320] R. C. Rau and W. J. Glover: "Thermal Decomposition of Europium Hydroxide". *J. Am. Ceram. Soc.* **47** 382 (1964). DOI: 10.1111/j.1151-2916.1964.tb13836.x. (Cit. on p. 120).

[321] L. Gmelin: *Gmelins Handbuch der anorganischen Chemie.* Verlag Chemie Weinheim (1960). (Cit. on p. 121).

[322] C. Vo-Van et al.: "Magnetism of cobalt nanoclusters on graphene on iridium". *Appl. Phys. Lett.* **99** 142504 (2011). DOI: 10.1063/1.3646480. (Cit. on pp. 125, 213).

[323] P. Ghigna et al.: "X-ray magnetic-circular-dichroism spectra on the superparamagnetic transition-metal ion clusters Mn12 and Fe8". *Phys. Rev. B* **64** 132413 (2001). DOI: 10.1103/PhysRevB.64.132413. (Cit. on p. 126).

[324] A. Lehnert et al.: "Magnetic anisotropy of Fe and Co adatoms and Fe clusters magnetically decoupled from $Ni_3Al(111)$ by an alumina bilayer". *Phys. Rev. B* **81** 104430 (2010). DOI: 10.1103/PhysRevB.81.104430. (Cit. on p. 126).

[325] S. S. Datta et al.: "Crystallographic Etching of Few-Layer Graphene". *Nano Lett.* **8** 1912 (2008). DOI: 10.1021/nl080583r. (Cit. on p. 127).

[326] R. Wu and A. J. Freeman: "Limitation of the Magnetic-Circular-Dichroism Spin Sum Rule for Transition Metals and Importance of the Magnetic Dipole Term". *Phys. Rev. Lett.* **73** 1994 (1994). DOI: 10.1103/PhysRevLett.73.1994. (Cit. on p. 127).

[327] P. Bruno: "Tight-binding approach to the orbital magnetic moment and magnetocrystalline anisotropy of transition-metal monolayers". *Phys. Rev. B* **39** 865 (1989). DOI: 10.1103/PhysRevB.39.865. (Cit. on p. 128).

[328] P. Ohresser et al.: "Magnetism of small Fe clusters on Au(111) studied by x-ray magnetic circular dichroism". *Phys. Rev. B* **64** 104429 (2001). DOI: 10.1103/PhysRevB.64.104429. (Cit. on p. 128).

[329] P. Gambardella et al.: "Giant magnetic anisotropy of single cobalt atoms and nanoparticles". *Science* **300** 1130 (2003). DOI: 10.1126/science.1082857. (Cit. on pp. 128, 130).

[330] N. Weiss et al.: "Uniform Magnetic Properties for an Ultrahigh-Density Lattice of Noninteracting Co Nanostructures". *Phys. Rev. Lett.* **95** 157204 (2005). DOI: 10.1103/PhysRevLett.95.157204. (Cit. on p. 128).

[331] M. Respaud et al.: "Surface effects on the magnetic properties of ultrafine cobalt particles". *Phys. Rev. B* **57** 2925 (1998). DOI: 10.1103/PhysRevB.57.2925. (Cit. on p. 130).

[332] M. Respaud: "Magnetization process of noninteracting ferromagnetic cobalt nanoparticles in the superparamagnetic regime: Deviation from Langevin law". *J. Appl. Phys.* **86** 556 (1999). DOI: 10.1063/1.370765. (Cit. on p. 130).

[333] D. A. Dimitrov and G. M. Wysin: "Magnetic properties of spherical fcc clusters with radial surface anisotropy". *Phys. Rev. B* **51** 11947 (1995). DOI: 10.1103/PhysRevB.51.11947. (Cit. on p. 130).

[334] T. Gerber et al.: "CO-Induced Smoluchowski Ripening of Pt Cluster Arrays on the Graphene/Ir(111) Moiré". *ACS Nano* **7** 2020 (2013). DOI: 10.1021/nn400082w. (Cit. on p. 130).

[335] H. Hattab et al.: "Growth temperature dependent graphene alignment on Ir(111)". *Appl. Phys. Lett.* **98** 141903 (2011). DOI: 10.1063/1.3548546. (Cit. on p. 132).

[336] A. J. Cox, J. G. Louderback, and L. A. Bloomfield: "Experimental observation of magnetism in rhodium clusters". *Phys. Rev. Lett.* **71** 923 (1993). DOI: 10.1103/PhysRevLett.71.923. (Cit. on pp. 137, 139).

[337] V. Sessi et al.: "Intrinsic orbital and spin magnetism in Rh clusters on inert xenon matrices". *Phys. Rev. B* **82** 184413 (2010). DOI: 10.1103/PhysRevB.82.184413. (Cit. on pp. 138, 141).

[338] V. M. T. S. Barthem et al.: "Spin Fluctuations of Paramagnetic Rh Clusters Revealed by X-Ray Magnetic Circular Dichroism". *Phys. Rev. Lett.* **109** 197204 (2012). DOI: 10.1103/PhysRevLett.109.197204. (Cit. on pp. 138, 142).

[339] J. Honolka et al.: "Absence of local magnetic moments in Ru and Rh impurities and clusters on Ag(100) and Pt(997)". *Phys. Rev. B* **76** 144412 (2007). DOI: 10.1103/PhysRevB.76.144412. (Cit. on p. 138).

[340] T. Gerber: "Interaction of Graphene and Templated Cluster Arrays with CO, H_2, and O_2". PhD thesis. Universiät zu Köln (2013). (Cit. on p. 138).

[341] A. Cavallin et al.: "Local Electronic Structure and Density of Edge and Facet Atoms at Rh Nanoclusters Self-Assembled on a Graphene Template". *ACS Nano* **6** 3034 (2012). DOI: 10.1021/nn300651s. (Cit. on p. 138).

[342] H. C. Galloway, J. J. Benitez, and M. Salmeron: "The structure of monolayer films of FeO on Pt(111)". *Surf. Sci.* **298** 127 (1993). DOI: 10.1016/0039-6028(93)90089-3. (Cit. on pp. 146, 154).

[343] G. Barcaro, I. O. Thomas, and A. Fortunelli: "Validation of density-functional versus density-functional + U approaches for oxide ultrathin films". *J. Chem. Phys.* **132** 124703 (2010). DOI: 10.1063/1.3366689. (Cit. on p. 147).

[344] C. S. Fadley et al.: "Photoelectron diffraction: new dimensions in space, time, and spin". *J. Electron. Spectrosc. Relat. Phenom.* **75** 273 (1995). DOI: 10.1016/0368-2048(95)02545-6. (Cit. on pp. 147, 152).

[345] B. Sachs et al.: "Adhesion and electronic structure of graphene on hexagonal boron nitride substrates". *Phys. Rev. B* **84** 195414 (2011). DOI: 10.1103/PhysRevB.84.195414. (Cit. on p. 147).

[346] R. Smoluchowski: "Anisotropy of the Electronic Work Function of Metals". *Phys. Rev.* **60** 661 (1941). DOI: 10.1103/PhysRev.60.661. (Cit. on p. 149).

[347] J. Goniakowski, C. Noguera, and L. Giordano: "Polarity of ultrathin MgO(111) films deposited on a metal substrate". *Phys. Rev. Lett.* **93** 215702 (2004). DOI: 10.1103/PhysRevLett.93.215702. (Cit. on p. 152).

[348] L. R. Merte et al.: "Correlating STM contrast and atomic-scale structure by chemical modification: Vacancy dislocation loops on FeO/Pt(111)". *Surf. Sci.* **603** L15 (2009). DOI: 10.1016/j.susc.2008.11.014. (Cit. on p. 154).

[349] A. D. Novaco and J. P. McTague: "Orientational Epitaxy - the Orientational Ordering of Incommensurate Structures". *Phys. Rev. Lett.* **38** 1286 (1977). DOI: 10.1103/PhysRevLett.38.1286. (Cit. on p. 154).

[350] J. P. McTague and A. D. Novaco: "Substrate-induced strain and orientational ordering in adsorbed monolayers". *Phys. Rev. B* **19** 5299 (1979). DOI: 10.1103/PhysRevB.19.5299. (Cit. on p. 154).

[351] C. G. Shaw, S. C. Fain, and M. D. Chinn: "Observation of Orientational Ordering of Incommensurate Argon Monolayers on Graphite". *Phys. Rev. Lett.* **41** 955 (1978). DOI: 10.1103/PhysRevLett.41.955. (Cit. on p. 154).

[352] L. Olesen et al.: "Apparent Barrier Height in Scanning Tunneling Microscopy Revisited". *Phys. Rev. Lett.* **76** 1485 (1996). DOI: 10.1103/PhysRevLett.76.1485. (Cit. on p. 157).

[353] T. König et al.: "Work Function Measurements of Thin Oxide Films on Metals - MgO on Ag(001)". *J. Phys. Chem. C* **113** 11301 (2009). DOI: 10.1021/jp901226q. (Cit. on p. 159).

[354] V. P. Ivanov et al.: "The chemisorption of oxygen on the iridium (111) surface". *Surf. Sci.* **61** 207 (1976). DOI: 10.1016/0039-6028(76)90415-5. (Cit. on p. 159).

[355] R. W. Strayer, W. Mackie, and L. W. Swanson: "Work function measurements by the field emission retarding potential method". *Surf. Sci.* **34** 225 (1973). DOI: 10.1016/0039-6028(73)90117-9. (Cit. on p. 159).

[356] K Jakobi: *3.1.2.4 Work function data*. SpringerMaterials - The Landolt-Börnstein Database (1994). DOI: 10.1007/10086058_16. (Cit. on p. 159).

[357] G. Busch, P. Cotti, and P. Munz: "Photoemission from europium chalcogenides". *Solid State Commun.* **7** 795 (1969). DOI: 10.1016/0038-1098(69)90669-3. (Cit. on p. 160).

[358] D. E. Eastman, F. Holtzberg, and S. Methfessel: "Photoemission Studies of the Electronic Structure of EuO, EuS, EuSe, And GdS". *Phys. Rev. Lett.* **23** 226 (1969). DOI: 10.1103/PhysRevLett.23.226. (Cit. on p. 160).

[359] J. Goniakowski, L. Giordano, and C. Noguera: "Polarity of ultrathin MgO(111) films deposited on a metal substrate". *Phys. Rev. B* **81** 205404 (2010). DOI: 10.1103/PhysRevB.81.205404. (Cit. on p. 160).

[360] E. D. L. Rienks et al.: "Surface potential of a polar oxide film: FeO on Pt(111)". *Phys. Rev. B* **71** 241404 (2005). DOI: 10.1103/PhysRevB.71.241404. (Cit. on p. 160).

[361] N. Nilius et al.: "Electronic and electrostatic properties of polar oxide nanostructures: MgO(111) islands on Au(111)". *Phys. Rev. B* **86** 205410 (2012). DOI: 10.1103/PhysRevB.86.205410. (Cit. on p. 160).

[362] J. Knudsen et al.: "Reduction of FeO/Pt(111) thin films by exposure to atomic hydrogen". *Surf. Sci.* **604** 11 (2010). DOI: 10.1016/j.susc.2009.10.008. (Cit. on p. 161).

[363] Y. Yao et al.: "Growth and Characterization of Two-Dimensional FeO Nanoislands Supported on Pt(111)". *J. Phys. Chem. C* **114** 17069 (2010). DOI: 10.1021/jp1036537. (Cit. on p. 161).

[364] O. Dulub, U. Diebold, and G. Kresse: "Novel stabilization mechanism on polar surfaces: ZnO(0001)-Zn". *Phys. Rev. Lett.* **90** 016102 (2003). DOI: 10.1103/PhysRevLett.90.016102. (Cit. on p. 164).

[365] E. J. Huber and C. E. Holley: "Enthalpy of formation of europium monoxide". *J. Chem. Thermodyn.* **1** 301 (1969). DOI: 10.1016/0021-9614(69)90049-4. (Cit. on p. 165).

[366] R. Schiller and W. Nolting: "Prediction of a Surface State and a Related Surface Insulator-Metal Transition for the (100) Surface of Stochiometric EuO". *Phys. Rev. Lett.* **86** 3847 (2001). DOI: 10.1103/PhysRevLett.86.3847. (Cit. on p. 165).

[367] F. Huttmann et al.: "Tuning the van der Waals Interaction of Graphene with Molecules via Doping". *In preparation* (2014). (Cit. on pp. 170, 214).

[368] S. Heinze et al.: "Spontaneous atomic-scale magnetic skyrmion lattice in two dimensions". *Nature Phys.* **7** 713 (2011). DOI: 10.1038/nphys2045. (Cit. on p. 171).

[369] M. Wuttig, Y. Gauthier, and S. Blügel: "Magnetically driven buckling and stability of ordered surface alloys: Cu(100)c(2x2)Mn". *Phys. Rev. Lett.* **70** 3619 (1993). DOI: 10.1103/PhysRevLett.70.3619. (Cit. on p. 171).

[370] S. Blügel: "Magnetically stabilized surface alloys". English. *Appl. Phys. A* **63** 595 (1996). DOI: 10.1007/BF01567215. (Cit. on p. 171).

[371] W. L. O'Brien and B. P. Tonner: "Magnetic properties of Mn/Cu(001) and Mn/Ni(001)c(2x2) surface alloys". *Phys. Rev. B* **51** 617 (1995). DOI: 10.1103/PhysRevB.51.617. (Cit. on p. 171).

[372] C. R. Ast et al.: "Giant Spin Splitting through Surface Alloying". *Phys. Rev. Lett.* **98** 186807 (2007). DOI: 10.1103/PhysRevLett.98.186807. (Cit. on p. 171).

[373] H. Mirhosseini et al.: "Unconventional spin topology in surface alloys with Rashba-type spin splitting". *Phys. Rev. B* **79** 245428 (2009). DOI: 10.1103/PhysRevB.79.245428. (Cit. on p. 171).

[374] E. A. Soares et al.: "Graphene-protected Fe layers atop Ni(111): Evidence for strong Fe-graphene interaction and structural bistability". *Phys. Rev. B* **88** 165410 (2013). DOI: 10.1103/PhysRevB.88.165410. (Cit. on p. 172).

[375] S. Schumacher et al.: "Europium Underneath Graphene on Ir(111): Intercalation Mechanism, Magnetism, and Band Structure". *In preparation* (2014). (Cit. on p. 213).

List of Publications

Parts of the results presented in this thesis can be found in:

[322] C. Vo-Van, S. Schumacher, J. Coraux, V. Sessi, O. Fruchart, N. B. Brookes, P. Ohresser, and T. Michely
Magnetism of Cobalt Nanoclusters on Graphene on Iridium
Appl. Phys. Lett. **99** 142504 (2011)

[62] S. Schumacher, D. F. Förster, M. Rösner, T. O. Wehling, and T. Michely
Strain in Epitaxial Graphene Visualized by Intercalation
Phys. Rev. Lett. **110** 086111 (2013)

[63] S. Schumacher, T. O. Wehling, P. Lazić, S. Runte, D. F. Förster, C. Busse, M. Petrović, M. Kralj, S. Blügel, N. Atodiresei, V. Caciuc, and T. Michely
The Backside of Graphene: Manipulating Adsorption by Intercalation
Nano Lett. **13** 5013 (2013)

[64] S. Schumacher, D. F. Förster, F. Hu, T. Frauenheim, T. O. Wehling, and T. Michely
Polar EuO(111) on Ir(111): A two-dimensional oxide
Phys. Rev. B **89** 115410 (2014)

The following manuscript containing results from this thesis is in preparation:

[375] S. Schumacher, F. Huttmann, M. Petrović, C. Witt, D. F. Förster, C. Vo-Van, J. Coraux, V. Sessi, M. Grüninger, R. Rückamp, I. Vergara, N. Schleheck, F. Meyer zu Heringdorf, P. Ohresser, M. Kralj, T. O. Wehling, and T. Michely
Europium Underneath Graphene on Ir(111): Intercalation Mechanism, Magnetism, and Band Structure
In preparation (2014)

Apart from the topics of this thesis I also contributed to the following articles:

[28] D. F. Förster, T. O. Wehling, S. Schumacher, A. Rosch, and T. Michely
Phase Coexistence of Clusters and Islands: Europium on Graphene
New J. Phys. **14** 023022 (2012)

[114] C. Herbig, M. Kaiser, N. Bendiab, J. Coraux, S. Schumacher, D. F. Förster, K. Meerholz, T. Michely, and C. Busse
Mechanical Exfoliation of Epitaxial Graphene on Ir(111) Enabled by Br_2 Intercalation
J. Phys.: Condens. Matter **24** 314208 (2012)

[102] D. Franz, S. Runte, C. Busse, S. Schumacher, T. Gerber, T. Michely, M. Mantilla, V. Kilic, J. Zegenhagen, and A. Stierle
Atomic Structure and Crystalline Order of Graphene-Supported Ir Nanoparticle Lattices
Phys. Rev. Lett. **110** 065503 (2013)

[50] J. Klinkhammer, D. F. Förster, S. Schumacher, H. P. Oepen, T. Michely, and C. Busse
Structure and magnetic properties of ultra thin textured EuO films on graphene
Appl. Phys. Lett. **103** 141601 (2013)

[367] F. Huttmann, A. J. Martínez-Galera, N. Atodiresei, V. Caciuc, S. Schumacher, S. Standop, T. O. Wehling, S. Blügel, and T. Michely
Tuning the van der Waals Interaction of Graphene with Molecules via Doping
In preparation (2014)

Acknowledgement (Danksagung)

Zum Gelingen dieser Arbeit haben viele Personen auf unterschiedliche Art und Weise beigetragen. Bei diesen möchte ich mich abschließend herzlich bedanken.
An erster Stelle danke ich Thomas Michely. Durch seine Vorlesungen hat er mein Interesse für die Oberflächenphysik geweckt. Im Rahmen meiner Diplomarbeit und Promotion hat er mir die Möglichkeit geboten, an interessanten Forschungsthemen zu arbeiten, und zudem zahlreiche Kooperationen vermittelt. Seine kritischen Fragen und das sichere Gespür für den Kern der Sache waren von unschätzbarem Wert für diese Arbeit.
Bei Tim Wehling möchte ich mich für die Zweitbegutachtung meiner Arbeit sowie die umfangreichen DFT-Rechnungen bedanken. Ohne diese Ergebnisse wäre ein so fundiertes Verständnis der Systeme nicht möglich gewesen. In zahlreichen Diskussionen hat er zudem stets Unterstützung von Seiten der Theoretischen Physik geboten.
Ich danke Sanjay Mathur für sein Interesse an der Arbeit und die Bereitschaft, den Vorsitz der Prüfungskommission zu übernehmen. Zudem bedanke ich mich bei Heiko Wende für die kurzfristige Erstellung eines Drittgutachtens. Ebenso danke ich Carsten Busse für die Übernahme des Beisitzes trotz seines Geburtstages. Ich danke ihm zudem für zahlreiche Anregungen und Anekdoten während des Mittagessens.
A large part of this work was done in the context of cooperations. Thus, I want to express my gratitude to all collaborators. Furthermore, I acknowledge all coauthors for their contributions to my publications. In this respect, I especially thank Malte Rösner, Feiming Hu, and Predrag Lazić for their DFT calculations and theoretical considerations.
In addition, I want to thank Marin Petrović and Marko Krajl for the facility to perform ARPES measurements in Zagreb and for their hospitality during my stay. Fruitful discussions with them have substantially contributed to this thesis.
My special thanks go to Philippe Ohresser, who shared his profound knowledge of XMCD with me and answered my questions always in great detail. I acknowledge Violetta Sessi and Andrea Fondacaro for the scientific and technical support at the ID08 beamline. Moreover, I thank Johann Coraux, Olivier Fruchart, Nicholas Rougemaille, and Chi Vo-Van for their contributions during and after the beamtimes at the ESRF.
Des Weiteren danke ich Frank Meyer zu Heringdorf und Michael Horn-von Hoegen für die Ermöglichung der LEEM/PEEM-Kooperation mit der Universität Duisburg-Essen. Ebenso danke ich Christian Witt für die Einführung in die beiden Messtechniken.

Mein besonderer Dank gilt Felix Huttmann, der im Rahmen seiner Masterarbeit wesentliche Beiträge zu dieser Arbeit geleistet hat. Seine unglaublich schnelle Auffassungsgabe und zahlreiche Diskussionen haben mir auch während unserer gemeinsamen Doktorandenzeit oft weitergeholfen. Darüber hinaus danke ich ihm für das Korrekturlesen.
Ich danke Daniel Förster, der mir ein umfassendes Wissen über STM, UHV und Oberflächen vermittelt hat. Mit seiner Doktorarbeit hat er zudem viele Grundlagen für die vorliegende Arbeit geschaffen. Ebenso danke ich ihm für das Korrekturlesen.
Furthermore, I acknowledge Antonio Martínez-Galera for the time as my office mate, for joining the LEEM measurements in Duisburg, and for proof reading.
Ich danke meinen Doktorandenkollegen Fabian Craes, Martin Engler, Charlotte Herbig und Ulrike Schröder für die gute Zusammenarbeit und freundschaftliche Atmosphäre - egal ob im Labor, Büro oder Kaffeeraum. Vielen Dank auch für das Korrekturlesen. Zudem danke ich meinen ehemaligen Kollegen Timm Gerber, Jürgen Klinkhammer, Sven Runte und Sebastian Standop für die schöne gemeinsame Zeit als Doktoranden. Darüber hinaus möchte ich allen noch nicht genannten Mitgliedern der Arbeitsgruppe Michely für das angenehme Arbeitsklima danken. Namentlich sind dies Daniela Dombrowski, Ferdinand Farwick zum Hagen, Sabina Simon und Domenik Zimmermann.
Ich bedanke mich bei unserem Techniker Norbert Henn, dessen technische Lösungen und Verbesserungen von unschätzbarem Wert waren. Ebenso danke ich der Mechanik- und Elektronikwerkstatt, den Sekretariaten und allen Mitarbeitern des II. Physikalischen Instituts für die guten Rahmenbedingungen dieser Arbeit.
Ich danke der Deutschen Forschungsgemeinschaft für finanzielle Unterstützung durch das Projekt "Two dimensional cluster lattices on graphene moires on dense packed metal surfaces" und den Sonderforschungsbereich 608. Der Aufenthalt in Zagreb wurde finanziell durch den Deutschen Akademischen Austauschdienst ermöglicht.
Ich danke meinen Freunden und Kommilitonen, die mich seit Beginn meines Studiums begleitet haben, darunter insbesondere Vera Derya und Lars Kluge für das Korrekturlesen. Schön, dass wir die regelmäßigen Mensatreffen über Jahre aufrecht erhalten konnten.
Ich danke meinen Freunden und insbesondere meiner Familie, die mich in allen Lebenslagen immer unterstützt haben. Abschließend möchte ich dir, Konrad, dafür danken, dass du immer für mich da warst und viel Geduld, aber auch Interesse für meine Arbeit aufgebracht hast. Deine Unterstützung war, ist und bleibt durch nichts zu ersetzen.

Offizielle Erkärung

Ich versichere, dass ich die von mir vorgelegte Dissertation selbständig angefertigt, die benutzten Quellen und Hilfsmittel vollständig angegeben und die Stellen der Arbeit - einschließlich Tabellen, Karten und Abbildungen -, die anderen Werken im Wortlaut oder dem Sinn nach entnommen sind, in jedem Einzelfall als Entlehnung kenntlich gemacht habe; dass diese Dissertation noch keiner anderen Fakultät oder Universität zur Prüfung vorgelegen hat; dass sie - abgesehen von den angegebenen Teilpublikationen - noch nicht veröffentlicht worden ist, sowie, dass ich eine solche Veröffentlichung vor Abschluss des Promotionsverfahrens nicht vornehmen werde. Die Bestimmungen der Promotionsordnung sind mir bekannt. Die von mir vorgelegte Dissertation ist von Prof. Dr. Thomas Michely betreut worden.

Köln, 25. März 2014 Stefan Schumacher